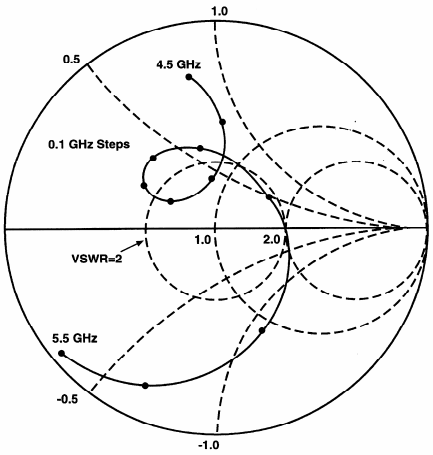

Applied Computational Electromagnetics Society Journal

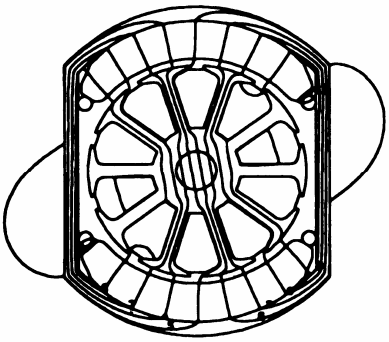

Editor-in-Chief
Atef Z. Elsherbeni

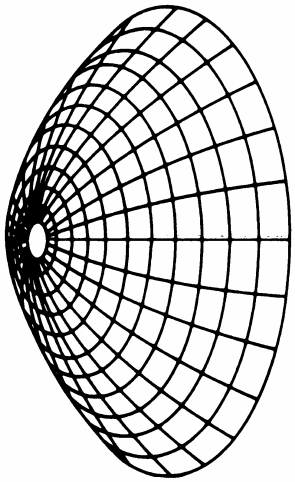

June 2009
Vol. 24 No. 3
ISSN 1054-4887

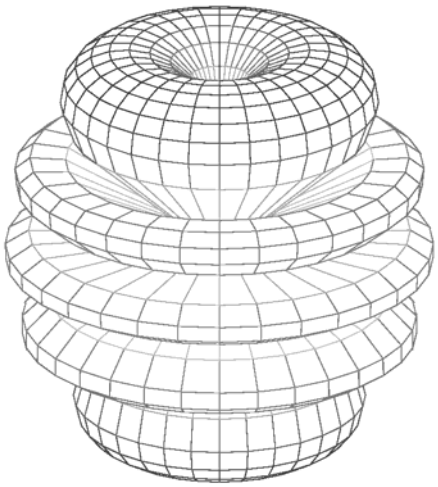

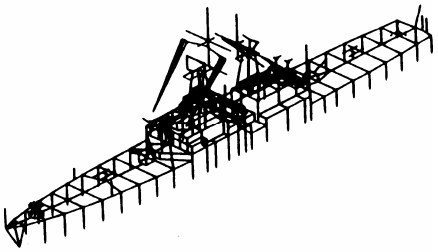

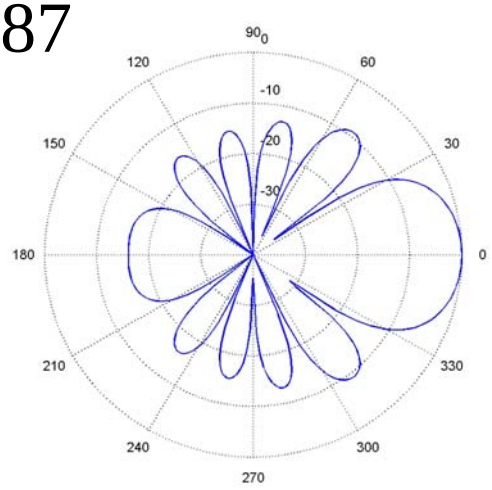

GENERAL PURPOSE AND SCOPE: The Applied Computational Electromagnetics Society ***(ACES)*** Journal hereinafter known as the ***ACES Journal*** is devoted to the exchange of information in computational electromagnetics, to the advancement of the state-of-the art, and the promotion of related technical activities. A primary objective of the information exchange is the elimination of the need to "re-invent the wheel" to solve a previously-solved computational problem in electrical engineering, physics, or related fields of study. The technical activities promoted by this publication include code validation, performance analysis, and input/output standardization; code or technique optimization and error minimization; innovations in solution technique or in data input/output; identification of new applications for electromagnetics modeling codes and techniques; integration of computational electromagnetics techniques with new computer architectures; and correlation of computational parameters with physical mechanisms.

SUBMISSIONS: The ***ACES Journal*** welcomes original, previously unpublished papers, relating to applied computational electromagnetics. Typical papers will represent the computational electromagnetics aspects of research in electrical engineering, physics, or related disciplines. However, papers which represent research in applied computational electromagnetics itself are equally acceptable.

Manuscripts are to be submitted through the upload system of ***ACES*** web site http://aces.ee.olemiss.edu See "Information for Authors" on inside of back cover and at ***ACES*** web site. For additional information contact the Editor-in-Chief:

Dr. Atef Elsherbeni
Department of Electrical Engineering
The University of Mississippi
University, MS 386377 USA
Phone: 662-915-5382 Fax: 662-915-7231
Email: atef@olemiss.edu

SUBSCRIPTIONS: All members of the Applied Computational Electromagnetics Society who have paid their subscription fees are entitled to receive the ***ACES Journal*** with a minimum of three issues per calendar year and are entitled to download any published journal article available at http://aces.ee.olemiss.edu.

Back issues, when available, are $15 each. Subscriptions to ***ACES*** is through the web site. Orders for back issues of the ***ACES Journal*** and changes of addresses should be sent directly to ***ACES***:

Dr. Allen W. Glisson
302 Anderson Hall
Dept. of Electrical Engineering
Fax: 662-915-7231
Email: aglisson@olemiss.edu

Allow four week's advance notice for change of address. Claims for missing issues will not be honored because of insufficient notice or address change or loss in mail unless the Executive Officer is notified within 60 days for USA and Canadian subscribers or 90 days for subscribers in other countries, from the last day of the month of publication. For information regarding reprints of individual papers or other materials, see "Information for Authors".

LIABILITY. Neither ***ACES***, nor the ***ACES Journal*** editors, are responsible for any consequence of misinformation or claims, express or implied, in any published material in an ***ACES Journal*** issue. This also applies to advertising, for which only camera-ready copies are accepted. Authors are responsible for information contained in their papers. If any material submitted for publication includes material which has already been published elsewhere, it is the author's responsibility to obtain written permission to reproduce such material.

APPLIED COMPUTATIONAL ELECTROMAGNETICS SOCIETY JOURNAL

Editor-in-Chief
Atef Z. Elsherbeni

June 2009
Vol. 24 No. 3
ISSN 1054-4887

The ACES Journal is abstracted in INSPEC, in Engineering Index, DTIC, Science Citation Index Expanded, the Research Alert, and to Current Contents/Engineering, Computing & Technology.

The first, fourth, and sixth illustrations on the front cover have been obtained from the Department of Electrical Engineering at the University of Mississippi.

The third and fifth illustrations on the front cover have been obtained from Lawrence Livermore National Laboratory.

The second illustration on the front cover has been obtained from FLUX2D software, CEDRAT S.S. France, MAGSOFT Corporation, New York.

THE APPLIED COMPUTATIONAL ELECTROMAGNETICS SOCIETY

JOURNAL

Vol. 24 No. 3 June 2009

TABLE OF CONTENTS

A Novel Space -Stepping Finite-Difference Frequency –Domain Method for Full Wave Electromagnetic Field Modeling of Passive Microwave Devices

[1] J. Mao, [1] L. Jiang, and [2] S. Luo

[1] School of Electronic, Information and Electrical Engineering, Shanghai Jiao Tong University, Shanghai, 200240, P. R. China (jfmao@sjtu.edu.cn, jianglele79@sjtu.edu.cn)
[2] Department of Electrical and Computer Engineering, Dalhousie University, Halifax, NS, B3J 1Z1, Canada (luos@dal.ca)

Abstract **–** In this paper a novel space-stepping finite-difference frequency-domain (SSFDFD) method is presented for the analysis of passive microwave devices. Unknown electromagnetic (EM) fields are solved from given EM fields at two initial planes space-step by space-step along a spatial direction. SSFDFD has the advantage over the traditional FDFD method in that all the EM field unknowns are local variables and the solution of a huge matrix equation is avoided. The stability condition for the SSFDFD method is derived as that for the finite-difference time-domain (FDTD) method. Application examples show that the stability condition is valid and the SSFDFD method is at least one magnitude faster than the traditional FDFD method with the same accuracy of analysis. SSFDFD has the potential to be a powerful and fast tool for full wave EM field modeling of passive microwave devices.

I. INTRODUCTION

Electromagnetic field analysis is very important in many scientific and technologic issues, among which full wave analysis has attracted much attention for high analysis accuracy at high frequencies. The finite -difference time-domain (FDTD) method has been one of the most widely used numerical full wave analysis methods. However, such time-domain simulations always consume huge computer time and memory space which is a big problem. The finite-difference frequency-domain (FDFD) method has been recognized as one of the most powerful numerical algorithms for full-wave solution of EM field problems because of its ability to take the frequency-dependent properties of material parameters into account [1, 2] and because FDFD simulates characteristics in the frequency domain directly. In FDFD the time variation of EM fields has the form of $e^{j\omega t}$ or e^{st}, thus the partial differential operator $\partial/\partial t$ in Maxwell's equations can be substituted with $j\omega$ or s. The remained spatial differential or integral Maxwell's equations are then approximated by central differences. The space grid mesh in FDFD is similar with the standard Yee's mesh of FDTD [3]. However, in all existing FDFD methods, the obtained difference equation is a very large matrix equation, the dimension of which is equal to the number N_v of the unknown EM field variables at all grid nodes. Although the coefficient matrix is a band diagonal matrix with bandwidth of 25, the number of multiplications needed to solve the equation by traditional Gauss elimination is still as large as N_v^{β} ($1.0<\beta<1.5$). In order to improve the efficiency of FDFD, some novel numerical methods usually used in circuit simulation, such as the CFH [4] and Pade approximation via Lanczos (PVL) [5, 6], have been implemented to accelerate the procedure for obtaining a response spectrum.

In Yee's FDTD, the EM fields can be solved from the initial condition (usually the electric fields at time t=0 and magnetic fields at time t=0.5Δt) time-step by time-step, and the EM fields at all grid nodes are local variables which are related only to the EM fields at the four surrounding nodes. Following this idea, a novel space-stepping finite-difference frequency-domain (SSFDFD) method is developed to analyze passive microwave devices. In SSFDFD, Maxwell's equations in the frequency-domain are first approximated with center difference, and a spatial coordinate axis, for example, the z-axis, is selected as the space stepping direction. Then the unknown EM fields are solved space-step by space-step along this space stepping direction from the given EM fields on two initial cross sectional planes perpendicular with the stepping direction. For passive microwave devices consist of waveguide structures, the longitude direction can be defined as the space stepping axis, and two transverse planes in the uniform guided wave structures can be chosen as the initial planes. All the EM fields to be solved at each node are local variables, which are related only to the EM fields at their neighboring nodes. Thus, the solution of a huge matrix equation as that in traditional FDFD is avoided. In SSFDFD, the number of multiplications for solution of all the unknown EM field variables is reduced to $2N_v$,

and much computer memory can be saved because at each space step only the EM fields on the planes under analysis need to be saved. Application examples show that SSFDFD is at least one magnitude faster than the traditional FDFD and the finite element method (FEM). Therefore, the SSFDFD method could be useful to solve complex microwave circuits.

In FDTD the space steps (Δx, Δy, and Δz) and time step (Δt) must satisfy a stability condition to guarantee the algorithm stability [3, 7]. In this paper, it is pointed out that, as with FDTD, there is a stability problem with SSFDFD. The space step size and the angular frequency must satisfy a condition to guarantee the stability of SSFDFD. If SSFDFD steps in the z-axis direction, then the stability condition for SSFDFD is,

$$2c_{\max}\sqrt{\frac{1}{(\Delta x)^2}+\frac{1}{(\Delta y)^2}} \le \omega \le \frac{2c_{\min}}{\Delta z}$$

where $c_{\max}$ and $c_{\min}$ are the maximum and minimum possible velocity of the EM waves in the media, respectively. For a given angular frequency ω, relatively smaller space step (Δz) in the stepping direction of the algorithm and larger space steps (Δx and Δy) in the cross sectional plane are required for the stability of SSFDFD. Also, for a given reasonable set of space steps, there is a frequency band in which SSFDFD is stable.

The validity, efficiency, and stability conditions of the proposed SSFDFD are tested and verified by simulating the EM field response of the TE_{10} mode in a rectangular waveguide containing a dielectric segment. Two cases where the permittivity of the dielectric segment is first constant and then frequency -dependent are considered.

II. SSFDFD ALGORITHM

In order to clearly illustrate the SSFDFD algorithm, the components of Maxwell's equations in the frequency-domain are written in a modified order as

$$\frac{\partial E_x}{\partial z} = \frac{\partial E_z}{\partial x} - j\omega\mu(\omega)H_y \tag{1}$$

$$\frac{\partial E_y}{\partial z} = \frac{\partial E_z}{\partial y} + j\omega\mu(\omega)H_x, \tag{2}$$

$$E_z = \frac{1}{j\omega\varepsilon(\omega)+\sigma(\omega)}\left(\frac{\partial H_y}{\partial x}-\frac{\partial H_x}{\partial y}\right), \tag{3}$$

$$\frac{\partial H_x}{\partial z} = \frac{\partial H_z}{\partial x} + j\omega\varepsilon(\omega)E_y + \sigma(\omega)E_y, \tag{4}$$

$$\frac{\partial H_y}{\partial z} = \frac{\partial H_z}{\partial y} - j\omega\varepsilon(\omega)E_x - \sigma(\omega)E_x, \tag{5}$$

$$H_z = \frac{1}{j\omega\mu(\omega)}\left(\frac{\partial E_x}{\partial y}-\frac{\partial E_y}{\partial x}\right) \tag{6}$$

where $\varepsilon(\omega)$, $\mu(\omega)$, and $\sigma(\omega)$ are the medium permittivity, permeability and conductivity, respectively, which can be frequency-dependent. Using the grid mesh in Fig. 1, equations (1) to (6) can be approximated by central difference as,

$$E_x(i,j,k+1) = E_x(i,j,k) + \frac{\Delta z}{\Delta x}\left[E_z(i+1,j,k) - E_z(i,j,k)\right] - j\omega\mu(\omega)\Delta z H_y(i,j,k) \tag{7}$$

$$E_y(i,j,k+1) = E_y(i,j,k) + \frac{\Delta z}{\Delta y}\left[E_z(i,j+1,k) - E_z(i,j,k)\right] + j\omega\mu(\omega)\Delta z H_x(i,j,k)\ , \tag{8}$$

$$E_z(i,j,k+1) = \frac{1}{\left(j\omega\varepsilon(\omega)+\sigma(\omega)\right)\Delta x}\left[H_y(i,j,k+1) - H_y(i-1,j,k+1)\right] - \frac{1}{\left(j\omega\varepsilon(\omega)+\sigma(\omega)\right)\Delta y} \cdot\left[H_x(i,j,k+1) - H_x(i,j-1,k+1)\right], \tag{9}$$

$$H_x(i,j,k+1) = H_x(i,j,k) + \frac{\Delta z}{\Delta x}\left[H_z(i,j,k+1) - H_z(i-1,j,k+1)\right] + \Delta z\left[j\omega\varepsilon(\omega)E_y(i,j,k+1) + \sigma(\omega)E_y(i,j,k+1)\right], \tag{10}$$

$$H_y(i,j,k+1) = H_y(i,j,k) + \frac{\Delta z}{\Delta y}\left[H_z(i,j,k+1) - H_z(i,j-1,k+1)\right] - \Delta z\left[j\omega\varepsilon(\omega)E_x(i,j,k+1) + \sigma(\omega)E_x(i,j,k+1)\right], \tag{11}$$

$$H_z(i,j,k+1) = \frac{1}{j\omega\mu(\omega)\Delta y}\left[E_x(i,j+1,k+1) - E_x(i,j,k+1)\right] - \frac{1}{j\omega\mu(\omega)\Delta x}\left[E_y(i+1,j,k+1) + E_y(i,j,k+1)\right]\ , \tag{12}$$

in which Δx, Δy , and Δz are grid sizes in the x, y, and z directions of the Cartesian coordinates, respectively. Next a spatial coordinate axis, for example, the z-axis, is

selected as the stepping direction of the algorithm to be developed for SSFDFD. For a given value of index k, suppose the EM fields $\varphi(i,j,k)$ for all i and j have already been obtained, then the fields φ $(i,j,k+1)$ for all i and j can be computed by the following procedure:

1. Compute $E_x(i,j,k+1)$ and $E_y(i,j,k+1)$ from equations (7) and (8).
2. Compute $H_z(i,j,k+1)$ from equation (12).
3. Compute $H_x(i,j,k+1)$ and $H_y(i,j,k+1)$ from equations (10) and (11).
4. Compute $E_z(i,j,k+1)$ from equation (9).

So, if we set the EM fields $\varphi(i,j,0)$ at $k=0$ (actually, E_x, E_y and H_z at plane $z=0$ and H_x, H_y and E_z at plane $z=0.5\Delta z$ in Fig. 1) as the given "initial" condition, then all the EM fields at $k > 0$ can be obtained space-step by space-step along the z-direction. The characteristic electrical parameters (such as the S-parameters) for the structure under analysis can be extracted from the obtained EM fields using the approach given in [2].

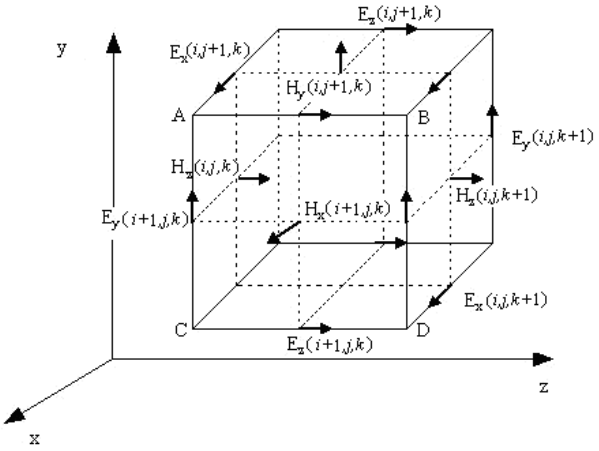

Fig. 1. The grid mesh for SSFDFD.

From the above SSFDFD algorithm, we can see that the unknown EM fields to be solved at each grid node are all local variables, which are only related to the EM fields at their four neighboring nodes. The solution of a huge matrix equation as required in the traditional FDFD method is avoided. The total number of multiplication operations of complex numbers to solve for all the N_v unknown EM field components with SSFDFD is $2N_v$, compared with the number N_v^{β} $(1.0<\beta<1.5)$ in traditional FDFD. Furthermore, significant computer memory can be saved with SSFDFD, because at each space step only the EM fields on the planes under analysis need to be saved.

The SSFDFD method can be used not only for waveguide structures, but also for open problems of EM field analysis. In an open space problem, absorbing boundary conditions (ABCs) can be used at the artificial computation boundaries in a similar way as in FDTD. But unlike in FDTD, the absorbing boundary condition is not necessary in SSFDFD for the two artificial computation boundaries perpendicular with the z-axis.

III. SSFDFD STABILITY CONDITION

It is found that, as with FDTD, there is the stability problem with SSFDFD. The space step size and the angular frequency must satisfy a condition to guarantee the stability of SSFDFD. The derivation of the stability condition for SSFDFD is similar to that for the FDTD stability condition [7]. For convenience, a normalized region of space with $\mu=1$, $\varepsilon=1$, and $\sigma=0$ is considered. Maxwell's equations can be written in the normalized space as,

$$j\nabla\times\vec{v}=\frac{\partial\vec{v}}{\partial t} \tag{13}$$

in which $\vec{v}=\vec{H}+j\vec{E}$. The frequency-domain form of equation (13) is,

$$\nabla\times\vec{V}=\omega\vec{V} \tag{14}$$

where $\vec{V}$ is the Fourier transform of $\vec{v}$. Suppose the SSFDFD algorithm steps in the z-axis direction, equation (14) is then rewritten as,

$$\nabla_t\times\vec{V}-\omega\vec{V}=-\frac{\partial\left(V_x\vec{a}_y-V_y\vec{a}_x\right)}{\partial z} \tag{15}$$

in which $\vec{a}_x$ and $\vec{a}_y$ are unit vectors in the x and y directions, respectively, and ∇_t is the lateral part of the operator ∇. The stability of a particular numerical representation of equation (15) can be examined simply by considering the following pair of eigenvalue problems,

$$-\frac{\partial\left(V_x\vec{a}_y-V_y\vec{a}_x\right)}{\partial z}=\lambda\left(V_x\vec{a}_y-V_y\vec{a}_x\right) \tag{16}$$

$$\nabla_t\times\vec{V}-\omega\vec{V}=\lambda\left(V_x\vec{a}_y-V_y\vec{a}_x\right). \tag{17}$$

SSFDFD employs central difference to approximate the derivative in Maxwell's equations. Using central difference for the derivative with respect to the z coordinate and letting $\vec{V}_n=\vec{V}(z=n\Delta z)$, equation (16) yields,

$$-\frac{\left(V_x\vec{a}_y - V_y\vec{a}_x\right)_{n+\frac{1}{2}} - \left(V_x\vec{a}_y - V_y\vec{a}_x\right)_{n-\frac{1}{2}}}{\Delta z} = \lambda\left(V_x\vec{a}_y - V_y\vec{a}_x\right)_n . \tag{18}$$

Defining a growth factor,

$$q = \left|\left(V_x\vec{a}_y - V_y\vec{a}_x\right)_{n+\frac{1}{2}}\right| / \left|\left(V_x\vec{a}_y - V_y\vec{a}_x\right)_n\right|$$

and substituting it into equation (18), we get,

$$q = -\frac{\lambda\Delta z}{2} \pm \left(1 + \left(\frac{\lambda\Delta z}{2}\right)^2\right)^{1/2} . \tag{19}$$

Algorithm stability requires $q \le 1$ for all possible spatial modes in the lattice. For this to occur,

$$\mathrm{Re}\,\lambda = 0,\ \left|\mathrm{Im}\,\lambda\right| \le \frac{2}{\Delta z} . \tag{20}$$

We now let,

$$\vec{V}(l,m) = \vec{V}_0 e^{-j(k_x l\Delta x + k_y m\Delta y)} \tag{21}$$

represent an arbitrary spatial mode. Using the central difference for the derivative with respect to x and y, we have,

$$\begin{aligned}\nabla_t \times \vec{V} &= \frac{\partial V_z}{\partial y}\vec{a}_x - \frac{\partial V_z}{\partial x}\vec{a}_y + \frac{\partial V_y}{\partial x}\vec{a}_z - \frac{\partial V_x}{\partial y}\vec{a}_z \\ &= -js_y V_z\vec{a}_x + js_x V_z\vec{a}_y - js_x V_y\vec{a}_z + js_y V_x\vec{a}_z \end{aligned} \tag{22}$$

where

$$s_x = 2\sin\left(\frac{k_x\Delta x}{2}\right)\Big/\Delta x,\ \ s_y = 2\sin\left(\frac{k_y\Delta y}{2}\right)\Big/\Delta y . \tag{23}$$

Substituting equation (22) into equation (17) yields,

$$-s_y V_z + j\omega V_x = j\lambda V_y \tag{24}$$

$$s_x V_z + j\omega V_y = -j\lambda V_x , \tag{25}$$

$$-s_x V_y + s_y V_x + j\omega V_z = 0 . \tag{26}$$

Solving equations (24) to (26), we get,

$$\lambda^2 = s_x{}^2 + s_y{}^2 - \omega^2 . \tag{27}$$

Substituting equation (27) into equation (20) yields the stability condition for SSFDFD,

$$s_x{}^2 + s_y{}^2 \le \omega^2 \le \left(\frac{2}{\Delta z}\right)^2 + s_x{}^2 + s_y{}^2 . \tag{28}$$

For any spatial modes in real media, equation (28) can be rewritten as,

$$2c\sqrt{\frac{1}{(\Delta x)^2} + \frac{1}{(\Delta y)^2}} \le \omega \le \frac{2c}{\Delta z} \tag{29}$$

where $c = 1/\sqrt{\mu\varepsilon}$ is the EM wave velocity in the real media. Considering that c is unknown and is not the same in different media region, equation (29) is modified as,

$$2c_{\max}\sqrt{\frac{1}{(\Delta x)^2} + \frac{1}{(\Delta y)^2}} \le \omega \le \frac{2c_{\min}}{\Delta z} \tag{30}$$

where $c_{\max}$ and $c_{\min}$ are the maximum and minimum velocity of EM waves in the media, respectively.

From the stability condition shown in equation (30) we can see that for a given angular frequency ω, a relatively smaller space step (Δz) in the stepping direction of the algorithm and larger space steps (Δx and Δy) in the cross sectional plane are required for the stability of SSFDFD, and that Δz must be smaller than Δx and Δy. The role of Δz in the stability condition of SSFDFD is similar with that of the time step Δt in the stability condition of FDTD. This is because a simulation with SSFDFD is supposed to iterate in the z-axis direction, while a simulation with FDTD iterates with increasing time t. From equation (30) we can also conclude that for a given reasonable set of space steps (Δx, Δy and Δz, $\Delta z<\Delta x$ and Δy), there is a frequency band in which SSFDFD is stable.

The stability condition in equation (30) is more difficult to satisfy for smaller ω. This is because the smaller ω is, the larger Δx and Δy are required to be to satisfy the stability condition, while in practical EM field simulations, Δx and Δy should not be too large in the interest of analysis accuracy.

IV. DISCUSSION OF SSFDFD

There are several points to be noted for the practical use of SSFDFD. The first is that, in equations (7) to (12) describing the proposed SSFDFD method, $E(i,j,k+1)$ and $H(i,j,k+1)$ are formally independent of $E(i,j,k+2)$ and $H(i,j,k+2)$ at the neighboring nodes. This is because SSFDFD simulates the frequency-domain steady-state EM field responses from the given EM fields at planes $z=0$ and $z=0.5\Delta z$, not the temporal propagation procedure of EM waves as FDTD does, although the stepping algorithm is employed in SSFDFD as in FDTD. It can be supposed that some harmonic incident EM waves

propagate in the $-z$ direction, react with (and may be multiply reflected between) the objects, and transmit through the two planes at z=0 and z=0.5Δz. When steady-state is reached after a long enough time and assuming that the steady-state EM fields at planes z=0 and z=0.5Δz are given (as in SSFDFD), then SSFDFD can be used to derive the EM field distribution of the steady-state response at z>0.5Δz. For given EM fields E_x, E_y and H_z at the z=0 plane and H_x, H_y and E_z at the z=0.5Δz plane, different incident EM waves are required for different objects. In the time domain and before steady-state is reached, $E(i,j,k+1)$ and $H(i,j,k+1)$ of course depend on $E(i,j,k+2)$ and $H(i,j,k+2)$ if there is an EM wave (either a reflected wave or a source wave) transmitting from $z=(k+2)\Delta z$ to $z=(k+1)\Delta z$. But at steady-state, the EM fields at the plane $z=k\Delta z$ contain the information of that at the plane $z=(k+2)\Delta z$, so the EM fields at the plane $z=(k+1)\Delta z$ can indeed be derived from those at the plane $z=k\Delta z$ according to the frequency-domain Maxwell's equations using a difference method as in SSFDFD. The steady-state EM fields at the plane $z=(k+1)\Delta z$ can also be derived from those at the plane $z=(k+2)\Delta z$ in a similar way. Actually, equations (7) to (12) are strictly derived from Maxwell's equations with no other approximations than the second order difference. The time-domain response can be obtained only by inverse Fourier transformation of the frequency -domain responses.

The second point is that, as the "initial" condition, the fields E_x, E_y and H_z at the plane z=0 and H_x, H_y and E_z at the plane z=0.5Δz cannot be arbitrarily given. These must be the sum of EM fields of actual propagation modes at the analysis frequency. In practical use, the position of z=0 and z=0.5Δz can be put within a uniform waveguide or at two parallel planes in free space for an open space problem, so that the mode fields at z=0 and z=0.5Δz are known or are able to be solved with a 2-dimensional (2-D) method such as the 2-D FDFD [8]. The physical insight of SSFDFD is to derive the EM field distribution of the steady-state response and the incident EM fields from the given EM fields at planes z=0 and z=0.5Δz. This is to say the "initial" planes (planes at z=0 and z=0.5Δz) in SSFDFD can be understood as the output port of the structure under analysis, where there are only EM waves propagating in the $-z$ direction. As a result, the EM fields E_x, E_y and H_z at the plane z=0 and H_x, H_y and E_z at the plane z=0.5Δz can be composed of any linear combination of the existing mode fields propagating in the $-z$ direction. In this way, the problem of the unknown ratio of the incident waves and reflected waves at the incident planes is avoided.

For a given incident wave, there may be evanescent waves and non-propagating waves at planes z=0 and z=0.5Δz resulting from the structure interaction. In SSFDFD, however, only existing propagation modes (eigen modes) in uniform waveguides or in free space are considered for giving the values of the EM fields E_x, E_y and H_z at the plane z=0 and H_x, H_y and E_z at the plane z=0.5Δz. This is reasonable for two reasons. One reason is that only the steady-state response of the EM fields is simulated by SSFDFD and the evanescent waves and non-propagating waves can be neglected. Another reason is that we can assume that the incident waves are so composed that the transmitted waves are exactly the given waves at the output port.

The third point concerns the case where there is a perfect conductor with the objects. The incident fields should be perturbed behind this conductor. However, it seems that calculating the EM wave going through the conductor from the output (i.e., from z=0 and z=0.5Δz) to the input with SSFDFD will not show any perturbation of the fields unless the structure is reached. But actually, considering that the task of SSFDFD is to derive the steady-state field distribution from the given response fields at the output planes (not from the incident fields), the perturbation effects of the conductor to the EM fields will be taken into account in the simulation results of the field distribution of the incident EM waves. The situation for a cavity structure is similar. Another confusion with a perfect conductor is that, if the grid mesh in Fig. 1 is used for the conductor, then the electric fields at the surface ABCD are tangential fields and should have a value of zero, while the simulated value from SSFDFD may not be zero. This confusion can be alleviated through moving the mesh surface ABCD by 0.5Δz along the z-direction, such that the electric fields on the surface are perpendicular and can be computed with SSFDFD. On the other five surfaces of the mesh of a perfect conductor, the EM fields are still tangential and the treatment of the electric boundary condition is similar to that in FDTD.

The last point concerns the stability condition. Suppose $\Delta x = \Delta y$, from equation (30) Δx and Δy must be larger than $\sqrt{2}\lambda_{\max}/\pi$ for the stability of SSFDFD, where $\lambda_{\max}$ is the maximum wavelength in the media. With such space steps, accuracy problems will be caused in an analysis of a steep distribution of EM fields and for small details of objects. Fortunately, although small Δx and Δy may make SSFDFD unstable, the phenomena of instability will occur only after a number of iterations of SSFDFD, and the analysis results along the z-direction before instability occurs can still be used. Our application practice indicates that the analysis results before instability occurs are always sufficient to reach an analysis target.

From the above discussion, although there are still some difficulties (especially the stability problem) with SSFDFD, it has great potential as a powerful and fast tool for full wave modeling of passive microwave

circuits, considering that it is a breakthrough in terms of analysis efficiency and computer memory.

V. APPLICATION EXAMPLES

To verify the proposed SSFDFD method, the steady-state EM field response of the TE_{10} mode in a rectangular waveguide containing a segment of dielectric (shown in Fig. 2) is simulated. We set the relative permittivity of the dielectric to be a constant, that is, ε_r=4.0 as the initial condition. The EM fields E_x, E_y and H_z at plane z=0 and H_x, H_y and E_z at plane z=0.5Δz are given with the value of the mode fields of TE_{10} wave propagating in the z-direction, and the steady-state response for incident waves from the other side of the dielectric segment is simulated. After the simulation with SSFDFD, the total fields including both the incident and the reflected waves are obtained within the dielectric segment and at the incident side of the dielectric segment.

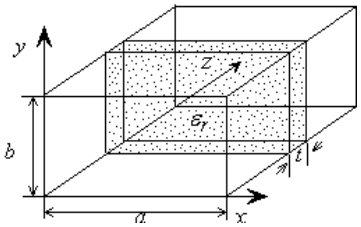

Fig. 2. Geometry of a dielectric loaded rectangular waveguide, where a=2cm, b=1cm, and the thickness of the dielectric segment is t=1.2 cm.

First the stability condition in equation (30) is tested. Because for the TE_{10} mode the EM fields are uniform in the narrow edge (y-axis) direction of the rectangular waveguide, the stability condition in equation (30) of SSFDFD becomes,

$$\frac{2c_{\max}}{\Delta x} \le \omega \le \frac{2c_{\min}}{\Delta z} \tag{31}$$

we set $c_{\max} = c_0$ and $c_{\min} = c_0/\sqrt{\varepsilon_r}$, where c_0 is the light velocity in vacuum. Suppose the analysis frequency is 40 GHz, the exact stability condition for the TE_{10} wave is $\Delta x \ge 0.2387$ cm, $\Delta z \le 0.1194$ cm. Practical simulations show that SSFDFD is stable when Δx=0.25 cm and Δz=0.11 cm, but is unstable when Δx=0.25 cm and Δz=0.12 cm, or when Δx=0.2 cm and Δz=0.11 cm. The distribution of the real part of the simulated complex electric field E_y along the longitudinal direction (z-axis direction) at x=0.5 cm with Δx=0.25 cm and Δz=0.11 cm is given in Fig. 3. Although the result is not accurate (compared with the result from Δx=0.25 cm and Δz=0.01 cm, which is also shown in Fig. 3) because of the large value of Δz, it is stable. The numerical results for the two unstable cases are shown in Fig. 4.

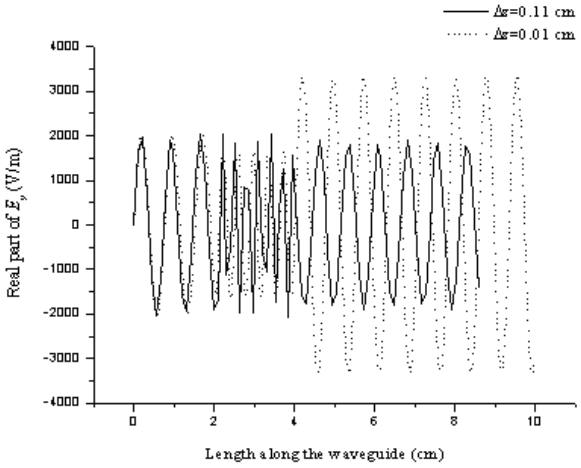

Fig. 3. Distribution of the real part of E_y along the z-axis in the dielectric loaded rectangular waveguide.

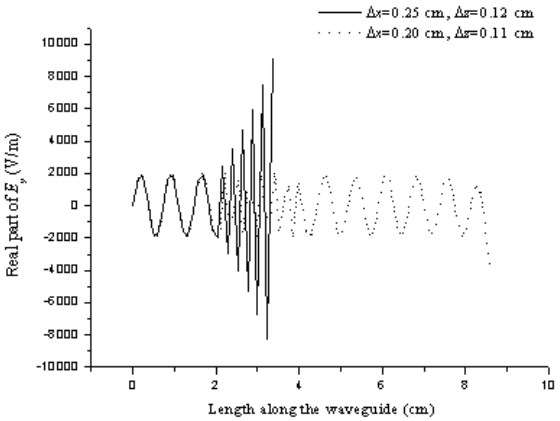

Fig. 4. Distribution of the real part of E_y along the z- axis in the two unstable cases.

Next the validity and efficiency of the proposed SSFDFD is tested. Let Δx=0.4 cm and Δz=0.05 cm in the simulation, then the frequency band where SSFDFD is stable is between 23.87 GHz and 95.49 GHz. If a frequency outside of the stable frequency band is simulated, the result will diverge with the stepping procedure. Figure 5 shows the unstable result at 10 GHz. From Fig. 5 we can see that, although the computation diverges, a slice of the result along the z-direction is correct and useful. The length of slice with correct results depends on the dielectric. If the length of the structure under analysis is shorter than the length in the z-direction where SSFDFD doesn't diverge, SSFDFD can still be used for the frequencies outside of the stable band. In Fig. 5 SSFDFD doesn't diverge until z=7 cm, then if the distance between the input port and output

port is less than 7 cm, correct S-parameter results are still available. Actually we set the ports separation to 6 cm, between which the dielectric segment is included. The obtained S-parameters are plotted in Fig. 6 for comparison the results from traditional FDFD and FEM are given as well, showing that excellent agreement is achieved. The computation times for the different methods are listed in Table 1.

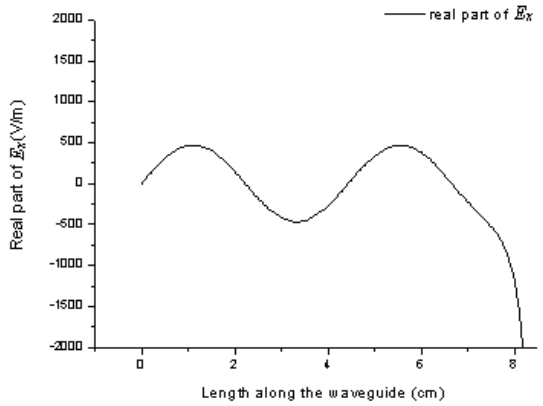

Fig. 5. Distribution of the real part of Ex along the z-axis at f=10.0 GHz.

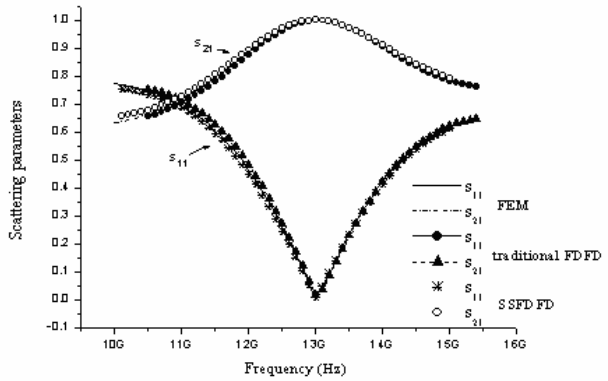

Fig. 6. Magnitude of the S-parameters from three different methods.

Table 1. Efficiency comparison among different approaches: SSFDFD, traditional FDFD, FEM with discrete frequency sweep and FEM Adaptive Lanzcos-Pada Sweep (ALPS). The CPU time is that for getting the curves in Fig. 6.

	SSFDFD	FDFD	FEM (discrete)	FEM (ALPS)
Mesh grids	3000 cubes	3000 cubes	3051 tetrahedra	3051 tetrahedra
CPU time	3 sec.	3 min. 20 sec.	4 min. 18 sec.	1 min. 19 sec.

These results are obtained with an Intel Pentium-IV 1.6 GHz computer, and using MATLAB software and ANSOFT HFSS software, respectively. From Table 1, we can see that the SSFDFD method is at least one order of magnitude faster than traditional FDFD, FEM and FEM's Adaptive Lanzcos-Pada Sweep (ALPS) which is a fast sweep approach. An algorithm for solving sparse matrix equations was used in the traditional FDFD. If compared with the FDTD method, suppose 1000 time steps are needed for FDTD to converge to a result and 100 sample frequencies are needed for SSFDFD to get a response spectrum, then, theoretically, SSFDFD should be 10 times faster than FDTD. Figure 7 gives the simulated S-parameters with SSFDFD for a wider range of frequencies.

As a second case of the above example, the dielectric segment is next supposed to be Lorentz material [9] with a frequency-dependent complex permittivity defined by,

$$\vec{D}(\omega) = \varepsilon_0(\varepsilon_\infty + \chi(\omega))\vec{E}(\omega)$$
$$\chi(\omega) = \frac{(\varepsilon_s - \varepsilon_\infty)\omega_0^2}{\omega_0^2 + j\,2\omega\delta - \omega^2} \tag{32}$$

where $\vec{E}(\omega)$ is the electric field vector, $\vec{D}(\omega)$ is the electric flux density vector, $\chi(\omega)$ is the electric susceptibility function, ε_0 is the permittivity in vacuum, ε_∞ is the limiting permittivity at infinite frequency, ε_s is the permittivity at zero frequency, ω_0 is the resonant frequency, and δ is the damping coefficient. For the Lorentz material in this example, $\varepsilon_\infty = 4.3$, $\varepsilon_s = 6.0$, $\omega_0 = 50\pi \times 10^9$, $\delta = 0.001\omega_0$, and $\sigma = 0$. We calculate the S-parameters for a frequency range from 10 GHz to 16 GHz by SSFDFD and compare the results in Fig. 8 with those from the FEM method. The results agree well as shown in Fig. 8, indicating that SSFDFD is able to simulate a frequency-dependent dielectric as well. The simulation efficiency is the same as that of the first case with constant dielectric permittivity.

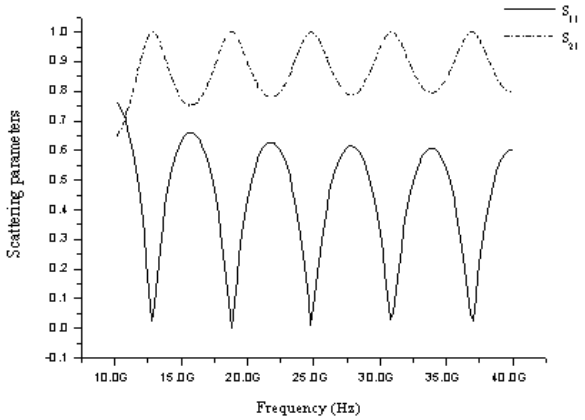

Fig. 7. Magnitude of the S-parameters from SSFDFD for a wider range of frequency.

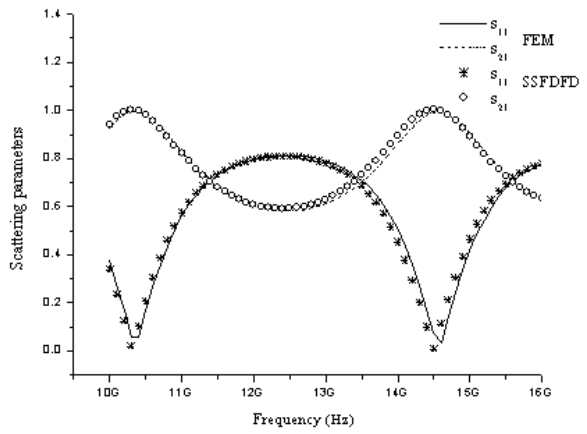

Fig. 8. Magnitude of the S-parameters from SSFDFD and FEM for the case of frequency-dependent complex dielectric permittivity.

VI. CONCLUSION

A novel SSFDFD method is presented in this paper for full wave EM field modeling of passive microwave devices. In SSFDFD all EM fields are local variables, which can be solved from the given EM fields at the initial planes space-step by space-step along a coordinate direction. The solution of a huge matrix equation as in the traditional FDFD is avoided, making the proposed SSFDFD at least one magnitude faster than the traditional FDFD, FEM and FDTD methods under the precondition of keeping similar simulation accuracy. Also, significant computer memory can be saved. The stability condition for SSFDFD is derived and analyzed. SSFDFD has great potential as a powerful and fast tool for full wave EM field analysis of guided wave structures, although much work is still required to make it practically applicable to some complex problems of microwave circuits.

ACKNOWLEDGMENT

This work was supported by National Basic Research Program of China (2009CB320200).

REFERENCES

[1] A. Christ and H. Hartnagel, "Three-dimensional finite-difference method for the analysis of microwave-device embedding," *IEEE Trans. Microwave Theory Tech.*, vol. 35, no. 8, pp. 688-695, Aug. 1987.

[2] S. Haffa, D. Hollmann, and W. Wiesbeck, "The finite difference methods for S-parameter calculation of arbitrary three-dimensional structures," *IEEE Trans. Microwave Theory Tech*., vol. 40, no. 8, pp. 1602-1610, Aug. 1992.

[3] K. Yee, "Numerical solution of initial boundary value problems involving Maxwell's equations in isotropic media," *IEEE Trans. Antennas Propagation*, vol. 14, no. 5, pp. 302-307, May 1966.

[4] M. Li, Q. Zhang, and M. Nakhla, "Finite difference solution of EM fields by asymptotic waveform techniques," *IEE Proceedings Microwaves, Antennas and Propagation*, vol. 143, no. 6, pp. 512-520, Dec. 1996.

[5] R. Remis and P. Van Den Berg, "A modified Lanczos algorithm for the computation of transient electromagnetic wavefields," *IEEE Trans. Microwave Theory Tech*., vol. 45, no. 12, pp. 2139-2149, Dec. 1997.

[6] T. Zhou, S. Dvorak, and J. Prince, "Application of the Pade approximation via Lanczos (PVL) algorithm to electromagnetic systems with expansion at infinity," *Electronic Components and Technology Conference, 2000,* pp. 1515 –1520, May. 2000.

[7] A. Taflove and M. Brodwin, "Numerical solution of steady-state electromagnetic scattering problems using the time dependent Maxwell's equations," *IEEE Trans. Microwave Theory Tech.*, vol. 23, no. 8, pp. 623-630, Aug. 1975.

[8] L.-Y. Li and J.-F. Mao, "An improved compact 2-D finite-difference frequency-domain method for guided wave structures," *IEEE Microwave and Wireless Components Letters*, vol. 13, pp. 520-522, Dec. 2003.

[9] F. Edelvik and B. Strand, "Frequency dispersive materials for 3-D hybrid solvers in time domain," *IEEE Trans. Antennas Propagation*, vol. 51, pp. 1199-1205, June 2003.

Junfa Mao (M'92–SM'98) was born in 1965. He received the B.S. degree in radiation physics from the University of Science and Technology of National Defense, China, in 1985, the M.S. degree in experimental nuclear physics form Shanghai Institute of Nuclear Research, Shanghai, China, in 1988, and the Ph.D. degree in electronic engineering from Shanghai Jiao Tong University, Shanghai, China, in 1992. Since 1992, he has been a Faculty Member in the Department of Electronic Engineering, Shanghai Jiao Tong University, Shanghai, China, where he is currently a chair professor. He was a visiting scholar at the Chinese University of Hong Kong, Hong Kong, from 1994 to 1995, and a postdoctoral researcher at the University of California, Berkeley, from 1995 to 1996. His research interests include the interconnect and EMC problem of high-speed integrated circuits and system, analysis and

design of microwave circuits. He has authored or coauthored more than 130 journal papers and 60 international conference papers. Dr. Mao earned the National Natural Science Award of China in 2004 and the National Technology Invention Award of China in 2008, earned the Best Paper Award of 2008 Symposium of APEMC in conjunction with 19th International Symposium of Zurich EMC. He is a Cheung Kong Scholar of the Ministry of Education, China, an Associate Director of the Microwave Society of China Institute of Electronics, and the 2007–2008 Chair of the IEEE Shanghai Section. He was a Topic Expert of the High-Tech Program of China during 2001–2003, an Associate Dean of the School of Electronic, Information and Electrical Engineering, Shanghai Jiao Tong University, from 1999 to 2005.

Lele Jiang was born in 1979. She received the B.S. degree in communication engineering and the M.S. degree in electromagnetic field and microwave technique from Anhui University, Hefei, Anhui, China, in 2001 and 2004, respectively. She is currently pursuing the Ph.D. degree at the Department of Electronic Engineering, Shanghai Jiao Tong University, Shanghai, China. Her research interests include numerical modeling and simulation, RF circuit design, interconnect and EMC problems of high-speed integrated circuits and system.

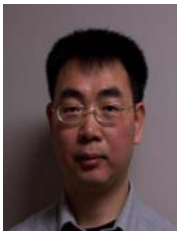

Shuiping Luo received the B.S. degree from University of Electronic Science and Technology of China, Chengdu, China, in 1989, the M.S. degree from Shanghai Jiao Tong University, Shanghai, China, in 1992, and the Ph.D. degree from Dalhousie University, Halifax, NS, Canada, in 2007. From March 1992 to March 1996, he was an Instructor in the Department of Electronic Engineering, Shanghai Jiao Tong University, Shanghai, China. From March 1996 to April 2000, he was a Software Engineer in Shanghai Bell Company, Shanghai, China. From November 2000 to May 2001, he was a Software Developer in Nortel Networks, Ottawa, ON, Canada. Currently, he is working on wireless sensor networks at Cape Breton University, Sydney, NS, Canada. His research interests include numerical modeling and simulation, RF circuit design, wireless communications, and real-time embedded systems.

A Comparison Among Fast Visibility Algorithms Applied to Computational Electromagnetics

[1] J. G. Meana, [1] F. Las-Heras, and [2] J. Á. Martínez-Lorenzo

[1] Área de Teoría de la Señal y Comunicaciones, Campus de Viesques, Gijón, University of Oviedo, Spain
[2] The Gordon CenSSIS, Northeastern University, Boston, MA, USA
jmeana@tsc.uniovi.es

Abstract – This paper presents a set of fast algorithms developed for solving the visibility problem in large complex geometric scenarios. The implemented algorithms are: *Binary Space Partitioning (BSP)* –based on a binary tree structure- and three new ones: *Trimming Method* – facets which are partially occluded are trimmed –, *Cone Method* – a cone emerges from the point of view to discard shadowed facets – and *Pyramid Method* – a pyramid is used to eliminate non-lit patches – . All the proposed algorithms are tested on a pair of scenarios for determining the field of view of electromagnetic waves in order to calculate the corresponding induced currents on the surfaces. The scenarios consist of two electrically large spheres and two PEC plates respectively where the surfaces are meshed with a variable number of flat triangular patches. The first reflection contribution is calculated using Physical Optics (PO) for both cases. The results show that the computational time can be drastically reduced by assuming small percentage of error in the computed scattered fields.

I. INTRODUCTION

Fast interrogation techniques for distinguishing between shadowed and lit regions, relative to a source point, are important in many computational-engineering areas including: image processing, virtual reality, video games and electromagnetic problems. Radar applications and radio-electric coverage are examples of electromagnetic problems where this distinction is necessary. In this way, the existence of line of sight between observation and source points can be one of the most consuming activities to afford at complex scenarios.

Traditional software methods, such as Painter's or Z-buffer algorithms [1-3], were applied successfully for solving the visibility problem. These methods have been combined with some pre-processing techniques to accelerate the basic algorithms. One of those techniques consists of grouping many planar facets into parallelepipedic or conical macro-domains. This information is then used to perform a first interrogation at the macro-domain level and discard some of them based on the source and observation points. Finally, a refined interrogation at the facet level is performed and, as a result, a high amount of computational time is saved. *Space Volumetric Partitioning* (SVP) or *Angular Z-buffer* (AZB) algorithms are good examples of this pre-processing technique [4-7].

Currently, a wide variety of the visibility problems can be solved in a fast way by employing GPU's [8] instead of CPU's. Good examples of this concept can be found in the literature [9, 10]. In [9] a specialized graphic card was introduced into a personal computer in order to compute real-time RCS. Its main disadvantage is that it implies the building of machine dependent software. On the other hand, non real-time solutions, but suitable for many applications, can also be performed by means of low cost generic graphic cards. The interface for communicating with the generic graphic card is done by using a set of libraries like DirectX or OpenGL [11]. One of the flaws in the latter method is that these libraries do not allow extracting the required information directly without first depicting the geometry. This depicting step is of no interest in applications where the main goal of the problem is not a graphical representation of the data as it implies an increase in the computational cost. This is the case of some electromagnetic problems -like radio-electric coverage or RCS applications- where the required information consists in getting mathematical structures indicating the facets in the scenario a point source is able to see for a set of sweeping angular directions. At this point, a return to the traditional geometric algorithms can be thought as a suitable solution for the problem. As a response to this requirement, new efficient and faster than traditional algorithms are investigated and presented in this paper.

The main features of the proposed techniques in the resolution of the visibility problems are: hierarchical classification and storage in *BSP*, accurate determination of visible geometry in *Trimming*, fast discrimination in *Cone* and *Pyramid Methods*.

The paper structure is as follows: the next section presents and describes step by step how the four visibility algorithms -*Binary Space Partitioning*, *Trimming Method*, *Cone Method* and *Pyramid Method*- work; the third section presents the numerical examples where all

the algorithms are tested and compared. The paper is closed with conclusion that summarizes the performance of each algorithm based on accuracy and computational cost.

II. ALGORITHMS DESCRIPTION

This section describes, step by step, all visibility algorithms. The mathematical notation and symbols are summarized in Table 1. The visibility algorithms satisfy the following conditions:

- The geometry is supposed to be modelled with flat triangular patches. As a consequence, the algorithms are optimized to these particular facets.
- The normal vector criterion is always taken in consideration. If the angle between the position vector and the outward normal vector of the patch is in the interval [-90º, 90º], the facet must be eliminated.

A feature to underline is that the source point **s** is located at the origin of the Cartesian coordinate system in order to simplify the equations. Any other emplacement can be considered by means of a translation transformation.

Table 1. Nomenclature for the visibility algorithms.

NOMENCLATURE		
Symbol	Description	Components
s	Source point	$(0,0,0)$
$\hat{t}$	Unitary target direction	(t_1,t_2,t_3)
$\hat{n}^i$	Unitary normal outward vector to facet i	(n_1^i,n_2^i,n_3^i)
$\mathbf{P}_c^i$	Barycentre of facet i	$(P_{c1}^i,P_{c2}^i,P_{c3}^i)$
$\mathbf{V}_l^i$	Vertices of facet i ($l=1,2,3$)	$(V_{l1}^i,V_{l2}^i,V_{l3}^i)$
P	Generic point	(x,y,z)
F_i	Facet i	---
´	Prime coordinates denote projection onto a plane.	---

A. BSP

Binary Space Partitioning algorithm (*BSP*) [12, 14] envelops a hierarchical structure (binary tree) in which all the patches can be arranged easily. First, a facet is randomly taken as reference (this is the root of the binary tree). The plane in which this triangle is contained splits the space into two subspaces (front and back). Therefore, some other patches could be intersected by this plane. In such a situation, every intersected patch would generate two new flat polygons (usually a triangle and a quadrilateral –discretized in two triangles–) One belongs to the front-half-space and the other to the back-half-space. All the patches (new and original) located in the front-half-space will take place in the left subtree while the back-half-space ones will do it in the right. For every subspace a new reference is chosen. This is inserted in the BSP tree as a node and the whole process is repeated recursively. When one facet is the unique element in a half-space, the patch acts as a leaf in the tree and the recursion finishes.

The relationship among different nodes in the binary tree remains invariable even though the location of the source would change. Consequently the tree needs to be built only once and its computational cost t_{Build} is [15],

$$(N+1)\log_2(N+1) \le t_{Build} \le \frac{N^2}{2} \qquad (1)$$

where N is the number of facets.

BSP algorithm is able to extract a list of patches which can be seen from a point of view when the direction of the target is specified. In order to extract those elements, the binary tree is walked and the decision of including the triangle in the list or not depends basically on the angle between the target direction and the outward normal vector of the patch (a parallel projection onto a plane perpendicular to the target vector is accomplished). This operation implies a linear cost t_{Walk} [15],

$$t_{Walk} = \Theta(N). \qquad (2)$$

The list resulting from walking the tree satisfies that the nth element could be occluded by elements 1 to n-1 (it is not necessary to test all the pairs of patches in the geometry). Therefore an additional algorithm to know whether a facet obscures other patches is indispensable.

One of the disadvantages to underline is that the parallel projection restricts the scope to scenarios where the point of view is situated far from the observation points. Otherwise, the hierarchical structure can be useful in other applications apart from visibility.

Our implementation classifies the patches in front-half-space or back-half-space based on the coordinates of the barycentre. As a result, the process of clipping the intersected patches is avoided and kept back to the *Trimming Method*.

B. Trimming Method

The *Trimming Method* is the most accurate visibility algorithm due to the fact that the output geometry coincides exactly with the lit zones. Every partially lit facet is trimmed, so new completely lit and completely shadowed polygons appear. This is an exact solution to avoid fixing a threshold for deciding whether a partial occluded triangle is viewed or not.

First, the *N* facets (shown in Fig. 1 (a)) are sorted by their distance from the source point **s** with indexes $i=1,2,\ldots,N$ (this is one of the basic actions to go into when a visibility problem must be solved). The nearest

facet F_1 can always be seen (marked in Fig. 1 (b)). The projection plane is defined by the target direction $\hat{t}$ and the barycentre of the furthest facet $\mathbf{P}_c^N$ and its equation can be written as,

$$\hat{t}\cdot\left(\mathbf{P}-\mathbf{P}_c^N\right)=0 \tag{3}$$

(the projection plane has also been depicted in Fig. 1 (b)).

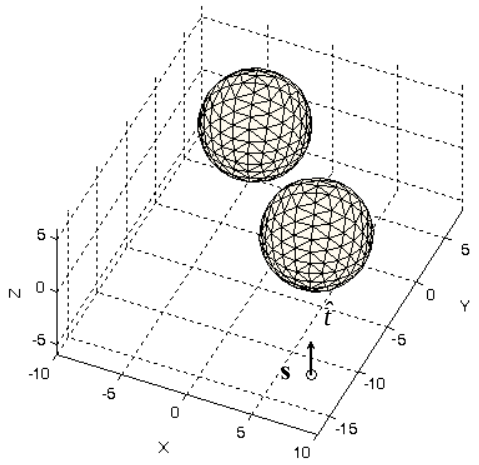

(a)

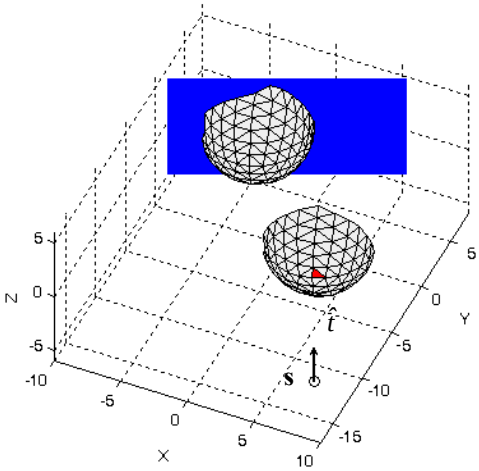

(b)

Fig. 1. (a) The original geometry, source point $\mathbf{s}$ and target direction $\hat{t}$. (b) Facets which verify the normal criterion. The nearest facet to the source point has been marked. The projection plane has been depicted too.

The three vertices $\mathbf{v}_d^i$ $(d=1,2,3)$ of each triangular patch $(i=1,2,\ldots,N)$ are projected onto the above mentioned plane by performing a perspective projection whose focus is the source point $\mathbf{s}$. The coordinates $\mathbf{P}'(x,y,z)$ of the projection of a generic point $\mathbf{P}(x,y,z)$ are,

$$\mathbf{P}' = \left(\hat{t}\cdot\mathbf{P}_c^N\right)\left[\left(\hat{t}\cdot\left(1,\frac{y}{x},\frac{z}{x}\right)\right)^{-1}\hat{x}+\left(\hat{t}\cdot\left(\frac{x}{y},1,\frac{z}{y}\right)\right)^{-1}\hat{y}+\left(\hat{t}\cdot\left(\frac{x}{z},\frac{y}{z},1\right)\right)^{-1}\hat{z}\right]. \tag{4}$$

Now let's take $\mathbf{P}_c^N=\mathbf{P}_c^{N'}$ the origin of a new rectangular coordinate system whose orthogonal vector basis is $[\hat{t},\hat{u},\hat{v}]$ where,

$$\hat{u}=\frac{\mathbf{V}_2^{N'}-\mathbf{V}_1^{N'}}{\left|\mathbf{V}_2^{N'}-\mathbf{V}_1^{N'}\right|} \tag{5}$$

and

$$\hat{v}=\frac{\hat{t}\times\hat{u}}{\left|\hat{t}\times\hat{u}\right|}. \tag{6}$$

It is clear that every point $\mathbf{P}'(t,u,v)$ in the projection plane can be expressed as,

$$\mathbf{P}'(t,u,v)=0\,\hat{t}+u\,\hat{u}+v\,\hat{v}=\mathbf{P}'(x,y,z)-\mathbf{P}_c^N \tag{7}$$

with

$$u=\left(\mathbf{P}'(x,y,z)-\mathbf{P}_c^N\right)\cdot\hat{u}\,, \tag{8}$$

$$v=\left(\mathbf{P}'(x,y,z)-\mathbf{P}_c^N\right)\cdot\hat{v}\,. \tag{9}$$

This transformation will be helpful to carry out union and intersection operations in two dimensions. Figure 2 shows the projection plane and all the projected triangular patches of the geometry in u-v coordinates.

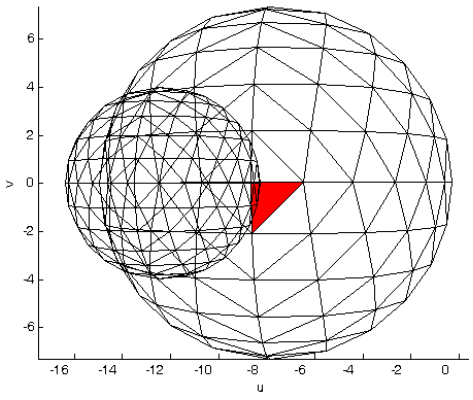

Fig. 2. Projection of the triangular patches onto the projection plane (u-v coordinates). The nearest facet is marked.

Afterward, the *test polygon O* is created with the aim of keeping updated the piece of surface associated with lit facets in the iteration i (i=1,2,...,N). That is, at the beginning,

$$O_1 = F_1 . \tag{10}$$

The next facet to consider is F_2. Therefore an intersection operation between the *test polygon* and F_2 is performed. If the result is the empty set, the triangular patch F_2 will join the *test polygon* as an independent domain. If both the *test* and F_2 share a piece of surface the updated *test polygon* O_2 will result from the union operation between that polygon and the facet F_2. The algorithm iterates over all the facets.

$$O_i = O_{i-1} \cup \left(F_i - \left(O_{i-1} \cap F_i\right)\right) \quad i = 2,3,\ldots,N . \tag{11}$$

Figure 3 summarizes different relative positions of the facet F_i and the *test polygon*.

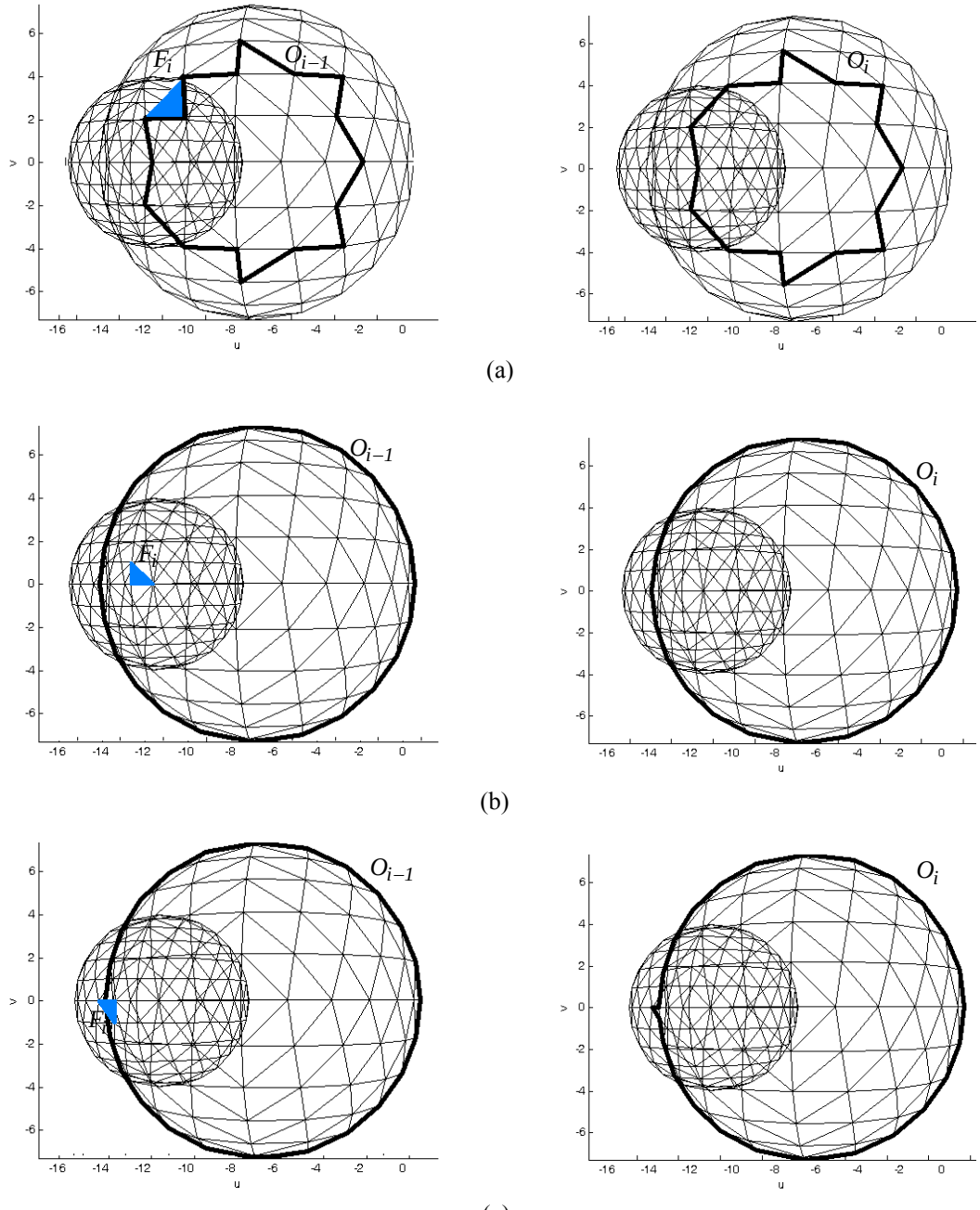

Fig. 3. Example of relative positions. Left, *test polygon* O_{i-1} and facet F_i. Right, *test polygon* O_i . (a) The facet is completely added to O_{i-1}. (b) The triangular patch is inside the test polygon. No modification of O_{i-1} occurs. (c) The facet is trimmed due to the intersection with O_{i-1}.

The following step consists of a reference system transformation and an inverse perspective projection to retrieve the 3D original coordinates (see Fig. 4). The trimmed geometry is made of the vertices in the *test polygon*. Nevertheless, a table which matches every projected point $\mathbf{P}'$ with its corresponding facet i has been previously filled (the projection of various points can coincide).

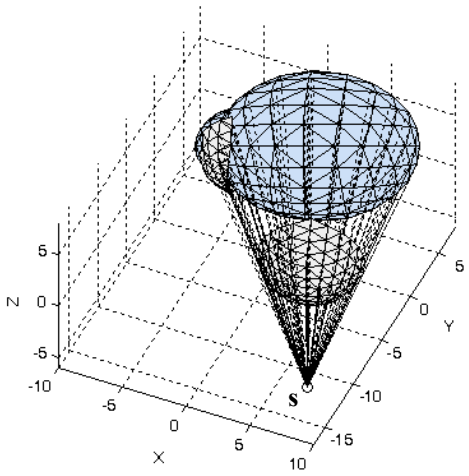

(a)

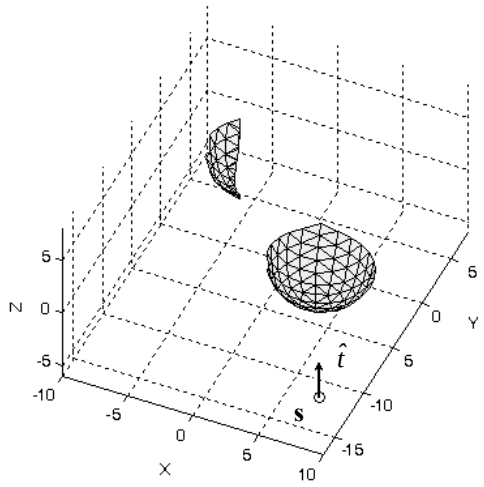

(b)

Fig. 4. (a) Inverse perspective projection of the trimmed facets. (b) Geometry after applying *Trimming method*.

An identical scheme can be maintained with two or more equally spaced projection planes (a division with dependence on the distance –in the plane XY– from the source point is now implemented). Let's denote B_1 the furthest projection plane from $\mathbf{s}$ and B_M, the nearest one (Figure 5 depicts three projection planes). A point $\mathbf{P}$ is located between two projection planes B_m and B_{m+1} when,

$$\left.\begin{aligned}\hat{t}\cdot\mathbf{P}+D_m>0\\ \hat{t}\cdot\mathbf{P}+D_{m+1}<0\end{aligned}\right\} \qquad (12)$$

where m ranges from 1 to M-1 and D_m depends on the distance from B_m to the source point $\mathbf{s}$. Note that all the projection planes are parallel to B_1 and, consequently, the normal vector is the same $\hat{t}$ for all of them.

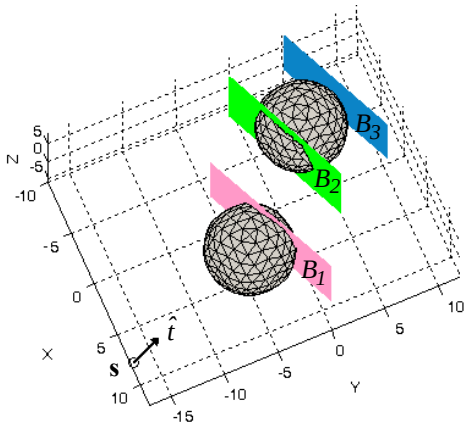

Fig. 5. Example of three projection planes ($M=3$) in the *Trimming Method*.

The process starts with the facets in front of B_M. The resulting *test polygon* O_N is utilized as a filter to discard facets for B_{M-1}.This process is faster than making the comparison facet per facet. In spite of this, a previous trimming operation is carried out for the first *M-1* planes. As a consequence, the location of the source, $\mathbf{s}$, the target direction , $\hat{t}$, and the number of facets, N, influence the reduction (or increase) of the computational time.

The main advantage, accuracy, has already been discussed but the complexity of the algorithm because of union and intersection operations leads to a high computational cost in comparison with other methodologies (see Section III). Likewise, the trimming process implies the generation of new facets. Therefore, the mesh will contain more triangles and the deviation from their mean size would be, in general, greater than the original one.

C. Cone Method

This method employs an approximation from triangles to circles in order to accelerate the process of reckoning visibility.

A facet F_j is selected to compute shadow and lit regions. The source point $\mathbf{s}$ and each of the three vertices $\mathbf{V}_1^j$, $\mathbf{V}_2^j$, $\mathbf{V}_3^j$ define the segments $\overline{\mathbf{sV}_1^j}$, $\overline{\mathbf{sV}_2^j}$, $\overline{\mathbf{sV}_3^j}$. The angles between those segments and the target

direction $\hat{t}$ are denoted by γ_1^j, γ_2^j, γ_3^j respectively. Then, the opening angle α^j can be easily calculated by weighting γ_1^j, γ_2^j and γ_3^j and stored for subsequent comparisons,

$$\alpha^j = \sum_{l=1}^{3} c_l \gamma_l^j \tag{13}$$

with c_l representing the weighting coefficients.

With the purpose of clarifying the procedure, Fig. 6 is presented: suppose that the three vertices $\mathbf{v}_l^j$ and the barycentre $\mathbf{p}_c^j$ are projected onto a plane perpendicular to the target direction $\hat{t}$, the same way *Trimming Method* does. Provided that $\mathbf{v}_l^{j'}$ and analogically $\mathbf{p}_c^{j'}$ are obtained from equation (4), the α^j value determines the radius R^j of the right cone whose axis is parallel to $\hat{t}$.

Any point in shadow will be situated behind the plane which contains the triangular patch F_j,

$$\hat{n}^j \cdot \left(\mathbf{P} - \mathbf{P}_c^j\right) < 0 \tag{14}$$

and inside the right cone previously defined. Therefore, in a local Cartesian coordinate system where the source point is in the origin, the angle between the position vector of that point and the target direction $\hat{t}$ must be smaller than the opening angle α^j,

$$\cos^{-1}\left(\frac{\mathbf{P}\cdot\hat{t}}{|\mathbf{P}|}\right) < \alpha^j . \tag{15}$$

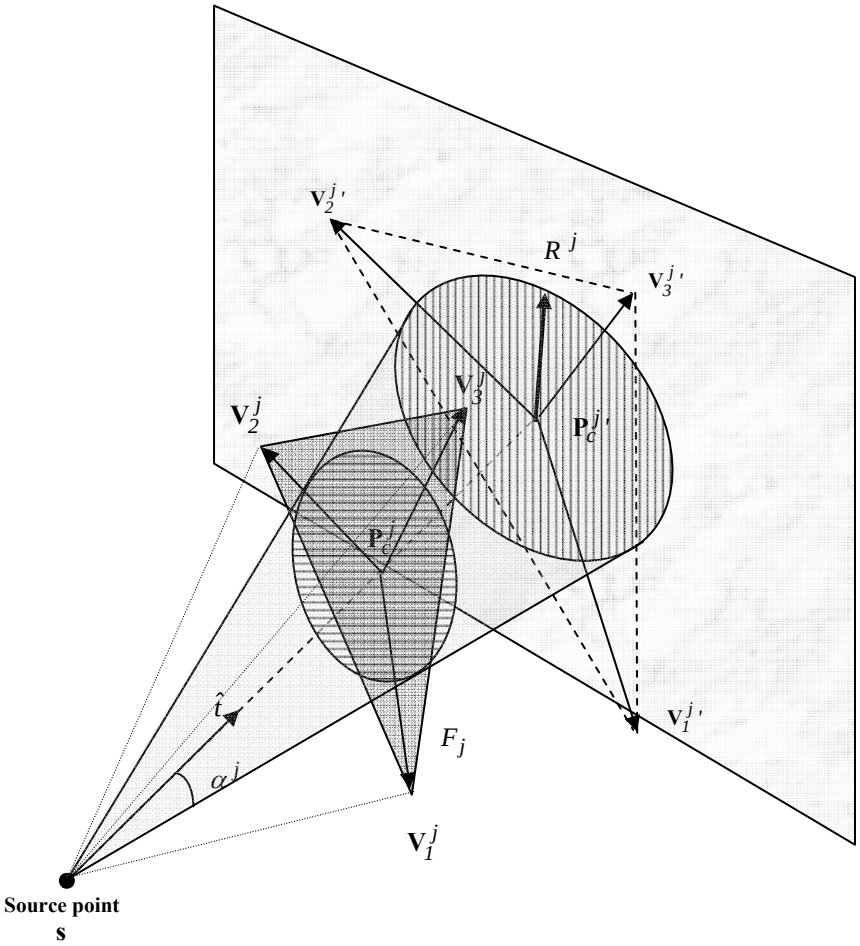

Fig. 6. *Cone Method*. The angle between the segments $\overline{\mathbf{sv}_1^j}$, $\overline{\mathbf{sv}_2^j}$, $\overline{\mathbf{sv}_3^j}$ and the target direction $\hat{t}$ is weighted so the opening angle α^j is obtained and consequently the radius of the cone R^j. Every facet whose barycentre $\mathbf{p}_c^i$ ($i \neq j$) is located inside the cone and behind the triangular patch F_j is assumed to be occluded.

The key of the accuracy in the *Cone Method*, apart from the number of points which characterizes a facet, is the choice of the factor which weights the angles γ_l^j: a great factor would not eliminate some contiguous triangular patches but a small one would keep some occluded facets. Simulations have proven that the best adjust to trimming results are achieved when the weighting factor corresponds with the arithmetic mean of the three angles.

Until this moment, the visibility problem in *Cone Method* has been reduced to points instead of facets. A facet is in shadow when there is, at least, one triangle which intersects the line of sight between the source point and its barycentre, although other characterizations can be performed for this and *Pyramid* methods –e.g. 3 vertices, inner points, etc– but an increase in the computational time must be expected. Finally, a sweep all over the facets in the sorted list is carried out.

D. Pyramid Method

The *Pyramid Method* is a special type of the *Cone Method* where the base is not circular. This algorithm determines if any point in the geometry is occluded by a specific facet.

Assume all the facets have been sorted by the distance from their barycentre to the source point $\mathbf{s}$. The closest triangular patch is always seen but could occlude other facets. The plane which contains the reference facet F_j is considered.

$$\hat{n}^j \cdot \left(\mathbf{P} - \mathbf{P}_c^j\right) = 0 \,. \tag{16}$$

Three additional planes are defined by taking into account every edge $\overline{\mathbf{V}_1^j\mathbf{V}_2^j}$, $\overline{\mathbf{V}_2^j\mathbf{V}_3^j}$, $\overline{\mathbf{V}_3^j\mathbf{V}_1^j}$ of F_j and $\mathbf{s}$. A generic point $\mathbf{P}$ in one of these planes must satisfy the corresponding plane equations in (17) to (19),

$$\frac{\mathbf{V}_2^j \times \mathbf{V}_1^j}{\left|\mathbf{V}_2^j \times \mathbf{V}_1^j\right|} \cdot \mathbf{P} = 0 \tag{17}$$

$$\frac{\mathbf{V}_3^j \times \mathbf{V}_2^j}{\left|\mathbf{V}_3^j \times \mathbf{V}_2^j\right|} \cdot \mathbf{P} = 0 \,, \tag{18}$$

$$\frac{\mathbf{V}_1^j \times \mathbf{V}_3^j}{\left|\mathbf{V}_1^j \times \mathbf{V}_3^j\right|} \cdot \mathbf{P} = 0 \,. \tag{19}$$

The intersection of the last three planes generates the faces of a pyramid whose base is F_j (see Fig. 7). In order to know if a point $\mathbf{P}$ is inside the pyramid, the left side in equation (20) is evaluated. When the result equals the number of vertices of the base, $\mathbf{P}$ is enclosed by the pyramid (the vertices of F_j are supposed to appear in clockwise or anti-clockwise order).

$$\sum_{i=1}^{3} sign\left|\frac{\mathbf{V}_{i+1}^j \times \mathbf{V}_i^j}{\left|\mathbf{V}_{i+1}^j \times \mathbf{V}_i^j\right|} \cdot \mathbf{P}\right| = 3 \tag{20}$$

where $\mathbf{V}_4^j = \mathbf{V}_1^j$. The other constraint is identical to equation (14) in *Cone Method*.

This method complements the *BSP* once the priority list has been obtained.

The mentioned idea about SVP and AZB in Section I is adapted to *Trimming*, *Cone* and *Pyramid* methods. Not only cubic or parallelepipedic domains are not created but also conical. Instead, the z-coordinate is neglected and equally-spaced angular sectors (corresponding with angle ϕ in a local cylindrical coordinate system) are delimited (Figure 8). Supposing L sectors, the equally-spaced limit angles are $\beta_1, \beta_2, \ldots, \beta_L$,

$$\beta_1 \le \phi \le \beta_{L+1} \,. \tag{21}$$

A facet F_j belongs to sector l if its barycentre $\mathbf{P}_c^l$ is inside its boundaries (except for *Trimming Method*, where the triangular patches are, of course, trimmed),

$$\begin{cases} -\mathbf{P}_{c1}^j \sin\beta_l + \mathbf{P}_{c2}^j \cos\beta_l > 0 \\ -\mathbf{P}_{c1}^j \sin\beta_{l+1} + \mathbf{P}_{c2}^j \cos\beta_{l+1} < 0 \end{cases} \tag{22}$$

with $l = 1,2,\ldots,L-1$.

Acceleration is expected depending on the number of triangles the geometry is composed of.

III. SIMULATED RESULTS

Once the algorithms have been presented, a comparison in terms of accuracy and computational time is carried out among the CPU implementation of the *BSP Method* and the three new methods *Trimming*, *Cone* and *Pyramid*.

A. PEC Plates

This example consists of a first comparison among the already presented algorithms and a simple Z-buffer implementation where the facets are not trimmed.

The scenario is compound of two square parallel PEC plates. They are the same size, 10λ, and the distance between them is d_p=5 λ. The first plate is located in the XY plane. The position of the center of the second plate varies along the Y-axis from (0,-10λ,-d_p) to (0, -10λ, d_p) with step $\Delta y = \lambda$. Three different meshes have been considered to evaluate the computational time with respect to the number of facets: 200, 800 and 1800.

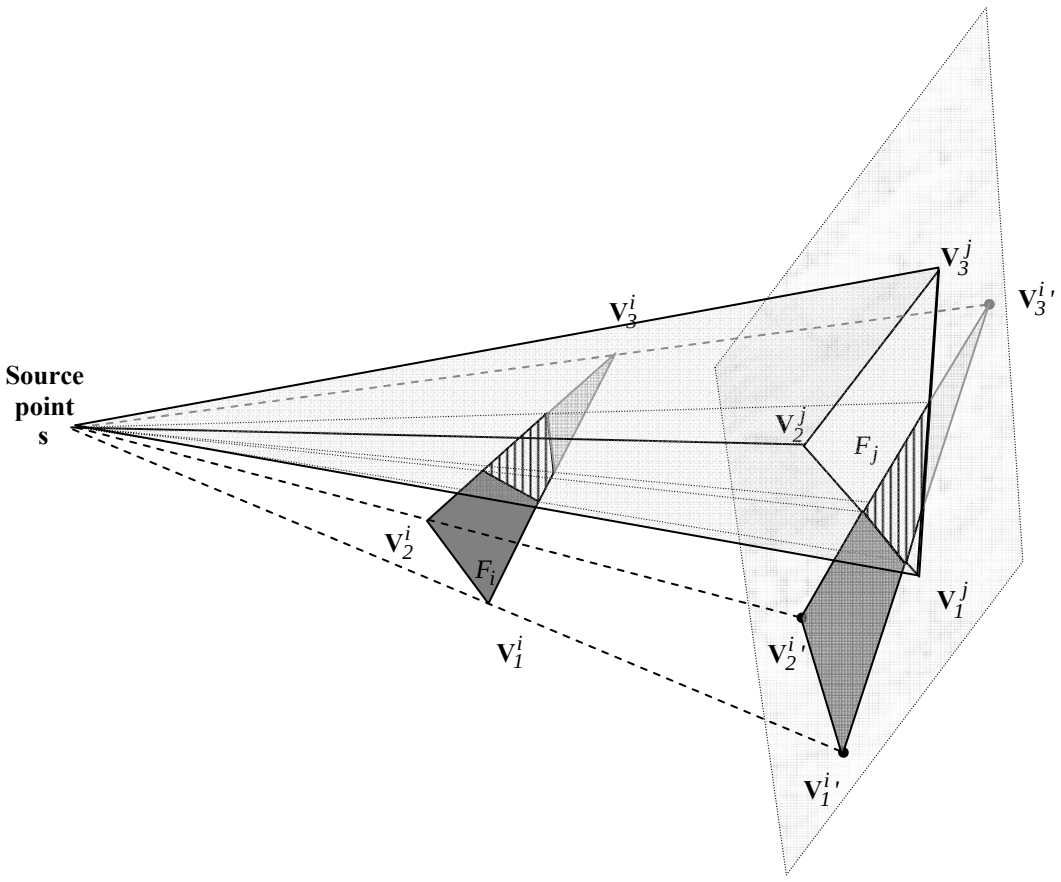

Fig. 7. *Pyramid Method*. The facet F_j acts as reference. Its edges and the source point **s** define three planes (pyramid). The facet F_i intersects some of them but is not in shadow because it is situated in front of F_j.

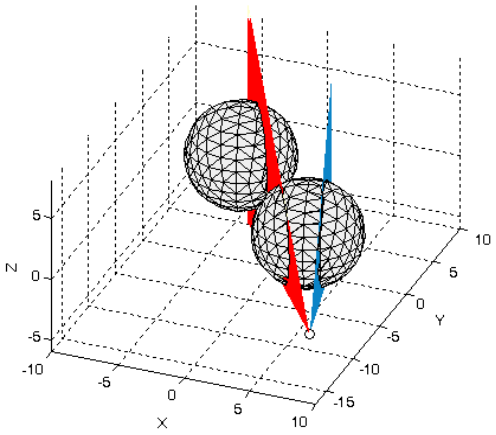

Fig. 8. Sectorial division ($L = 3$) of the geometry.

An incident plane wave impinges the surface after determining which facets are illuminated. The Physical Optics approximation [16] establishes that the incident field induces an electric current density $\mathbf{J}$,

$$\mathbf{J} \approx 2\hat{n} \times \mathbf{H}^{inc} \tag{23}$$

with $\hat{n}$ the outward normal vector and $\mathbf{H}^{inc}$ the magnetic incident field in the patch.

The scattered electric field $\mathbf{E}^s$ due to a flat triangular patch is reckoned analytically in [17] and the first reflection contribution (denoted by σ) is calculated as,

$$\sigma = \lim_{r \to \infty} 4\pi r^2 \frac{|\mathbf{E}_1^s|^2}{|\mathbf{E}^{inc}|^2} \tag{24}$$

where $\mathbf{E}^{inc}$ represents the incident electric field; $\mathbf{E}_1^s$, the total scattered electric field due to the contribution of the first reflection on the illuminated facets and r is the distance from the radar to the target.

The results in Fig. 9 show a perfect agreement where the facets do not need to be trimmed due to the selected step. Table 2 summarizes the computational time for each algorithm. Our simple Z-buffer implementation has associated higher computational time than *Pyramid* and *Trimming Method*s. Likewise, a generic scenario where the facets could be partially occluded would require a

more complex Z-buffer implementation capable of trimming facets. Consequently its computational time is estimated to surpass even the *Trimming Method* values.

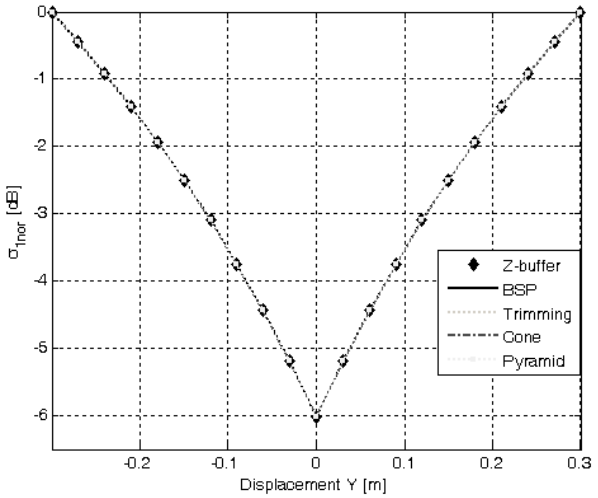

Fig. 9. Simulated results for two PEC plates. The first reflection σ contribution has been normalized.

Table 2. Plates example. Computational time comparison.

		Computational time (sec)		
		200 facets	800 facets	1800 facets
Methods	Trimming	0.6689	2.6486	6.0955
	Cone	0.0499	0.4123	1.4716
	Pyramid	0.0841	0.4432	1.6278
	BSP	0.1890	1.3012	5.2432
	Z-buffer	0.1711	0.6806	1.7561

B. PEC Spheres

A geometry consisting of two perfect electric conductor (PEC) spheres (radius r=10λ) whose centres are separated $d = 3r = 30\lambda$ is defined (Figure 10).

In order to analyze the influence of the discretization in the results, three meshes have been selected: 392, 1352 and 2888 triangles per sphere (the increase in the number of patches improves the correct modelling of the spherical surface). Therefore, the difference between two configurations lies in the fact of considering lit or hidden a facet which is occluded partially (when *Trimming* is not active).

A directional sweep is performed from $\phi = -45^o$ to $\phi = 135^o$ with step of $\Delta\phi = 1^o$. The simulated results are calculated analogically to the previous section. Tables 3 to 5 show the average computational time for each geometry discretization and aspect angle as a function of the number of sectors (except for *BSP Method* where the time due to the creation of the BSP tree has been uniformly distributed among the *Q=181* aspect angles). The least values (best time) have been marked and their corresponding first reflection contributions have been depicted in Figs. 11 to 13. The proposed methods present a good coincidence in the central area of the graphics but not in the limits where one sphere starts to partially occlude the other. In this context, the dimensions of the patches and the lit/shadowed classification based on their barycentre have relevance.

Table 3. Spheres example. Computational time and relative error comparisons. 784 facets.

784 facets		**Computational time (sec) | Relative Error δ(%)**		
		1 sector	3 sectors	6 sectors
Methods	Trimming	**1.54**	1.96	2.48
	Cone	0.045 | **4.58**	**0.035** | 4.92	0.036 | 5.24
	Pyramid	0.080 | **8.12**	**0.075** | 9.51	0.079 | 10.48
	BSP	**0.49 | 13.04**		

Table 4. Spheres example. Computational time and relative error comparisons. 2704 facets.

2704 facets		**Computational time (sec) | Relative Error δ(%)**		
		1 sector	3 sectors	6 sectors
Methods	Trimming	**5.02**	5.78	6.74
	Cone	0.29 | **6.42**	0.16 | 6.48	**0.13** | 6.54
	Pyramid	0.42 | **10.42**	0.30 | 11.11	**0.26** | 13.52
	BSP	**3.47 | 10.89**		

Table 5. Spheres example. Computational time and relative error comparisons. 5776 facets.

5776 facets		**Computational time (sec) | Relative Error δ(%)**		
		1 sector	3 sectors	6 sectors
Methods	Trimming	**11.52**	12.25	13.17
	Cone	1.15 | **4.67**	0.51 | 5.79	**0.32** | 5.94
	Pyramid	1.37 | **5.81**	0.78 | 6.29	**0.60** | 6.46
	BSP	**13.19 | 6.42**		

In order to compare the differences between the *Trimming Method* and the other techniques, the absolute error Δ has been calculated in equation (25),

$$\Delta = \left|\sigma_i - \sigma_i^{ref}\right| \tag{25}$$

where σ_i and σ_i^{ref} are the first reflection value and first reflection reference value (*Trimming*) in the i^{th}

aspect angle respectively. Figures 14 to 16 represent these absolute errors for the best fit solution. The graphics confirms that the error increases near $\phi = -45^{o}$ and $\phi = 135^{o}$ as mentioned. Equation (26) introduces a relative error $\delta(\%)$.

$$\delta(\%) = \frac{1}{Q}\sum_{i=1}^{Q}\left|\frac{\sigma_i - \sigma_i^{ref}}{\sigma_i^{ref}}\right| \cdot 100 \,. \qquad (26)$$

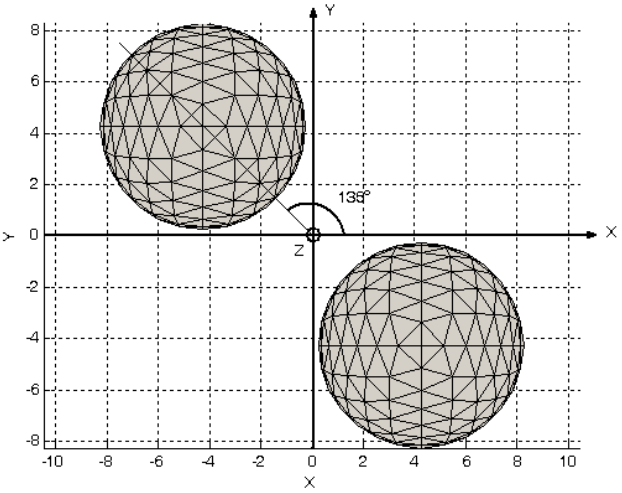

Fig. 10. Spheres example. Geometry description. Spherical coordinates for the centre of the spheres are: $C_1(\rho,\phi,z) = (1.5r, -\pi/4, 0)$ and $C_2(\rho,\phi,z) = (1.5r, 3\pi/4, 0)$. The radius r equals to 10λ and the separation between centres is $d = 3r = 30\lambda$.

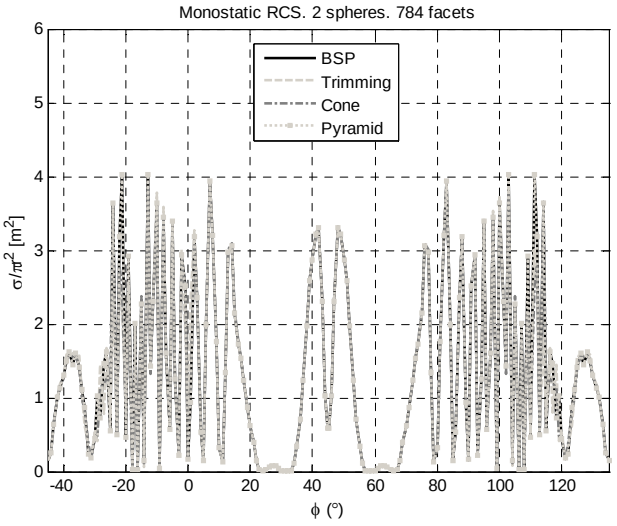

Fig. 11. Spheres example. First reflection contribution. Best time comparison, 784 facets.

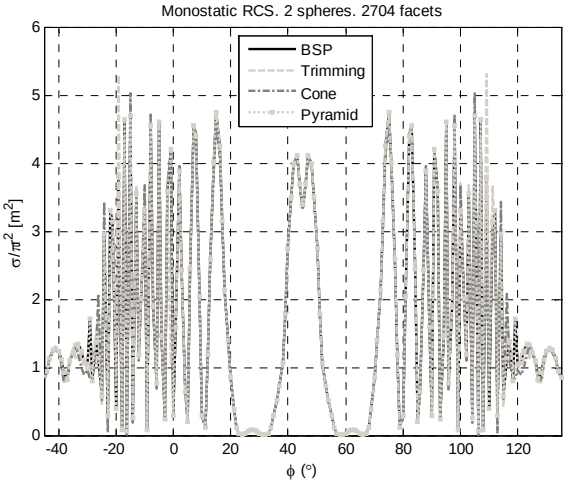

Fig. 12. Spheres example. First reflection contribution. Best time comparison, 2704 facets.

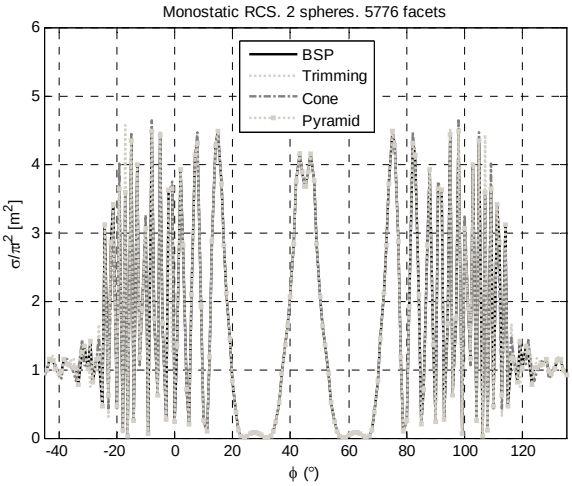

Fig. 13. Spheres example. First reflection contribution. Best time comparison, 5776 facets.

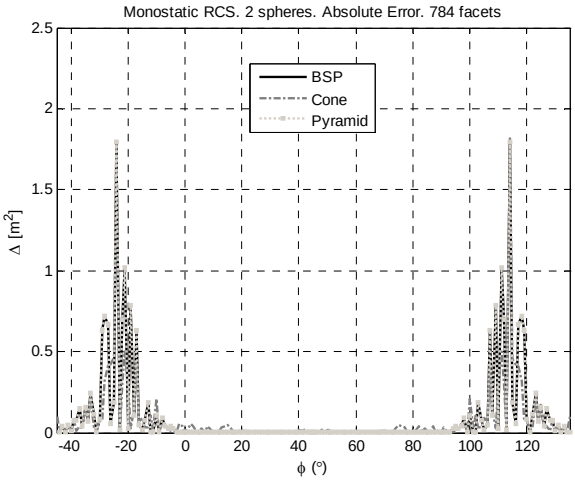

Fig. 14. Spheres example. Absolute error of the first reflection contribution with respect to *Trimming Method*, 784 facets.

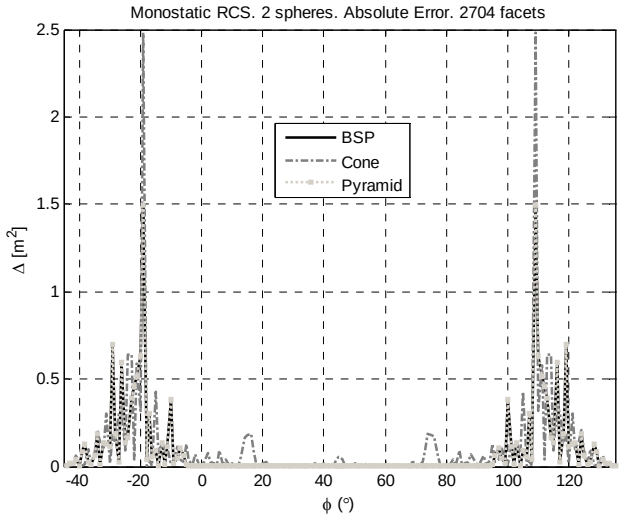

Fig. 15. Spheres example. Absolute error of the first reflection contribution with respect to *Trimming Method*, 2704 facets.

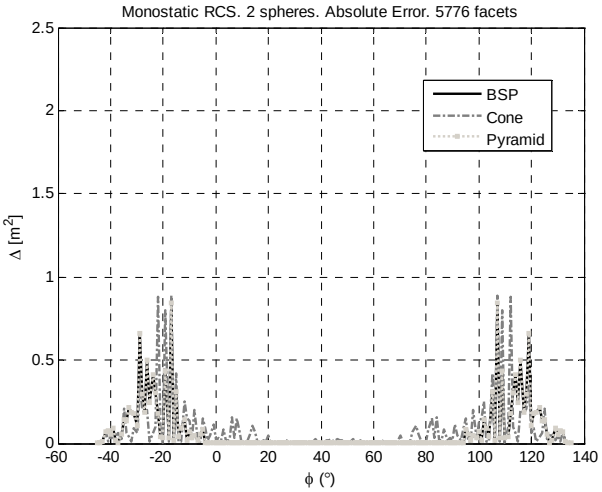

Fig. 16. Spheres example. Absolute error of the first reflection contribution with respect to *Trimming Method*, 5776 facets.

Tables 3 to 5 summarize these errors. The underlined cells are associated with the least errors for each of the techniques and discretizations. Best time and best fit results do not usually come from the same configuration. Therefore a midway solution must be adopted and an important computational time reduction is usually preferred, even though it would imply an error increase. *BSP* errors exceed *Trimming* and *Cone* results and all errors tend to increase with the number of sectors (because of the rough classification of the facets). Finally, an example of the lit triangular patches is presented in Fig. 17 in a Lambert azimuthal equal-area projection for the sphere in the second quadrant. Figure 17(b) corresponds to the *Trimming Method* and acts as reference for the graphics *(a)*, *(c)* and *(d)*.

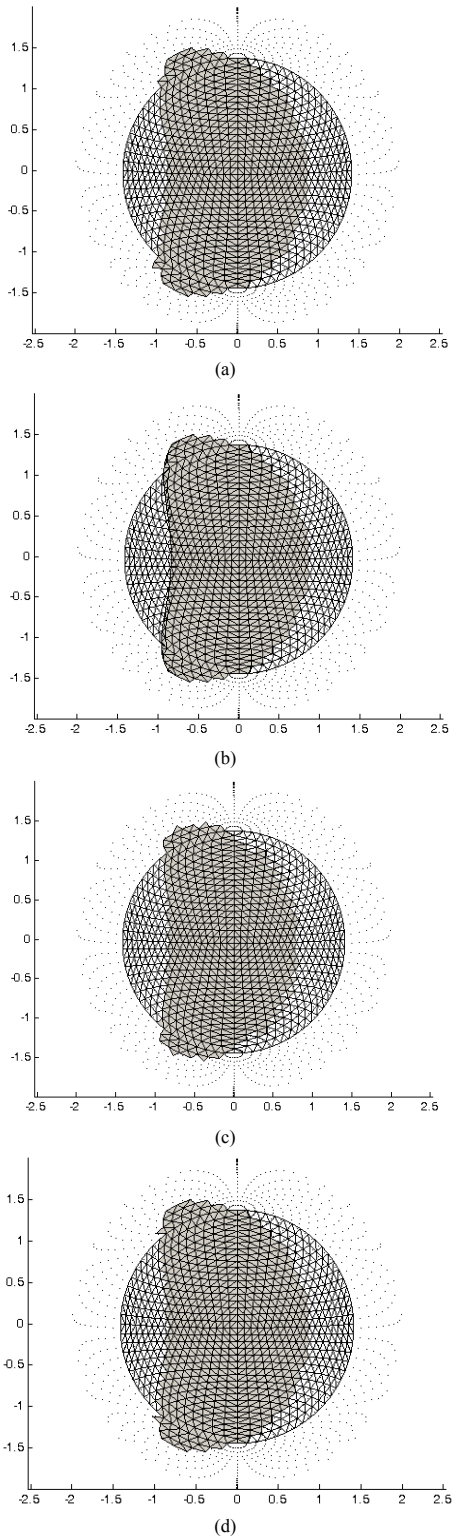

Fig. 17. Lambert azimuthal equal-area projection of the sphere in the second quadrant. Light grey facets correspond to a semi-sphere projection (grid). Dark grey facets represent the lit triangles due to (a) *BSP*, (b) *Trimming Method*, (c) *Cone Method*, (d) *Pyramid Method*. (Aspect angle=-21º).

IV. CONCLUSION

This paper has presented four different methods to solve the visibility problem and a comparison of the first reflection contribution in terms of computational time and error has been performed based on CPU implementations.

Binary Space Partitioning uses a hierarchical structure to sort the patches in the space. The implementation of this well known algorithm has been divided into three phases: building and walking the binary tree and discarding the occluded triangles. It is suitable for scenarios where the point of view is situated outside the geometry because of the parallel projection which is carried out. Nonetheless, the computational cost is greater than the other techniques which provide similar or better accuracy (only a huge amount of angular directions could justify the creation of the BSP tree in terms of computational cost).

The new *Trimming Method* solves the visibility problem in an exact manner by means of a perspective projection and the definition of a *test polygon*. As a result, the original facets are partially occluded are trimmed. Therefore, only the lit surface is returned. The number of patches increases and the facet mean size tends to be smaller than the initial one. The re-definition of the triangular patches is not convenient for computing reflections. On the other hand, the high number of operations lead to a high computational cost.

The *Cone Method* replaces the original facets by circles and creates a fictitious right cone whose vertex is the source point. The piece of surface behind the plane which contains a facet and inside its cone is in shadow. This technique is the fastest one and Figs. 11 to 13 and Tables 3 to 5 have shown that the corresponding relative error is small.

The *Pyramid Method* tests whether a point satisfies equation (20), where each summand is related to one of the faces of the pyramid in Fig. 7. It employs the plane equation to quickly solve the problem; but it still takes twice the computational time taken by *Cone Method*. In addition, the technique can be extrapolated to n-edged polygons, where substituting polygons by circles would be inadequate.

A simple CPU implementation of the Z-buffer algorithm, where the geometry is not trimmed, has been also evaluated. The results have proven Z-buffer algorithm to be less time-efficient for our purpose than *Pyramid* and *Cone Methods.*

As the number of patches in the geometry ranges from 784 to 5776, the first reflection contribution varies because of the improvement on the modelling of the geometry. In this context, a smoother surface leads to more realistic results.

ACKNOWLEDGEMENT

This work has been supported by Ministerio de Ciencia e Innovación of Spain /FEDER under projects TEC2008-01638/TEC (INVEMTA) and CONSOLIDER-INGENIO CSD2008-00068 (TERASENSE); by Unión Europea-Fondo Europeo de Desarrollo Regional under project EQP06-015; by Gobierno del Principado de Asturias- Plan de Ciencia y Tecnología (PCTI)/FEDER-FSE under grants BP08-082, BP06-101, BP06-155 and projects FC-08-EQUIP-06 and PEST08-02 and by Cátedra Telefónica- Universidad de Oviedo and CenSSIS, the Gordon Center for Subsurface Sensing and Imaging Systems under the ERC Program of the NSF (Award number EEC-9986821).

The authors would like to thank Mss. Sarah Brown for her kindness in correcting the English in the text.

REFERENCES

[1] B. R. Dewey, *Computer graphics for engineers*. USA: Harpercollins College Div., 1998.

[2] J. D. Foley *et al.*, *Computer Graphics*. USA: Addison-Wesley, 1992.

[3] J. Bittner and P. Wonka , "Visibility in computer graphics," *Environment and Planning B: Planning and Design* vol. 30, no. 5, pp. 729 – 755, 2003.

[4] M. F. Cátedra and J. P. Arriaga, *Cell planning for wireless communications*. Boston: Artech House, 1999.

[5] M. F. Cátedra, J. Pérez, F. S. de Adana, and O. Gutiérrez, "Efficient ray-tracing techniques for three-dimensional analyses of propagation in mobile communications. Application to picocell and microcell scenarios," *IEEE Antennas and Propagation Magazine*, vol. 40, no. 2, pp. 15-25, 1998.

[6] A. Woo and J. Amanatides, "Voxel occlusion testing: a shadow determination accelerator for ray tracing," *Proceedings of Graphics interface '90*, pp. 213-220, June 1990.

[7] Y. Zhou and H. Ling, "On the multiplaten Z-buffer algorithm for ray tracing in high frequency electromagnetic scattering computations," *Microwave and Optical Technology Letters*, vol. 43, pp. 298-301, 2004.

[8] M. Reyer, T. Rick, and R. Mathar, "Graphics hardware accelerated field strength prediction for rural and urban environments," *Proceedings of the Second European Conference on Antennas and Propagation –EuCAP 2007*, November 2007.

[9] J. M. Rius, M. Ferrando, and L. Jofre, "GRECO graphical electromagnetic computing for RCS prediction in real time," *IEEE Antennas and Propagation Magazine*, vol. 35, no. 2, 1993.

[10] M. J. Inman and A. Z. Elsherbeni, "Programming video cards for computational electromagnetics applications," *IEEE Antennas and Propagation Magazine*, vol. 47, no. 6, 2005.
[11] D. Shreiner, *OpenGL reference manual: the official reference document to OpenGL, Version 1.4*. London: Addison-Wesley, 2004.
[12] H. Fuch, Z. M. Kedem, and B. F. Naylor, "On visible surface generation by priori tree structures," *ACM Siggraph Computer Graphics*, vol. 14, no. 3, pp. 124-133, 1980.
[13] D. Gordon and S. Chen, "Front-to-back display of BSP trees," *IEEE Computer Graphics and Applications*, vol. 11, pp. 79-85, 1991.
[14] C. W. Fu, T. T. Wong, *et al.,* "Binary-space-partitioned images for resolving image-based visibility," *IEEE Transactions on Visualization and Computer Graphics*, vol. 10, no. 1, 2004.
[15] F. Las-Heras, J. L. Jambrina, and E. Iguacel "Different approximations for the double reflection contribution to the RCS in a Physical Optics algorithm," *Proceedings of the 7th European Electromagnetic Structure Conference*, pp. 11-14, September, 1993.
[16] C. A. Balanis, *Engineering electromagnetics*. New York, USA: John Wiley and Sons, 1989.
[17] A. M. Arias, J. O. Rubiños, I. Cuiñas, and A. G. Pino, "Electromagnetic scattering of reflector antennas by fast physical optics algorithms," *Recent Res. Devel. Magnetics*, no. 1, pp. 43-63, 2000.

J. G. Meana was born in Gijón, Spain, in 1982. He received his M.S. degree in Telecommunications Engineering in 2005 from the University of Oviedo (Spain). He joined the R&D department of CTIC Foundation in 2005 and since 2006 he is a Research Assistant with the Area of Theory of Signal and Communications (University of Oviedo). He was awarded a Ph.D. Scholarship of the Principado de Asturias and is currently pursuing the Ph.D. degree in electrical engineering. He received the "Novel Engineer Award. XI La nit de les Telecomunicacions Awards" in 2005. His interests and research studies are focus on the evaluation of electromagnetic coverage in rural/urban scenarios by means of high frequency techniques.

Fernando Las-Heras was born in Zaragoza, Spain. He received the M.S. degree in 1987 and the Ph.D. degree in 1990, both in telecommunication engineering, from the Universidad Politécnica de Madrid (UPM), Madrid, Spain. From 1988 to 1990, he was a National Graduate Research Fellow. From 1991 to 2000, he held a position of Associate Professor at the Department of Signals, Systems and Radiocommunications of the UPM. From 2001 to 2003, he held a position of Associate Professor at the Department of Electrical Engineering of the University of Oviedo, pioneering the Area of Theory of Signal and Communications at that University. Since December 2003, he has held a Full Professor position at the University of Oviedo where he is presently Vice-Dean for Telecommunication Engineering degree at the Polytechnic School of Engineering at Gijón, Spain. His main research interests include the analysis and design of antennas, electromagnetic interference (EMI) and the inverse electromagnetic problem with application to diagnostic, measurement and synthesis of antennas.

José Ángel Martínez-Lorenzo was born in Madrid, Spain, in 1979. He received the M.S. and Ph.D. degrees both in telecommunications engineering from the University of Vigo, Vigo, Spain, in 2002 and 2005, respectively. From 2002 until 2004, he worked as a teaching and Research Assistant at the University of Vigo. In 2004, he joined the faculty of the Department of Signal Theory and Communications, University of Oviedo, Gijon, Spain, where he was an Assistant Professor until 2006. During spring and summer 2006, he was a Visiting Researcher at the Bernard Gordon Center for Subsurface Sensing and Imaging Systems (Gordon-CenSSIS) Engineering Research Center, Northeastern University, Boston, MA. Since October 2006, he has been with Gordon-CenSSIS as a Senior Research Scientist and a Part-time Lecturer in the Electrical and Computer Engineering Department at Northeastern University. He has authored over 45 technical journal and conference papers in the areas of microwave antenna design, electromagnetic wave propagation and computational electromagnetics.

UTD Shooting-and-Bouncing Extension to a PO/PTD Ray Tracing Algorithm

F. Weinmann

Research Institute for High Frequency Physics and Radar Techniques, FGAN E.V.
Neuenahrer Str. 20, 53343 Wachtberg, Germany, weinmann@fgan.de

Abstract **–** This paper deals with the efficient combination of three well-established electromagnetic modeling methods, a Shooting-and-Bouncing-Rays (SBR) algorithm on the basis of the Geometrical Optics (GO), a source-based calculation of scattered field strengths using Physical Optics (PO) and Physical Theory of Diffraction (PTD), and diffraction calculation on the basis of the Uniform Theory of Diffraction (UTD). While the conventional GO-PO/PTD methods are able to accurately calculate wedge contributions to scattered fields, the further propagation of diffracted rays is generally not considered in SBR approaches. Thus, the aim of this paper is to describe the implementation of diffracted rays according to the UTD concept into an SBR code. This novel implementation allows for the modeling of double diffraction and reflected-diffracted-reflected paths in complex scenarios consisting of a very large number of surface elements as well as the accurate simulation of cavities. The comparison with numerically exact reference simulations proves that the proposed hybrid GO/UTD-PO/PTD algorithm yields excellent results and that the UTD-SBR extension definitely improves the simulations of the ray tracing algorithm also for realistic objects.

Keywords: Numerical modeling, physical optics (PO), radar cross section (RCS), ray tracing, and uniform theory of diffraction (UTD).

I. INTRODUCTION

Accurate simulation of electromagnetic scattered fields is a very important research topic, because it is generally faster and cheaper than performing measurements, especially if complex or large-scale objects are involved. Moreover, a variety of geometry parameters can be studied easily and optimized, if required. Thus, the main application of such simulation programs is the prediction of scattered fields as well as the indication of scattering centers. The simulation results can be used to generate databases for target identification, for testing low-observability (LO) measures, and for developing specifications for various radar systems.

For finding the relevant propagation paths, most high-frequency approaches are using either a Shooting-and-Bouncing-Rays (SBR) algorithm [1, 2], which is commonly applied for objects made up of a very large number of surface elements, or the so-called image method (sometimes also referred to as image-tree method or method of images) [3-5], which works fine for a small number of large surface elements. In the context of high-frequency methods, sometimes a distinction is made between ray launching (in the sense of SBR) and ray tracing (in the sense of an image approach), which might lead to confusion. Generally, however, the term ray tracing is applied as umbrella term for all approaches using rays in order to find relevant propagation paths, i.e. SBR and image method are considered as different ray tracing approaches. The latter is also the convention used within this paper.

A very powerful ray tracing simulation approach based on SBR has been proposed in [1], showing excellent results even for complex objects such as real-scale aircraft at radar relevant frequencies. The algorithm is able to treat arbitrary objects and has practically no limitations concerning object size and the number of reflections to take into account. Due to the use of asymptotic methods, it is well-suited for simulations of large objects that cannot be modeled with numerically exact methods such as the Method of Moments (MoM) on current computer equipment. A detailed description of the algorithm as well as a discussion on alternative methods is available in [1].

This paper presents a further hybridization of the algorithm in order to improve the accuracy for lower frequencies, where diffraction is relevant. Although the approach in [1] considers diffracted field contributions within the Physical Theory of Diffraction (PTD) – which is similar to the XPATCH code [2] – the further propagation of diffracted rays is neglected, and so diffracted-reflected and double-diffracted ray paths, for example, are not included. However, these contributions may be significant at lower frequencies or at special geometries, as is proven in the following. After a brief review of the ray tracing algorithm presented in [1], which also demonstrates its limitations, the implementation of the Uniform Theory of Diffraction (UTD) is discussed in Section III. It must be pointed out that the aim of this paper is to describe the implementation of the UTD into an SBR code, rather than

explaining the details and limitations of the UTD itself. The simulation results in Section IV clearly show that the UTD extension provides a very useful enhancement of the ray tracing algorithm and definitely improves the accuracy of the results.

The UTD is a well-known high-frequency concept, which has been applied earlier within asymptotic methods, including hybrid SBR-image approaches [6] hybrid Finite-Elements methods [7], and mode matching approaches [8, 9]. However, combined reflected-diffracted propagation paths are not easy to treat in most UTD implementations, especially if higher-order interactions are relevant [4, 5, 10]. Contrary, the UTD implementation as presented in this paper avoids the analytical calculation of relevant diffracted propagation paths by following the SBR principles, i.e., starting from the point of diffraction, new rays are calculated and traced further through the scenario. This approach makes the UTD ray tracing algorithm much more versatile with the cost of increased computation efforts, of course. Nevertheless, today's development in fast computers makes the calculations executable on a standard PC with reasonable expenditure of time, so facetted CAD models of complex objects consisting of thousands or even hundreds of thousands of surface elements can be modeled with excellent accuracy.

II. RAY TRACING USING DISCRETE RAYS AND PO/PTD

A. Summary and Aim of the Implemented Ray Tracing Technique

This section will give a brief review on the implemented ray tracing approach, which is the basis for the UTD extension described in the subsequent sections. Emphasis will be put on the ray concept applied in the simulation code, rather than explaining the underlying theoretical principles. A more detailed description of the ray tracing algorithm and various simulation examples are available in [1]. The aim of this algorithm is to constitute a universally applicable high-frequency prediction tool, which can be used for RCS calculation of arbitrary complex objects by performing the simulation on facetted CAD models. For example, realistic aircraft models may require more than 100,000 facets with multiple interactions, which is the main reason why SBR is chosen in [1].

First of all, it must be noted that the implemented ray tracing algorithm works with discrete rays, which are taken as representatives of the so-called astigmatic ray tubes [11]. Thus, intersection tests with geometric structures are rather fast (compared to the tracing of ray tubes) on the one hand and on the other hand such a ray carries all necessary information of a ray tube, e.g. the radii of curvature of the corresponding wave front. Starting from a given transmitter, a specified number of rays is launched towards the object and traced according to the well-known SBR technique [12]. This approach allows the accurate modeling of large and complex objects because the required memory is independent of the number of reflections to take into account. The approach of discrete rays is combined with a ray-density normalization (RDN) [13], which provides the number of rays per cross section at any point of the ray trajectories.

However, the GO is not well-suited for calculating scattered fields of arbitrary finite objects because it assumes, e.g., reflections at infinitely extended surfaces. That is the reason why the RDN has been combined with Physical Optics (PO) and the PTD, which are able to calculate scattered fields as an integral over the surface and edges, respectively. As the RDN states the number of rays per unit area, it is used to calculate the equivalent surface area or edge length of each single ray hitting a geometrical object. This figure serves as the integration area for the PO and PTD formulation, respectively. However, it must be noted that the exact shape of the surface area corresponding to a single ray remains unknown. Fortunately, provided a dense grid of rays hits the surface (e.g. 10 rays per wavelength), the PO integral is proportional to the geometrical size of that area, so the surface area corresponding to a single ray can be assumed to be a square and the PO integral reduces to a sum of ray contributions.

In summary, the hybrid GO-PO/PTD approach uses the laws of GO (i.e. the law of reflection) merely for calculating geometrical ray propagation paths and the fields on these paths, while at each intersection of a ray with the object PO/PTD is applied for the scattered field contributions towards the point of observation.

B. Rays and Propagation Paths

For the understanding of the approach presented in this paper, it is important to distinguish between rays and propagation paths. In this context, a ray shall be defined as a directional straight geometrical connection between two points in three-dimensional space. Thus, e.g., a ray might hit a surface and generate a reflected ray, whose direction is given by the laws of GO. Additionally, the first ray generates a PO (or PTD) contribution to a point of observation, so the combination of the incident ray and the PO/PTD contribution shall be denoted as a propagation path. More generally speaking, a GO-PO/PTD propagation path consists of the incident ray (which hits the object), m reflected rays ($m \geq 0$), and one PO or PTD contribution to the point of observation. Thus, the approach of [1] accounts for single diffraction occurring at the last step of the propagation path. However, as is shown in this paper, diffracted rays are relevant for certain geometric objects. A diffracted ray is generated by a ray hitting an edge of the object, which means that the diffracted ray starts at the edge. In the further ray tracing process, this ray may also generate

reflected rays and PO/PTD contributions. Therefore a new class of propagation paths is introduced by the extension of the original approach: GO/UTD-PO/PTD propagation paths, which consist of the incident ray, m_1 reflected rays ($m_1 \geq 0$), one diffraction according to the laws of UTD, m_2 reflected rays ($m_2 \geq 1$), and finally one PO or PTD contribution to the point of observation. Note that $m_2 \geq 1$ is assumed because $m_2 = 0$ would result in calculating the contribution of diffracted fields to the point of observation, which is performed using PTD [1].

The GO/UTD-PO/PTD approach introduces paths with double diffraction but also other important single diffraction paths, which are generally not included in SBR codes. For example, an incident ray might hit the aperture edge of a cavity and generate diffracted rays propagating into the cavity. After m_2 reflections inside the cavity, a relevant contribution towards the receiver in the exterior space might be observed. As is shown in the following, these additional paths can significantly improve the accuracy of an SBR code, especially when cavities or general non-convex objects are involved.

C. Examples and Limitations of the GO-PO/PTD Approach

While the simulation examples in [1] show an excellent agreement of the ray tracing results with the reference data, this subsection emphasizes on special scenarios where diffracted rays might experience further interactions with the object and thus yield significant contributions that are neglected in the GO-PO/PTD approach.

A classic reference object is the trihedral corner reflector (e.g., [5, 14]), which is made up of three right-angled triangles that are assembled like a pyramid. Here, the object has an edge length of $a = 1.41$ m at the aperture. The aperture angle is $\gamma = 90°$ and the Trihedral is inclined by $\alpha_0 = 35,3°$ in the direction of elevation (see Fig. **1**). Thus, the x-axis is perpendicular to the aperture. The faces of the Trihedral are assumed to have zero thickness.

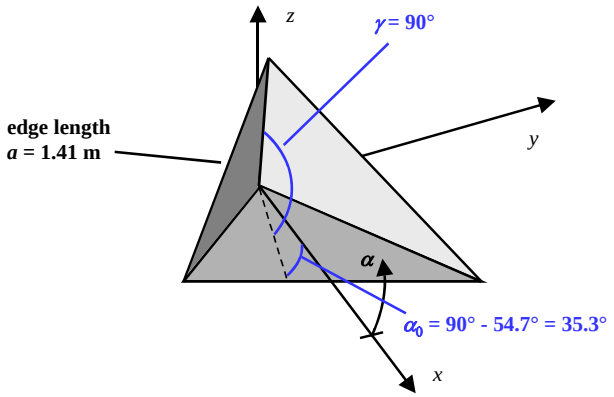

Fig. 1. Geometry of the trihedral corner reflector.

As can be seen in the monostatic RCS simulations in [1], the PTD provides a significant improvement compared to the PO only simulation (note that [1] uses $\alpha' = -\alpha$). However, deviations are observed at angles where the observation point is close to the aperture plane, i.e. $\alpha \rightarrow \pm 90°$. As will be shown later, these deviations are due to missing diffracted field contributions. An even more severe deviation is found in the results of the bistatic RCS simulation of the Trihedral. An example simulation has been performed depending on the elevation angle α with a total of $N = 10$ million rays (Fig. 2). The direction of the incident wave is perpendicular to the aperture, i.e., $\alpha_i = 0°$. As can be seen from the reference Boundary-Integral-MLFMM (BI-MLFMM) simulation, the RCS curve of the vv-polarization exhibits a distinct step around $\alpha = -35°$, which is not reproduced at all with the ray tracing simulation results. Furthermore, both polarizations show major deviations in the angular range from +90° to +145°, which is part of the forward-scattering halfspace. For a better understanding of these results, a detailed analysis of the corresponding scattering directions and the relevant propagation paths is necessary. Obviously, the maximum of the bistatic RCS corresponds to the backscattering case, whereas the second maximum at $\alpha = -70°$ is caused by rays hitting the Trihedral near the top corner (see Fig. 1). Due to geometrical reasons, the corners do not contribute to triple reflection [15]. Thus, such rays are doubly-reflected in that corner and – instead of a third reflection at the lower facet – exit the scenario towards the angle $\alpha = -70.6°$. From these considerations, the step at $\alpha = -35°$ can be interpreted as a shadow effect caused by the lower facet. From $\alpha = 0°$ to $\alpha = -35°$, the complete interior of the Trihedral is visible to the observation point, so no shadowing effects will occur. Contrary, the interior of the lower facet is not visible at angles beyond -35°. A similar effect is observed at angles beyond +90°. Here the interior of the Trihedral is not visible at all, which leads to rather small RCS values. In this angular region, diffraction at the aperture wedges is the main propagation mechanism. Note that the maximum at $\alpha = \pm 180°$ corresponds to forward scattering and does not represent the total field strength.

According to the ray tracing method described in [1], each reflection of a GO ray is associated with a PO (and possibly PTD) surface current, which yields a contribution to the scattered field strength. Thus, shadowing effects are reproduced by the superposition of at least two PO contributions. As an example, consider an incident ray hitting the lower facet. In the basic form of the algorithm, the PO surface current contribution is calculated to any observation point, regardless of visibility. The reflected ray hits one of the upper facets and generates a second PO surface current. Ideally, these contributions should interfere destructively for

observation points that are not visible from the point of the first reflection. However, this is true only for observation points located in the specular direction of the first reflection (at $\alpha = 110°$). That is the reason why the results are closer to the reference solution at this angle (see Fig. 2). For observation points within the angular range from +90° to +145° but deviating from the specular direction, the phases of the two contributions are no longer correct, which results in the major inaccuracies observed in Fig. 2. At angles beyond +145°, the observation points are located behind the plane containing the lower facet, so forward scattering is the main contribution and yields a good accuracy.

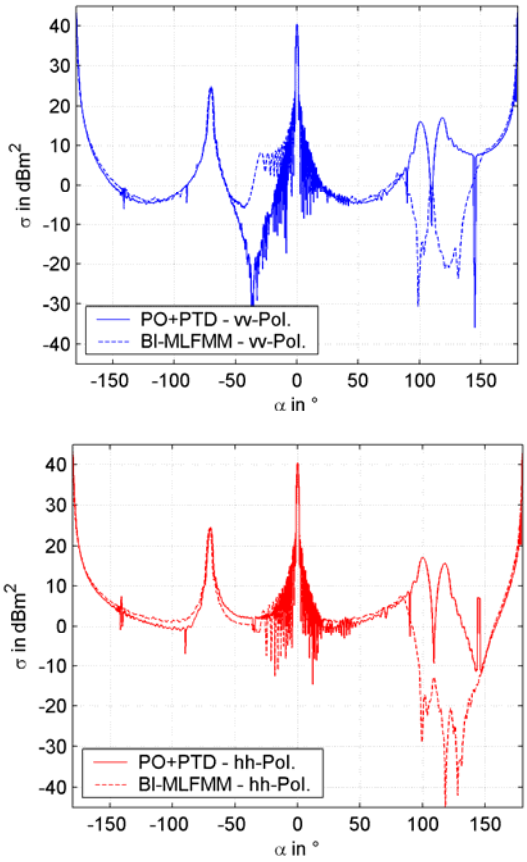

Fig. 2. Bistatic RCS of the trihedral corner reflector ($f = 15$ GHz, PO/PTD without shadowing).

As a possible improvement to the shadowing problem, in Fig. 3 contributions are calculated only if the observation point is visible from the point of interaction and, additionally, for forward scattering. The result of this approach shows definitely improved data in the range from +90° to +145°. But, unfortunately, the results are worse in other angular regions, especially for the vv-polarization at angles beyond -70°. Note that small peaks, e.g. at $\alpha = +145°$, are due to the fact that the implemented PTD shows a singularity at grazing angles. Thus, these observation points are excluded from the PTD calculation, leading to a distinct step in the RCS curve. To summarize these studies, the example of bistatic scattering from a trihedral corner reflector clearly shows that the GO-PO/PTD approach has definite limitations at certain geometrical structures.

Another important example of more practical use is a cavity, e.g. as described in [12]. Cavities are often used as simple models of jet engine inlet ducts, which are rather complex objects in the view of electromagnetic (EM) modeling. Thus, a variety of approaches has been studied in order to accurately model these objects, e.g. modal methods, GO with Aperture Integration, Gaussian Beams, Finite Element methods, and Iterative Physical Optics (IPO) [12, 16, 17, 18].

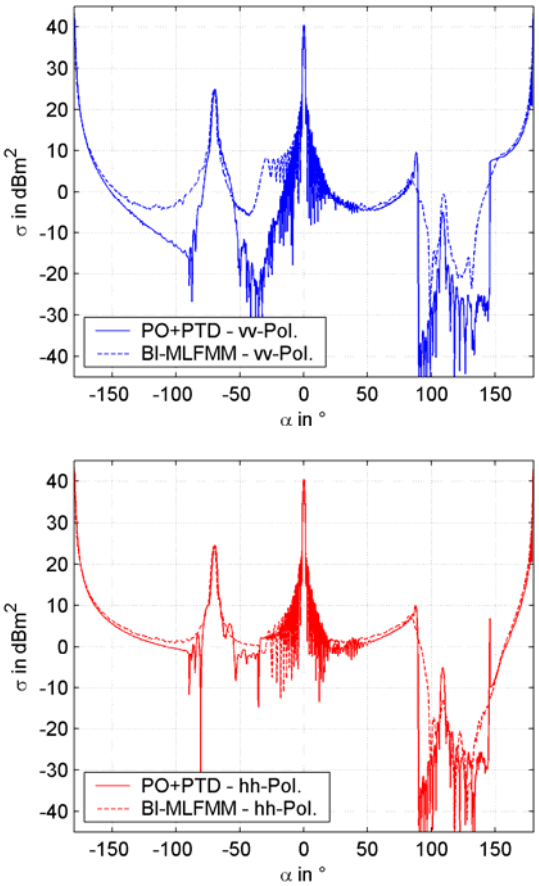

Fig. 3. Bistatic RCS of the trihedral corner reflector ($f = 15$ GHz, PO/PTD with shadowing).

The object of the following studies consists of a cubic cavity with a side length of 10 λ ($f = 3$ GHz) and is a very elementary step towards the modeling of engine ducts. Additionally, this object is surrounded by a wall of 1 λ thickness. The simulated monostatic RCS of the cavity is given in Fig. 4, together with the result of the

reference BI-MLFMM simulation. The angle α denotes the elevation angle with respect to the axis of the cavity, i.e., $\alpha = 0°$ corresponds to the incidence perpendicular to the aperture.

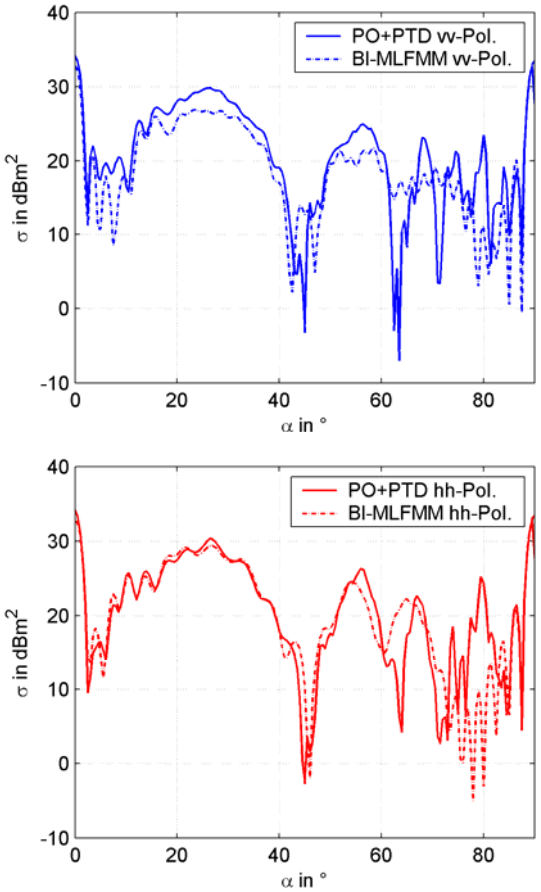

Fig. 4. Monostatic RCS of the cubic cavity ($f = 3$ GHz, $l = 10\ \lambda$, PO/PTD).

A longer cavity ($l = 30\ \lambda$) has also been modeled (see results in Fig. 5). Apart from the surrounding wall of 1 λ thickness, this object is identical to one of the simulation examples in [12]. As becomes obvious from Figs. 4 and 5, the GO-PO/PTD ray tracing algorithm basically provides a satisfying accuracy at most angles. However, major deviations can be found at large elevation angles, which partly originate from the almost grazing incidence of rays at the aperture. Thus, the rays experience a large number of reflections inside the cavity, which is accounted for by setting the maximum number of reflections to $R_{max} = 50$. Simulations with a higher number of reflections showed that this value is enough to ensure convergence. Thus, the deviations may be due to coupling effects that are not covered by the ray tracing approach.

A closer look at the cavities and the trihedral corner reflector reveals that a complete class of possibly relevant propagation paths has been neglected so far, because the ray tracing algorithm presented in [1] does not trace diffracted rays. However, a ray may be diffracted at the aperture, continue propagating into the cavity, and finally – when it exits from the cavity – provide a significant contribution to the scattered field. In order to accomplish the tracing of diffracted rays, the implementation of the Uniform Theory of Diffraction (UTD) into the algorithm presented in [1] is described in the following section. Concerning the ray tracing procedure, the UTD for diffracted rays is the counterpart to the GO for reflected rays. It is important to note that in the simulation approach presented in this paper, the geometrical propagation paths and the fields on these paths are calculated according to the laws of GO and UTD (i.e. the law of reflection and the law of edge diffraction on the Keller cone), while the field contributions towards the point of observation are determined by PO and PTD, respectively. Thus, each time a ray hits a surface or edge, a PO (and possibly also PTD) current is calculated, which generates a contribution to the total scattered field strength. Altogether, a hybrid GO/UTD-PO/PTD simulation approach is developed.

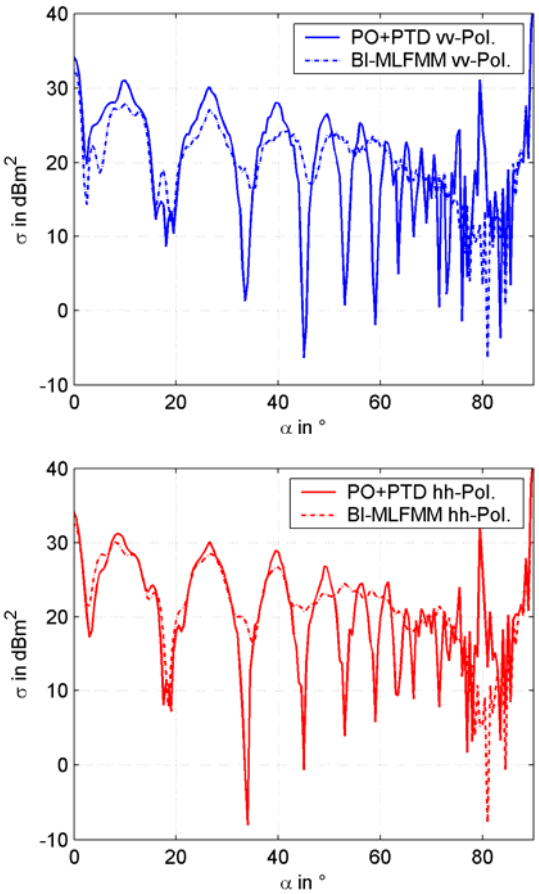

Fig. 5. Monostatic RCS of the cuboid cavity ($f = 3$ GHz, $l = 30\ \lambda$, PO/PTD).

III. THE UNIFORM THEORY OF DIFFRACTION

A. Principles of the UTD

The UTD is a well-known high-frequency technique for the asymptotic calculation of diffracted fields and has been studied in various publications. In the present paper, only the basic UTD approach of diffraction from an infinite perfectly conducting wedge will be applied [19] in order to keep the additionally required CPU efforts as small as possible. Thus, there is no special treatment of shadow boundaries and no distinction between near and far field [3]. There are also UTD approaches for impedance edges [21, 22], which, of course, are much more complex than the standard UTD formulation.

Concerning the implementation in a ray tracing algorithm, the most important attribute of the UTD concept is the assumed limitation of the diffracted field to the so-called Keller cone [20], which is the equivalent to the specular reflection of the GO. Each propagation path on the Keller cone can be identified with an angle ϕ, $0° < \phi < n\pi$, where $n\pi$ is the outer wedge angle. The angle β between the diffracted ray and the edge is identical to the angle β' between the incident ray and the edge. In the present form, UTD diffraction is applied only for first order diffraction. However, second order diffraction is implied by performing PTD on diffracted rays if they hit another edge.

The UTD diffracted fields are basically determined by diffraction coefficients D_s and D_h (soft and hard polarization), which – similarly to the Fresnel reflection coefficients – denote the ratio between the incident field strength E^i and the diffracted field strength E^d,

$$E^d(s) = D_{s,h} A(s) E^i \tag{1}$$

s denotes the distance from the edge to the point of observation [19]. $A(s)$ is the spread factor describing the divergence of the diffracted wave and the D_s and D_h depend on the angle of incidence, the wedge angle, frequency, etc., and in a secondary way also on the distance s. In the context of the present paper, s does not correspond to a real far field point of observation, but is equal to the distance to the next intersection point on the object. From the view of the ray tracing algorithm, the quantity s is unknown at the time of calculating the diffraction coefficients because, typical to a SBR-algorithm, no information on the future propagation path is available. Fortunately, this problem can be solved rather easily by launching a dummy ray to determine the distance to the next intersection or by applying the UTD coefficients later when s is known.

Of course, due to the assumed simplifications, inaccuracies might occur if the next intersection point is too far away from an edge with finite length. Nevertheless, the results in Section IV show good accuracy for all simulation examples.

B. Application to the Ray Tracing Technique

According to the electromagnetic problem to be solved, different implementations of the theoretical concept of the UTD are known in literature. For example, if the problem consists of large flat surface elements, an image approach of UTD is rather convenient [6, 7]. For resonant structures such as large open-ended waveguides, a modal approach has been developed, which converts UTD diffracted rays into modes [8, 9]. This paper proposes a novel implementation of the UTD in a ray tracing code using discrete rays and RDN. Thus, the UTD is implemented in a pure SBR fashion, which is consistent to the original ray tracing code as summarized in Section II.

Consider a ray that hits a wedge within the simulation scenario. According to the description in [1], this ray generates a PO contribution as well as a PTD contribution and afterwards is reflected towards the specular direction. Additionally, the UTD diffraction has to be performed, but at this stage, the relevant propagation paths are unknown. Note that a diffracted ray may experience several reflections before it generates a significant PO/PTD contribution towards an observation point. That is the reason why in the approach presented in this paper a large number N_{UTD} of rays is generated on the Keller cone and further traced through the scenario according to the SBR principles. Like the original ray, the diffracted rays will generate PO and PTD contributions each time they hit a surface or edge. Theoretically, even higher order UTD diffraction can be treated with this approach, provided that shadow boundaries are treated adequately, but in most practical cases, such effects will not provide a relevant contribution to the total scattered fields. Actually, double diffraction is considered implicitly by using PTD for the second diffraction.

As at the stage of diffraction the directions of relevant propagation paths are unknown, it is most convenient to uniformly distribute the diffracted rays on the Keller cone. Thus, each diffracted ray is defined by assigning an angle $\phi_k = (k\text{-}0.5)n\pi/N_{\mathrm{UTD}}$, $k = 1,\ldots, N_{\mathrm{UTD}}$. This means that the Keller cone is cut into N_{UTD} parts, and one ray is launched in the center of each part. This definition is implemented in the ray tracing algorithm, with an additional stochastic variation of the angles ϕ_k, so that in each part of the Keller cone a diffracted ray is launched at a random angle $(k\text{-}1)n\pi/N_{\mathrm{UTD}} < \phi_k < k\, n\pi/N_{\mathrm{UTD}}$, $k = 1,\ldots, N_{\mathrm{UTD}}$. As stated in [1], such a variation reduces aliasing effects, which might occur, for example, at the edges of plane facets.

While these considerations are more or less obvious, the remaining problem is more complicated. As the presented ray tracing algorithm works with the RDN, which weights each contribution according to the ray

density, the correct density of the diffracted rays has to be determined. Generally, the ray density n_d states the number of rays per unit area perpendicular to the direction of propagation. In the context of PO and PTD it is needed to calculate the equivalent surface area and edge length, respectively, of a ray hitting the object.

To clarify the problem, a two-dimensional configuration is considered first (Fig. 6). The object is represented by a half-plane, which is hit by an incident plane wave at the angle β. This scenario corresponds to a cut for a fixed diffraction angle ϕ. Note that in this specific 2D-case the "diffracted" rays have the same direction like the reflected rays, and the Keller cone reduces to a straight line, which means each incident ray will generate one diffracted ray towards the specular direction. According to the definition of the ray density, the distance between adjacent rays in the 2D-case is $1/n_d$. Thus, each ray can be assigned an equivalent edge length,

$$dl = \frac{1}{n_d \sin\beta} . \tag{2}$$

The distance between adjacent diffracted rays is,

$$\frac{1}{n_d'} = dl \sin\beta = \frac{1}{n_d} . \tag{3}$$

As expected, the ray density n_d' of the diffracted wave is equal to the ray density of the incident wave. This statement is also true if the incident rays are divergent. In that case, both n_d and n_d' contain a divergence factor, which depends on the path length. Nevertheless, equation (3) is still valid with these considerations.

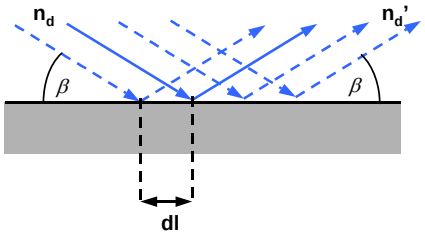

Fig. 6. Two-dimensional diffraction scheme for calculating the ray density.

The realistic case, however, is a three-dimensional scenario with incident rays being diffracted at an edge (outer wedge angle $n\pi$) of the object. Similar to the 2D-case, the incident ray density is denoted as n_d, but here the equivalent cross section of a ray is equal to $1/n_d$. Each ray that hits the edge generates a Keller cone of N_{UTD} diffracted rays, as described above. To calculate the ray density of the diffracted rays, the equivalent cross section of the diffracted rays, $1/n_d'$, has to be determined. Apparently, this equivalent cross section is equal to the distance between adjacent rays on one Keller cone (U / N_{UTD}) multiplied by the distance between adjacent Keller cones ($dl \sin\beta$), i.e.,

$$\frac{1}{n_d'} = \frac{U}{N_{\mathrm{UTD}}} dl \sin\beta , \tag{4}$$

where U denotes the perimeter of the Keller cone,

$$U = \frac{n\pi}{2\pi} 2\pi s \sin\beta . \tag{5}$$

In equation (5), s denotes the distance from the point of diffraction to the point of observation, which is equivalent to the next intersection point of the ray with the object. As a result, the ray density of the diffracted rays is calculated according to,

$$n_d' = N_{\mathrm{UTD}} \frac{1}{n\pi \sin^2\beta dl\, s} . \tag{6}$$

The equivalent edge length, dl, depends on the incident ray density n_d and the edge width relevant for diffraction [1]. Equation (6) provides the relationship for the correct weighting of UTD diffracted field contributions and is valid even if the incident wave is not a plane wave. In that case, a possible divergence, for example, is included in the incident ray density n_d and thus in the equivalent edge length dl [1].

The following section shows that the described implementation of the UTD into the SBR algorithm allows for a definite improvement of simulation results, especially for resonant structures. All simulations consider a maximum of one UTD diffraction on each propagation path, which might be followed by an additional PTD diffraction, so doubly-diffracted field contributions are included.

IV. GO/UTD-PO/PTD SIMULATION RESULTS

A. Trihedral and Cavities with UTD

In this section the simulation examples of Section II are modeled with the additional consideration of UTD diffracted rays. Figure 7 shows the UTD results of the trihedral corner reflector as described in Fig. 1. Obviously, the simulation results are definitely improved in comparison to Figs. 2 and 3. Especially the step in the curve for the vv-polarization around the angle α = -35° is reproduced almost exactly. Besides, the characteristic resonances in the angular range from -30° to +20° are exactly at the same angles like in the reference BI-MLFMM simulation. Apart from these excellent

agreements, Fig. 7 also shows a better accuracy than Fig. 2 in the angular range from +90° to +145°. The small peak in the curve of the hh-polarized RCS at $\alpha = 145°$ corresponds to the exclusion of PTD calculation at grazing angles, which has been discussed in Section II. Note that shadowing effects are not explicitly considered in Fig. 7.

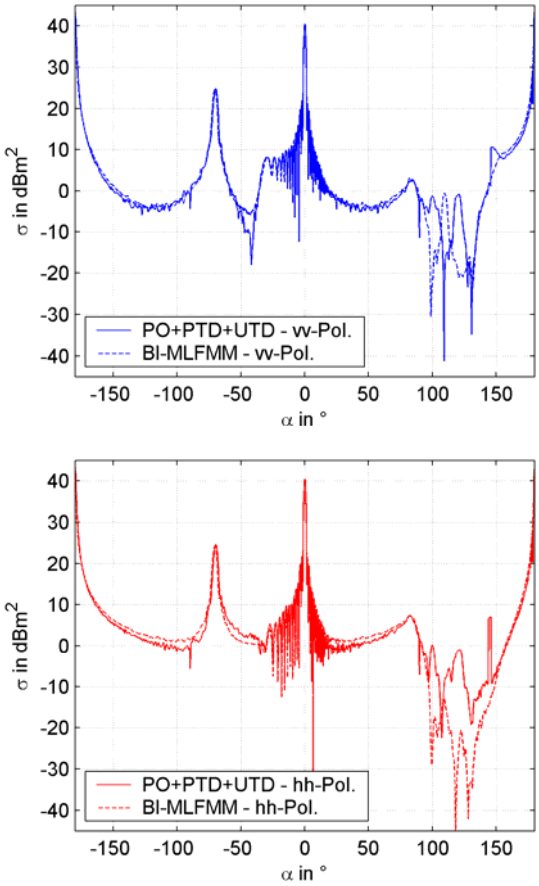

Fig. 7. Bistatic RCS of the trihedral corner reflector ($f = 15$ GHz, $N_{UTD} = 1{,}000$).

Altogether, it is apparent that the UTD provides a relevant contribution to the scattered field in the example of the trihedral corner reflector. Rays hitting the edges of the trihedral are diffracted and have at least one more reflection at the object. As can be deduced from Fig. 7, only the tracing of such propagation paths will provide accurate results over almost the complete angular range of the bistatic RCS.

However, the drawback of this UTD implementation is the increased CPU time for the simulation. The reason for this is the need for a fine scanning of the object, i.e. the number of diffracted rays must be "large enough". The precise meaning of this expression depends on the object, of course, but the value $N_{UTD} = 1000$ proved good results in all examples studied so far. The simulation of Fig. 7 has also been performed with $N_{UTD} = 100$ and $N_{UTD} = 10$ (see Section IV.B), which leads to basically the same results but the curves are less smooth. When using UTD-SBR with a very large number of diffracted rays ($N_{UTD} = 10{,}000$, see Table 1), a tremendous increase of CPU time is observed, while no further improvement of results is possible because the data show convergence with respect to the number of diffracted rays.

Table 1. CPU times for numbers of UTD rays (on Athlon XP3000+ processor).

Simulation parameters	CPU time
$N = 10$ million, without UTD	20 h
$N = 10$ million, $N_{UTD} = 10$	21 h
$N = 10$ million, $N_{UTD} = 100$	23 h
$N = 10$ million, $N_{UTD} = 1{,}000$	40 h
$N = 10$ million, $N_{UTD} = 10{,}000$	262 h

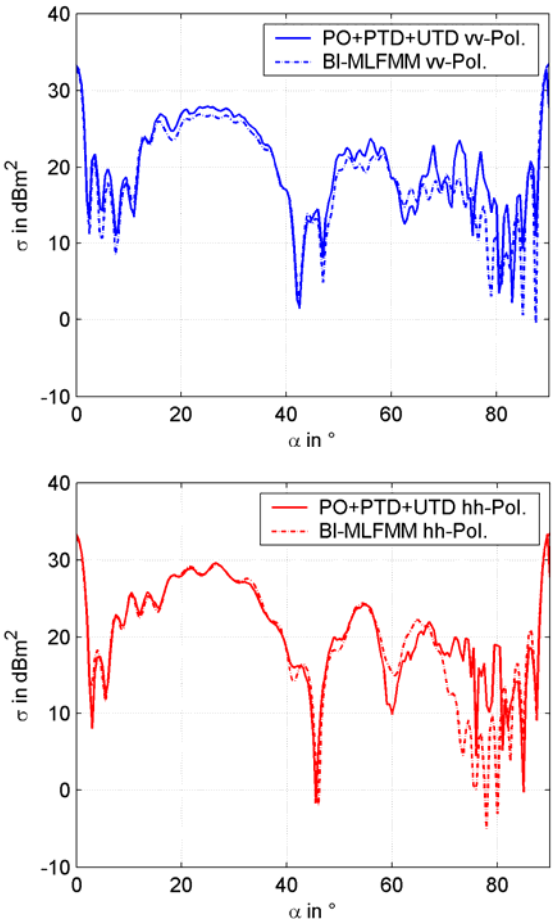

Fig. 8. Monostatic RCS of the cubic cavity ($f = 3$ GHz, $N_{UTD} = 1{,}000$).

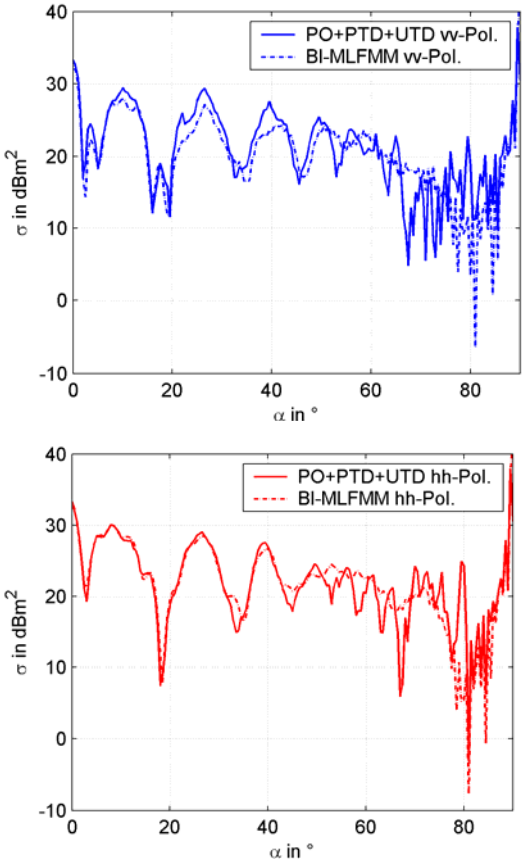

Fig. 9. Monostatic RCS of the cuboid cavity (f = 3 GHz, N_{UTD} = 1,000).

As can be deduced from Table 1, the CPU time for the calculation without UTD is around 20 h, which appears rather high for this simple object. The main reason for the stated CPU time is the angular resolution of the bistatic RCS, $\Delta\alpha = 0.25°$, which means that at each intersection of a ray with the object, PO and/or PTD contributions have to be calculated to 1,441 observation points. As the algorithm is not yet optimized for such a large number of receivers, the time for the PO/PTD calculations is much larger than the CPU time for the geometrical ray tracing, i.e. the calculation of propagation paths.

If UTD is considered with N_{UTD} = 100, the CPU time is increased only by 15%. In contrast, the CPU time is more than doubled with N_{UTD} = 1,000, and it increases by a factor 13 if N_{UTD} is set to 10,000. However, no significant improvement is observed at N_{UTD} = 10,000. From Table 1 it is obvious that at N_{UTD} = 1,000, more than half of the CPU time is spent with the calculation of UTD diffracted rays and the associated PO/PTD contributions. The convergence of results depending on the number of diffracted rays N_{UTD} is considered more in detail in Section IV.B.

For practical use, the example of the cavities studied in Section II.C is more important. Consider a ray that hits the object at one edge of the aperture. According to the method described in the previous section, this ray generates N_{UTD} diffracted rays, of which approx. one third will enter the cavity. Note that the outer wedge angle is $3\pi/2$, and only the angular range $\phi = 0$ to $\phi = \pi/2$ (measured from the inner walls) will lead to rays propagating into the cavity. These rays are further traced according to the SBR technique and provide additional contributions which are not included in the original PO/PTD version of the algorithm. The results of the simulations are shown in Figs. 8 and 9, which present an excellent improvement of the RCS data with respect to the reference MoM simulation, especially in the angular range from 0° to 60°. It is remarkable that in this range the RCS for hh-polarization is practically identical to the reference, while the RCS for vv-polarization is slightly higher than the results of the MoM simulation.

B. Convergence and Low-Frequency Considerations

As stated above, the simulation results in Section IV.A have been obtained by generating 1,000 diffracted rays for each ray hitting an edge of the object, i.e. N_{UTD} = 1,000. This setting proved to yield satisfying results but leads to the significant drawback of more than double CPU time in the case of the trihedral corner reflector. Thus, it is very important to study the convergence of the results when using the UTD extension at different values for N_{UTD}.

For this purpose, the simulation shown in Fig. 7 has been repeated at N_{UTD} = 10 and N_{UTD} = 100 (Figs. 10 and 11 – for convenience, only the results for vv-polarization are given in this paper). As becomes obvious from Fig. 10, the setting N_{UTD} = 10 already leads to the correct shape of the bistatic RCS curve, including the step at the angle α = -35°. However, the curve is overlaid by smaller fluctuations, which are caused by the stochastic nature of the described approach. Nevertheless, the relatively small number of diffracted rays provides good results in this test case, while only a small amount of additional CPU time is required.

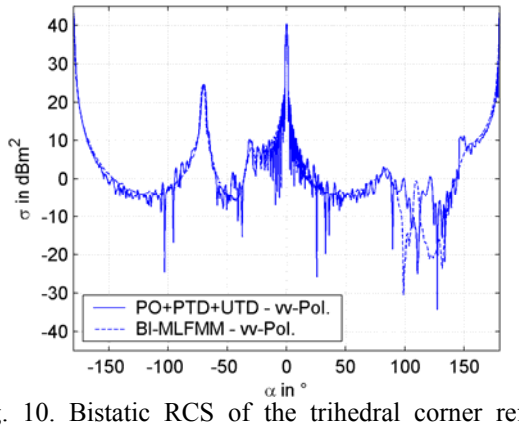

Fig. 10. Bistatic RCS of the trihedral corner reflector (f = 15 GHz, N_{UTD} = 10).

As can be expected from the law of large numbers, the fluctuations decrease at $N_{UTD} = 100$ (Fig. 11), but for high-quality results, $N_{UTD} = 1{,}000$ should be chosen (cf. results in Fig. 7). Also, it must be noted that the required number of diffracted rays is always connected to the number N of rays in the simulation. For example, if $N' = 10\,N$ is used in a second simulation, the number N_{UTD} of diffracted rays on a single Keller cone can be decreased to one tenth of the original value, in order to obtain the same density of diffracted rays and thus the same accuracy of the UTD diffracted rays contribution.

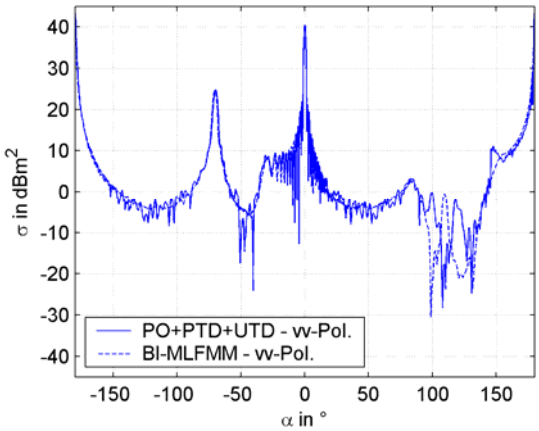

Fig. 11. Bistatic RCS of the trihedral corner reflector ($f = 15$ GHz, $N_{UTD} = 100$).

Further studies have been made with respect to the frequency range, in which the presented UTD implementation is valid. It is well-known that the UTD as implemented in the ray tracing algorithm assumes infinitely extended edges. That is the reason why this method is a typical asymptotic or high-frequency approximation. In the test case studied above ($f =$ 15 GHz) the length of the wedges at the aperture is 50 wavelengths. The same object has also been studied at $f = 6.4$ GHz and $f = 3$ GHz, where the relative wedge lengths are 21 wavelengths and 10 wavelengths, respectively. As can be deduced from Figs. 12 and 13, the UTD extension still works very well at both frequencies. Especially the step of the curve at $\alpha =$ -35°, which is independent of frequency, is reproduced almost exactly. Although there are some minor oscillation artefacts at 3 GHz, the accuracy of the GO/UTD-PO/PTD algorithm is remarkable.

It must be pointed out that the UTD simulations in this section have been performed by considering a maximum of one UTD diffraction for each ray. Thus, doubly diffracted paths (first UTD, later PTD, possible reflections before UTD or between UTD and PTD) are included. Further simulations at $f = 3$ GHz have been studied by considering a maximum of two and three UTD diffractions for each ray. These settings lead to an immense increase of CPU time but – apart from additional "clutter" – do not provide a significant change of simulation results. Consequently, double UTD diffraction does not yield a relevant contribution in this example, as might have been expected. Thus, the simulations in this section can be regarded to be convergent not only with respect to the number N_{UTD} of diffracted rays on the Keller cone, but also in terms of multiple diffractions.

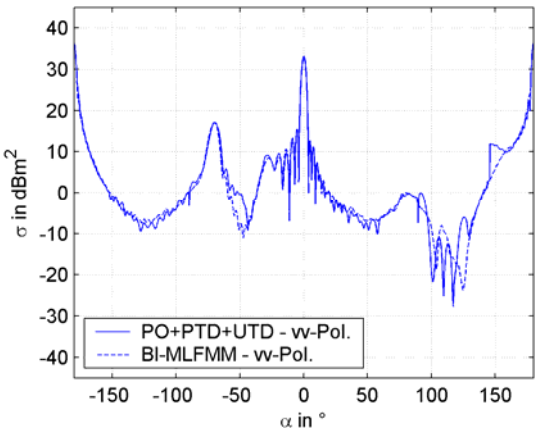

Fig. 12. Bistatic RCS of the trihedral corner reflector ($f = 6.4$ GHz, $N_{UTD} = 1000$).

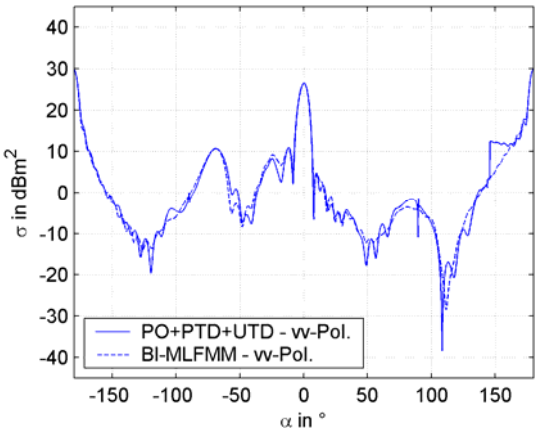

Fig. 13. Bistatic RCS of the trihedral corner reflector ($f = 3$ GHz, $N_{UTD} = 1000$).

C. Generic Missile Model

The last simulation example is a generic missile model consisting of 44,000 triangular facets, which has been proposed in [23]. A picture of the CAD model can be found in [1], where the monostatic RCS has been calculated in the azimuth plane for vv-polarization at $f = 12$ GHz. This simulation is repeated here with the additional consideration of UTD contributions as described above. Although the results in Fig. 14 suggest an even better agreement than without UTD, the mean error of both simulations is exactly the same (1.7 dB). However, if only the angular range from $\phi = 140°$ to

$\phi = 180°$ is considered, i.e. the angles with the most distinct deviation in [1], the mean error decreases from 2.5 dB without UTD to 2.2 dB with the use of UTD. Thus, the UTD improves the results for angles, where the wave impinges on the wedged back side of the wings, whereas a slight stochastic deviation is imposed at angles with excellent agreement compared to the reference data. Using $N_{UTD} = 1{,}000$ for this simulation, the CPU time is increased by approx. 16%, which is an acceptable effort for this object. Thus, this simulation example proves that the application of the implemented UTD is practicable not only for simple objects but also for realistic CAD models.

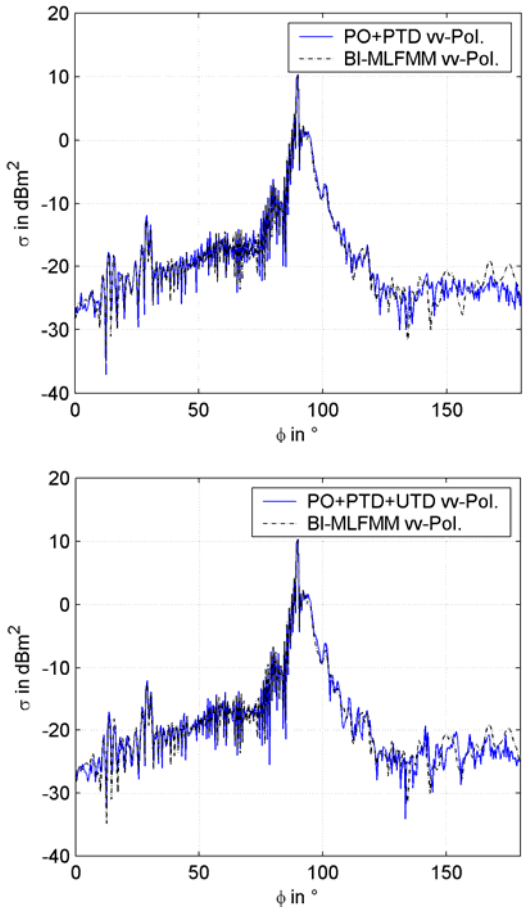

Fig. 14. Monostatic RCS of the generic missile at $f = 12$ GHz, vv-polarization.

The generic missile has also been studied in terms of bistatic RCS. The incident wave is parallel to the *xy*-plane and hits the object at $\phi_0 = 135°$, i.e. from the rear side (Fig. 15). For the evaluation of results, the bistatic angle ϕ is calculated from the nose direction. Specular reflection from the body of the missile is expected at $\phi = 45°$, forward scattering is equivalent to $\phi = 315°$. As in the previous simulation, the frequency is 12 GHz and the vv-polarized fields are evaluated.

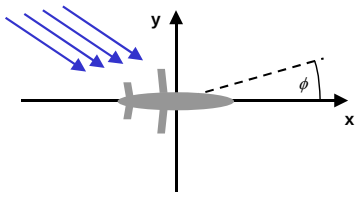

Fig. 15. Geometric scheme for bistatic RCS simulations of the generic missile.

From the results in Fig. 16, it can be observed that the original GO-PO/PTD algorithm already yields rather accurate results. However, as the dynamic range is very large, significant deviations occur at certain angles, leading to a mean error of 8.6 dB. By tracing UTD diffracted rays, this error is reduced to 7.9 dB. Obviously, additional propagation effects and coupling mechanisms, such as creeping waves, are relevant when studying bistatic RCS of a convex-like target. Nevertheless, the accuracy of the bistatic results obtained by the presented ray tracing algorithm is remarkable, both for the original GO-PO/PTD version as well as for the newly developed UTD Shooting-and-Bouncing extension.

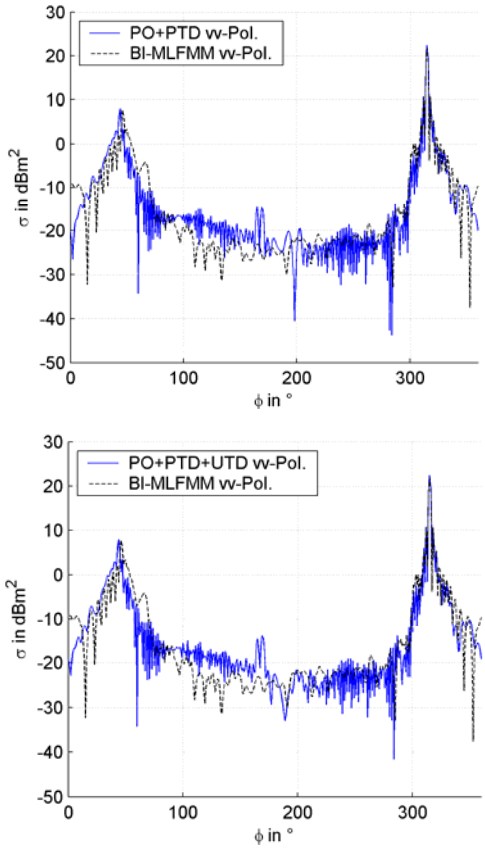

Fig. 16. Bistatic RCS of the generic missile at $f = 12$ GHz, vv-polarization.

V. CONCLUSION

This paper presents an important extension to the formerly proposed GO-PO/PTD ray tracing algorithm for RCS simulations of large and complex objects. The novel implementation of the UTD in a SBR fashion makes each relevant ray generate a given number of diffracted rays on the Keller cone, which are further traced through the scenario. Thus, reflected-diffracted-reflected propagation paths with multiple reflections and one diffraction in between are added to the original SBR concept. The combination of the well-known UTD and the newly developed, sophistiacted adaptation of the ray-density normalization to diffracted rays provides a very powerful algorithm to analyze the scattered fields of arbitrary objects. While the original GO-PO/PTD formulation provides excellent results at more or less convex objects, the UTD extension is required where diffracted rays might experience further interactions with the object and thus generate relevant contributions to the total scattered fields. A typical example for that case is a cavity, where rays are diffracted at the aperture and subsequently propagate into the cavity. However, also complex realistic objects can be treated by the hybrid GO/UTD-PO/PTD algorithm. As is shown by comparison with numerically exact solutions in the examples above, the elementary implementation of the UTD extension already provides very accurate results for both canonic and realistic objects.

REFERENCES

[1] F. Weinmann, "Ray tracing with PO/PTD for RCS modeling of large complex objects," *IEEE Trans. Antennas Propagat.*, vol. 54, pp. 1797-1806, June 2006.

[2] D. J. Andersh, M. Hazlett, S. W. Lee, D. D. Reeves, D. P. Sullivan, and Y. Chu, "XPATCH: A high frequency electromagnetic-scattering prediction code and environment for complex 3d objects," *IEEE Antennas and Propagation Magazine*, vol. 36, pp. 65-69, Feb. 1994.

[3] W. D. Burnside and R. J. Marhefka, "Antennas on Aircraft, Ships, or Any Large, Complex Environment," Chapter 20 in *Antenna Handbook Volume III, Applications*, edited by Y. T. Lo and S. W. Lee, Van Nostrand Reinhold, New York, 1993.

[4] E. H. Newman and R. J. Marhefka, "Overview of MM and UTD methods at the ohio state university," *Proc. IEEE*, vol. 77, pp. 700-708, May 1989.

[5] A. C. Polycarpou, C. A. Balanis, and C. R. Birtcher, "Radar cross section of trihedral corner reflectors: theory and experiment," *Electromagnetics*, vol. 15, no. 5, pp. 457-484, Sept.-Oct. 1995.

[6] S.-H. Chen and S.-K. Jeng, "An SBR-image approach for radio wave propagation in indoor environments with metallic furniture," *IEEE Trans. Antennas Propagat.*, vol. 45, pp. 98-106, Jan. 1997.

[7] A. Tzoulis and T. F. Eibert, "A hybrid FEBI-MLFMM-UTD method for numerical solutions of electromagnetic problems including arbitrarily shaped and electrically large objects," *IEEE Trans. Antennas Propagat.*, vol. 53, pp. 3358-3366, Oct. 2005.

[8] A. Altintas, P. H. Pathak, and M.-C. Liang, "A selective modal scheme for the analysis of EM coupling into or radiation from large open-ended waveguides," *IEEE Trans. Antennas Propagat.*, vol. 36, pp. 84-96, Jan. 1988.

[9] P. H. Pathak and A. Altintas, "An efficient high-frequency analysis of modal reflection and transmission coefficients for a class of waveguide discontinuities," *Radio Science*, vol. 23, pp. 1107-1119, Nov.-Dec. 1988.

[10] T. Griesser and C. A. Balanis, "Backscatter analysis of dihedral corner reflectors using physical optics and the physical theory of diffraction," *IEEE Trans. Antennas Propagat.*, vol. 35, pp. 1137-1147, Oct. 1987.

[11] C. A. Balanis, *Advanced Engineering Electromagnetics*, New York: John Wiley & Sons Inc., 1989.

[12] H. Ling, R.-C. Chou, and S.-W. Lee; "Shooting and bouncing rays: Calculating the RCS of an arbitrarily shaped cavity," *IEEE Trans. Antennas Propagat.*, vol. 37, pp. 194-205, Feb. 1989.

[13] D. Didascalou, T. M. Schäfer, F. Weinmann, and W. Wiesbeck, "Ray-Density normalization for ray-optical wave propagation modeling in arbitrarily shaped tunnels," *IEEE Trans. Antennas Propagat.*, vol. 48, pp. 1316-1325, Sep. 2000.

[14] J. Baldauf, S.-W. Lee, L. Lin, S.-K. Jeng, S. M. Scarborough, and C. L. Yu, "High frequency scattering from trihedral corner reflectors and other benchmark targets: SBR versus experiment," *IEEE Trans. Antennas Propagat.*, vol. 39, pp. 1345-1351, Sep. 1991.

[15] E. F. Knott, J. F. Shaeffer, and M. T. Tuley, *Radar Cross Section – Second Edition*, Norwood: Artech House Inc., 1993.

[16] P. H. Pathak and R. J. Burkholder, "Modal, ray, and beam techniques for analyzing the EM scattering by open-ended waveguide cavities," *IEEE Trans. Antennas Propagat.*, vol. 37, pp. 635-647, May 1989.

[17] H. T. Anastassiu, J. L. Volakis, D. C. Ross, and D. Andersh, "Electromagnetic scattering from simple jet engine models," *IEEE Trans. Antennas Propagat.*, vol. 44, pp. 420-421, Mar. 1996.

[18] R. J. Burkholder and T. Lundin, "Forward-backward iterative physical optics algorithm for computing the RCS of open-ended cavities," *IEEE Trans. Antennas Propagat.*, vol. 53, pp. 793-799, Feb. 2005.

[19] R. G. Koujoumijan and P. H. Pathak, "A Uniform geometrical theory of diffraction for an edge in a perfectly conducting surface," *Proc. IEEE*, vol. 62, pp. 1448-1461, Nov. 1974.

[20] J. B. Keller, "Geometrical theory of diffraction," *Journal of the Optical Society of America*, vol. 52, pp. 116-130, 1962.

[21] R. Tiberio, G. Pelosi, and G. Manara, "A uniform GTD formulation for the diffraction by a wedge with impedance faces," *IEEE Trans. Antennas Propagat.*, vol. 33, pp. 867-873, Aug. 1985.

[22] J. L. Volakis, "A uniform geometrical theory of diffraction for an imperfectly conducting half-plane," *IEEE Trans. Antennas Propagat.*, vol. 34, pp. 1172-1180, Feb. 1986.

[23] N. N. Youssef, "Radar cross section of complex targets," *Proceedings of the IEEE*, vol. 77, no. 5, pp. 722-734, May 1989.

Frank Weinmann received the diploma degree in physics from the University of Karlsruhe, Germany, in 1999, and the Dr.-Ing. degree in electrical engineering in 2004 from the same university. From 1999 to 2003, he was with the Institute of Industrial Information Technology, University of Karlsruhe, Germany, where he carried out studies in the field of electromagnetic compatibility of powerline communications, including modelling of radiation sources, propagation mechanisms and regulative aspects. Since 2004 he is with the FGAN-FHR Research Institute for High Frequency Physics and Radar Techniques in Wachtberg, Germany, as a Research Scientist in the Department Antennas and Scattering. His major areas of interest include propagation modeling of microwaves, high-frequency asymptotic techniques, RCS studies, and the design of broad-band planar antennas.

On the Direct Computation of the Time-Domain Plane-Wave Reflection Coefficients

[1] M. F. Pantoja, [2] A. G. Yarovoy, and [1] A. R. Bretones

[1] The Department of Electromagnetism, Facultad de Ciencias, University of Granada 18071 Spain
(phone: 34-958-240507; fax: 34-958-242353; e-mail: mario@ugr.es)

[2] The International Research Centre for Telecommunications-Transmission and Radar, Department of Information Technology and Systems, Delft University of Technology, Delft, The Netherlands (e-mail: a.yarovoy@its.tudelft.nl)

Abstract ― This communication compares different approximate techniques to calculate the transient reflection coefficient for TE and TM plane waves from a lossy half space in terms of accuracy, computational costs and area of validity. By varying angles of incidence and constitutive parameters of the half spaces, it is shown that approximate equations can efficiently and accurately calculate the reflection coefficients in the time domain, if the right equation and enough terms in the approximate series are chosen. To confirm these conclusions, it is considered, as a practical example, short pulses reflected by an operational Ground-Probing Radar from different half spaces.

I. INTRODUCTION

The calculus of the reflection coefficients (RC) for a plane-wave incident on an interface directly in the time domain has been a matter of interest for numerous practical applications, such as the characterization of materials of Ground-Penetrating Radar [1], non-destructive testing [2] and material characterization [3], and it is attracting renewed interest for estimating the multi-path propagation in UWB communication channel [4]. Efficient and accurate calculations are needed in these cases, in which the complexity of the case can require multiple computations of the RC. The first approach to solve this problem was based on the numerical evaluation of the inverse Fourier transform of the TE and TM Fresnel reflection coefficients [5, 6]. To reduce the high computational resources required by this approach, Barnes and Tesche [7] derived an approximate analytical expression for the time-domain reflection coefficients (TD-RC). This analytical expression assumes some restrictions related to the constitutive parameters of the media and angles of incidence of the plane wave. Later, Rothwell [8] and Rothwell and Suk [9] inferred other closed-forms of the TD-RC by means of a mathematical procedure involving analytic inverse Laplace transforms thereby avoiding the restrictions set by [7]. Starting from these closed-form solutions, recent papers [9, 10] have proposed expressions which can be numerically computed with efficiency. The accuracy of different approximations and related computational costs were, however, not compared.

In this paper, the aforementioned approaches are compared in terms of accuracy and computational costs. Also, some conclusions about the applicability areas for each method are drawn, by considering different media and angles of incidence for TE as well as TM polarizations. These inferences are confirmed in the last section of the work calculating the electric field radiated by a dielectric wedge antenna (DWA), which was designed for ground-penetrating radar applications [11], and the electric field reflected from lossy half-spaces.

II. TIME-DOMAIN REFLECTION COEFFICIENTS

The oblique incidence of a plane-wave from a general dielectric media onto a lossy frequency-independent half-space, of constitutive parameters (ε,σ), is solved in the frequency domain by using the Fresnel reflection coefficients [5]. Using θ_o as the angle between the incident wave and normal vector to the interface, the problem can be considered as TM or vertical-polarization incidence if the magnetic field is polarized parallel to the interface, or as TE or horizontal-polarization incidence in case of a parallel electric field to interface. The TD-RC is defined from the inverse Fourier transform of the Fresnel reflection coefficients [6]. Analytical expressions of the TD-RC are in the form,

$$\Gamma(t) = \Gamma_{die}\delta(t) + \Gamma_{con}(t)u(t) \tag{1}$$

where Γ_{die} is equal to the frequency-domain reflection coefficient for the lossless case, and $\Gamma_{con}(t)$ is a exponentially decreasing-in-time function associated with conductive processes in the lossy media. As this conductive term is composed by a sum of terms involving integrals of the modified first-class Bessel functions [8], its numerical evaluation is in general computationally

expensive, and thus approximate forms of this term are often used in practice. As Γ_{die} is identical in all the approximations [7, 9, 10], this paper will focused on comparisons of $\Gamma_{con}(t)$.

A. Approximate expressions of TD-RC

Several computationally affordable approximations of $\Gamma_{con}(t)$ have been proposed in the literature in the form of infinite expansion series. Barnes and Tesche [7] considered those cases where the condition $\sin^2\theta_0/\varepsilon_r$ <<1 is satisfied, which leads to an approximate equation of the Fresnel reflection coefficient in which an analytical inverse Laplace transform can be developed to derive expressions in the form,

$$\Gamma_{con}^{TE}(t) = K_1^{TE}\frac{e^{-\frac{\sigma t}{2\varepsilon}}}{t}\sum_{n=1}^{\infty} n\left(K_2^{TE}\right)^n I_n\left(\frac{\sigma t}{2\varepsilon}\right) \qquad (2)$$

and

$$\Gamma_{con}^{TM}(t) = K_1^{TM}\frac{e^{-\frac{\sigma t}{2\varepsilon}}}{t}\sum_{n=1}^{\infty} n\left(K_2^{TM}\right)^n I_n\left(\frac{\sigma t}{2\varepsilon}\right), \qquad (3)$$

where K_i^{TE} and K_i^{TM} are functions exclusively of ε_r and θ_0, while $I_n(x)$ represents the *n*-order modified Bessel function of the first class.

Another approximation arises by considering a Taylor series of the function $Q(x) = e^{-x}I_0(x) + e^{-x}I_1(x)$. Substitution of this series in the closed form of the TD-RC simplifies the integral terms, and expressions found are [9, 10],

$$\Gamma_{con}^{TE}(t) = \sum_{n=1}^{\infty} C_1^{TE}\left(C_2^{TE}\right)^n Q^{(n)}\left(C_0^{TE}t\right) \qquad (4)$$

and

$$\Gamma_{con}^{TM}(t) = \sum_{n=1}^{\infty}\left[C_1^{TM}\left(C_2^{TM}\right)^n + C_3^{TM}\left(C_4^{TM}\right)^n\right]Q^{(n)}\left(C_0^{TM}t\right) \qquad (5)$$

where C_i^{TE}, and C_i^{TM} depend only on ε, σ and θ_0; and $Q^{(n)}(x)$ represents the *n*-order derivative of $Q(x)$.

Despite that equations (4) and (5) are as exact as the closed-form TD-RC analytical expressions, the truncation of the infinite series carries loses accuracy for small *t*. In fact, this initial period of time produces the main contribution to the reflected field, and improvements of the truncation error at early times are achieved by using [9, 10],

$$\Gamma_{con}^{TE}(t) = \left[1 + C_3^{TE}e^{-C_0^{TE}t}\right]\sum_{n=1}^{\infty} C_1^{TE}\left(C_2^{TE}\right)^n Q^{(n)}\left(C_0^{TE}t\right) \qquad (6)$$

and

$$\Gamma_{con}^{TM}(t) = C_5^{TM}e^{-2C_0^{TM}t}\left(C_6^{TM}C_0^{TM}t + 1\right) + \sum_{n=1}^{\infty}\left[C_1^{TM}\left(C_2^{TM}\right)^n + C_3^{TM}\left(C_4^{TM}\right)^n\right]Q^{(n)}\left(C_0^{TM}t\right). \qquad (7)$$

Detailed expressions of K_i^{TE}, K_i^{TM}, C_i^{TE}, C_i^{TM} are given in the appendix.

B. Convergence and Accuracy of the Approximations

Prior to comparing the approximations, it is performed a preliminary study on the convergence of the series for different truncations. By varying the angles of incidence for different soils (lossy ground with ε_r=10 and σ =0.01 and sea water with ε_r =72 and σ =4) and considering TE and TM polarizations, it is found that good rates of convergence are assured by using series of N=5 for the equations (2) and (3), N=10 for equations (4) and (5), and N=3 for equations (6) and (7). Figure 1 illustrates this convergence for the particular case of normal incidence on sea water. Furthermore, relative computational times for each method are compared in table 1. Computational times are normalized taking as a reference the time to calculate the closed-form solution by using a numerical integration based on the Simpson rule over 100 points [12]. Due to the high degree of convergence of the equations (6) and (7), an approximation of these equations by using only one term is included in the results, as a faster approximation of TD-RC.

Table 1. Relative computational time for equations (2) and (7).

EXACT	*2-3, N=5*	*4-5, N=10*	*6-7, N=1*	*6-7, N=3*
1	0.011	0.168	0.008	0.030

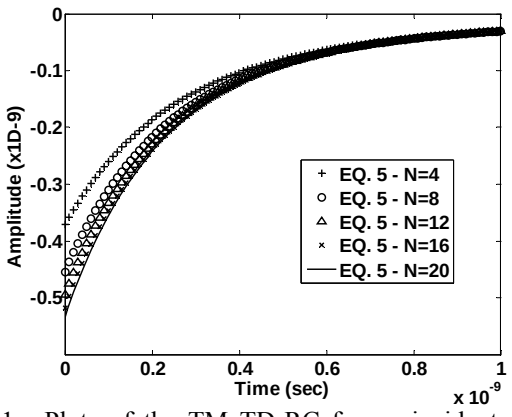

Fig. 1. Plots of the TM TD-RC for an incident plane wave forming θ_0=0º with sea water (ε_r =72, σ =4), calculated by using different truncations of equation 5.

Once the truncation of the different series is established, a study on the accuracy provided by each equation is carried out. Again, lossy ground and sea water are used as half-space, and different angles of incidence between the normal incidence and the Brewster angle of each interface are considered. Tables 2 and 3 summarize the results from both the TE and TM polarizations, taking as parameter of the comparison the maximum relative error over time made by each approximation. On examining Tables 2 and 3, it can be appreciated that equations (2) and (3) improve in performance when the condition required for their use is satisfied for cases where this approximation is poor (lossy ground and high angles of incidence), equations (5) and (6), with N=3, are closer to the exact solution. This fact is better seen both in TE polarization (Fig. 2 where marks correspond to equations (2) and (6), with N=3), and in TM polarization (Fig. 3, equations (3) and (7), with N=3). In both figures, all the approximations are very close to the exact solution, and little improvement is achieved by each one, depending on the aforementioned condition. Another remarkable fact is that Figs. 2 and 3 show that maximum relative errors appear in equations (6) and (7), with N=1 at late time. For short pulses, such as those used in UWB applications, these late-time errors have a minor effect on the calculus of the reflected field, and in principle the implementation of the computationally fastest solution should not be ruled out. A final conclusion related to these Tables is that poorest results are given by equation (3), and its use seems not to be advisable, either in terms of computational cost or in terms of accuracy.

Table 2 (a). Maximum relative error (%) for TM plane waves over ground.

	3, N=5	*5, N=10*	*7, N=1*	*7, N=3*
0º	1.74	4.69	11.90	2.31
10º	0.30	3.35	11.83	2.41
20º	1.19	0.52	11.50	2.69
30º	2.63	6.48	11.75	3.06
40º	4.50	13.18	12.69	3.02
50º	6.64	17.80	12.90	1.76
60º	8.82	16.61	11.20	0.38

Table 2 (b). Maximum relative error (%) for TE plane waves over ground.

	2, N=5	*4, N=10*	*6, N=1*	*6, N=3*
0º	1.74	4.69	13.55	4.31
10º	0.30	4.88	13.60	4.36
20º	1.16	5.47	13.74	4.54
30º	2.49	6.57	13.08	4.82
40º	4.13	8.35	13.28	4.85
50º	5.86	11.01	13.42	5.27
60º	7.49	14.79	13.42	5.71

Table 3 (a). Maximum relative error (%) for TM plane waves over sea.

	3, N=5	*5, N=10*	*7, N=1*	*7, N=3*
0º	2.36	19.39	3.74	1.73
10º	2.28	19.03	3.50	1.65
20º	0.16	17.96	3.24	1.35
30º	0.34	16.12	2.80	0.95
40º	0.58	13.45	12.96	2.30
50º	0.82	9.78	12.69	2.41
60º	1.06	4.86	12.23	2.51
70º	1.25	0.94	11.44	2.76
80º	1.38	2.75	8.55	0.57

Table 3 (b). Maximum relative error (%) for TE plane waves over sea.

	2, N=5	*4, N=10*	*6, N=1*	*6, N=3*
0º	2.36	19.39	12.39	5.88
10º	2.43	19.57	12.38	5.90
20º	0.16	20.14	12.34	5.93
30º	0.34	21.08	12.27	5.97
40º	0.57	22.39	12.16	6.03
50º	0.81	24.06	12.01	6.08
60º	1.04	26.07	11.79	6.13
70º	1.22	28.38	11.05	6.15
80º	1.34	30.93	10.72	5.88

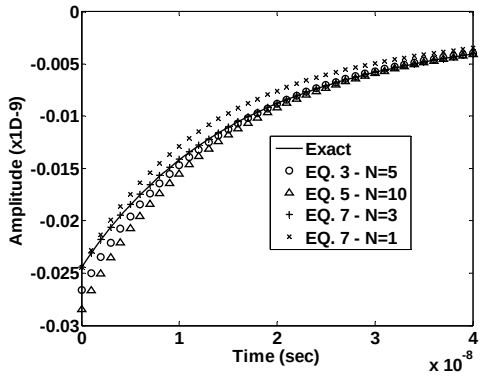

Fig. 2. TM TD-RC for an incident plane wave forming θ_0=60º with a lossy ground (ε_r=10, σ =0.01).

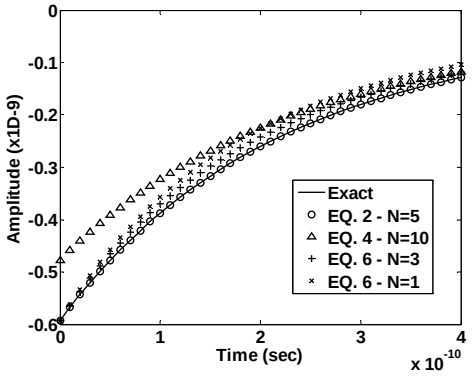

Fig. 3. TE TD-RC for an incident plane wave forming θ_0=0º with sea water (ε_r =72, σ =4).

Figure 4 shows the behaviour of the transient reflection coefficient for an incidence angle near the Brewster angle. For angles above the Brewster case, equations (5) an (7) are no longer valid [8], and significant variations compared with the exact solution appear. Nevertheless, restrictions in the applicability of equation (3) do not depend specifically on the proximity to the Brewster angle, offering thus better results.

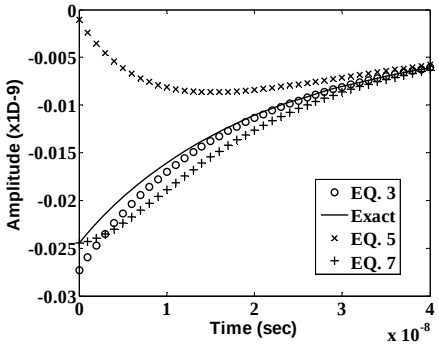

Fig. 4. TM TD-RC for an incident plane wave forming θ_0=78º with a lossy ground (ε_r =10, σ =0.01). N=10 for approximate equations.

III. EXAMPLE OF APPLICATION: DWA ANTENNA

As a practical example of application, the incidence of the electric field radiated by a DWA (Fig. 5) on different kind of soils is considered. Figure 6 depicts a comparison of the main peak of $E^r_{con}(t)$ for the incidence of the pulse of Fig. 5 in the same conditions as those of the Fig. 3 (normal incidence and sea water). As an illustration of cases where the condition for applying equation (2) does not strictly hold, the incidence of the DWA radiated pulse at a interface of a lossy concrete (ε_r =3 , σ=0.01), with an angle of 60º, is simulated (Fig. 7). To estimate the accuracy of the different approximations, the reflected electric field is compared. According to the definition of Fresnel RC, the reflected field is calculated numerically by applying,

$$\begin{aligned} E^r(t) &= E^r_{die}(t) + E^r_{con}(t) = \Gamma(t) * E^i(t) \\ &= \Gamma_{die} E^i(t) + \int_0^t \Gamma_{con}(\xi) E^i(t-\xi) d\xi \end{aligned} \quad (8)$$

where the TE or TM reflection coefficient has to be used in accordance with the polarization of the electric field.

Figure 6 show that both equations (2) and (3), as well as equations (6) and (7) (with N=1 and N=3) give an accurate representation of the reflected field. As pointed out above, errors made by equation (6) with N=1 do not lead to any appreciable difference for this UWB pulse. In Fig. 7, we clearly appreciate errors in plot corresponding to equation (2), as was expected taking into account that $\sin^2\theta_0/\varepsilon_r = 0.25$ for the lossy concrete with an incidence of 60º. The rest of the equations, which are not restricted by this condition, reproduce more accurately the exact solution. Therefore, it can be concluded that equations (2) and (3) are more sensible to the effect of the medium parameters than the others, as long as the angle of incidence remains enough low to hold the accuracy of equations (4) to (7).

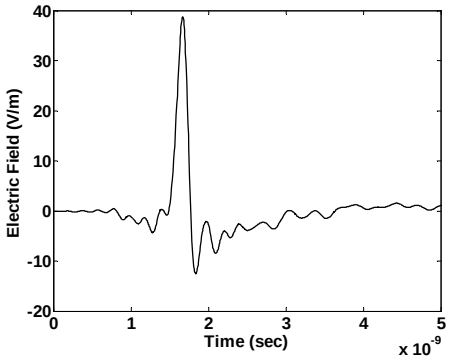

Fig. 5. Electric field radiated by a dielectric wedge antenna.

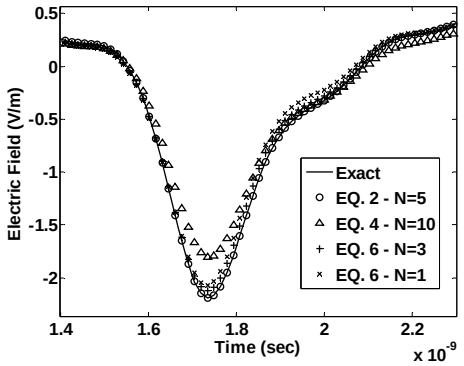

Fig. 6. Conductive part of the reflected electric field for the normal incidence of the DWA radiated pulse at sea water (ε_r =72, σ =4).

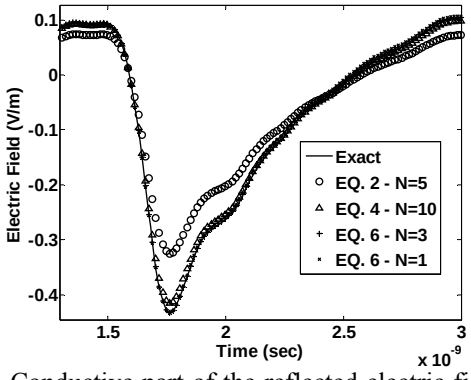

Fig. 7. Conductive part of the reflected electric field for the incidence with θ_0=60º of the DWA radiated pulse at lossy concrete (ε_r =3, σ =0.01).

IV. CONCLUSIONS

A comparison of the different approximations to estimate the TD-RC reveals the relevance of their implementation for accurate simulation of the electromagnetic pulses reflected from homogeneous half-spaces. Equations (2) and (3) proved computationally faster than any other approximation and very accurate, but they have a limited area of validity and thus their use has to be restricted to cases which satisfy a specific condition. Equations (6) and (7) constitute another good choice. They are in general computationally fast, and their accuracy can be increased by adding only a few more terms to the series. They are not restricted to particular combinations of angles of incidence or constitutive soil parameters, and their use guarantees accurate results. Equations (4) and (5) are definitely poor choices in comparison with the other approximations. Therefore, a correct choice in these approximations enables faster and accurate simulations of interaction of electromagnetic waves with real media, which is a matter of interest in such fields as ground-penetrating radar and material characterization.

APPENDIX

Equations (2) to (7) have arisen to the set of functions K_i^{TE}, K_i^{TM}, C_i^{TE}, C_i^{TM} whose operational expressions are given below. Note that integer N represents the order of the truncation of the infinite series appearing in those equations, and $Q^{(n)}(0)$ can be derived from the recurrence relations of the modified Bessel functions $I_n(0)$ [13].

The K_i^{TE}, K_i^{TM} of equations (2) and (3) are,

$$K_1^{TE} = -\frac{4k_{TE}}{1-(k_{TE})^2}$$
$$K_2^{TE} = \frac{1-k_{TE}}{1+k_{TE}},$$
$$K_1^{TM} = \frac{4k_{TM}}{1-(k_{TM})^2},$$
$$K_2^{TM} = \frac{1-k_{TM}}{1+k_{TM}},$$

where

$$k_{TE} = \frac{\cos\theta_0}{\sqrt{\varepsilon_r - \sin^2\theta_0}},$$
$$k_{TM} = \frac{\sqrt{\varepsilon_r - \sin^2\theta_0}}{\varepsilon_r \cos\theta_0}.$$

Equations (4) and (6) are expressed in terms of C_i^{TE},

$$C_0^{TE} = \frac{\sigma}{2\varepsilon_0\left(\varepsilon_r - \sin^2\theta_0\right)}$$
$$C_1^{TE} = \frac{\sigma\cos\theta_0}{\varepsilon_0\left(\varepsilon_r - 1\right)\sqrt{\varepsilon_r - \sin^2\theta_0}},$$
$$C_2^{TE} = \frac{1-\varepsilon_r}{2\left(\varepsilon_r - \sin^2\theta_0\right)},$$
$$C_3^{TE} = \frac{c_{TE}^a}{C_1^{TE}\sum_{n=1}^{N}\left(C_2^{TE}\right)^n Q^{(n)}(0)},$$

where

$$c_{TE}^a = -\frac{\cos\theta_0}{\varepsilon_0\left(\cos\theta_0 + \sqrt{\varepsilon_r - \sin^2\theta_0}\right)^2\sqrt{\varepsilon_r - \sin^2\theta_0}}.$$

Finally, C_i^{TM} in equations (5) and (7) are,

$$C_0^{TM} = \frac{c_{TM}^b}{2}$$
$$C_1^{TM} = -4C_0^{TM}\frac{\left(c_{TM}^p + \frac{\sigma}{\varepsilon}\right)\sqrt{c_{TM}^d}}{\left(c_{TM}^p - c_{TM}^q\right)\left(c_{TM}^d - 1\right)}$$
$$C_2^{TM} = \frac{c_{TM}^b}{2c_{TM}^p}$$
$$C_3^{TE} = -4C_0^{TM}\frac{\left(c_{TM}^q + \frac{\sigma}{\varepsilon}\right)\sqrt{c_{TM}^d}}{\left(c_{TM}^q - c_{TM}^p\right)\left(c_{TM}^d - 1\right)}$$
$$C_4^{TM} = \frac{c_{TM}^b}{2c_{TM}^q}$$
$$C_5^{TM} = \frac{\sqrt{c_{TM}^d}}{\left(1+\sqrt{c_{TM}^d}\right)^2}\left(c_{TM}^b - 2\frac{\sigma}{\varepsilon}\right) - \sum_{n=1}^{N}\left[C_1^{TM}\left(C_2^{TM}\right)^n + C_3^{TM}\left(C_4^{TM}\right)^n\right]Q^{(n)}(0)$$
$$C_6^{TM} = \left|\frac{C_5^{TM}\left(1+\sqrt{c_{TM}^d}\right)^2}{\left(c_{TM}^b - 2\frac{\sigma}{\varepsilon}\right)\sqrt{c_{TM}^d}}\right|$$

where

$$c_{TM}^b = \frac{\sigma}{\varepsilon_0\left(\varepsilon_r - \sin^2\theta_0\right)}$$
$$c_{TM}^d = \frac{\left(\varepsilon_r\cos\theta_0\right)^2}{\varepsilon_r - \sin^2\theta_0},$$
$$c_{TM}^e = \frac{2\sigma c_{TM}^d - \varepsilon c_{TM}^b}{\varepsilon\left(1-c_{TM}^d\right)},$$
$$c_{TM}^f = \frac{\sigma^2 c_{TM}^d}{\varepsilon^2\left(c_{TM}^d - 1\right)},$$
$$c_{TM}^p = \frac{1}{2}\left(c_{TM}^b + \sqrt{\left(c_{TM}^b\right)^2 - 4c_{TM}^f}\right),$$
$$c_{TM}^p = \frac{1}{2}\left(c_{TM}^b - \sqrt{\left(c_{TM}^b\right)^2 - 4c_{TM}^f}\right).$$

ACKNOWLEDGMENTS

We thank the FP6 Network of Excellence ACE (contract 026957), Spanish Government (Projects TEC2007-66698-C04-02/TCM and PTR95-1025.0P.01), Junta de Andalucia (Project of excellence TIC1541), and European Commission within the FP6 STREP project Orfeus (project number 036856) for supporting this work.

REFERENCES

[1] D. J. Daniels, *Ground Penetrating Radar*. The Institution of Electrical Engineers, 2004.

[2] D. M. Mc Cann and M. C. Forde, "Review of NDT methods in the assessment of concrete and masonry structures," *NDT&E International*, vol. 34, pp. 71-84, 2001.

[3] V. A. Vinogradov, V. V. Kopeikin, and A. V. Popov, "An approximate solution of 1D inverse Problem," *Proceedings of the Tenth International Conference on Ground Penetrating Radar*, pp. 95-98, 2004.

[4] Q. Zeng and G. Y. Delisle, "Time-domain analysis for ultrawideband pulse reflection from a lossy interface," *Proceedings of the EMTS 2007 Internat. URSI Commision B Symposium*, 2007.

[5] J. R. Wait, *Electromagnetic Waves in Stratified Media*, Pergamon, 1962.

[6] D. G. Dudley, T. M. Papazoglou, and R. C. White, "On the interaction of a transient electromagnetic plane wave and a lossy half-space," *Journal of Applied Physics*, vol. 45, pp. 1171–1175, 1974.

[7] P. R. Barnes and F. M. Tesche, "On the direct calculation of a transient plane wave reflected from a finitely conducting half space", *IEEE Transactions on Electromagnetic Compatibility*, vol. 33, pp. 90–96, 1991.

[8] E. J. Rothwell and M. J. Cloud, *Electromagnetics*, CRC Press, 2001.

[9] E. J. Rothwell and J. W. Suk, 2005, "Efficient computation of the time domain TE plane-wave reflection coefficient", *IEEE Transactions on Antennas and Propagation*, vol. 53, pp. 3417–3419, 2005.

[10] E. J. Rothwell and J. W. Suk, "Efficient computation of the time domain TE plane-wave reflection coefficient", *IEEE Transactions on Antennas and Propagation*, vol. 51, pp. 3283–3285, 2003.

[11] A. G. Yarovoy, A. D. Schukin, I. V. Kaploun, and L. P. Lighthart, "The dielectric wedge antenna", *IEEE Transactions on Antennas and Propagation*, vol. 50, pp. 1460–1472, 2002.

[12] W. H. Press, B. P. Flannery, S. A. Teukolsky, and W. T. Vetterling, *Numerical Recipes. The Art of Scientic Computing*, Cambridge University Press, 1992.

[13] M. Abramowitz and I. Stegun, *Handbook of Mathematical Functions*, Dover, 1972.

Mario Fernández Pantoja is Associate Professor of the is with the Department of Electromagnetism at the University of Granada, Spain. His research is focused mainly on the areas of time-domain analysis of electromagnetic radiation and scattering problems, and optimization methods applied to antenna design.

Alexander G. Yarovoy is with the International Research Centre for Telecommunications, Transmission and Radar at TUDelft, The Netherlands. His main research interests are in ultra wideband technology and its applications, applied Electromagnetics and computational methods in Electromagnetics.

Amelia Rubio Bretones is with the Department of Electromagnetism at the University of Granada, Spain, as a Full Professor. Her research interest is mainly in the field of numerical techniques for applied Electromagnetics with an emphasis on time-domain techniques such as finite-difference time domain, the application of the method of moments in the time domain for antenna and scattering problems, and hybrid techniques.

Quasi Monte Carlo Integration Technique for Method of Moments Solution of EFIE in Radiation Problems

M. Mishra and N. Gupta

Department of Electronics and Communication Engineering
Birla Institute of Technology, Mesra,
Ranchi 835 215, INDIA
mrinal.mishra@gmail.com, ngupta@bitmesra.ac.in

Abstract – In this work, a Quasi Monte Carlo Integration (QMCI) Technique using Halton Sequence is proposed for the Method of Moments (MoM) solution of the Electric Field Integral Equation (EFIE) in radiation problem. It is found that this scheme is capable of handling the singularity issue in the EFIE automatically and at the same time provides solution to the radiation problems very efficiently.

I. INTRODUCTION

Multidimensional numerical quadratures are of great importance in many practical areas, ranging from radiation/scattering problems in computational electromagnetics to atomic physics. The EFIE in solution of MoM for scattering problems involves multidimensional integrals especially when the Galerkin's technique for solution is employed. It is well known that a *D* dimensional scattering problem using Galerkin's technique involves solution of 2*D* dimensional integral equation. Gaussian quadrature methods, on the one hand, yield precise results with relatively few integrand evaluations, but they are not too robust and work best for very smooth functions and the time complexity in numerical quadrature methods increases as the dimension of the problem increases. Monte Carlo methods [1-3], on the other hand, impose few requirements on the integrand, but are known to converge slowly. It is an integration approach that is well suited for irregular or singular integrands and requires no analytic knowledge about the form of the integrand. The conventional Monte Carlo integration (MCI) method is independent of the dimension of the integral, and that is why MCI is the only practical method for many high-dimensional problems.

QMCI methods are based on the idea that random Monte Carlo techniques can often be improved by replacing the underlying source of random numbers with a more uniformly distributed deterministic sequence. The fundamental feature underlying all QMCIs, however, is the use of a quasi-random number (QRN) sequences in place of the usual pseudorandom numbers which often improves the convergence of the numerical integration.

One of the key issues in the solution of the EFIE using Galerkin's technique is the singularity appearing the Green's function kernel of the Integral Equation. The type of the singularity is weak in nature. Several techniques [4-7] have been used in the past to deal with the issue of singularity in order to solve the problem. The conventional MCI takes care of the singularity aspect without employing any analytical techniques such as singularity subtraction/removal, polar co-ordinate transformation, etc. and implements the idea just by avoiding the random points to fall in the singular region. This happens by including a simple statement in the program code used for the simulation purpose. However, the proposed Halton sequence in QMCI takes care of the singularity issue automatically without even modification or inclusion of any condition in the program code and provides solution to the problem much faster than the conventional MCI with randomly generated point sequences. The inherent nature of the Halton sequences automatically avoids inclusion of singular points in the integration.

II. MATHEMATICAL CONCEPT

The idea of Monte Carlo integration is to evaluate an integral using random sampling of points for function evaluation. In this method, if *I* is a *D* dimensional integral,

$$I = \int_{\Omega} f(x_1, x_2, ..., x_D) dx_1 dx_2 ... dx_D \qquad (1)$$

where $f(x_1, x_2, ..., x_D)$ is the integrand function and Ω is domain of integration in *D* dimensional space. The Monte Carlo integration is done by independently sampling *N* random points $\{(x_{11}, x_{12}, ..., x_{1D}), (x_{21}, x_{22}, ..., x_{2D}), ..., (x_{N1}, x_{N2}, ... x_{ND})\}$ in Ω, according to some convenient probability density

function $p(x_{i1}, x_{i2}, ..., x_{iD})$, and then computing the estimate,

$$F_N = \frac{\Omega}{N} \sum_{i=1}^{N} \frac{f(x_{i1}, x_{i2}, ..., x_{iD})}{p(x_{i1}, x_{i2}, ..., x_{iD})}. \quad (2)$$

Here the notation F_N is used rather than I to emphasize that the result is approximate, and that its properties depend on how many sample points are chosen. If $p(x_{i1}, x_{i2}, ..., x_{iD})$ is the uniform probability density, then the integral is simply,

$$I \cong \frac{\Omega}{N} \sum_{i=1}^{N} f(x_{1i}, x_{2i}, ..., x_{Di}). \quad (3)$$

Unlike the conventional Monte Carlo integration that uses sampling of random points in Ω, the Quasi Monte Carlo Integration methods use the sampling points with uniform probability distribution that are more evenly distributed than the random points over the domain Ω. The classical QMCI method replaces the independent random points used in MCI by a deterministic set of distinct points. The problem of clustering of random numbers in the domain can be removed by the use of Halton numbers. The use of quasi random sequences in place of the usual pseudorandom numbers often improves the convergence of the numerical integration.

There are several well-known constructions for QRN sequences. In the one dimensional case, it is achieved, for example, by the Van der Corput sequence [3]. This construction uses a prime number as base for generation of numbers between 0 and 1, obtained by reversing the digits in the representation of some sequence of integers in a given base. To obtain a QRN sequence in several dimensions, we use a different radical inverse sequence in each dimension.

The classic example of this construction in several dimensions is the Halton sequence [8]. In one dimension for a prime base p_n, the n^{th} number in the sequence corresponding to the digit n is obtained by the following steps [1].

For each n:

1. n is written as a number in base p_n. Thus if $p_n = 3$ and $n = 22$, then 22 in base 3 is written as $22 = 2 * 3^2 + 1 * 3^1 + 1 * 3^0 = 211$.
2. The digits are reversed and a radix point (i.e., a decimal point base p_n) is put in front of the sequence (in the example, we get 0.112 base 3).
3. The sequence for one dimension is obtained by application of the above process for different values of n.

Every time the number of digits in n increases by one place, n's digit-reserved fraction becomes a factor of p finer-meshed. So, at each step as n increases points of Halton sequence are better and better filling Cartesian grids. The Halton numbers generated for first three dimensions using 2, 3, and 5 as the prime numbers for bases, respectively, for n ranging from 1 to 8 are shown in Table 1.

Table 1. Halton sequences for first 3 dimensions.

n	Dim 1 $p=2$	Dim 2 $p=3$	Dim 3 $p=5$
$n=1$	1/2	1/3	1/5
$n=2$	1/4	2/3	2/5
$n=3$	3/4	1/9	3/5
$n=4$	1/8	4/9	4/5
$n=5$	5/8	7/9	1/25
$n=6$	3/8	2/9	6/25
$n=7$	7/8	5/9	11/25
$n=8$	1/16	8/9	16/25

The samplings of two dimensional space $[0,1]^2$ with 500 points are shown for both Monte Carlo using random sequences in both dimensions; and Quasi Monte Carlo sampling using Halton sequences with $p_n = 2$ and $p_n = 3$ respectively in two dimensions are shown in Fig. 1. It is clear from the figure that the Halton sequence points sample the region more uniformly than the random sequences. The problem of clustering of points in Monte Carlo sampling is significantly reduced in Quasi Monte Carlo sampling.

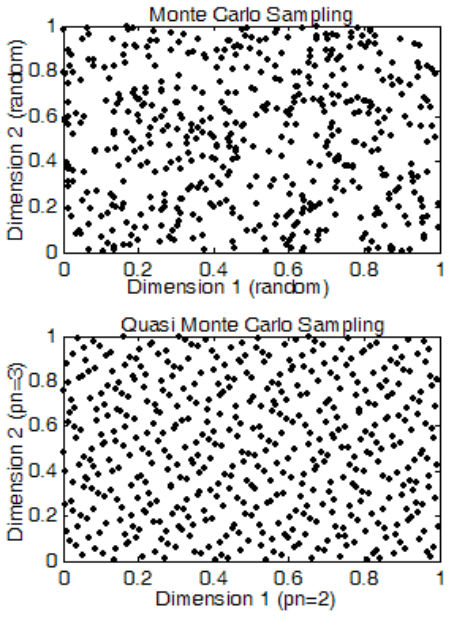

Fig. 1. Sampling of the two dimensional space using random and Halton sequences, respectively.

Another very important aspect of the Halton sequences, as is clear from table 1, is that the sequences in any two different dimensions are not the same, i.e., the sample points in a quasi-random sequence are, in a precise sense, "maximally avoiding" of each other. This property has been utilized in the Galerkin approach for the MoM solution of the radiation from wire antenna with the exact form of the kernel. The two dimensional problem in this approach leads to integration of four dimensional singular functions in which the integrands have line singularities. This problem of singularity can be removed automatically by the QMCI using Halton sequences with different bases for each dimension.

III. FORMULATION OF THE PROBLEM

The numerical modeling of a wire dipole antenna [9-14] is taken up as a test problem A dipole wire antenna of finite radius *a,* and length *l* is shown in Fig. 2. The wire has a finite thickness, but it is considered thin as $a << \lambda$. For a thin antenna, the unknown current varies on the surface only along the z axis and variation along the coordinate φ is negligible. Figure 2 shows a center fed dipole wire antenna of radius *a*, and length *l*. Both source and observation points are on the surface of the antenna characterized by both axial and circumferential coordinates. The wire antenna is usually formulated using two approaches, depending on whether the exact (full) kernel (EK) or the approximate (reduced) kernel (AK) of the integral equation is used. In the exact kernel formulation [15], where the kernel is singular, several singularity extraction and correction techniques have been used that require analytical methods.

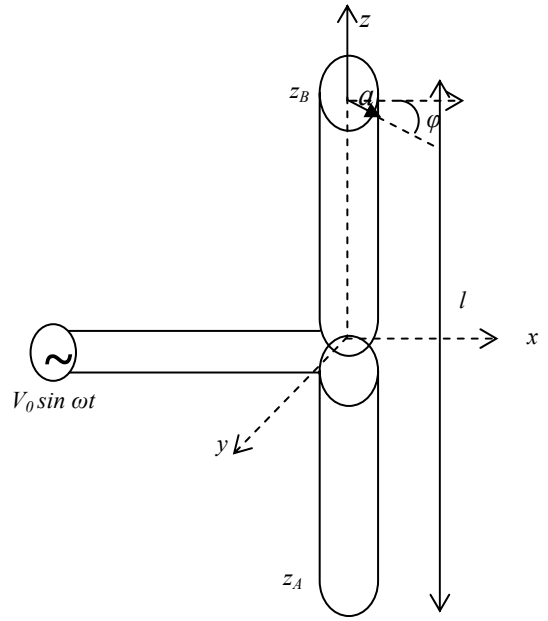

Fig. 2. A center fed dipole wire antenna of radius *a*, and length *l*.

Thus, the evaluation of matrix elements requires analytical pre processing of the kernel, before numerical integration, making the entire procedure very complicated.

The need to get rid of the singularity has resulted in the approximated or the reduced form of the kernel by Richmond [16]. The corresponding EFIE is,

$$-E_z^{\,i} = \frac{\lambda Z_0}{j8\pi^2}\int_l J_z(z')\frac{e^{-jkR}}{R^5}[(1+jkR)(2R^2-3a^2)+(kaR)^2]dz' \tag{4}$$

where $R=\sqrt{a^2+(z-z')^2}$ and $Z_0 = 337\Omega$, the free space impedance.

It is clear from equation (4) that both the observation and the source points are not on the surface, but the source coordinates are along the z-axis. The exclusion of the ϕ coordinates from the kernel is a very crude approximation of it, and therefore the reduced kernel formulation results in loss of one dimension of the problem.

In the exact kernel formulation, on the surface of the antenna, the EFIE takes the form,

$$-E^{inc}(z,\phi) = \frac{1}{j4\pi\omega\varepsilon_0}\int_{z_A}^{z_B} J(z')\left(\frac{\partial^2}{\partial z^2}+k^2\right)G(z,\phi;z'\phi')adz'\,d\phi' \tag{5a}$$

where

$$G(z,\phi;z',\phi') = \frac{e^{-jk\sqrt{(2a^2(1-\cos(\phi-\phi')+(z-z')^2}}}{\sqrt{(2a^2(1-\cos(\phi-\phi')+(z-z')^2}}\,. \tag{5b}$$

A. MoM Formulation

The unknown current on the surface of the antenna is expanded as,

$$J(z') = \sum_{n=1}^{M}\alpha_n f_n(z') \tag{6}$$

where α_n ; n = 1, 2, . . .,*M;* are unknown amplitudes to be determined.

The point matching technique leads to the matrix equation of the form,

$$-j4\pi\omega\varepsilon_0\begin{bmatrix} E_z^{inc}(z_1)\\ E_z^{inc}(z_2)\\ \cdot\\ \cdot\\ E_z^{inc}(z_M)\end{bmatrix} = [A_{mn}][\alpha_n] \tag{7}$$

with

$$A_{mn} = \int_{z_A}^{z_B} f_n(z')\left(\frac{\partial^2}{\partial z^2} + k^2\right) G(z_m, \phi; z'\phi')\, a\, dz'\, d\phi'. \tag{8}$$

And the Galerkin's technique leads to the matrix equation of the form,

$$-j4\pi\omega\varepsilon_0 \begin{bmatrix} \int_{z_A}^{z_B} E_z^{inc}(z) f_1(z) dz \\ \int_{z_A}^{z_B} E_z^{inc}(z) f_2(z) dz \\ \vdots \\ \int_{z_A}^{z_B} E_z^{inc}(z) f_M(z) dz \end{bmatrix} = [A_{mn}][\alpha_n] \tag{9}$$

with

$$A_{mn} = \int_{z_A}^{z_B}\int_{z_A}^{z_B} f_n(z') G(z, \phi; z'\phi')\left(\frac{\partial^2}{\partial z^2} + k^2\right) f_m(z) a^2 dz'\, d\phi'\, dz d\phi. \tag{10}$$

B. MCI and QMCI Technique Implementation

The fact that the kernel of the EFIE is singular is evident from equation (5). For the point matching technique, the local correction technique is applied to deal with the singularity arising in the integration of equation (8) where the integrand diverges at the points where $\phi' = \phi_m$ and $z' = z_m$. Both the MCI and QMCI can be utilized for treating this singularity. This technique can be implemented by excluding small regions about the points of singularity ϕ_m and z_m when the random points are generated for the variables ϕ' and z' respectively by embedding the required condition directly in the program code employed for the purpose in simulation.

For Galerkin's technique, in the problem under investigation, QMCI is applied to remove the singularity arising in the integration of equation (10). This is a four dimensional integration in variables ϕ, ϕ', z and z', where the integrand shows line singularity at the points where $\phi = \phi'$ and $z = z'$. This problem of line singularity can be is done by generating quasi random Halton sequences with different bases for the variables ϕ, ϕ', z and z', since no two Halton sequences with different bases are same, the singularity in the kernel is taken care off automatically.

IV. NUMERICAL EXAMPLES

As a test example for the proposed technique, a half wavelength wire dipole antenna, fed at its center by a signal generator of frequency 850 MHz is considered. The corresponding wavelength is λ = 0.3529 m. The radius is $a = 0.001\lambda$. The two ends of the antenna have the coordinates $z_A = -\lambda/4 = -0.088235$ m; $z_B = \lambda/4 = 0.088235$ m.

Three cases for the problem have been studied:

Case I: The proposed exact kernel with the sinusoidal incident field modeling and implementation of MCI with sub domain pulse basis functions. The entire length of the antenna is divided into equal length segments and each segment is at least λ/10 in length. Further, the number of segments is odd, so that the feed gap is modeled as a single segment. Taking these two factors into consideration, the antenna is divided into 21 equal length segments and the point matching technique with mid points of each segment as the observation points is adopted. In this modeling, the diagonal terms of the matrix are from equation (8). The incident electric field is,

$$E_z^{inc}(z) = \sin(k(z - z_A)). \tag{11}$$

The total number of random points taken for the MCI is N = 5000.

Case II: The proposed exact kernel with the sinusoidal incident field in equation (11) and implementation of MCI with entire domain polynomial basis functions. Since the incident field is parallel to the z axis, from the geometry of the antenna, the z directed current will be zero at the edges perpendicular to z axis, i.e., at $z = z_A$ and $z = z_B$. The entire domain basis function employed is the polynomial,

$$J(z') = \sum_{even\ n=2}^{M} z'^n - (z_A)^n. \tag{12}$$

The simulation is carried out for M = 4, making number of terms in the expansion is equal to 2. It is observed that the results convergence for M > 4. The total number of random points taken for the MCI is N = 10000.

Case III: The reduced kernel with conventional quadrature integration and the delta gap source modeling with sub domain pulse basis functions. The antenna is divided into 21 equal length segments, with mid points of each segment as the observation points, as in case I. The simulation results of the normalized

current distribution over the length of the wire antenna, obtained for the three cases mentioned above is plotted in Fig. 3. As is evident from the figure, all the three results are in excellent agreement, which justifies the effectiveness of the proposed method. The efficiency of the MCI techniques adopted for integration of the singular function used with the entire domain polynomial basis functions given by equation (9) is evident from Table 2. As can be seen, this combination results in reduction in storage requirements by more than 100 times, making the proposed technique very efficient.

Next, the efficiency of the QMCI technique is tested on two problems. First, a half wavelength wire dipole antenna, fed at its center by a signal generator of frequency 300 MHz is considered. The corresponding wavelength is λ = 1 m. The radius is $a = 0.001\lambda$. The two ends of the antenna have the coordinates z_A = -0.25m and z_B = 0.25m.

The results are obtained by QMCI implementation and sub domain pulse basis function with 21 segments using N = 500 for both point matching and Galerkin's approach and plotted in Fig. 4. The results are in very good agreement.

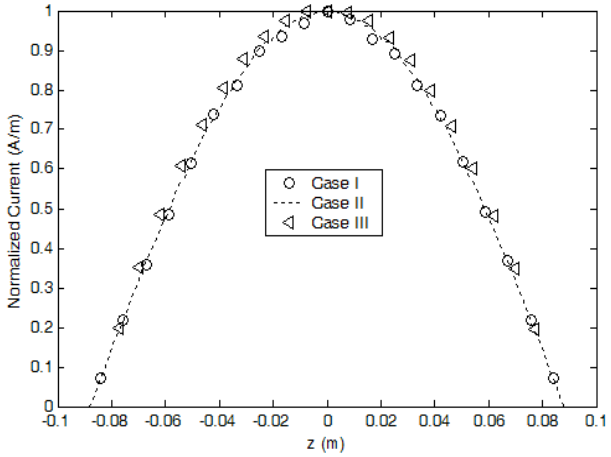

Fig. 3. The normalized current distribution on the wire dipole antenna ($l = \lambda/2$) for the three cases.

Table 2. A comparison of matrix size.

kernel	*Basis function*	*Integration technique*	*Matrix Size*
Exact	Sub sectional pulse	MCI N = 5000	21 x 21
Exact	Poly nomial, given by (12) with M = 4	MCI N = 10000	2 x 2
Reduced	Sub sectional pulse	Conventional	21 x 21

Secondly, a one wavelength wire dipole center fed antenna, of frequency 600 MHz is considered. The corresponding wavelength is λ = 0.5 m. The radius is $a = 0.001\lambda$. The two ends of the antenna have the coordinates z_A = -0.25m and z_B = 0.25m. The results are obtained by QMCI implementation and sub domain pulse basis function with 21 segments.

Figure 5 compares the both point matching and Galerkin's methods for QMCI implementation using N = 500 for one wavelength dipole which again shows a very good agreement between the two results. It is seen that QMCI is very efficient as is gives the desired results in only 500 quasi random points.

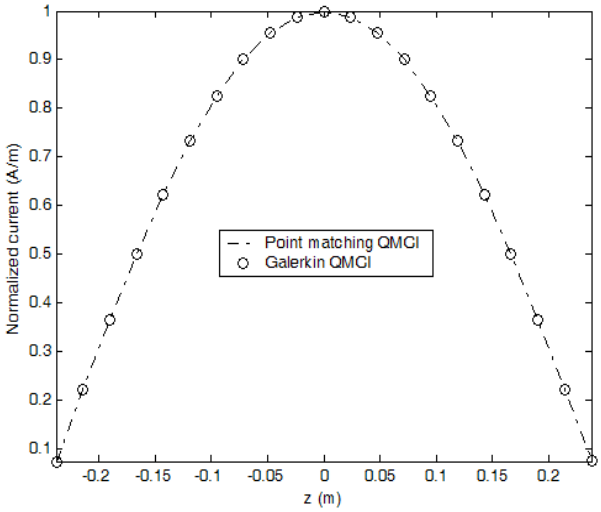

Fig. 4. The normalized current distribution on the wire dipole antenna ($l = \lambda/2$) using QMCI technique, f = 300 MHz.

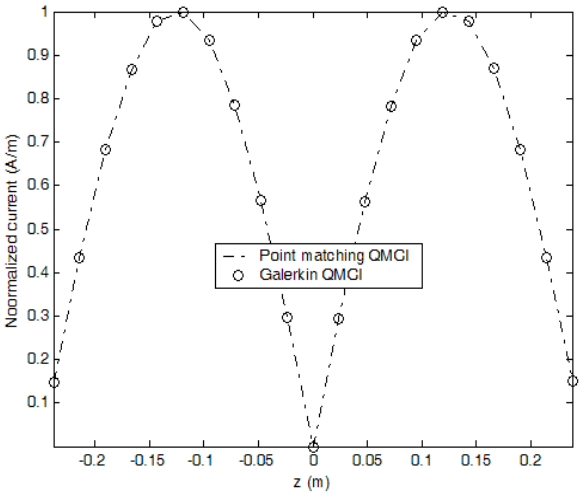

Fig. 5. The normalized current distribution on the wire dipole antenna ($l = \lambda$) using QMCI technique, f = 600 MHz.

V. CONCLUSION

The QMCI technique using Halton sequence is proposed in the MoM solution of the EFIE for some radiation problems. As an example, radiation from a simple wire antenna is investigated. It is found that the proposed technique not only solves the radiation problem efficiently but also takes care of the singularity problem appearing in the kernel of the integrand due to the inherent property of the Halton sequence.

ACKNOWLEDGEMENT

This research work was supported by the council of scientific and industrial research (CSIR), PUSA, New Delhi, India – 110012.

REFERENCES

[1] W. H. Press, S. A. Teukolsky, W. T. Vetterling, and B. P. Flannery, *Numerical Recipes*, second edition, Cambridge University Press, 1992.

[2] B. D. Ripley, *Stochastic Simulation*, John Wiley & Sons, Inc., 1987.

[3] H. Niederreiter, *Random Number Generation and Quasi-Monte Carlo Methods*,. SIAM, Pennsylvania, 1992.

[4] W. Cai, Y. Yu, and X. C. Yu, "Singularity treatment and high-order RWG basis functions for integral equations of electromagnetic scattering," Int. *J. Numerical Methods Eng*., vol. 53, pp. 31–47, 2002.

[5] M. G. Duffy, "Quadrature over a pyramid or cube of integrands with a singularity at a vertex," *SIAM Journal on Numerical Analysis*, vol. 19, pp. 1260 –1262, December 1982.

[6] M. A. Khayat and D. R. Wilton, "Numerical evaluation of singular and near-singular potential integrals," *IEEE Trans. Antennas Propagat*., vol. 53, no. 10, pp. 3180 – 3190, October 2005.

[7] M. Mishra and N. Gupta, "Singularity treatment for integral equations in electromagnetic scattering using Monte Carlo integration technique," *Microwave and Optical Technology Letters*, vol. 50, no. 6, pp. 1619-1623, June 2008.

[8] J. H. Halton, "On the efficiency of certain quasi-random sequences of points in evaluating multi-dimensional integrals," *Numer. Math*., vol. 2, pp. 84-196, 1996.

[9] B. M. Kolundzija and B. D. Popovic, "Entire domain Galerkin method for analysis of generalized wire antennas and scatterers," *IEE Proceedings Part-H*, vol. 139, pp. 17-24, Feb. 1992.

[10] G. Fikioris and T. T. Wu, "On the application of numerical methods to Hall´en's equation," *IEEE Trans. Antennas Propagat*., vol. 49, pp. 383–392, Mar. 2001.

[11] D. H. Werner, "A method of moments approach for the efficient and accurate modeling of moderately thick cylindrical wire antennas," *IEEE Trans. Antennas Propagat*., vol. 46, pp. 373–382, Mar. 1998.

[12] S. Alyones, C. W. Bruce, and A. K. Buin, "Numerical methods for solving the problem of electromagnetic scattering by a thin finite conducting wire," *IEEE Transactions on Antennas and propagation*, vol. 55, pp. 1856-1861, June 2007.

[13] G. Fikioris and C. A. Valagiannopoulos, "Input Admittance arising from explicit solution to integral equations for infinite-length dipole antennas," *Progress In Electromagnetics Research, PIER 55*, pp. 285-306, 2005.

[14] P. J. Papakanellos and G. Fikioris, "A possible remedy for the oscillations occurring in thin-wire MOM analysis of cylindrical antennas," *Progress In Electromagnetics Research, PIER* 69, pp. 77–92, 2007.

[15] W. X. Wang, "The exact kernel for cylindrical antenna," *IEEE Trans. Antennas Propagat*., vol. AP-39, pp. 434–435, 1991.

[16] C. A. Balanis, *Antenna Theory: Analysis and Design*, Harper & Row, New York, 1982.

Mrinal Mishra was born in India on 14th June 1977. He received M.Sc. degree in Physics from Jawaharlal Nehru University, New Delhi, India, in the year 2002. He was awarded Research fellowship from the Council of Scientific and Industrial Research, Ministry of Human Resource Development, New Delhi, India in the year 2003 through National Eligibility Test (NET). Thereafter, he joined the Department of Electronics and Communication Engineering, Birla Institute of Technology, Mesra, Ranchi, India as a Junior Research Fellow towards pursuing his Ph.D. degree. He was upgraded to Senior Research Fellow in the year 2005. In March 2008, he joined the post of Lecturer in Ranchi University.

Nisha Gupta received the Bachelor's and Master's degrees in Electronics and Telecommunication and Electrical and Electronics engineering both from Birla Institute of Technology, Mesra, Ranchi, India and Ph.D. degree from the Indian Institute of Technology, Kharagpur, India. She was a Maintenance Engineer at Shreeram Bearings Ltd., Ranchi during 1982-83 and was a Programmer at Ranchi University, Ranchi from 1983 to 1986. She was a Junior Scientific Officer in a DRDO sponsored project, at Department of Electronics and Electrical Communication Engineering, Indian Institute of Technology, Kharagpur, from 1986-1989 and a Institute Research Scholar and Research Associate (CSIR) in the same department from 1990-1996. She was a post doctoral fellow at University of Manitoba, Canada from 1997-1998 before joining the department of Electronics and Communication Engineering, Birla Institute of Technology in 1999 as a Reader. Currently, she is a Professor in the same department. She has authored and coauthored more than 40 technical journal articles and conference papers. Her research interests are Computational Electromagnetics, Antennas for Wireless Communication and AI techniques in Wireless and Mobile Communication.

Validation of Fast Site-Specific Mean-Value Models for Indoor Propagation

[1] C. W. Trueman, [1] D. Davis, [2] B. Segal, and [3] W. Muneer

[1] Department of Electrical and Computer Engineering, Concordia University, Montreal, Canada
trueman@ece.concordia.ca , don@ece.concordia.ca

[2] McGill University and SMBD Jewish General Hospital, Montreal, Canada
b_segal@sympatico.ca

[3] Department of Electrical and Computer Engineering, University of British Columbia, Vancouver, Canada
wadahmuneer@yahoo.co.uk

Abstract – A fast assessment of the local mean value of the electric field strength throughout a floor plan is useful for the design of local-area networks. Site-specific models require coding the location of walls, doorways, and other features and modelling their structure and electrical properties. Using ray tracing to find the field strength throughout the floor plan is slow and expensive because a grid of closely-spaced points is needed to trace the rapid variations called fast fading; then the *ray-tracing local area average* is found by explicit spatial averaging, to obtain the slow fading behavior. The *ray-tracing mean value* is obtained by combining the amplitudes of the fields associated with the rays on an energy basis; widely-spaced grid points can be used because the local mean value varies slowly with position, making the calculation fast and inexpensive. The *Sabine method* provides a energy-balance approach for an inexpensive estimate of the local mean value field strength. This paper tests the accuracy of the fast methods (the ray-tracing mean value and the Sabine mean value) against the local area average found from dense ray tracing, and against measurements. In a 40 m^2 room of roughly square floor plan, the fields from the fast methods were close to those of dense ray tracing and to the measurements. But it is shown that in a long corridor, the ray-tracing mean value and the Sabine mean value were low compared to dense ray tracing, and so these fast methods should be used with caution.

I. INTRODUCTION

Indoor propagation is the study of the electric field strength due a transmitter operating at a given location and frequency in the floor plan of a building [1, 2]. A "site-specific model" uses the actual location of the walls, windows, doors, and other major features of a floor plan in a three-dimensional model. The location of a transmitter is specified, and a model of the behavior of the field is used to predict the electric field strength throughout the floor plan. If there are many transmitters, such as the access points of a wireless local area network, it is necessary to assess the coverage of each individual transmitter. Also, if two or more transmitters operate on the same frequency, the signal-to-interference ratio at each point in the floor plan is needed. To assess electromagnetic interference with other equipment, the location of mobile transmitters must be known, and the net field strength due to all transmitters must be estimated. For problems with many sources, a fast, inexpensive estimate of the field strength over the whole floor plan due to each individual source is required.

A recent paper [3] uses the array decomposition fast multiple method to obtain a full-wave solution for the fields in a classroom at 2.4 GHz. The technique offers accuracy that may be better than ray tracing, and permits furniture to be included in the model, such as an array of chairs. A finite-difference method based on transmission-line modelling and the "multiresolution frequency domain parflow method" is used in [4] to solve the system of equations. The fields of a 2.4 GHz transmitter are found in a floor plan having eight rooms and a hallway, using a two-dimensional (2D) approximation. The finite-difference time-domain method is used in [5] to solve a 2D model of a floor plan having several rooms and hallways, at 900 MHz. The internal details of walls, such as pipes and ducts, can be represented in this approach. The authors comment that a slab wall model is not a good representation of a wall constructed of blocks having internal hollow spaces. However, 2D approximations do not account for the floor or ceiling and hence cannot predict the variation of the field with height above the floor. None of these models can be considered inexpensive or "fast" for computation.

The "log distance path loss model" [1, 2, 6, 7, 8] represents the local mean power as declining with distance in an indoor environment according to P_0 / r^n,

where P_0 is the power at 1 m distance, and n is the "path loss exponent" [8] or "slope index" [6]. This model is empirical in nature with the value of n determined from measured received powers [7]. When the ray joining the source to the receiver passes through a wall, a wall attenuation factor is used to account for the transmission loss. The attenuation can be dependent on the type of wall, and is often derived from measurements. This model makes minimal use of the site-specific nature of the model, and relies on values of n determined by measurement from similar sites, rather than deduced from the construction and electrical properties of the walls. This model is very fast for computation but has limited accuracy.

Ray tracing (RT) is commonly used to analyze site-specific models [8-10]. The transmitter and observer are joined by a straight-line path called the "direct" ray. The field strength is that of the transmitter in free space, attenuated by transmission through walls in the path of the ray. The transmitter and receiver are joined by many reflected rays, including single reflections from the walls, the floor or the ceiling, double reflections involving two room surfaces, multiple reflections, and indeed transmission through one or more walls. The net field strength due to all the reflected rays together is the "multipath field" [3]. Attenuation due to reflection or transmission is often accounted for by modelling walls as uniform layered structures, sometimes called "slab walls," and using polarization- and angle-dependent reflection and transmission coefficients [11]. Diffraction from edges can also be accounted for [2]. Ray tracing is considered to provide good accuracy for site-specific field calculation. As the number of reflections that is accounted for increases, the cost of the ray-tracing computation increases sharply. If ray tracing is used to identify N ray paths joining a transmitter (Tx) to a receiver (Rx) and each ray path has an associated complex-valued vector electric field, $\overline{E}_k$ for $k = 1,...,N$, the local electric field vector at the observer is given by the "vector sum method" [12] as,

$$\overline{E} = \sum_{k=1}^{N} \overline{E}_k \,. \tag{1}$$

The magnitude of the electric field strength is assessed by combining the vector components on an energy basis.

A. Slow Fading, Fast Fading and the Ray-Tracing Local Area Average

As the observer moves, the length of each ray path changes, with an associated phase change, leading to the rapid fluctuation in the local electric field strength with distance called "fast fading" [1, 2]. These rapid variations are often removed by spatial averaging to find the underlying "slow fading". The resulting average value is variously called the "local mean power" [13], the "sector average" [6], the "local mean signal strength" [12], or the "local area average" [2]. A local-area-average field strength can be calculated by averaging the local field strength on a power basis over an area S according to,

$$\tilde{E} = \sqrt{\frac{1}{S}\iint E^2 ds} \tag{2}$$

but this is rarely done due to the computational cost of evaluating the electric field over a grid of closely-spaced points. The area average is often approximated with a linear average,

$$\tilde{E}_{LAA} = \sqrt{\frac{1}{\Delta}\int E^2 d\ell} \tag{3}$$

where ℓ is distance along the path and Δ is the averaging interval, called the *window size* in this paper, and is typically 5 to 40 wavelengths [2, 6]. Windowing smoothes out the rapid fluctuations associated with fast fading, and reveals the slow fading associated with the attenuation of the field strength with distance travelled, and due to shadowing by the walls and other obstructions in the floor plan. In [1, 2, 9, 14, 15], the field strength is measured around a circular path and the integral around the circumference is used to approximate the local area average of the field strength at the center of the circle. The average value of the signal along a straight-line path with a window size of "twenty or so" wavelengths is termed the "sector average" in [6].

Using ray tracing to compute the field strength over a grid of points spaced by approximately a tenth of the wavelength is sufficient to predict the fast fading of the electric field strength. Then an explicit spatial average can be evaluated over an area with equation (2), or along a straight-line path with equation (3), to find the local mean field strength. In this paper, the *ray-tracing local area average* (RTLAA) is obtained using equation (3) with a path length of about six wavelengths.

B. Ray-Tracing Mean Value

The phase of the field associated with each ray arriving at an observer is often assumed to be a random variable with a uniform distribution [1]. Then the field strength at the observer is also a random variable, with a Rayleigh distribution if there is no dominant component, or a Rician distribution if one component, such as the direct field, is much larger than other components [1]. Then an estimate of the mean value of the random variable is obtained at a single point by the "power sum method" [12, 16] by combining the field strengths of the individual rays $\overline{E}_k$ for $k = 1,...,N$ on an energy basis according to,

$$\tilde{E}_{MV} = \sqrt{\sum_{k=1}^{N} |E_k|^2} \tag{4}$$

which in this paper equation (4) will be called the *ray-tracing mean value* (RTMV) field strength. The sum in equation (4) is proportional to the volume-averaged energy density in the field, and is expected to vary slowly with position, because the ray amplitudes vary slowly with position, whereas the phases vary rapidly.

The computation of the RTLAA is expensive because a dense grid of points is needed to trace fast fading, which is then smoothed by explicit averaging, whereas the computation of the RTMV is much less expensive, because it requires field strength data only at a single point, and because the RTMV varies slowly with position, a much less dense grid of points can be used.

C. The Sabine Local Area Average

The Sabine method in acoustics [17] is based on the assumption that the volume-averaged energy density in a room is constant throughout the room. It has been extended to Electromagnetics in [18-21]. The Sabine method is applied in [18] to calculate the Q factor of a reverberation chamber, and the decay time, which depends on the volume, the angle-averaged power absorption coefficient of the surfaces, and on the surface area. The acoustical analogy is used in [19] to estimate the reverberation time and to calculate the power delay profiles in an indoor environment. For highly-absorbent or "dead" environments, [19] replaced the Sabine absorption by the Eyring formula. The formula for the reverberant field strength is given in [11] and the "reverberation distance" is defined as the distance from the source at which the direct field is equal to the reverberant field. In [18], power delay profiles based on the reverberation model are compared with measured power delay profiles, with good agreement. However, the Sabine method is not well known for calculating the coverage of an access-point antenna in a site specific model.

The Sabine method was extended in [22] so that it could be applied to estimate the field strength throughout a complex floor plan in a site-specific model. Then the Sabine method was used to assess the possibility of interference with medical devices due to a wireless local area network made up of several access point antennas and handheld terminals.

D. Objectives and Paper Organization

Ray tracing is widely used in site-specific studies to compute electric field strengths. Although it is difficult to obtain agreement between fast-fading electric field strengths computed with ray tracing and those obtained by measurement, it is generally accepted that the RTMV of equation (4) is a good predictor of the local mean value computed by windowing measured data with equation (3). An objective of this paper is to assess the accuracy of the frequently-used RTMV against the RTLAA, that is, the local area average obtained by explicitly windowing closely-spaced field values. Similarly, an objective of this paper is to assess the accuracy of the Sabine local area average against the RTMV and the RTLAA.

First, this paper summarizes the Sabine method and extends it to be useful in long, narrow spaces such as a corridor, by introducing an exponential decay of the field strength with distance. Two problems have been selected to assess the accuracy of the computationally-fast RTMV and Sabine methods against the slower RTLAA and against measurements. The first is a room of rectangular shape, where the fast methods are expected to have good accuracy, and the second is a long, narrow corridor, where the fast methods are shown to be less accurate. In the rectangular room, it is shown that the RTLAA agrees reasonably with the measured field strength, and that both the RTMV and the Sabine field strength are reasonable approximations to the RTLAA. In the long corridor, the RTLAA field strength is similar in behaviour to the measured field strength. It is shown that, using the exponential decay term, the Sabine field strength in the corridor agrees reasonably with the RTMV. However, both fast methods underestimate the RTLAA field strength along the corridor centerline. Finally, when a small reflecting screen is placed behind the transmitter, it is shown that the Sabine method accounts poorly for the image of the source in the screen, and the field strength agrees poorly with the RTMV estimate. The two cases of the long corridor illustrate situations where the fast estimates should be used with caution.

II. THE SABINE METHOD

The Sabine method [17] is used in acoustics to determine the sound pressure level in a room or concert hall due to a source of acoustic power. It is assumed that the field of the source is reflected many times from the walls of the room, and that the energy density becomes uniform throughout the room at steady state, with the power radiated by the transmitter equal to the power absorbed by the room surfaces. It may be shown that the reverberant energy density is [21],

$$\tilde{\Psi}_{rev} = \frac{4P_r}{Ac} \quad \text{J/m}^3 \tag{5}$$

where P_r is the power radiated by the transmitter, c is the speed of light, and the room absorption is defined as,

$$A = \sum_{k=1}^{N} S_k \tilde{\alpha}_k \quad \text{m}^2 \tag{6}$$

where there are N different surfaces in the room, such as wall, doors, windows, floor, and ceiling, each of area S_k. The angle-averaged power absorption of a surface is [18],

$$\tilde{\alpha} = 2\int_0^{\pi/2}\left[1-\frac{1}{2}\left(\left|\Gamma_{\|}\right|^2+\left|\Gamma_{\perp}\right|^2\right)\right]\sin\theta\cos\theta d\theta \qquad (7)$$

where $\Gamma_{\|}$ and $\Gamma_{\perp}$ are the angle-dependent amplitude reflection coefficients for the parallel and perpendicular polarization, respectively. The angle-averaged power-absorption coefficient (7) for a slab wall model is readily evaluated by numerical integration of the reflection coefficients in [11]. Then given the floor plan of a room, the room absorption (6) can be found and used to find stored energy in the reverberant field with equation (5). The corresponding reverberant electric field strength $\tilde{E}_{rev}$ is obtained by equating the energy density to that in a plane wave, $\tilde{\Psi}_{rev} = \varepsilon\tilde{E}_{rev}^2$.

To calculate the field strength as a function of distance from the antenna, it is useful to split the field into the sum of the "direct" field, which is the field of the transmitter in free space, and the "multipath" or "indirect" field, which is sum of the fields associated with all the reflected and multiply-reflected rays that pass through the observer [22]. The energy density in the reverberant field, $\tilde{\Psi}_{rev} = \tilde{\Psi}_{dir} + \tilde{\Psi}_{in}$, is the sum of the energy density in the direct field $\tilde{\Psi}_{dir}$ and that in the indirect field, $\tilde{\Psi}_{in}$. If the walls of the room are perfectly absorbing, then there is no indirect field, $\tilde{\Psi}_{in} \to 0$, the wall absorption coefficients become unity, $\tilde{\alpha} = 1$, so the room absorption is equal to the total area of the walls, $A = S_T = \sum S_i$. As $A \to S_T$ and $\tilde{\Psi}_{in} \to 0$, the reverberant energy density $\tilde{\Psi}_{rev} \to \tilde{\Psi}_{dir}$. In equation (6), with perfectly-absorbing walls $A = S_T$ and $\tilde{\Psi}_{rev} = \tilde{\Psi}_{dir}$, so the energy density in the direct field is,

$$\tilde{\Psi}_{dir} = \frac{4P_r}{S_T c}. \qquad (8)$$

It follows that for a room of absorption *A*, the energy density in the indirect field is,

$$\tilde{\Psi}_{in} = \tilde{\Psi}_{rev} - \tilde{\Psi}_{dir} = \frac{4P}{A_{in}c} \qquad (9)$$

where the indirect room absorption is,

$$A_{in} = \frac{AS_T}{S_T - A}. \qquad (10)$$

The corresponding electric field strength $\tilde{E}_{in}$ obeys $\tilde{\Psi}_{in} = \varepsilon\tilde{E}_{in}^2$, and so the indirect field strength is,

$$\tilde{E}_{in} = \sqrt{\frac{4\eta P_r}{A_{in}}} \qquad (11)$$

where field strengths are given in V/m RMS. Note that if the walls are perfectly absorbing, then $A_{in} \to \infty$ and the indirect field becomes zero, as expected. Since the indirect field strength is based on the assumption of a uniform distribution of energy throughout the room, the tilde is used to indicate that $\tilde{E}_{in}$ is a volume average.

The direct field strength of a wireless source radiating power P_t at distance r is given by,

$$E_{dir}(r) = \sqrt{\frac{\eta D P_t}{4\pi r^2}}. \qquad (12)$$

The directive gain of the source is *D* and η is the intrinsic impedance of free space. To estimate the mean value of the field strength, the direct and indirect fields are combined on an energy basis to obtain,

$$\tilde{E}_{Sab}(r) = \sqrt{\left(\frac{\eta D P_t}{4\pi r^2}\right) + \left(\frac{4\eta P_t}{A_{in}}\right)}. \qquad (13)$$

For distances very close to the transmitter, the direct field is much larger than the indirect field and equation (13) approaches the local field strength of the transmitter.

The Sabine method has been applied to realistic floor plans such as that in [22]. The room absorption of equation (10) is evaluated by a numerical approximation called the "patch method". The walls, floor and the ceiling are subdivided into patches of area ΔS, of size approximately 25 cm square. The center of each patch is joined to the observer by a ray. If the ray is blocked by an intervening wall panel, then the patch is not line-of-sight to the observer, and does not contribute to the absorption. If the ray is not blocked, then the patch contributes $\tilde{\alpha}\,\Delta S$. The algorithm is very simple and fast in execution. The room absorption is then dependent on the location of the observer. If the observer is in a small room, the observer "sees" patches of wall that add up to a small total area, and lead to a small room absorption. But if the observer is in a large hall, the observer "sees" a large wall surface area and a large value for the room

absorption and the environment approaches free space behavior.

It will be demonstrated below that equation (13) provides a reasonable estimate in a box-shaped room, but that in a long corridor, equation (13) becomes increasingly in error with distance from the source. The following presents a novel correction factor for long corridors.

A. Correction for Long Narrow Spaces

Consider a long corridor of width w and height h. Let the power flowing through a cross-section wh of the corridor be $P(z)$, where z is distance from the transmitter along the corridor. For a slice of corridor of length dz, power $P(z)$ is the "source" for the reverberant field, and the energy density in the slice is given by equation (9) as $\tilde{\Psi}_{rev}(z) = 4P(z)/Ac$. From equation (6), the power incident on the surface area $2(w+h)dz$ of the slice is $\left(\tilde{\Psi}_{rev}c/4\right)\left(2(w+h)dz\right)$ and the decrease in power across the slice is,

$$dP = -\alpha \frac{\tilde{\Psi}_{rev}c}{4}\left(2(w+h)dz\right) \tag{14}$$

where $\alpha = A/S_T$ is the average power absorption coefficient for the surfaces, and A is the room absorption at the location of the slice. Thus the power obeys the first-order differential equation,

$$\frac{dP}{dz} + \frac{1}{\delta}P = 0 \tag{15}$$

where the "penetration depth" along the corridor is,

$$\delta = \frac{A}{2(w+h)\alpha}. \tag{16}$$

The power available to drive the reverberant field at distance z from the source is,

$$P(z) = P_t e^{-z/\delta} \tag{17}$$

where the power at z=0 is equal to the power transmitted by the source P_t. Exponential decay with distance is consistent with the attenuation of fields in waveguides.

A simple formula for the penetration depth was sought that could be applied to arbitrary observer locations in a complex floor plan. The ceiling height h is known and constant throughout the floor plan, but the width w is ambiguous, because it could be taken as either the length or the width of the room. To eliminate w it will be assumed that the "footprint" of the room has area w^2. With this assumption, the area of the walls, floor and ceiling is,

$$S_T = 2w^2 + 4wh. \tag{18}$$

In a complex floor plan, the room absorption A and the surface area S_T are found for any observer by the "patch method". Then equation (18) is solved for w, and the penetration depth approximated as,

$$\delta = \frac{S_T}{\sqrt{4h^2 + S_T}} \tag{19}$$

where $\alpha = A/S_T$ has been used to eliminate the power absorption coefficient. With these assumptions, the penetration depth is a purely geometrical parameter, and is readily applied in the context of an observer embedded in a complex floor plan.

The indirect field is calculated with equation (11), where the power of the source P_t is replaced by the attenuated power of equation (19). The indirect field thus attenuates exponentially with distance from the source. It will be demonstrated below that this "corrected" indirect field is a good approximation of the ray-tracing mean value field strength in a long corridor.

III. APPLICATIONS

This section applies ray tracing and the Sabine method to calculate the field strength in a rectangular room and in a long, narrow corridor, and compares the results to measured field strengths.

A. The Rectangular Room

Measurements and simulations were done in a laboratory, shown in Fig. 1. The lab measured 6.83 m wide by 8.68 m deep, with a ceiling height of 3.75 m. The lab was rectangular in shape, and was quite different from the long, narrow corridor considered in the following section. It was filled with lab benches and equipment, which were not included in the simulation. The measurement setup was described in [23, 24]. The receive antenna was located on a phenolic tripod 1.61 m from a side wall and 4.97 m from the front wall of the room. The center of the receive antenna was 1.03 m above the floor. The receive antenna was an ETS Lindgren #3126 sleeve dipole, and the received power was measured by an HP8569B spectrum analyzer. The transmit antenna was carried by a moving platform or "robot" that followed tape stuck to the floor along a straight-line path starting 30 cm from the receiver and ending 4.92 m from the receiver. The transmitter consisted of a battery-operated oscillator at 2388 MHz driving a quarter-wave monopole

on top of a small aluminum box. The base of the monopole was 1.07 m above the floor. The system measured the received power every 1.5 cm along the path. Because the transmitted power was not known, the system was uncalibrated and the measured field strengths required scaling to match the transmitted power in the simulation.

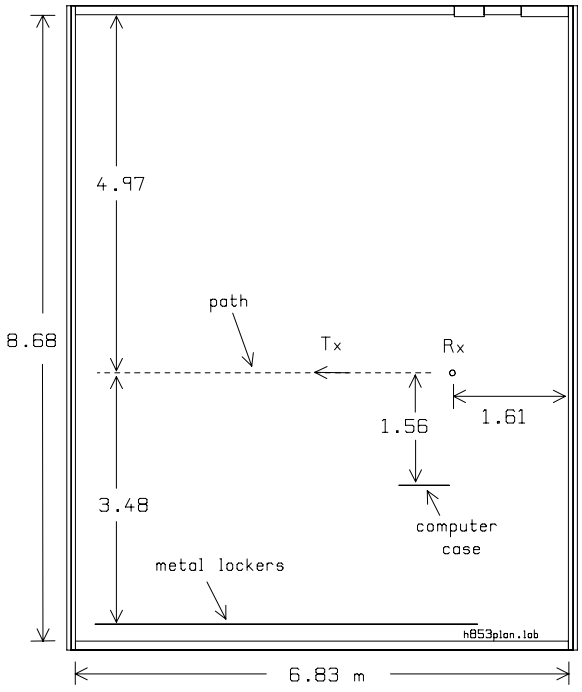

Fig. 1 Plan of the rectangular room.

The room of Fig. 1 was modelled for simulation by ray tracing. Each wall was modelled as a layered structure with 1.5 cm of concrete (ε_r =5.37, σ =149.5 mS/m), 0.8 cm of brick (ε_r =4.38, σ =18.5 mS/m), a center air layer 7.8 cm thick, and symmetric layers of brick and concrete. The floor and ceiling were modelled as concrete slabs of thickness 30 cm, with 3.75 m height from floor to ceiling. The room had various pipes and ducts below the ceiling, which were not included in the model. The near side of a metal computer case measuring 70 cm wide by 46 cm tall was 1.56 m from the path, and was included in the model because it was found to reflect the field very significantly. One wall of the room had a row of metal lockers, 3.48 m from the path, which were included in the model. But lab benches, other instruments, and other clutter in the room were not modelled. In the simulation, the transmitter was a vertical, half-wave dipole radiating 100 mW, with directivity $D = 1.64$, and the transmitter was at the fixed location Rx in Fig. 1 while the receiver moved along the path. Ray paths with up to 32 reflections were calculated. Including more reflections did not change the result substantially. The electric field strength was evaluated every 0.5 cm to trace the fast fading of the signal in detail, and then equation (4) was used to evaluate the RTLAA with a window size of 0.7 m.

Figure 2 compares the measurements and simulations in the rectangular room. The electric field strength in dB relative to 1 V/m is shown as a function of the separation between the transmitter and the receiver. The measured data was scaled such that the measured RMS value was equal to the RMS value of the simulated data in the distance interval 0.5 m to 2 m separation between the Tx and the Rx. To study the slow fading of the signal, the measured and simulated field strengths were "windowed" by taking the local area average over a 70 cm or 6-wavelength interval, using equation (2).

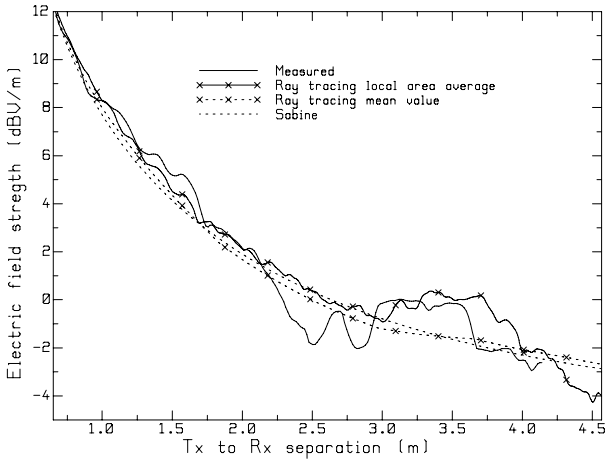

Fig. 2 Measurement and simulations in the rectangular room.

Figure 2 compares the scaled, measured field strength (solid line) with the RTLAA field strength (solid line with crosses) and shows reasonable agreement. At a separation of about 2.5 m, the measured field strength had a minimum not seen in the simulation, and the measured field was about 2.1 dB smaller than the simulation. At a separation of about 3.5 m, both the simulation and the measurement had a maximum. The RMS error between the measured curve (in dB) and the RTLAA curve (in dB) from 0.7 to 4.1 m separation was 0.90 dB, which we considered to be good agreement.

The RTMV field strength (not shown) of equation (5) had step discontinuities because rays switched in and out of the solution as the observer moved, for example due to reflections from the computer case. The RTMV was smoothed using equation (2) with a 70 cm window, and is shown in Fig. 2 by the dashed curve with crosses. For most of the path, the phasing of the rays was such that the RTMV estimate was smaller than the RTLAA by less than half a dB. The maximum at 3.5 m separation in the RTLAA is not seen in the RTMV estimate.

To evaluate the field strength using the Sabine method, the angle-averaged power absorption coefficient in equation (7) was found for the layered wall and for the concrete slab modelling the floor and ceiling. Then room absorption was found for each point along the path, using equation (6) evaluated by the patch method. For this simple rectangular-box room, the room absorption was about $A = 165$ square meters. The indirect absorption in equation (10) was about $A_{in} = 541$ square meters. For each point on the path, equation (12) was used to find the direct field and equation (11) was used to find the indirect field, and these were combined on an energy basis using equation (13) to find the Sabine estimate of the local mean field strength. The distance correction of equation (17) is intended for long, narrow spaces, and not rectangular rooms, and so was not used. For comparison with the windowed field strength from ray tracing, the Sabine field strength was averaged over a 70 cm window.

To compare the accuracy of the fast estimates of the local mean field strength with the much-more-computationally-expensive RTLAA value, Fig. 2 shows the RTMV field strength and the Sabine field strength, in comparison to the RTLAA estimate. The figure shows that the RTMV field strength (dashed curve with crosses) and Sabine field strength (dashed curve) were very close in value, with an RMS difference between them of 0.27 dB. The error between the RTMV and the RTLAA estimate was 0.82 dB; that between the Sabine field strength and the RTLAA estimate was 0.86 dB. Both of the quick estimates were within one dB of the much-more-computationally-costly RTLAA field strength. For the rectangular room, the Sabine method provided an accurate approximation of the behavior of the field with distance from the transmitter.

B. The Long Corridor

Figure 3 shows the plan of the 50.6 m corridor that was used to compare simulations with measurements. The rectangular room of the previous section is shown for comparison. The Sabine method assumes that the energy density is uniform throughout the volume of the space, which was a reasonable assumption for the rectangular room, but not for the corridor, where the length was much longer than the width. The distance correction in equation (17) models the energy density as declining exponentially along the corridor and it will be shown that this was in reasonable agreement with the RTMV estimate.

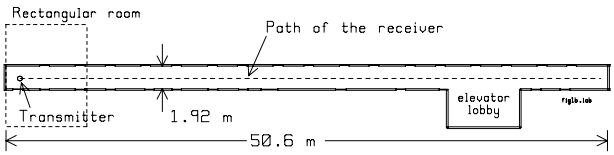

Fig. 3 The geometry of the 50.6 m corridor.

The corridor of Fig. 3 was 50.6 m long and 1.92 m wide. The corridor had a hanging ceiling at 2.27 m height. Above the hanging ceiling, there was wiring, pipes and ducting which were not included in the simulation model. The bottom of the concrete slab for the next floor of the building was at a height of 2.75 m. The transmit antenna for the simulations and the measurements was 1.6 m above the floor and 1.2 m from the end wall, and was in the center of the corridor, 0.96 m from each side wall. The receiver was moved along a path at height 1.6 m above the floor along the centerline of the corridor for a distance of about 50 m. Measurements and simulations were done at 850 MHz.

The end wall behind the transmitter was of glass-block construction of thickness about 10.2 cm. There was a window inserted into the glass-block wall, measuring 63 cm wide and 43 cm tall. Two different corridors were measured. For the eighth floor corridor, there was no insect screen in the window, but for the fifth floor corridor the window had a metal insect screen. The transmitter was approximately centered on the metal window screen on the fifth floor, and the screen reflected the field effectively, and profoundly changed the field strength in the corridor. It will be demonstrated below that the Sabine method accounts poorly for the window screen.

The measurements were done using the system described in [25]. The transmitter was a Motorola SLF1690C analog cellular telephone, programmed to transmit continuously at its full power of 600 mW, and the power transmitted was monitored periodically. The base of the cell phone's antenna was 1.6 m above the floor and approximately 1.2 m from the glass-block end wall, and 0.96 m from the side walls. The receive antenna was an Electromechanics 3121C-dB4 dipole, of length one-half wavelength at 850 MHz or 17.65 cm, oriented vertically. The receive antenna was carried by a moving platform or "robot" along the corridor centerline, and was supported on a stand made of PVC pipes with the dipole's midpoint 1.6 m above the floor. The received power was measured with an Anritsu MS2610B spectrum analyzer. The receive dipole was connected to the spectrum analyzer by a cable of length approximately 10 m. As the robot moved, the received power was recorded at 30 cm (0.85 wavelength) intervals. The measurement points were too far apart to trace the fast fading of the field strength.

For the ray-tracing simulation, the transmit antenna was represented as a vertical half-wave dipole antenna radiating 600 mW at 850 MHz, and so the field incident on the side walls and end walls of the corridor had the "perpendicular" polarization. The walls of the corridor were of clay block construction and were modelled for simulation with five layers: plaster (ε_r =6.1, σ =60.1 mS/m) of thickness 1.5 cm; brick (ε_r =5.1, σ =10 mS/m)

of thickness 0.8 cm; and air space 9.2 cm thick; and symmetrical layers of brick and plaster. The reflection coefficient for the perpendicular polarization was about 0.8 for 0 degree or "normal" incidence; 0.86 at 70 degrees from the normal; and rising to unity for grazing incidence. The concrete slab floor and ceiling were 30 cm thick and were represented with ε_r =6.1 and σ =60.1 mS/m. The doorways were filled with wood doors (ε_r =2.5, σ =1.18 mS/m) 10 cm thick, except for the fire door near the antenna, which was metal. The glass block end walls were modelled with a 0.5 cm layer of glass (ε_r =4), a 9.6 cm air layer, and a symmetric 0.5 cm glass layer. The reflection coefficient for the perpendicular polarization was less than 0.1 for incidence from the normal to about 50 degrees from the normal, and then rose rapidly to unity for grazing incidence. Thus, the glass block end wall was almost transparent over a wide range of angles of incidence. On the eighth floor, the window in the glass-block wall had no metal screen. But on the fifth floor, the window had a metal insect screen which was modelled as perfectly reflecting.

In ray-tracing simulations, computational error can be reduced by increasing the number of reflections. Sufficient reflections have been accounted for when little change is seen by including further reflections. For this study, the field strength along the corridor centerline was examined as the number of reflections was increased. The field strength with three reflections agreed reasonably with that using 14 reflections to a distance of about 15 m along the hallway. Five reflections were sufficient to about 20 m distance; seven to 30 m distance; ten reflections to about 40 m. The broad minimum in the local field strength around 42.5 m distance and the maximum around 46 m distance required 14 reflections to be tracked. Computing more than 14 reflections did not substantially change the field in the corridor, and so 14 reflections were used in the results that follow.

Eighth Floor: Figure 4 shows measured and simulated field strength along the corridor on the eighth floor. Ray tracing was used to compute the field strength at 1 cm intervals and the RTLAA was calculated with equation (3) using a 2 m window size, which is 5.7 wavelengths at 850 MHz. To scale the measured values to the same radiated power as the simulations, the RMS value from 1.6 m to 3 m separation between the Tx and the Rx was made equal to the RMS value of the RTLAA field strength. The measured data was also averaged with a 2 m window, which used six measured points at 30 cm separation.

Figure 4 compares the measured field strength (solid curve) with the RTLAA field strength (solid curve with crosses). Both the measured and simulated field strengths had a broad maximum at 9.5 m distance, and again at 22 m distance and 36 m distance. The measured field strength was larger than the RTLAA field strength from 11 m to 16 m distance. The measured field had a peak at 29 m distance whereas the simulation had a minimum. The general behaviour of the measured and simulated field strength was similar although details differed. In the separation interval from 1.6 m to 44.5 m, the RMS error between the measured field strength and the RTLAA field strength was 2.17 dB.

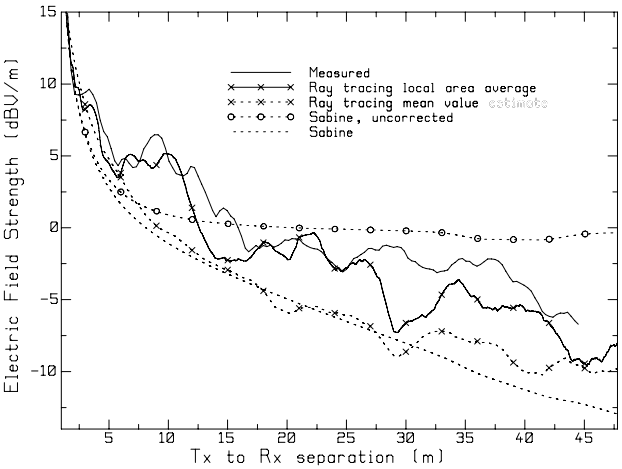

Fig. 4 Measurement and simulations on the eighth floor corridor.

The dashed curve with crosses in Fig. 4 shows the RTMV estimate in equation (4) after smoothing with a 2 m window. It might be expected that the RTMV curve would pass through the "average" of the RTLAA curve. Yet in Fig. 4, the RTMV estimate was less than the RTLAA field strength for separations greater than about 6 m. The RTMV combines the ray amplitudes on an energy basis to obtain an estimate of the mean value, which assumes that the fields have random phase angles with a uniform distribution. But with the transmitter and receiver on the centerline of the corridor, the path lengths for reflections from the left wall and right wall were identical, and rays arrived in phase, violating the assumption of random phase. This problem is one where the RTMV is not a good estimate of the true local area average field strength. The RMS error between the RTMV and the RTLAA values was 3.13 dB.

The Sabine model of the corridor had absorption of about $A = 314$ square meters, about twice that of the rectangular room. The indirect absorption was about $A_{in} = 968$ square meters, again about twice the value for the rectangular room. The dashed curve with circles shows the Sabine estimate given by equation (13). For "close" separations less than about 6 m, the Sabine field strength was about 2 dB less than the RTMV estimate. For separations greater than about 10 m, the Sabine field strength in Fig. 4 was much too large. For distances where the direct field strength is much less than the

indirect field strength, equation (13) predicts that the net field strength should be approximately constant and equal to the indirect field. Thus, towards the end of the corridor, the Sabine approximation became approximately constant and was not a good approximation to the ray-tracing mean value field strength. The distance correction of equation (17) introduces an exponential reduction in the indirect field with distance along the corridor and the field strength is shown by the dashed curve in Fig. 4, and was a reasonable approximation of the RTMV field strength. The RMS error between the Sabine field strength including the distance correction and the RTLAA field strength was 3.93 dB. The Sabine field strength and the RTMV field strength were in reasonable agreement, with an RMS error of 1.36 dB between them,

Figure 4 shows that neither the RTMV nor the Sabine field strength is a good approximation of the RTLAA field strength along the centerline of a long corridor. Thus the fast methods should be used with caution in this situation.

Fifth Floor: The wall construction of the eighth and fifth floors appeared to be very similar and it would be expected that the slow fading of the field strengths would be similar. However, the measured curves for the fifth floor (Fig. 5) and eighth floor (Fig. 4) were quite different. This difference arose partly because there was a metal screen in the window directly behind the transmitter on the fifth floor, separated from the antenna by 121 cm. The metal screen strongly reflected the field so that the antenna and its image in the metal screen behaved as a two-element array, with the antenna and its image separated by about 6.88 wavelengths. For an observer in the far field of the array in the direction of the corridor centerline, the phasing of the field of the transmitter and of its image in the screen was such that the net field strength was 1.14 dB *less* than that of the transmitter alone. On the eighth floor, the glass-block wall was almost transparent and contributed little to the field in the corridor. But on the fifth floor, the metal screen reflected substantially into the corridor. An observer on the corridor centerline would see two sets of rays. One set would be the same as the rays seen in the eighth floor corridor. The second set would be rays that reflected from the screen behind the transmitter and then found their way to the observer. Thus, the mean value of the multipath field would be approximately doubled. The RTMV estimate of equation (4) was larger on the fifth floor than on the eighth floor because about twice as many rays passed through the observer.

Figure 5 shows the measured field, smoothed with a 2 m window (solid curve) and the RTLAA simulated field strength (solid curve with crosses). The large maximum at 8.5 m separation was seen in both the measurement and the simulation. The rapid decline in the measured field from 10 m to 13 m separation was reproduced well in the simulation. There was a maximum in the measured field at 17.5 m distance, and a corresponding but larger maximum in the simulated field strength. For larger distances the measurement and simulation did not align as well.

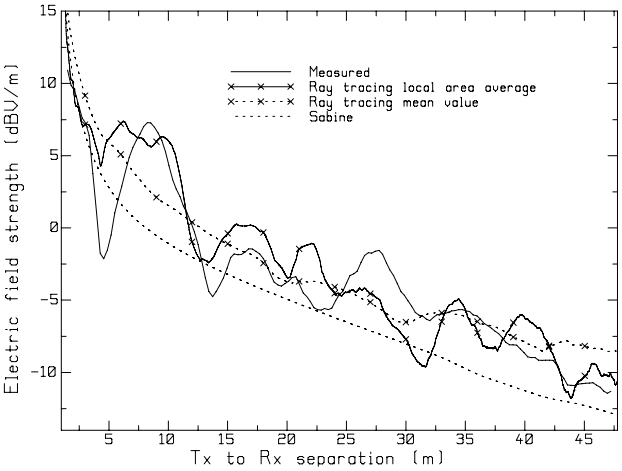

Fig. 5 Measurement and simulations on the fifth floor corridor.

The sharp minimum at 4.5 m distance in the measured field strength was not reproduced in the simulation. If the wall model were changed to have three layers, ε_r =3 for 2.3 cm thickness on both surfaces, separated by a 9.4 cm air layer, then the reflection coefficient for the perpendicular polarization at 69 degrees incidence from the normal would be zero, and the wall would not reflect fields from the transmitter to the receiver for separations around 5 m. Then the simulated field strength would have a sharp minimum like that in the measurement. However, the walls on the eighth floor and the fifth floor appeared to have similar construction, and it did not seem reasonable to use a different wall model in the simulations for the eighth and fifth floors.

The RMS error between the RTLAA field strength and the measured field strength in the distance interval from 1.6 m to 44.5 m was 2.37 dB, not quite as good agreement as the error of 2.l7 dB found for the eighth floor.

The ray-tracing approximation accounted quite well for the metal screen in the window behind the transmitter, by calculating ray paths that reflect from the screen. The RTMV field strength estimate with the screen in Fig. 5 was larger than that with no screen in Fig. 4, and was a reasonable approximation of the much-more-expensive RTLAA estimate. The RMS error between the RTMV field strength and the RTLAA field strength was 1.9 dB.

The fifth floor results illustrate a situation where the Sabine method performed poorly. The Sabine calculation did not explicitly evaluate reflection paths and so could not account directly for the image of the transmitter in the

screen. Instead, the presence of the screen was accounted for by its angle-averaged power absorption coefficient of zero, replacing the power absorption of window opening with no screen, which was unity. But the surface area of the 63 cm × 43 cm screen was very small compared to the surface area of the entire hallway, and so the change in the room absorption of equation (6) was negligible. Hence the indirect field hardly changed at all due to the presence of the screen. The Sabine estimate of the field strength for the fifth floor was the same as that for the eighth floor, and agreed poorly with the RTLAA estimate, with an error of 3.4 dB, not nearly as good as the agreement of the RTMV estimate. Thus, when a transmitter is close to a highly-reflecting surface, the Sabine method should be used with caution.

IV. CONCLUSION

This paper has compared computationally-fast estimates of the local-area-average field strength with the much-slower detailed ray-tracing calculation, and with measurements. The "fast" estimates are firstly, the ray-tracing mean value given by equation (4), which is a slowly-varying function and can be computed at widely separated points, and secondly, the Sabine method given by equation (13), which is obtained by a very simple calculation. Conversely, a detailed ray-tracing calculation uses a dense grid of points to calculate the fast fading of the field, and then explicitly averages the field with equation (3), to obtain the RTLAA estimate, and is therefore a computationally-expensive calculation.

In a typical rectangular room, the agreement of the RTLAA field strength with the measurement was good. Both the RTMV estimate and the Sabine estimate were good approximations to the RTLAA field strength.

The long corridor problem illustrated that the fast methods can have significant errors. The RTLAA estimate of the field strength along the centerline of the corridor was generally larger in value than the RTMV estimate, with an RMS error of about 3.1 dB. The Sabine estimate was poor for the long corridor unless the exponential distance correction of equation (17) was used. With the distance correction, the Sabine estimate differed from the RTMV estimate by 1.4 dB and from the RTLAA estimate by 3.9 dB.

The fifth floor corridor illustrated that the Sabine method was inaccurate when a small reflecting screen was located behind the transmitter. Ray tracing accounted well for rays reflected from the screen, and the RTMV field strength was about 2 dB different from the RTLAA value. But the Sabine method accounted for the screen only through the change in the room absorption, which was negligible because the area of the screen was small compared to the overall surface area of the corridor. The error in the Sabine method was 3.4 dB, much poorer than the error in the RTMV estimate.

This paper has shown that the RTLAA field strength agrees reasonably with measurements for both the rectangular room and the long corridor. The significance of this paper is that it establishes that both the commonly-used RTMV estimate and the little-known Sabine field strength estimate are accurate in a rectangular room, but are less accurate in a long, narrow corridor. The Sabine method provides a computationally-inexpensive estimate of the field strength in rectangular rooms, and can be readily extended to complex floor plans with multiple sources.

ACKNOWLEDGEMENT

The authors gratefully acknowledge the support of PROMPT, Bell Canada, Nortel, FQRNT, and National Science and Engineering Research Council of Canada.

REFERENCES

[1] H. Hashemi, "The indoor propagation channel," *Proc. IEEE*, vol. 81, no. 7, pp. 943-968, July 1993.

[2] J. B. Andersen, T. S. Rappaport, and S. Yoshida, "Propagation measurement and models for wireless communication channels," *IEEE Communications Magazine*, vol. 33, no. 1, pp. 42 – 49, Jan. 1995.

[3] C.-P. Lim, J. L. Volakis, K. Sertel, R. W. Kindt, and A. Anastasopoulos, "Indoor propagation models based on rigorous methods for site-specific multipath environments," *IEEE Trans. on Ant. and Prop.*, vol. 54, no. 6, pp. 1718-1725, June, 2006.

[4] J. M. Gorce, K. Jaffres-Runser, and G. de la Roche, "Deterministic approach for fast simulations of indoor radio wave propagation," *IEEE Trans. on Ant. and Prop.*, vol. 55, no. 3, pp. 938-948, March 2007.

[5] Z. Yun, M. F. Iskander, and Z. Zhang, "Complex-wall effect on propagation characteristics and MIMO vapacities for an indoor wireless communication environment," *IEEE Trans. on Ant. and Prop.*, vol. 42, no. 4, pp. 914- 922, April 2004.

[6] H. Bertoni, W. Honcharenko, L. R. Maciel, and H. H. Xia, "UHF propagation prediction for wireless personal communications," *Proc. IEEE*, vol. 82, no. 9, pp. 1333-1359, Sept. 1994.

[7] T. S. Rappaport, *Wireless Communications, Principles and Practice.* New Jersey: Prentice-Hall PTR, 1996.

[8] K. W. Cheung, J. H. M. Sau, and R. D. Murch, "A new empirical model for indoor propagation prediction," *IEEE Trans. on Veh. Tech.*, vol. 47, no. 3, pp. 996-1001, Aug. 1998.

[9] V. Degli-Esposito, G. Lombardi, C. Passerini, and G. Riva, "Wide-band measurement and ray-tracing simulation of the 1900 MHz indoor propagation channel: comparison criteria and results," *IEEE*

Trans. on Ant. and Prop., vol. 49, no. 7, pp. 1101-1110, July 2001.

[10] D. Didascalou, J. Maurer, and W. Wiesbeck, "Subway tunnel guided electromagnetic wave propagation at mobile communication frequencies," *IEEE Trans. on Ant. and Prop.*, vol. 49, no. 11, pp. 1590-1596, Nov. 2001.

[11] E. H. Newman, *Plane Multilayer Reflection Code.* Technical Report 712978-1, ElectroScience Laboratory, The Ohio State University, July 1980.

[12] R. A. Valenzuela, O. Landron, and D. L. Jacobs, "Estimating local mean signal strength of indoor multipath propagation," *IEEE Trans. on Veh. Tech.*, vol. 46, no. 1, pp. 203-212, Feb. 1997.

[13] F. Van Der Wijk, A. Kegel, and R. Prasad, "Assessment of a pico-cellular system using propagation measurements at 1.9 GHz for indoor wireless communications," *IEEE Trans. on Veh. Tech.*, vol. 44, no. 1, pp. 155-162, Feb. 1995.

[14] R. Tingly and K. Pahlavan, "Space-time measurement of indoor radio propagation," *IEEE Trans. on Inst. and Meas.*, vol. 50, no. 1, pp. 22-31, Feb. 2001.

[15] T. M. Schafer, J. Maurer, J. Von Hagen, and W. Wiesbek, " Experimental characterization of radio wave propagation in hospitals," *IEEE Transactions on EMC*, vol. 47, no. 2, pp. 304-311, May 2005.

[16] D. Lee, M. J. Neve, and K. W. Sowerby, "The impact of structural shielding on the performance of wireless systems in a single floor office building," *IEEE Trans. on Wireless Comm.*, vol. 6, no. 5, pp. 1787-1795, May 2007.

[17] L. E. Kinsler, A. R. Frey, A. B. Coppens, and J. V. Sanders, *Fundamentals of Acoustics*, New York: Wiley, 2000.

[18] D. A. Hill, "A reflection coefficient derivation for the Q of a reverberation chamber," *IEEE Trans. on EMC*, vol. 38, no. 4, pp. 591-592, Nov. 1992.

[19] C. L. Holloway, M. G. Cotton, and P. McKenna, "A model for predicting the power delay profile characteristics in a room," *IEEE Trans. on Veh. Tech.*, vol. 48, no. 4, pp. 1110-1120, July 1999.

[20] C. L. Holloway, D. A. Hill, J. M. Ladbury, and G. Koepke, "Requirements for an effective reverberation chamber: loaded or unloaded," *IEEE Trans. on EMC* , vol. 48, no. 1, pp. 187-194, Feb. 2006.

[21] J. B. Andersen, J. O. Nielsen, G. F. Pedersen, G. Bauch, and M. Herdin, "Room electromagnetics," *IEEE Ant. and Prop. Mag.* vol. 49, no. 2, pp. 27-33, April 2007.

[22] C. W. Trueman, S. S. Muhlen, D. Davis, and B. Segal, "Field strength estimation in indoor propagation by the Sabine method," in *Proceedings of the 24th Annual Review of Progress in Applied Computational Electromagnetics.* Niagara Falls, Ontario, Canada: ACES, pp. 876-881, 2008.

[23] W. Muneer, I. Abdallah, D. Davis, and C. W. Trueman, " A novel automated site survey system," in *Proceedings of the Symposium on Antenna Technology and Applied Electromagnetics.* Montreal, Quebec, Canada: ANTEM, pp. 147-150, 2006.

[24] W. Muneer, *Rician-K Factor Study for Temporal and Spatial Variations*, M.A.Sc. Thesis, Dept. of Electrical and Computer Engineering, Concordia University, Dec. 2007.

[25] D. Davis, *Indoor Radio-Wave Behavior at 850 and 1900 MHz with Electromagnetic Compatibility Applications in Hospitals: An Experimental, Theoretical, Statistical and Morphological Characterization*, PhD. Dissertation, Dept. of Electrical and Computer Engineering, McGill University, Montreal, Quebec, Canada, 2003.

Christopher W. Trueman received his Ph.D. from McGill University in 1979. He has applied the methods of computational electromagnetics to problems such as aircraft antenna performance, antenna-to-antenna coupling and EMC on aircraft, aircraft and ship radar cross-section at HF frequencies, suppression of scattering of the signal of a commercial radio station from power lines, dielectric resonators, unconditionally-stable formulations for the finite-difference time-domain method, and the fields of portable radios such as cellular phones held against the head. Recently, his research has investigated the radar cross-section of ships at VHF frequencies, composite materials for aircraft, indoor propagation, and EMC issues between portable radios and medical equipment. Dr. Trueman is currently the Chair of the Department of Electrical and Computer Engineering at Concordia University.

Bernard Segal is a highly-inter-disciplinary Research Engineer (Electrical Engineering, with a Master's in Electrical (Biomedical) Engineering and a PhD in Neurophysiology, all from McGill University). He is an Associate Professor in the Ear-Nose-Throat (ENT) Department of McGill University, with appointments in Biomedical Engineering and in Physiology. He is the Director of Research in ENT at McGill, and at the SMBD-Jewish General Hospital. He is the Director of Graduate Studies in ENT at McGill. He has contributed to many medical-EMC standards, EMC-healthcare policies, and EMC-healthcare recommendations. He has organized over thirty national

and international conferences, workshops and teaching sessions on EMC in Healthcare. His current research is directed towards clarifying the nature of electromagnetic-interference risk in hospitals, towards minimising this risk, and towards evaluating how to best use wireless informatics in health care safely.

Donald P. Davis received the B.Eng in electrical engineering degree from Concordia University in 1991, the MaSc. degree in electrical engineering from Concordia University in 1994 and the PhD. Degree in electrical engineering from McGill University 2004. Since 1995 he has been a sessional instructor teaching both graduate and undergraduate engineering courses at Concordia University. In 2006 he joined the Jewish General Hospital of Montreal as a post-doctoral researcher studying electromagnetic compatibility of medical equipment due to the presence of wireless communication systems. His research interests include indoor radio wave propagation measurement and modeling, electromagnetic interference estimation and safe implementation of wireless communication systems within clinical environments.

Wadah M. Muneer received his M.A.Sc. degree from Concordia University in 2007 under the supervision of Dr. Trueman. His research was in the field of indoor propagation for wireless channels. Wadah built an indoor automated site-survey system. This system was used in his research for taking measurements in two environments, a hallway and a microwave lab. The results obtained were used to estimate the Rician-K factor using four methods from literature, and compare them with K factor values obtained from simulating the two measurement environments using geometrical optics. Wadah is now a PhD student in the Department of Electrical and Computer Engineering at the University of British Colombia.

Soft Computing Techniques for Free-Space Measurements of Complex Dielectric Constant

[1]D. Escot, [1]D. Poyatos, [1]I. Montiel, and [2]M. A. Patricio
[1] Laboratorio de Detectabilidad. Instituto Nacional de Tcnica Aeroespacial (INTA)
Ctra. Ajalvir Km. 4, 28850, Torrejn de Ardoz, Spain
[2] Grupo de Inteligencia Artificial Aplicada (GIAA). Universidad Carlos III de Madrid
Avda. Universidad Carlos III, 22, 28270, Colmenarejo, Spain

Abstract – A novel method for estimating the dielectric properties of materials by applying different soft computing techniques is presented. Dielectric properties allow us to know other material characteristics such as moisture content, bio-content, chemical concentration, etc., which are of great importance on industrial or science fields. In this paper, we present a free-space measurement method along with soft computing techniques, such as Genetic Algorithms (GA) and Particle Swarm Optimization (PSO), and other approaches like Artificial Neural Networks (ANN), for estimating the dielectric properties of materials. The proposed method is validated by measurements and synthetic materials, which were generated to test the performance of these soft computing algorithms.

I. INTRODUCTION

For many years, the evaluation of dielectric properties of materials has been a fundamental aspect and a challenging problem with an important variety of applications [1]. There are several works focused in the estimation of dielectric properties of materials in the investigations of material and structural assessment [2, 3]. Application of materials in the aerospace, textile, microwave, microelectronics, and communication industries requires the exact knowledge of material parameters such as permittivity and permeability [4, 5, 6]. Complex dielectric permittivity and magnetic permeability (ϵ_r^*, μ_r^*) are two fundamental parameters that describe the response of matter to the external electric and magnetic fields. Nowadays, a heightened interest on the development of new methods that provide accurate determination of both parameters has arisen, particularly, from the fact that contemporary Electronic Design Automation (EDA) software contribute to the design process by allowing us to extensively characterize a constructed device prior to making a physical prototype. To prepare a trustworthy simulation, it is necessary to have good knowledge of the dielectric properties of all media involved.

During the last years, INTA's Detectability Lab has investigated in the field of material measurements [7, 8], as well as in characterization of their electromagnetic properties [9, 10] for radar applications (protective/coating materials, Radar Absorbing Materials (RAM),...) in which a plane wave will impinge on a target. There are many ways to measure the complex electromagnetic constants of samples in the time and frequency domain [11] and they all basically fall into two categories: either destructive methods, in which sample preparation is needed for accurate evaluation, or nondestructive methods, which require very little or no sample preparation [12]. The measured quantity(s) of the sample will enable the computation of its permittivity and permeability.

The open-ended coaxial probe is a cut-off section of a transmission line. The material is measured by immersing the probe into a liquid or touching it to the flat face of a solid (or powder) material. The method offers the advantages of being a broadband and nondestructive method, but in the case of solids requires perfect contact between the probe and the sample. The surface roughness of the sample seriously limits the accuracy of the measurement [13]. Other techniques such as the perturbation of a resonant cavity by the introduction of a dielectric sample can be utilized to compute electrical properties by measuring the change in resonant frequency and its quality factor. However, the sample should fit exactly into the sample holder, and small misalignments can cause large measurement errors [14]. Recently, the methods based on numerical techniques have been arising due to the increase of capacity and accuracy of the numerical methods [15, 16].

In the free-space method (Fig. 1), the antennas focus microwave energy at the measurement plane, and the sample is fixed at the common focal plane between the two antennas. Since the sample is at the focal plane of the antenna and is not in contact with the applicator, it can be adapted easily for measurements at high or low temperatures and hostile environments [17]. Traditionally, whatever the measurement method may be, an iterative process need to be implemented to find the roots of the error function and extract complex permittivity and permeability (ϵ, μ) from the measured quantity(s) [18].

Soft computing is a general term covering a number of methodologies, where the common thread through all of them is that, unlike conventional algorithms, they are tolerant of imprecision, uncertainty, and partial truth. Soft

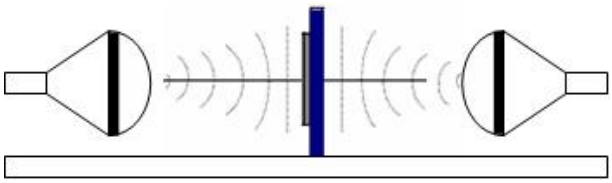

Fig. 1. Free-space measurement set-up.

computing techniques offer adaptivity, since they can track a changing problem quite well. The aim of this paper is to apply soft computing techniques to estimate the electromagnetic characteristics of materials, using the free-space method. First, the measurement method is described and the problem is defined. Then, the soft computing techniques used in our experimentation are presented. This techniques are Genetic Algorithms (GA) and Particle Swarm Optimization (PSO) and Artificial Neural Networks (ANN). GA and PSO are used to obtain the dielectric constant from artificial, synthetic materials. After that, different topologies of ANNs are applied to the same set of materials to compare performance. Finally, these techniques are used on real measurements obtained from INTA's anechoic chamber.

II. PROBLEM DEFINITION

In this section, a theoretical representation of the estimation problem is introduced. The free-space method employed at INTA follows the configuration shown in Fig. 2(a), where a PC controls the positioner and a Vector Network Analyzer (VNA), which is also connected to a transmitting and receiving antenna. For radar applications, this method has some advantages:

1) Allows broadband and contactless nondestructive measurements.
2) The materials are measured under free-space conditions, which are the same conditions of the actual applications of the these materials.
3) The samples used must not be highly elaborated in shape.

Using this setup, S_{11} parameter is measured and reflection coefficient is obtained for a metal-backed sample (Fig. 2(b)). From transmission line theory, reflection coefficient is related to complex permittivity and permeability via the following general equations (no assumptions or approximations for low losses materials have been made) derived from [19],

$$\Gamma_{\perp} = \frac{\sqrt{\frac{\mu_r^*}{\epsilon_r^*}}cos(\theta_i)tanh(jk_0d\sqrt{\mu_r^*\epsilon_r^*}cos(\theta_t)) - cos(\theta_t)}{\sqrt{\frac{\mu_r^*}{\epsilon_r^*}}cos(\theta_i)tanh(jk_0d\sqrt{\mu_r^*\epsilon_r^*}cos(\theta_t)) + cos(\theta_t)} \quad (1)$$

$$\Gamma_{\parallel} = \frac{\sqrt{\frac{\mu_r^*}{\epsilon_r^*}}cos(\theta_t)tanh(jk_0d\sqrt{\mu_r^*\epsilon_r^*}cos(\theta_t)) - cos(\theta_i)}{\sqrt{\frac{\mu_r^*}{\epsilon_r^*}}cos(\theta_t)tanh(jk_0d\sqrt{\mu_r^*\epsilon_r^*}cos(\theta_t)) + cos(\theta_i)}, \quad (2)$$

where $\Gamma_{\perp}$ and $\Gamma_{\parallel}$ are perpendicular and parallel reflection coefficients, d is the sample thickness, $k_0 = \frac{2\pi}{\lambda}$ is the free-space wavenumber, θ_i is the incidence angle, θ_t the transmitted angle (Fig. 2(b)) and ϵ_r^* and μ_r^* are relative complex permittivity and permeability,

$$\epsilon_r^* = \epsilon_r^{'} - j\epsilon_r^{''} \quad (3)$$

$$\mu_r^* = \mu_r^{'} - j\mu_r^{''}. \quad (4)$$

Because ϵ_r^* and μ_r^* cannot be easily expressed in terms of the reflection coefficients and d, this paper propose to find them by soft computing techniques.

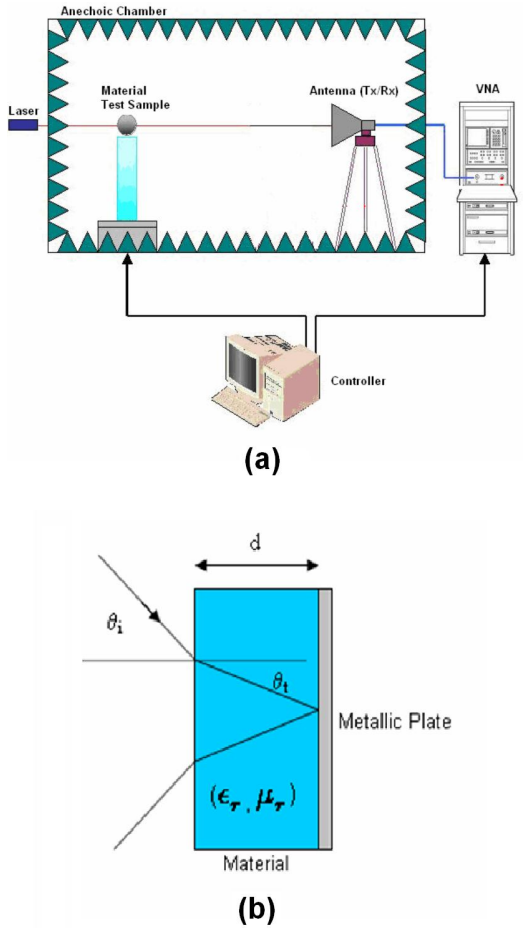

Fig. 2. Measurement set-up in anechoic chamber.

III. SOFT COMPUTING TECHNIQUES IN THE ESTIMATION OF DIELECTRIC PROPERTIES OF MATTER

Bearing in mind equations (1) and (2), the first approach to solve the problem has been the use of Genetic Algorithms (GA) and PSO algorithms, that looks for the proper values of ϵ_r^* and μ_r^* starting from the reflection coefficients of the test samples.

A. Genetic Algorithms

Evolutionary algorithms are a broad class of stochastic optimization algorithms, inspired in the biological process that allow populations to adapt to their surrounding environment [20]. One of the first proposals of these kind of algorithms was the Genetic Algorithms (GA) by John Holland [21]. GA maintains a population of candidate solutions to a specific problem, and makes it evolve by iteratively applying a set of stochastic operations, known as mutation, recombination, and selection [22]. In GA, individuals are codified as strings of binary digits, which represent the solution to the problem and it is called chromosome. The selection of the best candidate solution (or chromosome) is guided by how the candidate solution minimize a fitness function.

For the work contained in this document, MATLAB has been used to perform the optimization by GAs (*Genetic Algorithms and Direct Search Toolbox*). This implementation of GA uses several typical parameters such as population size (*PopulationSize*), number of generations (*Generations*), number of individuals to be kept for next generation (*EliteCount*), selection, crossover and mutation functions (*SelectionFcn, CrossoverFcn, MutationFcn*), etc, which can be adjusted and modified.

The main GA parameters selected in our experimentation are depicted in table 1.

B. Particle Swarm Optimization

Particle swarm optimization (PSO) is a recently proposed algorithm by James Kennedy and R. C. Eberhart in 1995 [23], motivated by social behavior of organisms such as bird flocking and fish schooling. PSO are very similar to Genetic Algorithms, where a population of random solutions is initialized and the aim is the search for optima by updating generations. However, in PSO there is no evolution operators such as crossover or mutation. The potential solutions, called particles, '*fly*' through the problem space by following the current optimum particles.

This optimization approach was first applied to electromagnetic by [24]. In this case, a PSO code has been programed specifically for this work. For the propose of our experimentation, authors have developed a PSO tool that includes a graphical user interface that permits different simulations varying easily its parameters, and seeing its results and convergence. The main parameters used to obtain the results contained in this paper are presented in table 1.

IV. ARTIFICIAL NEURAL NETWORKS

Artificial neural networks (ANN) have their origin in the attempt to simulate by mathematical means an idealized form of the elementary processing units in the brain and of their interconnections, signal processing, and self-organization capabilities [20]. An important issue about ANN is the ability to progressively improve their performance on a given task by somehow learning how to do the task better. They are at their best for problems where there is little or incomplete understanding, so that building a faithful mathematical model is difficult or even impossible.

Our next approach to solve the described problem is to model it through ANNs using the *Neural Network Toolbox* provided by MATLAB.

The actual reflection coefficients measured in the anechoic chamber are contaminated with noise and it is well known the skill of ANNs to adapt its behavior to noisy signals and to obtain good results. Moreover, before feeding the search algorithms with the actual reflection coefficients, some kind of preprocessing must be done. For the case of ANNs, this preprocessing can be avoided, reducing the time and complexity of the process.

Another theoretical advantage is the fact that the ANN training is time and computational consuming, but is done only a limited number of times, and after that the determination of the dielectric constants for a material is practically instantaneous. On the other hand, the search algorithm (GA or PSO) is time consuming each time it is executed. So, the global computational cost derived from the ANNs will be less than the derived from the GA or PSO.

V. RESULTS

For this first approach, both synthetic and real materials are used to test the algorithms proposed. As actual available materials in our lab are non-magnetic, there is no need to measure off-normal, so $\theta_i = 0$ and equations (1) and (2) are the same, and consequently one of them is enough to extract real (ϵ_r') and imaginary parts (ϵ_r'') of ϵ_r^*. For this reason, the synthetic materials created are non-magnetic and the problem is reduced to the estimation of the dielectric permittivity. This simplification diminish the complexity of the problem but does not limit its utility as the conclusions could be easily extrapolated to oblique incidence and μ_r^* determination.

A. GA and PSO

Given electric permittivity, thickness, and frequency, reflection coefficients can be calculated from equation (1). Table 2 shows the fifteen different synthetic materials generated.

For each of these materials, GA and PSO are applied separately using the MATLAB *Toolbox* and the tool developed respectively. For the GA the genes are formed by two chromosomes whereas for PSO each position vector has also two coordinates, it is, in both cases, real and imaginary parts of ϵ_r^* are searched. Codification is real for both alternatives and the chosen fitness function to be minimized is,

Table 1. GA and PSO parameters.

GA		PSO	
Parameter	Value	Parameter	Value
PopInitRange	[1 0;20 20]	Range	[1 0;20 20]
PopulationSize	50	Population	20
EliteCount	4	C1, C2	2
Generations	100	Iterations	140
SelectionFcn	@selectionroulette	Initial inertia	0.9
CrossoverFcn	@crossoverintermediate,0.5	Final inertia	0.4

Table 2. Synthetic materials.

Material	$\epsilon_r^{'}$	$\epsilon_r^{''}$	$d(mm)$	Freq. (GHz)
AR1	2	0	2	8-12.4
AR2	5	0	2	8-12.4
AR3	10	0	2	8-12.4
AR4	10	1	2	8-12.4
AR5	10	10	2	8-12.4
AR6	2	0	1	8-12.4
AR7	5	0	1	8-12.4
AR8	10	0	1	8-12.4
AR9	10	1	1	8-12.4
AR10	10	10	1	8-12.4
AR11	2.45	0	0.796	8-12.4
AR12	2.55	0	1.589	8-12.4
AR13	2.01	0	1.539	8-12.4
AR14	9.8	0	1.234	8-12.4
AR15	2.2	5.2	1.2	8-12.4

$$f = |Re(\Gamma_{\perp_{actual}}) - Re(\Gamma_{\perp_{iteration}})| + |Im(\Gamma_{\perp_{actual}}) - Im(\Gamma_{\perp_{iteration}})|. \quad (5)$$

The output of both algorithms is excellent, as they can match the desired real and imaginary parts of the complex permittivity for all the cases at all the frequencies with practically inexistent error. As an example, material AR15 is shown in Fig. 3.

To emulate the measurement error and evaluate its influence in the determination of $\epsilon_r^{'}$ and $\epsilon_r^{''}$, the reflection coefficient related to AR15 is contaminated with a gaussian error (zero mean and a variance of 0.5 dB in modulus and 0.1 in phase). The results obtained are nearly the same for GA and PSO (Fig. 4), and the influence of this error become clear, deriving in an incorrect estimation of ϵ_r^*.

In the next step, a 20x20 cm real sample of Arlon© CuClad 250GX-0620 55 11 is measured in the anechoic chamber, and the reflection coefficient is treated with GA and PSO to obtain the dielectric constant. The sample has a thickness of $d = 1.70\ mm$ and the manufacturer asserts that its nominal real part and loss tangent ($tan\delta = \frac{\epsilon_r{''}}{\epsilon_r{'}}$) are 2.55 and 0.0022 respectively, with minimum variations over a wide frequency band[1]. Comparisons with results obtained with the estimation presented in this paper are

[1]The measurement method followed by Arlon© is the accepted industry standard IPC TM-650 2.5.5.5, a stripline resonator test for permittivity and loss tangent (dielectric constant and dissipation factor) at X-Band–3/98

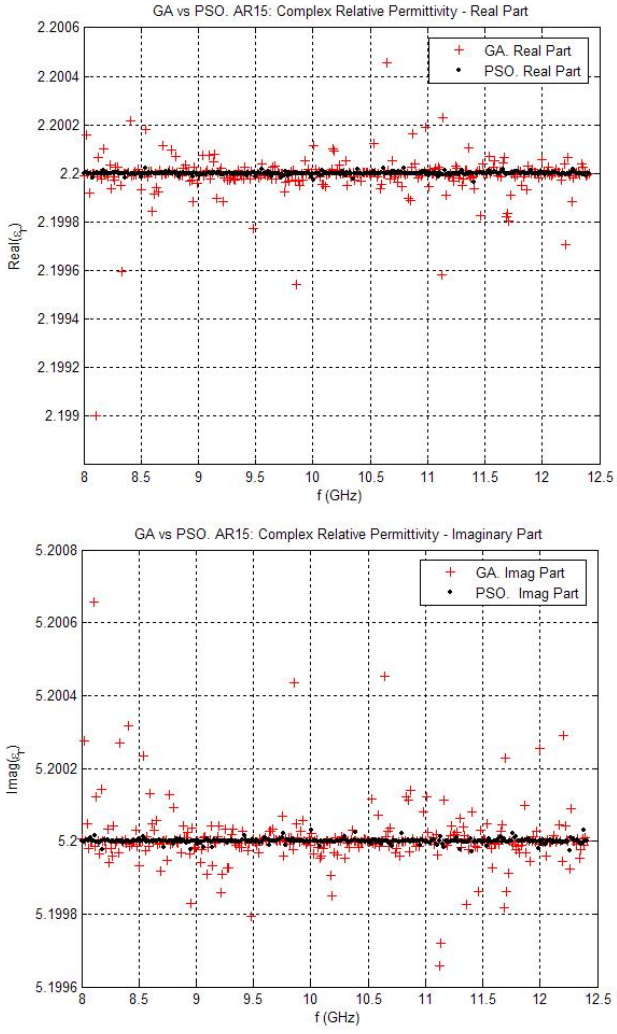

Fig. 3. Estimated real and imaginary part of AR15 for GA and PSO.

shown in Fig. 5, proving that soft computing techniques are a good and easy-to-implement alternative. This good results are supported by the fact that the actual measurement error is lower than the proposed for AR15.

B. ANN

Different multilayer feed-forward backpropagation networks are designed. All of them have four inputs and

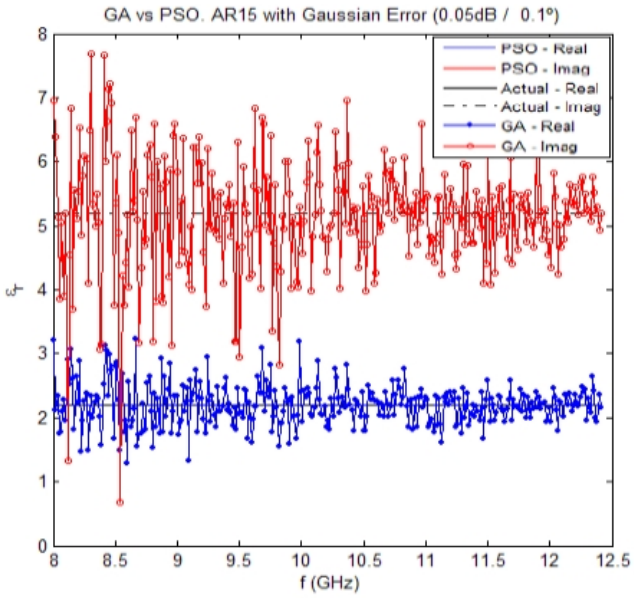

Fig. 4. GA and PSO results for AR15 reflection coefficient contaminated with noise.

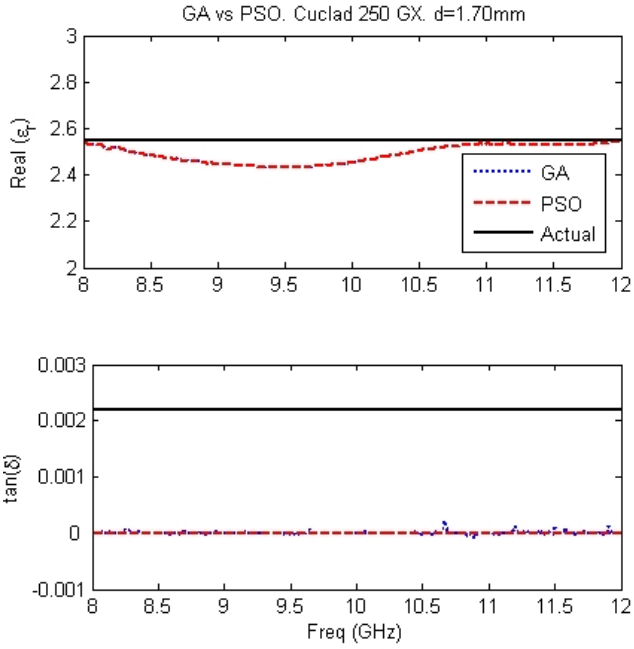

Fig. 5. Real part and loss tangent estimation with GA and PSO of CuClad 250GX.

two outputs. The inputs are the real and imaginary parts of the reflection coefficient, the frequency and the thickness of the sample and the two outputs are the real and imaginary parts of complex relative permittivity (Fig. 6). For training, validation and test, a set of twenty synthetic materials is used, where random values have been chosen: $\epsilon_r^{'} \in [1, 10]$, $\epsilon_r^{''} \in [0, 10]$ and $d \in [0.5, 2]\ mm$. After grouping the materials by frequency, 1/2 of data is used for training, 1/4 for validation and 1/4 for test.

Minmax normalization is applied for input and output parameters and hyperbolic tangent sigmoid transfer function (`tansig`), linear transfer function (`purelin`) and Levenberg-Marquardt backpropagation (`trainlm`) are used as hidden layers activation function, output layer activation function and training function respectively.

Different architectures have been tested, namely with one hidden layer and 10, 15 or 20 neurons and with two hidden layers with 20-10 neurons or 25-15 neurons. Starting at a given value, increasing the number of layers and neurons, the net follows better the training, test and validation materials but fails in predicting new materials.

The best output is achieved for the one layer and 20 neurons case. In Fig. 7, it can be seen the training performance for the materials used for test in this configuration.

Fig. 6. Artificial neural network inputs and outputs.

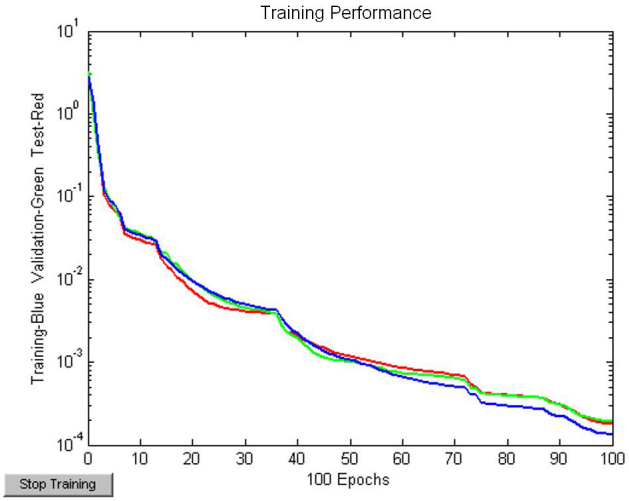

Fig. 7. Training Performance: 1 Layer and 20 neurons.

The result for AR15 material (table 2) without noise is presented in Fig. 8 and with noise in Fig. 9. Figure 9 also shows the performance for the synthetic test material ARPr (with dielectric constant $\epsilon_r^{'} = 6.52$ $\epsilon_r^{''} = 2.22$). Simulations show that GA and PSO have better performance than ANN except for the case of AR15 with noise.

The measurements made for Arlon© CuClad 250GX-0620 55 11 are introduced to the trained network and the output obtained is presented in Fig. 12. GA and PSO approaches show better performance also for the real measurement.

At this point, the net is trained with the random artificial materials but adding gaussian noise in phase

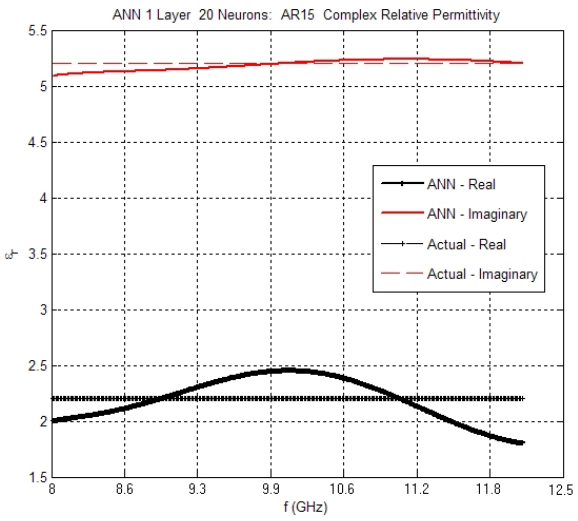

Fig. 8. ANN applied to synthetic material AR15: 1 layer, 20 neurons.

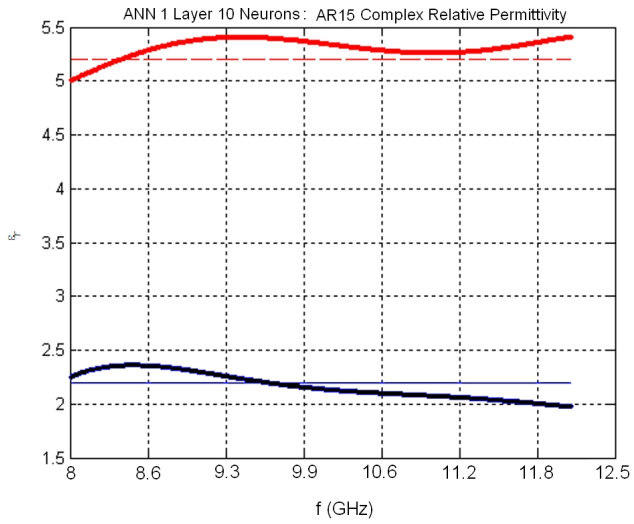

Fig. 10. ANN applied to synthetic material AR15: 1 layer, 10 Neurons.

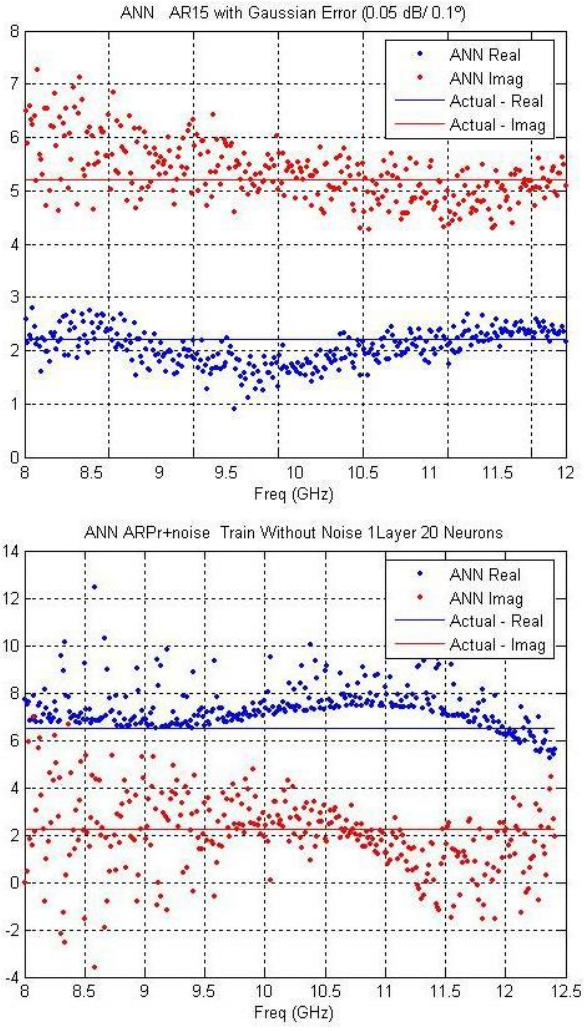

Fig. 9. ANN applied to contaminated synthetic material AR15 and ARPr: 1 layer, 20 neurons.

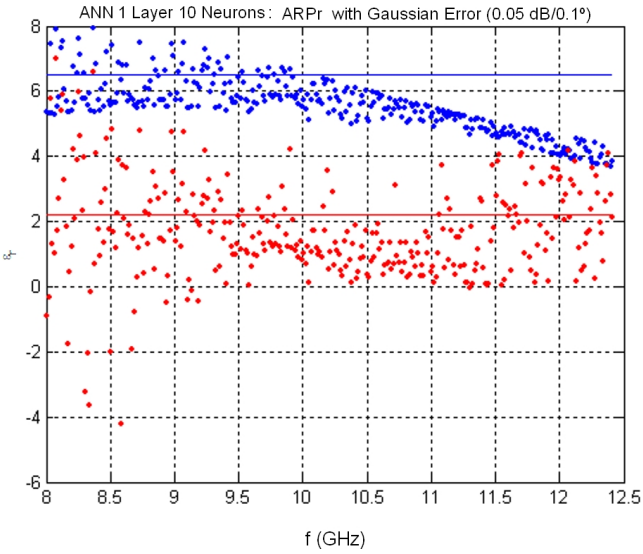

Fig. 11. ANN applied to synthetic material ARPr+Noise: 1 layer, 10 Neurons.

and amplitude (with zero mean and 0.05dB and 0.1 of variance) to the odd materials. Then, half of the training, test and validation samples contains noise. In this case, the adaptation of the net to the training materials is worse, and the training error is higher. The best output is achieved for the one layer and 10 neurons case. Figure 13, shows the training performance for the materials used for test in this configuration.

The results for AR15 and ARPr+Noise can be seen in Figs. 10 and 11. It can be appreciated that no improvement has been reached with this training.

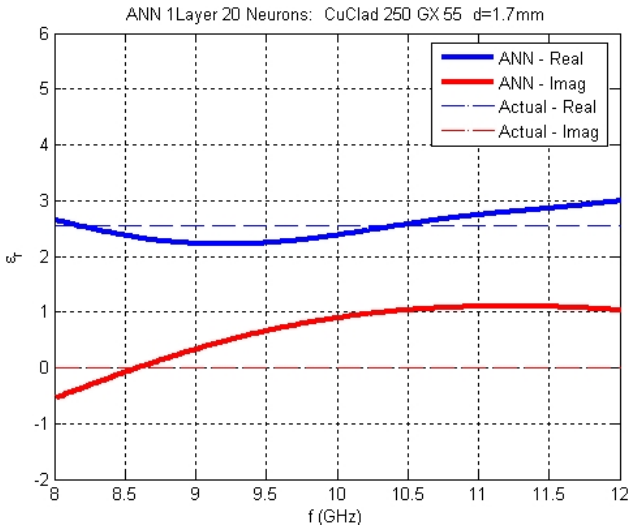

Fig. 12. ANN applied to measured Arlon© CuClad 250GX-0620 55 11: 1 layer, 20 neurons.

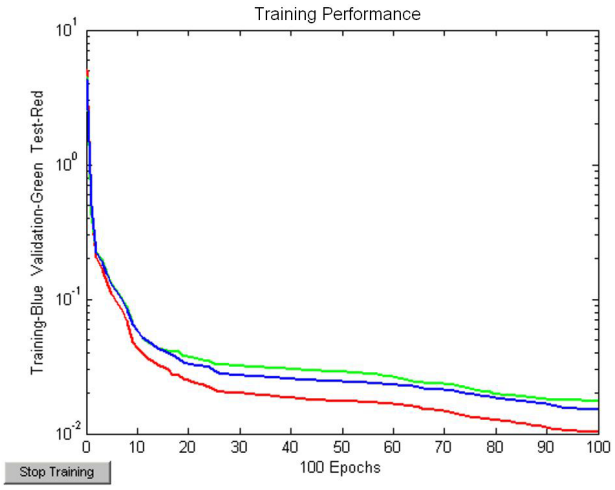

Fig. 13. Training Performance: 1 layer, 10 neurons.

VI. CONCLUSIONS AND FUTURE WORK

The application of soft computing techniques to dielectric constant estimation via free-space measurements has been presented. Results obtained are promising and demonstrate the validity of this approach.

GA and PSO show better performance for actual measurements if the error is not high. This approach can be used for real tests. On the other hand, ANNs present promising behavior in presence of high noise, although further improvement is needed.

Future work must include the training of networks with a set of actual measurements, and the experimentation with other architectures/topologies.

REFERENCES

[1] A. Von Hippel, "Dielectric materials and applications," *Technology Press of MIT*, Cambridge, MA, 1954.

[2] L. P. Lighthart, "A fast computational technique for accurate permittivity determination using transmission line methods," *IEEE Trans. Microwave Theory and Techniques*, vol. 31, no. 3, pp. 249-254, 1983.

[3] J. Grigas. "Microwave Dielectric Spectroscopy of Ferroelectrics and Related Materials," *Gordon and Breach Sci. Publ. Inc.*, New York, pp. 336, 1996.

[4] J. L. Suthar, J. R. Laghari, A. N. Hammoud, E. D. Baumann, I. T. Myers, and S. Domitz, "Evaluation of dielectric films for aerospace and space power wiring insulation," Proc. of the *IEEE International Symposium on Electrical Insulation*, pp. 17-20, 1992.

[5] A. S. A. Bakar, M. I. Misnon, D. K. Ghodgaonkar, N. Khadri, J. H. Salleh, W. Y. W Ahmad, M. D. M. Ramli, Y. M. Taib, and Z. Salleh, "Comparison of electrical physical and mechanical properties of textile composites using microwave nondestructive evaluation," Proc. of the *RF and Microwave Conference*, pp. 164-168, 2004.

[6] Q. Zeng, W. Li, J. Shi, and J. Guo, "Fabrication and microwave dielectric properties of a new LTCC ceramic composite based on Li2O-Nb2O5-TiO2 system," *Materials Letters*, vol. 60, no. 27, pp. 3203-3206, 2006.

[7] I. Montiel, "INTA's free space NRL arch system and calibration for absorber material characterization," Proc. of the *Antenna Measurement Techniques Association*, pp. 323-328, 1995.

[8] I. Montiel, "Arc method for measurement of absorbent materials," Proc. of the *Spanish Union Radio-Scientifique Internationale Symposium*, Valladolid, Spain, 1995.

[9] I. Montiel, "Effects of diffraction of edges in the measures of characterization of materials in free space," Proc. of the *Spanish Union Radio-Scientifique Internationale Symposium*, Madrid, Spain, 1996.

[10] I. Montiel, "System of measurement of RCS by means of a single port Vector Analyzer," Proc. of the *Spanish Union Radio-Scientifique Internationale Symposium*, Bilbao, Spain, 1997.

[11] J. Baker-Jarvis, R. G. Geyer, J. H. Grosvenor, M. D. Janezic, C. A. Jones, B. Riddle, C. M. Weil, and J. Krupka, "Dielectric characterization of low-loss materials: A comparison of techniques," *IEEE Trans. Dielectrics and Electrical Insulation*, vol. 1, no. 4, pp. 571577, 1998.

[12] H. C. Rhim and O. Buyukozturk. "Wideband microwave imaging of concrete for nondestructive testing," *ASCE J Struct Eng* pp. 14517, 2000.

[13] D. K. Misra, "On the measurement of the complex permittivity of materials by an open-ended coaxial probe," *IEEE Microwave and Guided Wave Letter 5*, vol. 5, no. 5, pp. 161163, 1995.

[14] B. Meng, J. Booske, and R. Cooper, "Extended cavity perturbation technique to determine the complex permittivity of dielectric materials," *IEEE Trans. Microwave Theory and Techniques*, vol. 43, no. 11, pp. 26332636, 1995.

[15] R. Coccioli, G. Pelosi, and S. Selleri, "Characterization of dielectric materials with the finite-element method," *IEEE Trans. Microwave Theory and Techniques*, vol. 47, no. 10, pp. 1106-12, 1999.

[16] E. E. Eves, P. Kopyt, and V. V. Yakovlev, "Determination of complex permittivity with neural networks and FDTD modeling," *Microwave Optical Technology Letters*, vol. 40, no. 3, pp. 183-8, 2004.

[17] J. Musil and F. Zacek, "Microwave measurements of complex permittivity by free-space methods and their applications," *Elsevier*, New York, pp. 44-60, 92-166, 1986.

[18] D. K. Ghodgaonkar, V. V. Varadan, and V. K. Varadan, "Free-space measurement of complex permittivity and complex permeability of magnetic materials at microwave frequencies," *IEEE Trans. Instrumentation and Measurement* vol. 39, no. 2, pp. 387-394, 1990.

[19] C. A. Balanis, "Advanced engineering electromagnetics," *John Wiley & Sons*, New York, pp. 223, 1989.

[20] A. Tettamanzi and M. Tomassini, "Soft Computing. Integrating Evolutionary, Neural, and Fuzzy Systems," *Springer-Verlag*, Heidelberg, 2001.

[21] J. H. Holland, "Adaptation in Natural and Artificial Systems," *The University of Michigan Press*, Ann Arbor, Michigan, 1975.

[22] T. Bäck, "Evolutionary algorithms in theory and practice," *Oxford University Press*, Oxford, 1996.

[23] J. Kennedy and R. C. Eberhart, "Particle swarm optimization," Proc. of the *IEEE International Conference on Neural Networks*, Perth, Australia, 1995.

[24] J. Robinson and Y. Rahmat-Samii, "Particle Swarm Optimization in Electromagnetic," *IEEE Trans. on Antennas and Propagation*, vol. 52, no. 2, 2004.

David Escot was born in Madrid, Spain, and received his MSc degree in Telecommunication Engineering from the Universidad de Alcal de Henares (UAH) in 2002. Since 2005 he is pursuing the PhD degree. He was a Research Assistant at ENSTB (*cole Nationales Suprieure des Tlcommunications de Bretagne*), Brest, France, from 2002 to 2003. Since 2004 he is with the Detectability Laboratory, Instituto Nacional de Tcnica Aeroespacial (INTA, Madrid) and his research activities and interests are in the area of the application of bio-inspired techniques to electromagnetics and the analysis, measurement and simulation of radar cross section (RCS).

David Poyatos was born in Madrid, Spain. He received the MSc degree in Telecommunication Engineering from the Universidad Politcnica de Madrid (UPM) in 1998 and he is currently pursuing the PhD degree. From 1997 to 1998 he was an undergraduate Research Assistant at the Electromagnetic Compatiblility (EMC) Area, Instituto Nacional de Tcnica Aeroespacial (INTA, Madrid). Since 1999 he is with the Detectability Laboratory, INTA, and his research and activities are in the area of computational electromagnetics, in particular, the application of bio-inspired algorithms and the simulation, measurement and analysis of radar cross section (RCS).

Ignacio Montiel was born in Madrid, Spain. He received the MSc degree in Telecommunication Engineering from the Universidad Politcnica de Madrid (UPM) in 1990 and the Ph.D. degree from the Universidad de Alcal de Henares (UAH) in 2003. Since 1990 he is working at Instituto Nacional de Tcnica Aeroespacial (INTA, Madrid). In 1997 he founded the Detectability Laboratory at INTA, researching on Electronic Warfare, Non Cooperative Target Identification by Radar, and the analysis, measurement and simulation of radar cross section (RCS) of aerial targets. From 2006 he is heading the Communications, Navigation and Radar Area. Currently, he is Chairman of the RTO Task Group SET-112/RTG63 on Advanced Analysis and Recognition of Radar Signatures for Non-Cooperative Air Target Identification.

Miguel A. Patricio received his BSc in Computer Science from the Universidad Politcnica de Madrid in 1991, his MSc in Computer Science in 1995 and his PhD degree in Artificial Intelligence from the same university in 2002. He has held an administrative position at the Computer Science Department of the Universidad Politcnica de Madrid since 1993. He is currently Associate Professor at the Escuela Politcnica Superior of the Universidad Carlos III de Madrid and research fellow of the Applied Artificial Intelligence Group (GIAA). He has carried out a number of research projects and consulting activities in the areas of automatic visual inspection systems, texture recognition, neural networks and industrial applications.

Application of Wavelets and Auto-Correlation-Function For Cancellation of High-Frequency EMI Noise

W. Chen, X. Yang, and Z. Wang

State Key Lab. of Electrical Insulation and Power Equipment
Xi'an Jiaotong University, Xi'an Shaanxi, P.R.China

Abstract – This paper presents a wavelet transforms and auto-correlation function based approach for the high-frequency switching noise cancellation. The noise is extracted by wavelet multi-resolution analysis. The enough features of signal in frequency and time domains are obtained by using arguments and magnitudes of complex wavelet transform as well as main frequency evaluation of auto-correlation function. The simulation results showed that the high frequency noise could be detected and reconstructed accurately and the average noise attenuation is larger than 20dB. This new method provides a multi-level process and multi-level description method for disturbance identification and cancellation.

I. INTRODUCTION

To achieve electromagnetic compatibility (EMC) compliance, filtering approaches are commonly used. Many practical forms of active EMI filters (AEF) have been reported [1-8]. In voltage canceling filters, a voltage is introduced in series with the noise voltage to cancel it [1, 3, 6]. In current canceling filters, a cancellation current is injected at a node traversed by the noise current [2, 4, 5]. Feed-forward filters achieve noise reduction by measuring a noise component and injecting its inverse [1,4], while feedback filters operate to suppress the noise with high gain feedback control [2, 3 ,6 ,7]. Hybrids of these filter types are also possible [5, 8].

Unfortunately, although the basic concept has been known for some time, there seems to be no change in the noise identifying approach. The existing technique is an analogue method, which uses a band-pass filter to identify a certain bandwidth noise signal. The design of the analogue filter has to incorporate at least a 6th-order filter to ensure a reasonable roll-off frequency. The main disadvantage with this method is that the sensor thus derived has magnitude and phase errors. The phase error normally reaches more than 100°, which is unacceptable for EMI filter applications.

Complex wavelet has been widely used as a time-frequency analysis algorithm for signal processing. Often the wavelet transform of a real signal with complex wavelet is plotted in modulus-phase form, rather than in real and imaginary representation. In the complex wavelet transform analysis, the modulus maxima and the phase crossings point out the locations of sharp signal transitions. Nevertheless, the phase information reveals isolated singularities in a signal more accurately than does the modulus [9-11]. Also, using the phase information, different kinds of transition points of the analyzed signal, i.e. local maxima and inflection points, can be distinguished.

This paper proposes a multi-level process and multi-level description method for disturbance identification and cancellation. In this work, a wavelet-based method incorporated with autocorrelation function is used in the active EMI filter to perform the following tasks: detecting the switching noise, feature extraction and reconstruction of the disturbed signal, canceling the disturbance. The paper has the following structure: section II treats the wavelet bases and deals with the implementation of digital active EMI filter. Some results provided by simulations are given in Section III. Finally, Section IV presents the conclusions.

II. IMPLEMENTATION OF DIGITAL ACTIVE EMI FILTER

Given a time-varying signal $f(t) \in L^2(R)$, wavelet transform can be seen as the computation of coefficients that are inner products of the signal and family of wavelet basis functions. From this function, one can obtain a family of time-scale waveforms by translation and scaling,

$$\mathrm{WT}(f(t);a,b) = \int_{-\infty}^{+\infty} f(t)\psi_{a,b}^{*}(t)\mathrm{d}t \qquad (1)$$

where $\psi(t)$ is the wavelet function that can be also deemed a band-pass function, and $\psi^{*}(t)$ is the complex conjugate of $\psi(t)$. This function can be dilated through the control parameter of a and time-shifted by the parameter of b, in which the factor of $1/\sqrt{a}$ is to ensure the energy preservation.

The complex Gaussian wavelet is chosen as the mother wavelet in this approach. Since the Gaussian

This work was supported by the National Natural Science Foundation of China (NSFC) under Project 50707024.

wavelet looks more like a switching noise generated by parasitic oscillation in geometric shape especially when its shape control parameter is adjusted to be a small value. According to the "matching mechanism" of wavelet transform, the better the wavelet function matches the signal in geometric shape, the more accurate the feature of the signal can be represented by wavelet coefficients. The complex Gaussian wavelet is defined from the derivatives of the Gabor wavelet and is given by,

$$\psi_n(x) = C_n \frac{\mathrm{d}^n}{\mathrm{d}t^n}(e^{-j\omega t}e^{-t^2}) \tag{2}$$

where n denotes the order, $\mathrm{d}/\mathrm{d}t$ is the symbolic derivative and C is a normalizing constant, which depends of n. This wavelet can be easily turned into analytic wavelet by canceling its negative frequencies by means of the Hilbert transform. The frequency response is then,

$$\psi_n(x) = K_n \xi^n e^{-\frac{\xi^2}{2}} \chi(0,\infty)(\xi)\,. \tag{3}$$

where $\chi(0,\infty)(\xi)$ denotes the Heaviside step function, which is equal to 1 when $\xi > 0$ and to 0 otherwise. K_n denotes normalization constant. The parameter n gives different numbers of vanishing moments of wavelets. When performing wavelet singularity analysis, the number of vanishing moments is very important, as it provides an upper bound measurement for singularity characterization.

Therefore, the amplitude (WTM) and phase (WTPH) of wavelet transform can be calculated by use of the following equations,

$$WMT = \sqrt{\mathrm{Re}[\psi(x)]^2 + \mathrm{Im}[\psi(x)]^2}\,, \tag{4}$$

$$WTPH = \arctan(\mathrm{Im}[\psi(x)]/\mathrm{Re}[\psi(x)])\,. \tag{5}$$

That is, the complex wavelet bases are capable to deliver instantaneous amplitude of signal as well as instantaneous phase angles. As these new variables contain more information about the signal analyzed, alternative feature extraction with scalogram and phase spectrum can be derived.

The noise source is a 500W switching mode power supply (SMPS) with 100 kHz switching frequency. The original noise current at the AC input side of the equipment is recorded from a digital oscilloscope Tektronix 3012. Wavelet EMI detection and cancellation is simulated through Matlab 6.5 and the flow diagram is shown in Fig.1.

Compared with conventional analogue noise detection method, the high-frequency switching noise could be separated accurately by means of wavelet transform. The disadvantage of spectrum leakage and fence effect appeared in the classical method are overcome with ease. However, the delay effect of signal must be considered carefully. As we know, the switching noise always contains a main frequency signal that concentrates most of the noise energy. Therefore, if the main frequency of the noise could be estimated successfully, and combined with the above-mentioned amplitude and phase message, the compensation signal could be injected at the right time.

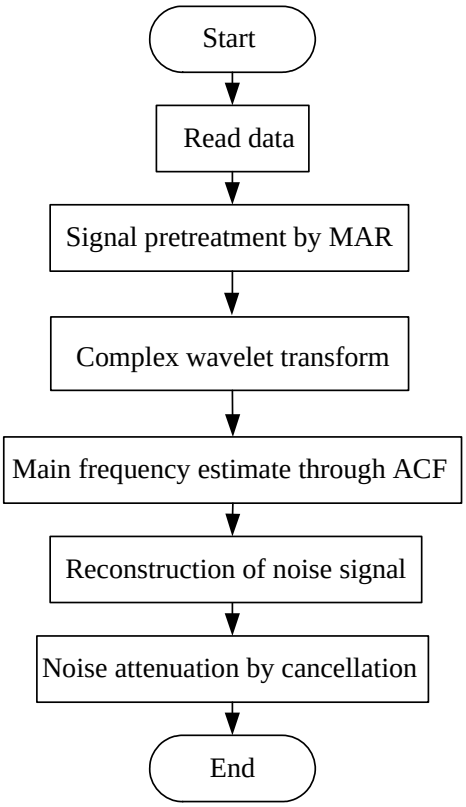

Fig. 1. Flow diagram for the proposed approach.

This paper use auto-correlation function to estimate the main frequency of switching noise. Auto-correlation function showing the relationship of a signal with a time shifted version of itself. The auto-correlation function is defined as,

$$r_X(m) = E\{x^*(n)x(n+m)\} \tag{6}$$

where $x(n)$ is a real continuous signal. If N is the number of data and for each fixed lag m, the estimation of correlation function is,

$$\hat{r}_X(m) = \frac{1}{N-|m|}\sum_{n=0}^{N-1-|m|} x_N(n)x_N(n+m)\,. \tag{7}$$

III. ANALYSIS RESULTS

Since the high frequency noise is sampled with some harmonics, certain pretreatment should be down to the original signal to get rid of low frequency harmonics. Figure 2 shows coefficients of high frequency noise signal through wavelet filter. The result of complex wavelet analysis is shown in Fig. 3. The characteristic features of high-frequency parasitic oscillating noise are exposed in those figures. From Fig. 3 (b), we found the modulus coefficient changes from maximum to minimum, indicates the regular change of oscillation amplitude. The abscissa of the scalogram plots time in samples, and the ordinate plots the frequency scale of the dilation of wavelet in samples of its time period.

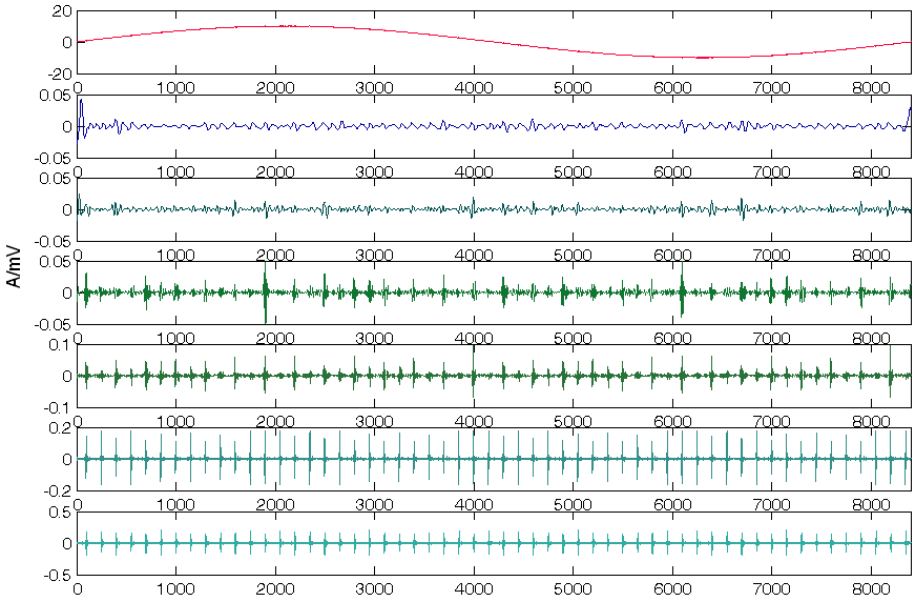

Fig. 2. Coefficients of switching noise through wavelet filter.

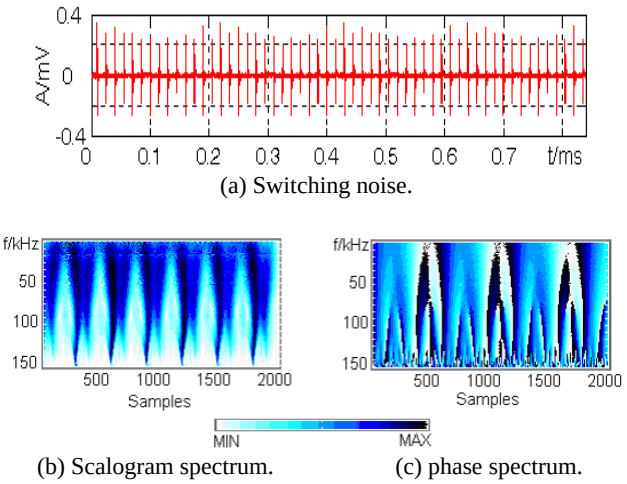

(a) Switching noise.

(b) Scalogram spectrum. (c) phase spectrum.

Fig. 3. Complex wavelet analysis.

At the highest scale (the highest y-axis values), the time window is very short, and the boundary distortion appeared. At lower scales, the frequency localization is more apparent and characterized by regularly spaced dark to bright transitions, indicates that impulses is present at different intervals. Fig. 3 (c) is the phase spectrum and angle coefficient of noise signal; they are also the characteristic feature that distinguished this approach from other wavelet detection method. Each narrow stripe in the phase spectrum represents the cycle corresponding to time zone of the signal. With the increase of frequency, the narrow stripe will split automatically until its width matches the cycle of a certain frequency. This example demonstrates the tracking of a changing frequency due to the zooming nature of the scale mother functions and the ability to discriminate frequencies created by parasitic oscillation.

Figure 4 is the reconstructed noise signal. It is found that the reconstructed one reflects the basic feature of the original signal perfectly. Figure 5 is the error between the two signals. The maximum absolute error is no more than 2%.

When the reconstructed noise signal is rejected into the original high frequency noise, the results are shown in

Fig. 6. The simulation results showed that the average noise attenuation is larger than 20dB.

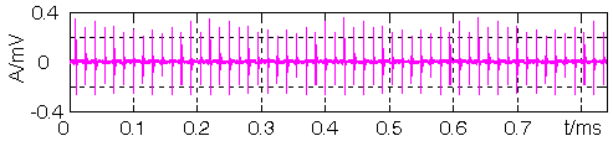

Fig. 4. Reconstructed noise signal.

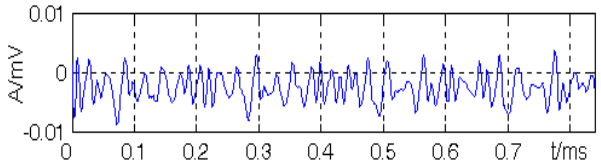

Fig. 5. Error between original signal and reconstructed signal.

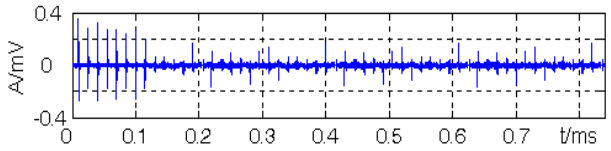

Fig. 6. Noise signal after active EMI cancellation.

IV. CONCLUSIONS

This paper has presented a new method technique possesses the advantages of complex wavelet transform and auto-correlation function for the high-frequency switching noise cancellation in power electronics equipments. The simulation results have shown that the satisfactory performance has been achieved. Therefore, it is reasonable to believe that the proposed method will be widely adopted and extensively applied to the attenuation of switching noise signals.

REFERENCES

[1] P. Cantillon-Murphy, "An active ripple filtering technique for improving common-mode inductor performance," *IEEE Power Electronics Letters*, vol. 2, pp. 45- 50, Jun. 2004.

[2] Y. C. Son and S.-Ki Sul, "A new active common-mode EMI filter for PWM inverter," *IEEE Trans. Power Electronics*, vol. 18, pp. 1309 – 1314, Nov. 2003.

[3] N. K. Poon, J. C. P. Liu, C. K. Tse, and M. H. Pong, "Techniques for input ripple current cancellation: classification and implementation," *IEEE Trans. Power Electronics*, vol. 15, pp. 1144 – 1152, Nov. 2000.

[4] M. Zhu, D. J. Perreault, V. Caliskan, *et al*., "Design and Evaluation of Feedforward Active Ripple Filters," *IEEE Trans. Power Electronics*, vol. 20, pp. 276 – 285, May 2005.

[5] A. C. Chow and D. J. Perreault, "Design and evaluation of a hybrid passive/active ripple filter with voltage injection," *IEEE Trans. Aerospace and Electronic Systems*, vol. 39, pp. 471 – 480, Apr. 2003.

[6] L. LaWhite and M. F. Schlecht, "Design of active ripple filters for power circuits operating in the 1-10 MHz range," *IEEE Trans. Power Electronics*, vol. 3, pp. 310 – 317, Jul. 1988.

[7] T. Farkas and M. F. Schlecht, "Viability of active EMI filters for utility applications," *IEEE Trans. Power Electronics*, vol. 9, pp. 328 – 337, May 1994.

[8] D. C. Hamill, "An efficient active ripple filter for use in DC-DC conversion," *IEEE Trans. Aerospace and Electronic Systems*, vol. 32, pp.1077 – 1084, Jul. 1996.

[9] S. A. P. Haddad *et al*, "Analog Complex Wavelet Filters," *IEEE International Symposium on Circuits and Systems* (ISCAS), Kobe, Japan, pp. 3287-3290, 23-26 May 2004.

[10] W.-X. Yang, J. B. Hull, and M. D. Seymour, "A contribution to the applicability of complex wavelet analysis of ultrasonic signals," *NDT and E International*, vol. 37, pp. 497 - 504, Mar. 2004.

[11] C.-L. Tu, W.-L. Hwang, and J. Ho, "Analysis of singularities from modulus maxima of complex wavelets," *IEEE Trans. Information Theory*, vol. 51, pp. 1049-1062, Mar. 2005.

Wenjie Chen was born in Xi'an, China, in 1974. She received the B.S. M.S. and Ph.D. degrees in electrical engineering from Xi'an Jiaotong University, Xi'an, China, in 1996, 2002, and 2006 respectively. She has been a member of the faculty of School of Electrical Engineering, Xi'an Jiaotong University since 2002, where she is currently a Lecturer. Her main research interests include soft-switching dc/dc converters and EMI filters, and power electronic integration.

Xu Yang was born in China in 1972. He received the B.S. and Ph.D. degrees in electrical engineering from Xi'an Jiaotong University, Xi'an, China, in 1994 and 1999, respectively. He has been a member of the faculty of School of Electrical Engineering, Xi'an Jiaotong University since 1999, where he is presently a Professor. His research interests include soft switching topologies, PWM control techniques and power electronic integration, and packaging technologies.

Zhaoan Wang was born in Xi'an, China, on June 9, 1945. He received the B.S. and M.S. degrees from Xi'an Jiaotong University, Xi'an, China, in 1970 and 1982, respectively, and the Ph.D. degree from Osaka University, Osaka, Japan, in 1989. Starting in 1982, he became a Lecturer at Xi'an Jiaotong University, where he is now a Professor. He is engaged in research on power conversion system, harmonics suppression, reactive power compensation and power electronic integration, and active power filters. He has published over 150 technical papers

and has led numerous government and industry-sponsored projects in the areas of power and industrial electronics.

Interpolation Algorithm for Fast Evaluation of EM Coupling between Wires

C. Marasini, E. S. A. M. Lepelaars, and P. A. M. Zwamborn

Radar and EW Group, TNO Defence Security and Safety,
P.O. Box 96864, 2509 JG The Hague, The Netherlands
cecilia.marasini@tno.nl, eugene.lepelaars@tno.nl, peter.zwamborn@tno.nl

Abstract – Efficient and accurate evaluation of the EM field radiated by a current flowing along a wire is essential to solve the electromagnetic coupling between arbitrary oriented wires. In this paper, a numerically efficient algorithm for the evaluation of coupling is presented. The currents along the wires are expressed in terms of local basis functions. The coupling between each two expansion functions of different wires, using an exact kernel and the Galerkin Method of Moments, requires an integration over the mantle of the radiating element and an integration over the mantle of the receiving element. The computational cost for this 2×2D integration is reduced by an interpolation technique. In order to reduce the number of evaluation points and to control accuracy, the interpolation technique is applied to a function that represents the difference between the electric field radiated by a wire element and the analytically known point dipole field. The proposed algorithm is implemented using already available standard routines.

Keywords: Exact and reduced kernel, electromagnetic scattering, Method of Moments, integral equation, fast algorithms, and antennas.

I. INTRODUCTION

Consider the analysis of the electromagnetic coupling between arbitrary oriented wires along which the currents are expanded by means of basis functions. Applying the Galerkin Method of Moments (MoM) [1], the computation of electromagnetic coupling between different wires is based on the evaluation of the electric field radiated by the current of a single wire expansion function over the surface of the observation element (e.g. a segment or two adjacent segments). This field induces a current on all other wires, appointing therefore the mutual interaction. Efficient and accurate field evaluation is therefore essential to solve electromagnetic coupling between wires especially when wires are close to each other.

Focusing on the analysis of scattering from an arbitrary oriented wire, an Electric Field Integral Equation (EFIE) known as Pocklington's equation is solved by applying the Galerkin MoM. The induced current and the scattered fields are interrelated by a so called "kernel". Choosing the observation point on the central axis of the wire results in the "reduced kernel" formulation, while choosing the observation point on the mantle surface results in the "exact kernel" [2, 3]. In particular the exact kernel formulation provides more accurate results than the reduced one for the analysis of thick wires ($ka \approx 0.1$, being a the wire radius) [4, 5]. As a consequence, in order to be consistent with the exact kernel formulation, the evaluation of coupling matrices requires the calculation of the field on the mantle of wires yielding the computation of 2D integrals.

Even though efficient techniques are employed for the computation of impedance matrix elements of a single wire [4, 5], a computational burden is present when coupling matrices have to be evaluated.

A similar computational bottleneck has been encountered in the analysis of electromagnetic scattering from 3D objects [6] where the time spent on calculation of matrix elements is much more than solving the system matrix. Furthermore when computing time-harmonic scattering from 1D/2D large PEC objects, the computational complexity is in the evaluation of fields produced by a given current distribution [7, 8]. In all these cases, tabulation and interpolation techniques have been investigated in order to accelerate the evaluation of the problem solution and to guarantee the required accuracy.

In a similar fashion this paper presents a novel, efficient and accurate scheme well suited to accelerate the computation of coupling matrix elements. The electric field radiated by a current flowing along a wire element can be adequately sampled on a non-uniform grid defined in a way that is consistent with the field behavior [9] and subsequently interpolated [10]. In order to further accelerate the generation of coupling matrix elements and to control the accuracy, an interpolation technique is applied to a smoothed function obtained by subtracting a properly chosen analytical term from the actual electric field contribution.

II. FORMULATION

In this section, our attention is firstly focused on the analysis of the current induced along a single wire by an impressed voltage and/or by an incident plane wave.

Secondly, an expression for the electric field radiated by such induced current distribution is derived.

A. Single Wire

In free space consider a single PEC wire antenna along the positive z axis fed by a voltage delta gap or/and illuminated by an incident field. A cylindrical coordinate system (ρ, φ, z) is introduced. The induced current along the mantle satisfies the frequency domain electric field integral equation (EFIE), well-known as Pocklington's equation [2],

$$\left(\partial_z^2 + k^2\right) \int_0^L K_E(z - z', \omega) I(z', \omega) dz' = -j\omega\epsilon \left(V(\omega)\delta(z - z_g) + E_z^i(z\mathbf{i}_z, \omega)\right) \quad (1)$$

where L is the wire length and $K_E(z - z', \omega)$ denotes the exact kernel [4, 5]. Equation (1) is discretized by applying the Galerkin Method of Moments [1]. Therefore, a set of N rooftop basis functions $\psi_n(z)$ is defined with a uniform mesh-size $\Delta = L/(N + 1)$ such that the current distribution is approximated as,

$$I(z) \approx \sum_{n=1}^{N} I_n \psi_n(z). \quad (2)$$

Next, by choosing the same type of rooftop functions $\psi_j(z),\ j = 1, \ldots, N$ as testing functions, an inner product is defined and applied on both sides of equation (1). Thus, equation (1) is discretized as,

$$\underline{\underline{\mathbf{Z}}}\ \underline{\mathbf{I}} = \underline{\mathbf{F}}_e \quad (3)$$

where $\underline{\underline{\mathbf{Z}}}$ denotes a $N \times N$ symmetric Toeplitz matrix, and the N-dimensional vectors $\underline{\mathbf{I}}$, $\underline{\mathbf{F}}_e$ represent the unknown current distribution vector and the weighted forcing excitation vector due to external sources, respectively.

The general expression of the electric field as a function of the magnetic vector potential is here recalled,

$$\mathbf{E} = \frac{1}{j\omega\epsilon} \left(k^2 \mathbf{A} + \nabla (\nabla \cdot \mathbf{A})\right) \quad (4)$$

$$\mathbf{A}(\mathbf{r}) = \mathbf{i}_z \int_{z'=0}^{L} \frac{I(z')}{2\pi a} \int_{\varphi'=0}^{2\pi} \frac{\exp(-jkR)}{4\pi R} a d\varphi' dz', \quad (5)$$

and then employed in order to find the electric field radiated by a straight wire. In equation (5), $R = |\mathbf{r} - \mathbf{r}'|$ denotes the distance between the source point $\mathbf{r}'$ on the wire mantle and the observation point $\mathbf{r}$ where the field is computed. In particular, since the current is expanded in terms of N rooftop basis functions $\psi_n(z)$, the radiated electric field can be expressed as a sum of N separate electric field contributions,

$$\mathbf{E}(\mathbf{r}) = \sum_{n=1}^{N} I_n \mathbf{E}_n(\mathbf{r}). \quad (6)$$

The elementary field $\mathbf{E}_n$ represents the field radiated by the current of the n-th basis function (i.e., two adjacent segments). This field is explicitly formulated as,

$$\mathbf{E}_n(\mathbf{r}) = \frac{1}{j\omega\epsilon} \frac{1}{8\pi^2} \int_{z'=(n-1)\Delta}^{(n+1)\Delta} \psi_n(z') \int_{\varphi'=0}^{2\pi} \frac{\exp(-jkR)}{R^3} \times \left\{ -\left[(jkR)^2 + jkR + 1\right] \mathbf{i}_z + \left[(jkR)^2 + 3jkR + 3\right] \frac{(\mathbf{r} - \mathbf{r}')}{R} \frac{(z - z')}{R} \right\} d\varphi' dz'. \quad (7)$$

Note the double integration that follows from considering the electric current flow on the surface of the wire.

B. Mutual Coupling

As a simplification, without loss of generality, the mutual coupling between two wires in the configuration depicted in Fig. 1 is here discussed.

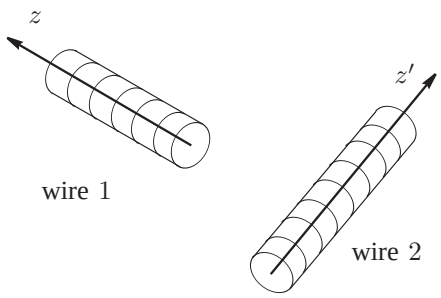

Fig. 1. Wires geometry.

Consider two perfectly conducting wires, wire 1 and wire 2, with their own local coordinate systems. External sources are present (i.e., voltage delta gap or/and incident field). The currents are approximated by means of N_1 and N_2 rooftop basis functions defined on $N_1 + 1$ and $N_2 + 1$ segments, respectively. It is noted that a wire element is formed by two adjacent wire segments which represent the support of an expansion function. Henceforth, the n-th basis function of wire 2 and the m-th testing function of wire 1 will be referred to as n-th source (or radiating) and m-th observation element. In this environment, an induced current of the n-th basis function ψ_n of wire 2, radiates an elementary electric field $\mathbf{E}_n(\mathbf{r})$ as in (7). This field impinges on wire 1 and induces a current along each of its segments. To describe the mutual coupling, the total incident field on the m-th observation element of wire 1 is written as the sum of two parts,

$$\mathbf{E}_m^{(1)}(\mathbf{r}) = \mathbf{E}_{ext}^{(1)}(\mathbf{r}) + \sum_{n=1}^{N_2} \mathbf{E}_n^{(1,2)}(\mathbf{r}). \quad (8)$$

The first term on the right-hand side of equation (8) denotes the field due to external sources. The summation represents the field induced on wire 1 by the current

flowing along all the source elements of wire 2. It is noted that wire 1 and wire 2 can be interchanged without losing validity of the approach.

By applying the Galerkin MoM procedure to this problem, the system matrix equation $\underline{\underline{\mathbf{Z}}}\underline{\mathbf{I}} = \underline{\mathbf{F}}_e$, is elegantly extended as follows

$$\begin{bmatrix} \underline{\underline{\mathbf{Z}}}^1 & -\underline{\underline{\mathbf{C}}}^{1,2} \\ -\underline{\underline{\mathbf{C}}}^{2,1} & \underline{\underline{\mathbf{Z}}}^2 \end{bmatrix} \begin{bmatrix} \underline{\mathbf{I}}^1 \\ \underline{\mathbf{I}}^2 \end{bmatrix} = \begin{bmatrix} \underline{\mathbf{F}}_e^1 \\ \underline{\mathbf{F}}_e^2 \end{bmatrix} \tag{9}$$

in which each forcing vector on the right-hand side represents the weighted field of external origin. The diagonal "self matrices" $\underline{\underline{\mathbf{Z}}}^1$, $\underline{\underline{\mathbf{Z}}}^2$, represent the interaction between elements of the same wire, while, the off-diagonal "coupling matrices" $\underline{\underline{\mathbf{C}}}^{1,2}$, $\underline{\underline{\mathbf{C}}}^{2,1}$, describe the interaction between elements of different wires.

In a similar fashion equation (9) can be expanded to a generic number of P arbitrary oriented wires by using,

$$\begin{bmatrix} \underline{\underline{\mathbf{Z}}}^1 & -\underline{\underline{\mathbf{C}}}^{1,2} & \dots & -\underline{\underline{\mathbf{C}}}^{1,P} \\ -\underline{\underline{\mathbf{C}}}^{2,1} & \underline{\underline{\mathbf{Z}}}^2 & \dots & -\underline{\underline{\mathbf{C}}}^{2,P} \\ \vdots & \vdots & \vdots & \vdots \\ -\underline{\underline{\mathbf{C}}}^{P,1} & -\underline{\underline{\mathbf{C}}}^{P,2} & \dots & -\underline{\underline{\mathbf{Z}}}^P \end{bmatrix} \begin{bmatrix} \underline{\mathbf{I}}^1 \\ \underline{\mathbf{I}}^2 \\ \vdots \\ \underline{\mathbf{I}}^P \end{bmatrix} = \begin{bmatrix} \underline{\mathbf{F}}_e^1 \\ \underline{\mathbf{F}}_e^2 \\ \vdots \\ \underline{\mathbf{F}}_e^P \end{bmatrix}. \tag{10}$$

III. EFFICIENT EVALUATION OF MATRIX ELEMENTS

Elements of self matrices and the known excitation vectors are efficiently evaluated as explained in [4]. Our attention is focused on the computation of coupling matrix elements. Each one of them involves the evaluation of two times a double integral. Consider the (m, n)-th element of matrix $\underline{\underline{\mathbf{C}}}^{1,2}$. It represents the mutual interaction between the field radiated by a current flowing along element n of wire 2 and the m-th element of wire 1. A first double integration has to be carried out to evaluate the field $\mathbf{E}_n^{(2)}$ radiated by a current distribution along the n-th source element of wire 2, (see equation (7)). An additional double integral has to be computed to determine the mutual interaction between this field and the induced current distribution along the m-th observation element of wire 1. This kind of straightforward calculation is a time-consuming process since many integrals are involved. To simplify the notation, the n-th radiating element is placed in the center of a cylindrical coordinate system (ρ', φ', z') as shown in Fig. 2.

Noting that the electric field $\mathbf{E}_n^{(2)}$ is rotationally symmetric, the observation region of the n-th source element can be defined in a plane (ρ', z') with $\rho' > 0$ by $\rho_{\min}$, $\rho_{\max}$, $z_{\min}$, $z_{\max}$, as depicted in Fig. 2. This region contains the projection of the mantle of the m-th observation element of wire 1.

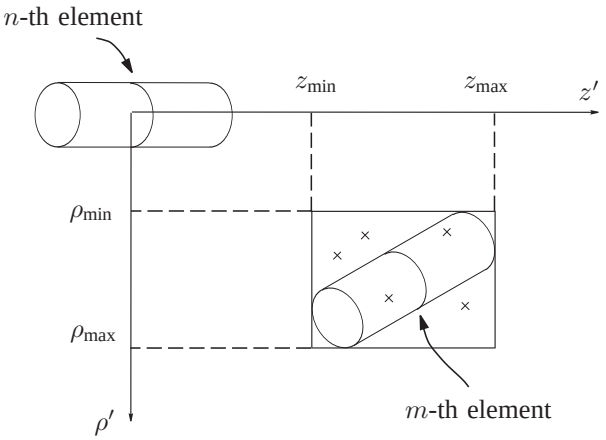

Fig. 2. Interpolation area defined to evaluate the electromagnetic interaction between two wire elements.

A. Interpolation technique

Instead of carrying out the straightforward double integration in equation (7), the field $\mathbf{E}_n^{(2)}$ is computed on a discrete grid of points within the observation region and is subsequently interpolated. For this purpose, we have investigated tabulation and interpolation techniques for the evaluation of the radiated electric field in order to accelerate the computation of coupling matrix elements, [6]. Even though uniform and random sampling algorithms have been explored, the most efficient technique in choosing points is by sampling the radiated electric field in a way that follows the behavior of the field. The proposed algorithm is developed based on the following three ideas:

1) An interpolation technique is applied to reduce the number of points where the radiated electric field is computed.
2) By making use of standard routines a set of points on a non-uniform grid is generated and an interpolation function is then defined. A numerical adaptive multidimensional integration routine [9] has been modified in order to generate a set of points used in a subsequent interpolation step where a piecewise polynomial surface is defined as interpolant function following the method proposed by Renka and Cline [10] (routines E01SAF, E01SBF). In this way, the integration routine will choose the distribution of points according to the behavior of the field $\mathbf{E}_n^{(2)}$ which is to be interpolated.
3) By subtracting the analytically known point dipole field from the elementary electric field $\mathbf{E}_n^{(2)}$ and by applying the interpolation technique to this difference, the efficiency of the method is improved for a fixed accuracy.

In order to accelerate the generation of coupling matrices, further efficiency is expected by observing that the function to be interpolated is relatively smooth. This term

should be quick to evaluate and resemble the (far) field of the n-th radiating element. A function difference $\mathbf{D}_n^{(2)}$ is defined as the difference of the field $\mathbf{E}_n^{(2)}$ and the electric field $\mathbf{E}^{(p)}$ radiated by a point dipole placed in the origin of the coordinate system. Function $\mathbf{E}^{(p)}$ behaves asymptotically (i.e., for $R \to \infty$) as $\mathbf{E}_n^{(2)}$ and is singular when the distance R vanishes,

$$\mathbf{E}^{(p)}(\mathbf{r}) = \frac{1}{j\omega\epsilon}\frac{\Delta_1}{4\pi}\frac{\exp(-jkR)}{R^3}\left\{-\left[(jkR)^2 + jkR + 1\right]\mathbf{i}_z + \left[(jkR)^2 + 3jkR + 3\right]\frac{\mathbf{r}z}{R^2}\right\}. \quad (11)$$

Thanks to these properties, the resulting function $\mathbf{D}_n^{(2)} = \mathbf{E}_n^{(2)} - \mathbf{E}^{(p)}$ has a behavior considerably smoother than $\mathbf{E}_n^{(2)}$ and is therefore interpolated in a numerically easier way with a higher accuracy. The flow chart in Fig. 3 shows the fundamental steps of the proposed algorithm. Our numerical scheme begins by setting a desired accuracy ε with which the elementary radiated electric field of equation (7) has to be evaluated. While the adaptive routine [9] integrates numerically the function difference $\mathbf{D}_n^{(2)}$, choosing points (ρ_i', z_i') in the observation region $[\rho_{\min},\ \rho_{\max}] \times [z_{\min},\ z_{\max}]$ following the behavior of this function, the implemented scheme gathers the first N_a points $\{(\rho_i', z_i')\}_{i=1}^{N_a}$. Next, on this non-uniform set of N_a points an interpolated function $\widetilde{\mathbf{D}}_n^{(2)}$ is defined by using a NAG routine [10]. To examine the obtained accuracy of $\widetilde{\mathbf{D}}_n^{(2)}$ compared to $\mathbf{D}_n^{(2)}$ and normalized to the incident field $\mathbf{E}_n^{(2)}$, a relative error $\widetilde{\varepsilon}$ has been defined as,

$$\widetilde{\varepsilon} = \frac{|\mathbf{D}_n^{(2)} - \widetilde{\mathbf{D}}_n^{(2)}|}{|\mathbf{E}_n^{(2)}|}. \quad (12)$$

The proposed algorithm calculates the error $\widetilde{\varepsilon}$ in N_e points and terminates if $\widetilde{\varepsilon} \le \varepsilon$. If the error condition is not met, extra N_a points are added via the integration routine to the previously defined set. An interpolant function is determined on this new grid of $N_a + N_a$ points and the error $\widetilde{\varepsilon}$ is subsequently calculated. Until the error condition is met, the algorithm keeps adding N_a points. Finally, the approximated value of the radiated field is computed as follows,

$$\widetilde{\mathbf{E}}_n^{(2)} = \widetilde{\mathbf{D}}_n^{(2)} + \mathbf{E}^{(p)}. \quad (13)$$

It is worth mentioning that the computational efficiency of the proposed algorithm is strictly related to the number N_a and on the termination condition (i.e., the choice of the N_e points). Based on our numerical experience, we suggest N_a to be in the order of ten and $1 \le N_e \le 4$. The N_e points are chosen in anticipation of the subsequent N_a points by the implemented algorithm.

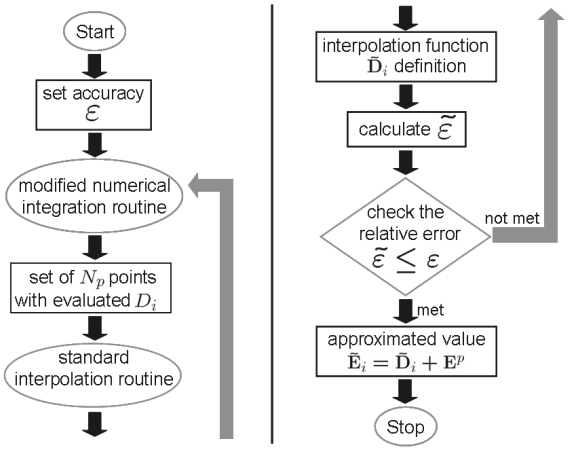

Fig. 3. Flow chart of the proposed numerical interpolation algorithm.

IV. NUMERICAL RESULTS

To validate the method, three representative examples containing mutually coupled wires are given. All simulations were performed on an Intel Xeon platform running at 2 GHz with 3 GB of RAM. First, the case of two parallel thin wires of length $L = \lambda/2$ and radius $a = \lambda/1000$, placed at a distance d, is considered. Both wires are subdivided in $N+1$ segments and N rooftop functions are defined. A desired accuracy of $\varepsilon = 10^{-3}$ is used. The computational time required for evaluating the system matrix $\underline{\underline{\mathbf{Z}}}$ by the straightforward double 2D integration and by the interpolation method is compared by varying the distance d and the number of expansion functions N. As can be observed in Table 1, the interpolation method greatly reduces the CPU time needed to calculate the impedance matrix even in case of a coarse discretization, (e.g. $N = 10$). When the two wires are close to each other (e.g. $d \le 0.1\lambda$) the computational time reduction can be appreciated only by refining the segmentation. As a matter of fact at small distances the function difference $\mathbf{D}_n$ may not be as smooth as when the distances are larger since the source field $\mathbf{E}_n$ differs from the point dipole field $\mathbf{E}^{(p)}$. Moreover, the maximum relative error ε_c on coupling elements is defined as,

$$\varepsilon_c = \max\left\{\frac{|C_{m,n} - \widetilde{C}_{m,n}|}{|C_{m,n}|}\right\}_{m,n=1}^{N} \quad (14)$$

and evaluated as the distance d and the number of expansion functions N vary (see Table 1). Coupling value $C_{m,n}$ represents the value computed with the integration method while $\widetilde{C}_{m,n}$ is computed with the proposed interpolation method.

The number of field evaluations using the straight forward 2D integration and using the interpolation method is also analyzed. Fig. 4 shows how the number of evaluations N_p required for the computation of

Table 1. Computational cost analysis and maximum relative error on coupling elements of two parallel thin wires $ka \approx 0.006$ by varying the distance d and the number of expansion functions N. Desired accuracy $\varepsilon = 10^{-3}$.

d [λ]	CPU Time ratio (2 × 2D Int) : (Interp)		
	$N = 68$	$N = 34$	$N = 10$
1	10.12 : 1	10.09 : 1	7.00 : 1
0.5	10.14 : 1	9.34 : 1	5.00 : 1
0.3	8.72 : 1	7.45 : 1	3.28 : 1
0.1	5.31 : 1	1.32 : 1	0.046 : 1

d [λ]	$\varepsilon_c = \max\left\{\frac{\lvert C_{m,n} - \widetilde{C}_{m,n}\rvert}{\lvert C_{m,n}\rvert}\right\}_{m,n=1}^{N}$		
	$N = 68$	$N = 34$	$N = 10$
1	$4.958 \cdot 10^{-13}$	$2.000 \cdot 10^{-11}$	$1.952 \cdot 10^{-9}$
0.5	$4.058 \cdot 10^{-12}$	$1.673 \cdot 10^{-10}$	$1.221 \cdot 10^{-8}$
0.3	$7.767 \cdot 10^{-11}$	$3.094 \cdot 10^{-9}$	$1.662 \cdot 10^{-6}$
0.1	$2.114 \cdot 10^{-6}$	$4.290 \cdot 10^{-5}$	$9.628 \cdot 10^{-5}$

coupling matrix $\underline{\underline{\mathbf{C}}}^{1,2}$ varies as a function of the desired accuracy ε for the configuration depicted above of two parallel thin wires at a distance $d/\lambda = 0.5$ and discretized with 35 segments. Fig. 4 shows that the total number of evaluations for the interpolation method is usually far less than for the integration, resulting in a considerable reduction of computation time. Fig. 4 also shows that increasing the accuracy in computing the electric field corresponds to an increase in the number of field evaluations N_p. This increment is much smaller when the double integration is carried out than when the interpolation is applied.

Second, we compare the computational time together with the relative error ε_c on coupling elements $C_{m,n}$ for the case of two parallel mutually coupled thick wires. In this case $L = \lambda/2$, the radius $a = \lambda/60$, and the wires are equally discretized with $N + 1$ segments. A desired accuracy of $\varepsilon = 10^{-3}$ is defined. Table 2 again shows how the proposed method enhances efficiency in the computation of coupling matrix elements even for thick wires.

Finally, two arbitrary oriented thin wires with $L_1 = \lambda/2$, $L_2 = 0.2236\lambda$ and radius $a_1 = a_2 = \lambda/1000$ are analyzed. The first wire has end points $\mathbf{r}_1 = (0.3, 0.3, 0.5)\lambda$ and $\mathbf{r}_2 = (0.3, 0.3, 1.0)\lambda$, while the second wire has end points $\mathbf{r}_3 = (0.3, 0.7, 0.5)\lambda$ and $\mathbf{r}_4 = (0.3, 0.8, 0.7)\lambda$. Again the CPU time comparison is carried out for different segmentations with a desired $\varepsilon = 10^{-3}$. Note that minimum and maximum distances between the two wires are $d_{\min} = 0.4\lambda$, $d_{\max} = 0.64\lambda$, respectively. Results for this case are shown in Table 3.

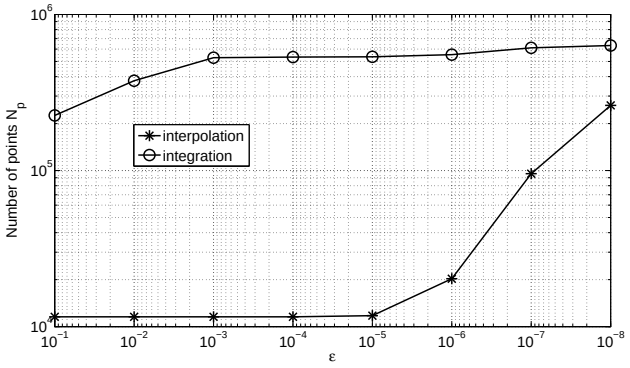

Fig. 4. Number of evaluations N_p versus the desired accuracy ε for two parallel thin wires of length $L = \lambda/2$ and radius $a = \lambda/1000$ placed at a distance $d/\lambda = 0.5$ and discretized with 35 segments.

Table 2. Computational cost analysis and maximum relative error on coupling elements of two parallel thick wires $ka \approx 0.105$ by varying the distance d and the number of expansion functions N. Desired accuracy $\varepsilon = 10^{-3}$.

d [λ]	CPU Time ratio (2 × 2D Int) : (Interp)	
	$N = 50$	$N = 20$
1	10.13 : 1	9.29 : 1
0.5	10.11 : 1	8.49 : 1
0.3	8.37 : 1	8.04 : 1
0.1	0.12 : 1	0.18 : 1

d [λ]	$\varepsilon_c = \max\left\{\frac{\lvert C_{m,n} - \widetilde{C}_{m,n}\rvert}{\lvert C_{m,n}\rvert}\right\}_{m,n=1}^{N}$	
	$N = 50$	$N = 20$
1	$2.726 \cdot 10^{-9}$	$1.086 \cdot 10^{-9}$
0.5	$1.141 \cdot 10^{-8}$	$1.383 \cdot 10^{-9}$
0.3	$1.043 \cdot 10^{-7}$	$1.920 \cdot 10^{-8}$
0.1	$2.396 \cdot 10^{-5}$	$5.201 \cdot 10^{-5}$

Table 3. Computational cost analysis of two arbitrarily oriented thin wires $ka \approx 0.006$, by varying the number of expansion functions N. Desired accuracy $\varepsilon = 10^{-3}$.

N	CPU Time ratio (2 × 2D Int) : (Interp)
68	10.83 : 1
34	10.83 : 1
10	7.07 : 1

V. CONCLUSION

A numerically efficient interpolation algorithm for the calculation of the coupling matrix elements has been

presented. Within a prescribed accuracy, coupling matrix elements can be computed more efficiently than by straightforward double integrations. This method is developed based on three main ideas elucidated in Sec. III-A.

Numerical examples show that the proposed algorithm results in a reduction of the CPU time of typically a factor 7. When the distance between the source and the observation element is small compared to the wavelength (e.g. $d \leq 0.1\lambda$) the smoothness of the function difference deteriorates and the advantages of the algorithm are lost. This is mainly due to the different behavior of the point dipole field and the field radiated by a source element in the near-field region. In this case the straightforward double integration may be more efficient than the interpolation technique.

When designing antennas to be installed on conducting surfaces, optimization routines can be used to properly select the best configuration. In this case, the proposed basic concept can be used to gain efficiency in the optimization process, drastically reducing the filling time of the wire-surface coupling matrices. Research towards the feasibility of this application is pursued.

REFERENCES

[1] R. F. Harrington, *Field Computation by Moment Methods*, IEEE Press, New York, 1993.

[2] A. G. Tijhuis, Z. Q. Peng, and A. Rubio Bretones, "Transient excitation of a straight thin–wire segment: a new look at an old problem," *IEEE Trans. on Antennas and Propag.*, vol. 40, no. 1, pp. 1132–1146, 1992.

[3] C. M. Butler and D. R. Wilton, "Analysis of various numerical techniques applied to thin wire scatterers," *IEEE Trans. on Antennas and Propag.*, vol. 23, no. 4, pp. 534–540, 1975.

[4] P. J. Davies, D. B. Duncan, and S. A. Funken, "Accurate and efficient algorithms for frequency domain scattering from a thin wire," *Journal of Computational Physics*, vol. 168, no. 1, pp. 155–183, 2001.

[5] C. Marasini, E. S. A. M. Lepelaars, and A. P. M. Zwamborn, "Analysis of the resonant behavior of a complex loaded wire by using the exact kernel MoM," *Proc. of 9th Int. Conf. on Electromagnetics in Advanced Applications - ICEAA 05, 12–16 Sept. 2005*, Torino, Italy, 2005.

[6] L. Xu, et al., "Spatial interpolation method for solution of electromagnetic scattering from objects located in half–space," *Proc. of 4th Int. Conf. on Microwave and Millimeter Wave Technology - ICMMT 2004, 18–21 Aug. 2004*, Beijing, China, 2004.

[7] A. Boag, E. Michielssen, and A. Brandt, "Nonuniform polar grid algorithm for fast field evaluation," *IEEE Antennas and Wireless Propag. Let.*, vol. 1, no. 1, pp. 142–145, 2002.

[8] H. G. Espinosa, et al., "Multilevel field interpolation algorithm for large PEC objects," *Proc. of European Conf. on Antenna and Propagation - EuCAP 2006, 6–10 Nov. 2006*, Nice, France, 2006.

[9] J. Berntsen, T. O. Espelid, and A. Genz, "An adaptative multidimensional integration routine for a vector of integrals," *ACM Trans. Math. Software*, vol. 17, pp. 452–456, 1991.

[10] *NAG Fortran Library Manual Set*, Numerical Algorithms Group Ltd., Oxford.

Cecilia Marasini received the M.Sc. degree in telecommunication engineering from the University of Pisa, Pisa, Italy, in 2001 and the Ph.D. in electrical engineering degree from the Eindhoven University of Technology, Eindhoven, The Netherlands, in 2008. During her M.Sc. work she spent six months with the Electromagnetic Department of Chalmers University of Technology in Göteborg, Sweden, where she performed part of her final project developing a SW implementation of the CG-FFT numerical method for calculating the electromagnetic properties of conducting elements placed on, or embedded in, a multilayer planar structure. After receiving her M.Sc. degree, from 2001 to 2003, she was a System/Software Engineer in the Motorola Technology Centre in Torino, Italy, where she was involved in the integration of dual-mode UMTS/GSM terminals in mobile service networks working on interoperability testing process. Since March 2008, she is a researcher with TNO Defence, Security and Safety in The Hague. Her research interests include efficient numerical modeling techniques for the design of antennas for naval applications, antenna theory and modeling of radar clutter.

Eugene S.A.M Lepeaars is a mathematician who specialized in electromagnetics. After receiving his Ph.D. degree in 1997 he has been a postdoc for ten months with the University of Delaware. Since 1998 he is a researcher with TNO Defence, Security and Safety in The Hague. In the period 1998 - 2002, he has been a University teacher in electromagnetics at the Eindhoven University of Technology. His research activities consist of mathematical modelling and computational electromagnetics, mainly for the Ministry of Defence. Although most of his work is related to underwater electromagnetic signatures of ships, among other topics, he has also been involved with Integrated Topside Design, radome modelling, antenna theory, eddy current modelling, transmission line theory, High Power Microwaves and radar performance.

A.P.M. Zwamborn was born in Schiedam on October 13th, 1963 and received the Ph.D degree in electrical engineering “Cum laude” from Delft University of Technology in 1991. He served his military duties as an officer in the Royal Netherlands Navy and worked on the development of Advanced Phase Array Radars. In 1993, he started to work as a scientist within the Netherlands Organization for Applied Scientific research (TNO) in the field of electromagnetic effects. In 1997, he was appointed part-time professor at Eindhoven University of Technology within the field of Electromagnetic Field Theory and its Applications. The same year, he was appointed head of the Electronic Warfare and Electromagnetic Effects research group at TNO. Since 2000, he has been a senior member of the scientific staff within the Electronic Warfare research group. Dr. Zwamborn has several committee responsibilities. From 1995 he is a member of the Health Council of the Netherlands and a full member of the Dutch National Committee of the URSI. He is the Dutch chairman of URSI Commission K. He received the Young scientist award in 1993 and since 2004, he is an EMP Fellow of the SUMMA foundation. His research interests are the development of efficient electromagnetic field design tools, electromagnetic aspects (EMC/EMI) of integrated top-side design of complex platforms and the development of detection, classification and neutralization systems for defense purposes.

Numerical Electromagnetic Analysis of GSM Tower under the Influence of Lightning Over-voltage

M. O. Goni and M. S. I. Hossaini

Faculty of Engineering, Khulna University of Engineering & Technology, Bangladesh
osman@ieee.org, saif_hossaini@yahoo.com

Abstract – In the last twenty years, the widespread use of sensitive electronic devices in telecommunication systems and power systems has increased the interest in transients, in particular those caused by lightning (direct and/or indirect) strokes. Lightning over-voltage causing unpredictable and accidental interruption in these systems is a very important factor also in telecommunication systems and transmission lines. So the electromagnetic interference (EMI) analysis of different communication towers under the influence of lightning over-voltage on tall structures is necessary to avoid these unexpected interruptions. This paper presents a numerical electromagnetic simulation of direct lightning stroke for the EMI analysis of a GSM tower utilizing Method of Moments. This analysis is also a primary factor and can give approximate solution, helpful for correct EMC design of transient protection circuits for GSM base-station.

I. INTRODUCTION

The prediction of lightning-induced over-voltage on tall structures like communication towers is important, which is motivated by the widespread use of sensitive electronic devices in telecommunication systems and data transmission networks. From this point of view, transients caused by lightning (direct and/or indirect) can be one of the major causes of malfunction, or even destruction, of electronic equipment of the installations. In particular, Lightning over-voltages which can cause disruption in the telecommunication or data-transmission networks, or sudden micro-interruptions of the power supply during thunderstorms have been seriously reconsidered, due to the increasing demand for good quality and reliability in the transmission of information.

There is no clear evidence in the literature of the relationship between the number of outages during thunderstorms and lightning-flash density in the proximity of the place of failure. However a report shows that more than 27% failure of electronic components is caused by over-voltages caused by lightning transients.

The idea of numerical solution of lightning transients is not new and is more cost effective method of lightning transient analysis than the direct experimental method.

One of the earliest applications of a numerical electromagnetic (EM) analysis to lightning study [1] modeled a lightning channel attached to a tall structure. A time-domain code was used in that study. A similar time-domain code was also used in a study on induced voltages on a distribution line [2] over perfectly conducting ground. A recent study also employs a similar time-domain code [3, 4] to model a lightning channel [5].

However, more authors have applied the Numerical Electromagnetic Code (NEC-2) [6], a frequency-domain code, to lightning electromagnetic pulse (LEMP) studies or lightning-surge analysis [7-14]. Heidler *et al.* [7] used NEC-2 to analyze induced voltages on conductor loops illuminated by LEMP.

Cristina *et al.* [8] employed it to evaluate the EM field inside a building struck by lightning. Chai *et al.* [9] employed this code to study field inside a wire-array lightning protection system for a launch vehicle when it is struck by lightning. The code also has been applied to analyze transient voltages across an insulator of a power transmission tower struck by a direct lightning [9, 10].

Moini *et al*. [10] and Kordi *et al.* [11] applied the time-domain approach utilizing the Thin-Wire Time-Domain code (TWTD) [12], and Baba and Ishii [14, 15] applied the frequency-domain approach utilizing NEC-2 [13-18].

For practical purposes, one of the classes of models applied recently in lightning studies is the so-called electromagnetic models [17]. They are usually based on thin-wire antenna approximation and involve a numerical solution of Maxwell's equations using the method of moments (MoM) [18] to find the current distribution along the lightning channel, from which electromagnetic fields can be computed. This paper presents transient analysis of GSM tower using frequency domain approach, Wire-MoM which is based on thin-wire approximation.

II. METHODOLOGY

A. *Lightning Channel-Base Current Model*

The test waveshapes adopted by various standards for simulating the effects of lightning in the laboratory are 1.2/50μs, 8/20μs, and 10/350μs (in τ_1/τ form; where τ_1 = front time constant, τ = tail time constant) wave shapes.

The time function of lightning current used for numerical analysis purposes also known as the Heidler's model of current source, can be described with the following expression and the waveform is shown in Fig. 1 [19].

$$i(t) = \frac{I_0}{\eta} \cdot \frac{(t/\tau_1)^n}{1 + (t/\tau_1)^n} \cdot e^{-\frac{t}{\tau}} \quad (1)$$

where: I_0 - The peak value of the lightning current

η - The correction factor for the peak value of lightning current peak

n - The factor influencing the rate of rise of the function

τ_1 - Duration of the lightning surge front.

τ - The strike duration; interval between t = 0 and the point on the tail where the function amplitude has fallen to 50 % of its peak value

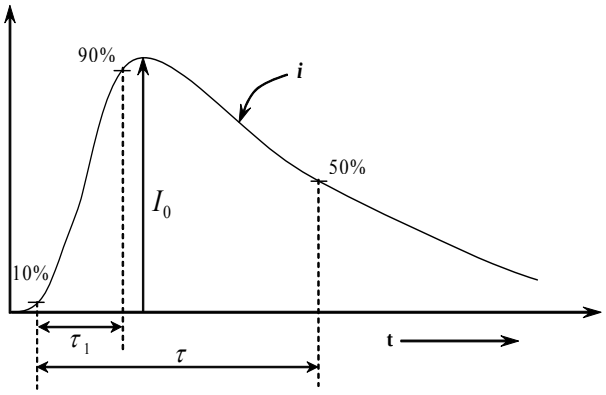

Fig. 1. Waveform of Heidler's model of current source.

B. Numerical Method

In this paper, *Field Theory Approach* [20-23] is adapted for the evaluation of the effects of the lightning over-voltage as this method is more accurate and easier to apply to complex structures consisted of many differently interconnected or oriented conductors. For numerical solution computer program "Wire-MoM" is used which is based on Method of Moments (MoM). Here the computed results are obtained in frequency domain for a current input.

C. FFT and IFFT for Domain Conversion

The method presented in this paper adopts a frequency-domain approach, MoM along with an appropriate Fast Fourier Transform (FFT) algorithm for spectral representation of the lightning channel-base current. By applying an inverse-FFT (IFFT) technique to the derived frequency spectra of required quantities, the time domain result is finally obtained. The FFT and IFFT operations are carried out in MATLAB.

The frequency domain computed result (current or field) for any geometric input data is then multiplied with the Fourier Transform of the input waveform and finally transformed into time domain using IFFT.

The complete flow chart for the time domain analysis of the lightning transients using FFT, IFFT and MoM is shown in Fig. 2.

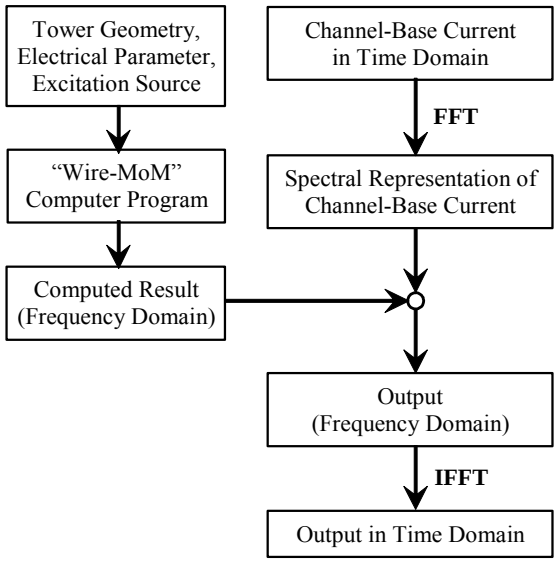

Fig. 2. Time domain transient analysis using Wire-MoM.

D. Modeling Considerations

The lightning channel was represented by a single vertical conductor of 30 m length above the tall tower structure. Lightning channel-base current model used for the simulations throughout this paper is based on the Heidler's model of current source of 10/350 μs wave shape and I_0 = 30 kA, $\eta = \exp(-\tau_1/\tau)$, n = 10, τ = 350 μs, τ_1 = 10 μs unless stated otherwise. For the thin-wire antenna approximation of the tower structure, the tower can be modeled as a complex structure represented by a group of conductors. The segment length is limited by the highest frequency of interest for the frequency domain computation. For numerical computation of the thin-wire approximation of the tower structure, the segment length (ΔL) of the wire must be less than 1/10 of the wavelength of the highest frequency of interest [23-26]. That is,

$$1/1000\,\lambda_{max} \le (\Delta L) \le 1/10\,\lambda_{max}. \quad (2)$$

To obtain consistent result from the MoM, the radius of the wire should be much less than the segment length (ΔL). Through the analysis performed in this paper, the

relation between segment length and radius (a) are kept as follows [24-26].

$$\frac{(\Delta L)}{a} > 120 \cdot \tag{3}$$

For tower modeling lumped impedance elements were used. Various values of footing resistance such as 40 Ω [7] or higher have been postulated in analyzing lightning current waveforms observed on tall structures. Tower footing resistance of 30 Ω was considered for the simulations carried out. All the simulations were carried out with PEC (Perfect Electric Conductor) ground plane.

III. EMI ANALYSIS OF GSM TOWER

To perform the numerical electromagnetic analysis of a GSM tower struck by a direct lightning stroke, the following simulations are performed by the authors using Wire-MoM. The frequency domain to time domain computation using FFT and IFFT was carried out in MATLAB as mentioned in Fig. 2.

The GSM tower under analysis is considered 42 m high, four legged "Green Field Tower". The lightning channel was represented by cylindrical elements of segment lengths of approximately 2 m and radius of 1.5 cm and the tower was modeled by cylindrical elements of approximately 2 m segment length and radius of 1 cm. Both the lightning channel and the elevated structure (tower) are considered to be lossless uniform transmission line model having propagation velocity is equal to the velocity of light.

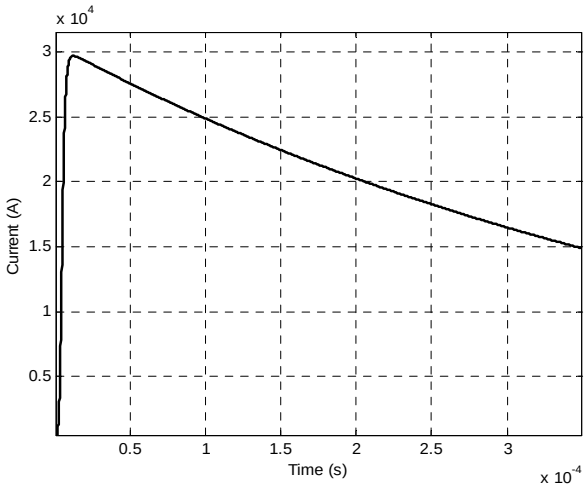

Fig. 3. Waveshape of Heidler's model of current source.

The lightning channel-base current (Heidler's model) used for all the simulations is shown in Fig. 3. Here the front time constant (the time required to increase from 10% to 90% of the peak) is 10 μs; and the tail time constant (time interval between t = 0 to point of 50% peak fall) is 350 μs. The time derivative of the channel-base current is shown in Fig. 4. The peak rate of change is 7.63e10 A/s.

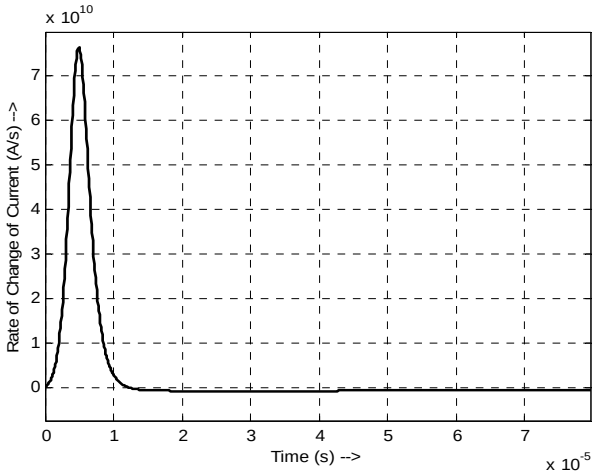

Fig. 4. Rate of change of channel-base current.

A. *Current and Surge Response Computation*

The model for simulating the current and surge response measurement (by direct method) of the GSM tower is shown in Fig. 5. The current distributions for the complex tower at different heights (for the Leg-A) obtained from the numerical simulations are plotted in Fig. 6 within a 30 microsecond.

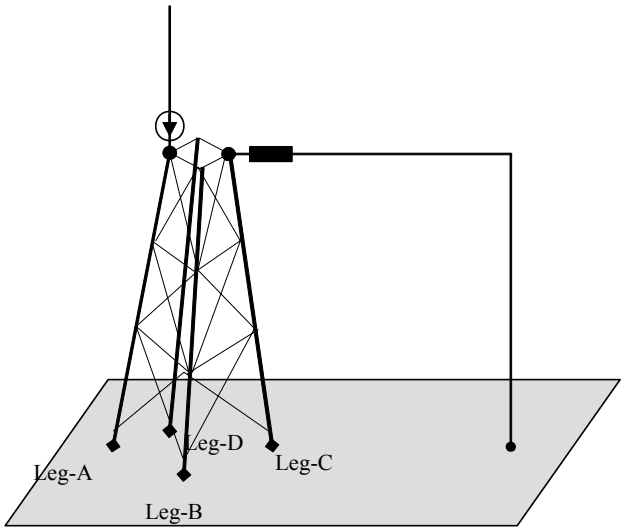

Fig. 5. Computation of current and surge response of 42m high GSM tower.

Fig. 6 shows that the peak current at the top is about 4.7 kA and at the foot of the tower is about 5.5 kA for 30 kA peak channel-base current. These results also agree with the computational results of Rachidi *et al.* [27-29].

In Fig. 7 (magnified plot of Fig. 6), the reflections from the ground are observed in the current waveforms of

the GSM tower within 2.5 microsecond window. The reflection time is approximately 0.27 microseconds at the top and 0.22 microseconds at the ½ of the height.

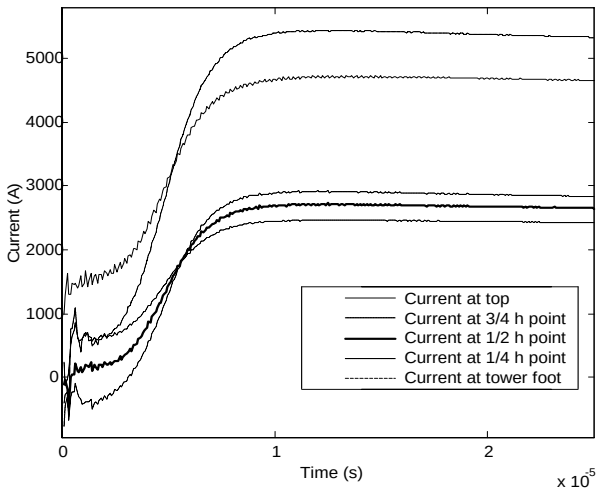

Fig. 6. Current at the leg A of the GSM tower at different heights.

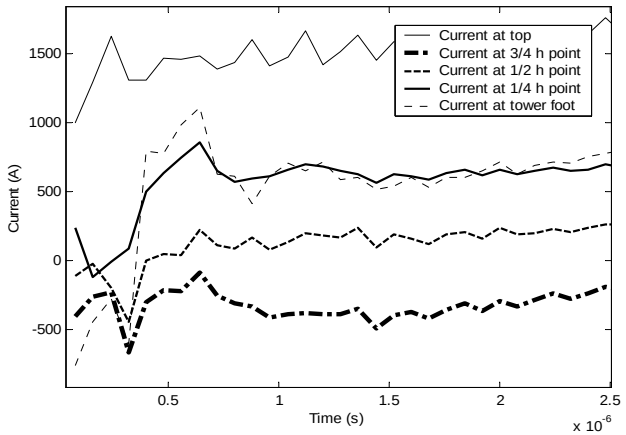

Fig. 7. Reflections of current from the ground and the different parts of the GSM tower.

The surge response of the complex tower was also computed by simulating the surge response measurement by direct method. In this method an auxiliary voltage measuring wire is connected at the top and is extended horizontally over the ground and finally terminated to the ground [9], [10], [14]. The response of the voltage at the top is plotted in Fig. 8. It has an initial transient peak value of 1.4 MV at the top of the tower for the peak channel-base peak current of 30 kA and footing resistance 30 Ω for each of the foot. Then for the positive value of the rate of change of current the voltage is approximately 300 kV and crosses the zero line at 5μs. The voltage is negative for the negative rate of change of channel-base current.

As it can be seen from Fig. 8, the surge response is characterized by a faster rise time and a shorter duration with respect to the channel-base current. And as the peak value of the voltage is up to few hundreds of kV (300kV), therefore can cause flashover [30]. There are lots of fluctuations in the response, which may be caused by the mismatch of the tower and the ground resistivity and the reflections from the different interconnected arms of the tower.

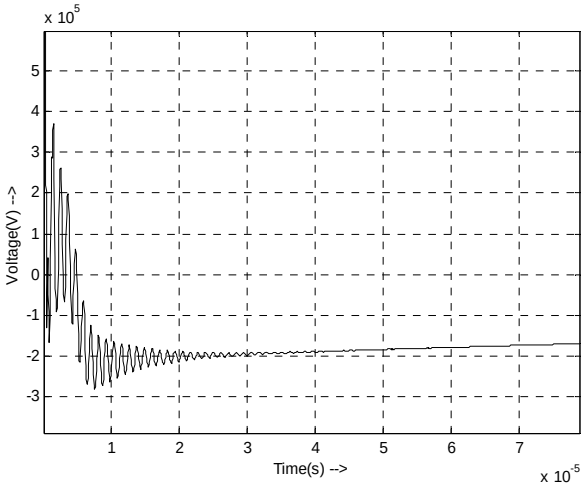

Fig. 8. Voltage at the top of the GSM tower computed by simulating the direct method.

B. Induced Current and Voltage on a Mounted Dipole

In this simulation, the induced current and voltage on a dipole antenna mounted vertically and horizontally was computed. The model simulating the induced current distribution and voltage on a mounted dipole antenna is shown in Fig. 9.

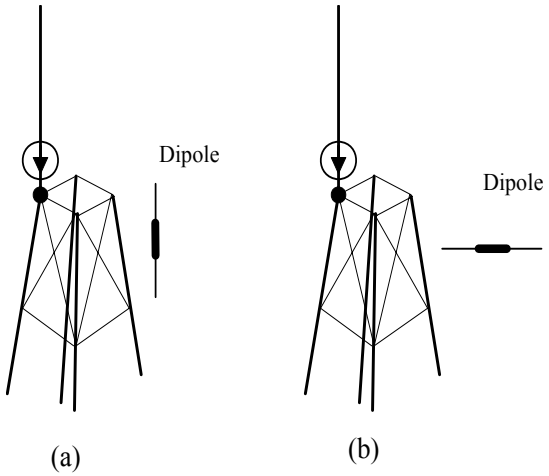

Fig. 9. Induced current and voltage computation for (a) Vertically mounted, and (b) Horizontally mounted dipole.

The current distribution and the induced voltage at the feed point of the dipole was computed both for horizontal and vertical mounting. The characteristic impedance of the dipole was 50 Ω, length of the dipole is 0.75 m, and radius of the wire is 1mm.

The induced current on the dipole in time domain are shown in Fig. 10. From the induced current waveforms, we see that larger amount of current and voltages are induced while the dipole is mounted vertically rather than horizontally. The induced peak current and voltage for vertical mounting is several amperes (3.75A) and several hundred volts (188 V). For horizontally mounted dipole, the peak current induced is several mA (30 mA) and the induced peak voltage is of several volts (1.52V). And the induced voltage is characterized by a faster rise time and a shorter duration with respect to the channel-base current.

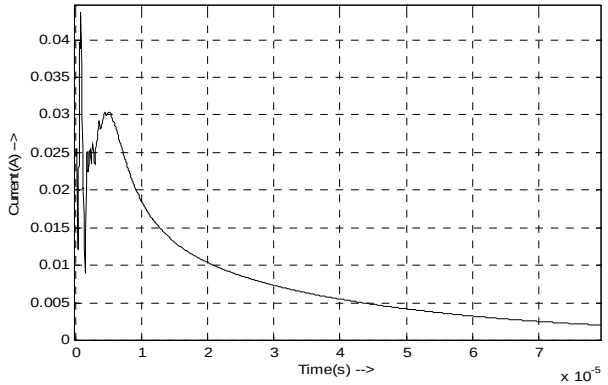

(a)

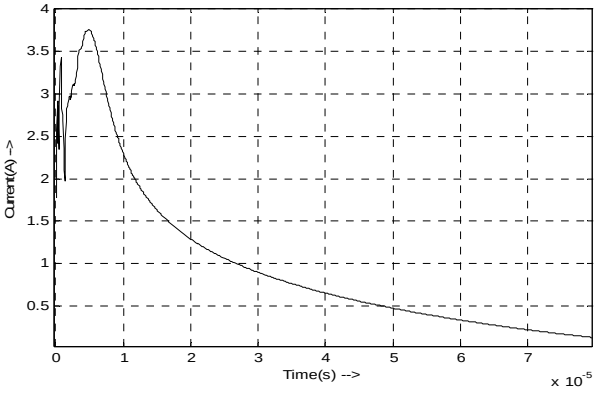

(b)

Fig. 10. Induced current on the dipole antenna: (a) Horizontally mounted, and (b) Vertically mounted.

C. Field Computation at Different Points

The model simulating the field computed at different distances from the tower is shown in Fig. 11.

For the model shown in Fig. 11, *x*, *y* and *z* components of the electric and magnetic field intensities of the electromagnetic pulses radiated by the tower undergoing direct lightning strike was computed in time domain up to 500 m from the tower foot. Near field points were y = 5m; z = 40 m; x = 10 m, 30 m, 50 m … 470 m, 490 m.

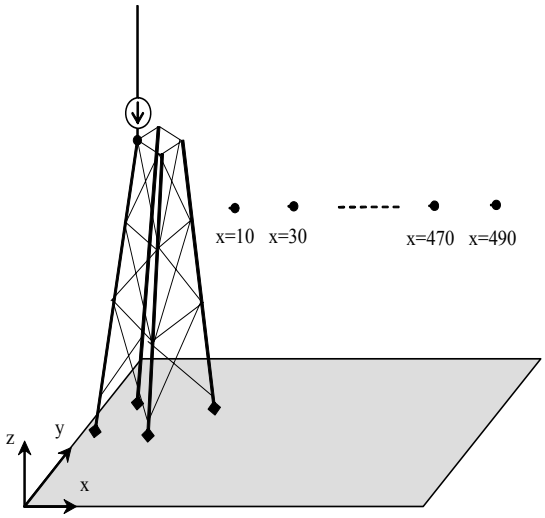

Fig. 11. Near field points for field computation.

From the simulation results it is obtained that the vertical component of the electric field, Ez and the horizontal component of the magnetic field, Hy are the most dominating. The time dependent characteristics of the Ez and Hy are plotted in Figs. 12 and 13. From the figures it can be seen that for the vertical electric field, there is a slower initial peak and a faster decay. But for the magnetic field, the initial peak is sharper and the decay is slower than that of the electric field. Similar results have been presented by Diendorfer who extended the Diendorfer and Uman (DU) model [31] to take into account the presence of an elevated strike object, and while the strike objects considered in his study were not taller than 20 m, and further investigated by Baba *et al*. (Figs. 3 (a) and 4 (a) of [32]).

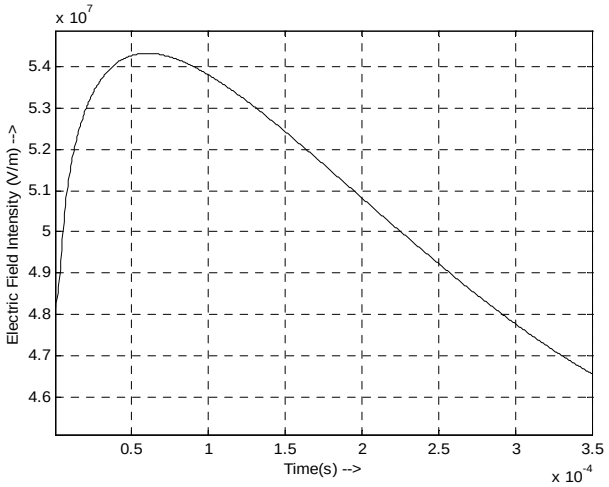

Fig. 12. E_z at the point (10 m, 5 m, 40 m) near the GSM tower.

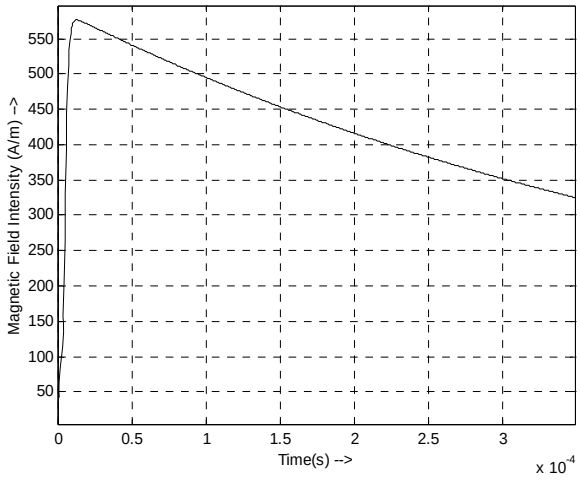

Fig. 13. Hy at the point (10 m, 5 m, 40 m) near the GSM tower.

The peak values of the electric and the magnetic field intensities from the simulation are provided in tabular forms in tables 1 and 2, respectively at different near field points.

Table 1. Peak electric field intensities at different near field points.

x (m)	E_x (V/m)	E_y (V/m)	E_z (V/m)	E_{total} (V/m)
10	3.4881e7	1.0987e7	5.4321e7	3.4881e11
70	1.7432e6	7.3191e4	1.3883e6	2.033e7
130	3.4437e6	7.2219e3	3.9457e5	4.782e5
190	1.0059e5	1.4247e3	1.6252e5	1.7416e5
250	3.8013e4	415.9924	8.0323e4	8.0828e4
310	1.7149e4	157.7499	4.5004e4	4.424e4
370	8.7793e3	72.3284	2.763e4	2.674e4
430	4.9357e3	38.3323	1.8175e4	1.74e4
490	2.9814e3	22.736	1.2614e4	1.2085e4

Table 2. Peak magnetic field intensities at different near field points.

x (m)	H_x (A/m)	H_y(A/m)	H_z (A/m)	H_{total} (A/m)
10	72.6485	579.778	94.6636	591.9303
70	0.2646	40.0539	1.3174	40.0764
130	0.1252	19.1144	0.3572	19.1181
190	0.0609	11.649	0.1591	11.6502
250	0.0343	8.0713	0.0893	8.0719
310	0.0216	6.0606	0.0571	6.0609
370	0.0147	4.8028	0.0397	4.8030
430	0.0106	3.9538	0.0292	3.9539
490	8.0324e-3	3.3476	0.0224	3.3477

The peak values of field intensities as a function of distance from the tower are shown in Fig. 14. They demonstrated that the peak electric and magnetic field intensity decreases exponentially with the increase in distance from the lightning channel regardless of ground conductivities [33].

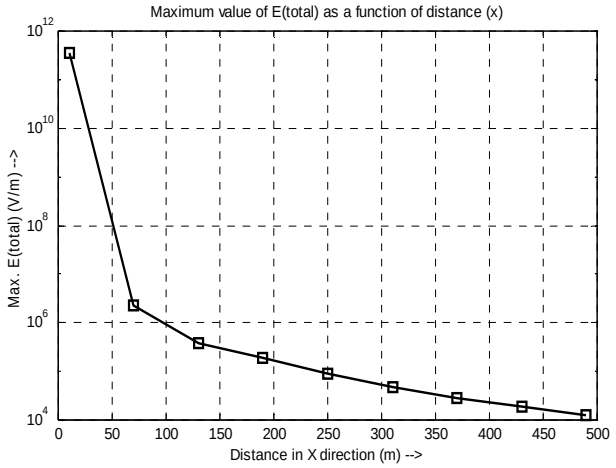

(a)

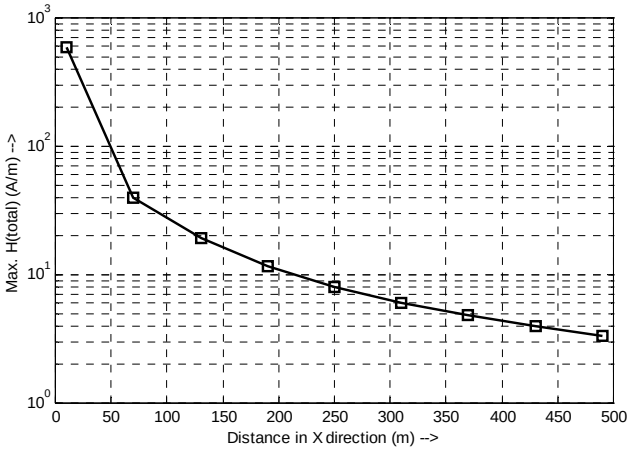

(b)

Fig. 14. Peak value of (a) $E_{(total)}$ (V/m) (b) $H_{(total)}$ (A/m) at different near field points along x-axis.

CONCLUSION

The experimental evaluation for the lightning transient study is much expensive than the numerical solutions. The authors of this paper carried out the numerical electromagnetic analysis of a GSM tower undergoing a direct lightning strike for the lightning transient study. As the MoM automatically computes the electromagnetic coupling between the conductors so no coupling model was required and the solution by MoM is

more accurate than the time domain electromagnetic transient program (EMTP) solution [16], [17], [26].

The analysis shows that the amount of current and voltage induced on the dipole elements are also of large magnitude enough for the degradation and disruption of the transmission information. The result and analysis also provides that a large amount of current and voltage (few hundreds of kV) is generated by the lightning over-voltage which can cause flash over and implies the installation of surge arrester or lightning current arrester for the protection of the base station.

The results of current and its associated fields at near to the lightning source are observed to be agreed well with other numerical results. In this analysis the ground plane was considered to be perfectly conductive; so, the effect of finite ground conductivity is out of the scope of this analysis.

ACKNOWLEDGMENT

The authors wish to thank the Committee for Advanced Studies and Research (CASR) of Khulna University of Engineering and Technology (KUET) for providing financial and logistic support in this research work.

REFERENCES

[1] S. Podgorski and J. A. Landt, "Three dimensional time domain modeling of lightning," *IEEE Trans. Power Delivery*, vol. 2, pp. 931–938, July 1987.

[2] R. Moini, B. Kordi, and M. Abedi, "Evaluation of LEMP effects on complex wire structures located above a perfectly conducting ground using electric field integral equation in time domain," *IEEE Trans. Electromagn.Compat.*, vol. 40, pp. 154-162, May 1998.

[3] E. K. Miller, A. J. Poggio, and G. J. Burke, "An integro-differential technique for time-domain analysis of thin wire structures," *J. Comput. Phys.*, vol. 12, pp. 24-48, 1973.

[4] R. Moini, B. Kordi, and M. Abedi, "Evaluation of LEMP effects on complex wire structures located above a perfectly conducting ground using electric field integral equation in time domain," *IEEE Trans. Electromagn. Compat.*, vol. 40, pp. 154-162, May 1998.

[5] R. Moini, B. Kordi, G. Z. Rafi, and V. A. Rakov, "A new lightning return stroke model based on antenna theory," *J. Geophys. Res.*, vol. 105, no. D24, pp. 29 693–29 702, 2000.

[6] G. J. Burke and A. J. Poggio, "Numerical electromagnetic code (NEC) - method of moments," in *Technical Document 116*. San Diego: Naval Ocean Systems Center, 1980.

[7] F. Heidler and K. Muller, "LEMP calculations with the traveling current source model," in *Proc. Int. Conf. Lightning Static Electricity*, Bath, U. K. , Sept. 1989.

[8] S. Cristina and A. Orlandi, "Lightning channel's influence on currents and electromagnetic fields in a building struck by lightning," in *Proc. IEEE Int. Symp. Electromagn. Compat.*, Washington, D.C., pp. 338–342, Aug. 1990.

[9] J. C. Chai, H. A. Heritage, and R. Briet, "Electromagnetic effects of the four-tour supported catenary wires array lightning protection system," in *Proc. 16th Int. Aerospace Ground Conf. Lightning Static Electricity*, Mannheim, CA, pp. 377–386, May 1994.

[10] R. Moini, B. Kordi, G. Z. Rafi, and V. A. Rakov, "A new lightning return stroke model based on antenna theory," *J.Geophys. Res.*, vol. 105, no. 29, pp. 693-29, 702, 2000.

[11] B. Kordi, R. Moini, and V. A. Rakov, "Comment on 'Return stroke transmission line model for stroke speed near and equal that of light' by R. Thottappillil, J. Schoene, and M. A. Uman," *Geophys. Res. Lett.*, 29, 10, art. no. 1369, 10.1029/2001GL014602, 2002.

[12] M. Van Blaricum and E. K. Miller, "TWTD–A computer program for time-domain analysis for thin-wire structures," *Lawrence Livermore National Laboratory, Rept.* UCRL-51277, 1972.

[13] M. Ishii and Y. Baba, "Numerical electromagnetic field analysis of tower surge response," *IEEE Trans. Power Delivery*, vol. 12, pp. 483–488, Jan. 1997.

[14] Y. Baba and M. Ishii, "Numerical electromagnetic field analysis on lightning surge response of tower with shield wire," *IEEE Trans. Power Delivery*, vol. 15, pp. 1010–1016, Apr. 2000.

[15] Y. Baba, M. Ishii, and R. K. Pokharel, "Numerical electromagnetic analysis of lightning induced voltages associated with lightning attached to tall structure," in *Proc. 26th Int. Conf. Lightning Protection*, Cracow, Poland, pp. 149–154, Sep. 2002.

[16] Y. Baba and M. Ishii, "Numerical electromagnetic field analysis of lightning current in tall structures," *IEEE Trans. Power Del*., vol. 16, pp. 324 -328, April 2001.

[17] Y. Baba and M. Ishii, "Characteristics of electromagnetic return-stroke models," *IEEE Trans. EMC*, vol. 45, no. 1, pp. 129-135, Feb. 2003.

[18] G. J. Burke and A. J. Poggio, "Numerical electromagnetic code (NEC) - Method of moments," *Naval Ocean Systems Center, San Diego, CA, Tech. Doc.* 116, 1980.

[19] V. A. Rakov and M. A. Uman, "Review and evaluation of lightning return stroke models including some aspects of their application," *IEEE*

Trans. Electromagn. Compat., vol. 40, pp. 403-426, Nov. 1998.

[20] R. F. Harrington, "Field computation by Moment Methods," *New York: IEEE & Wiley*, 1993.

[21] V. A. Rakov and M. A. Uman, "Lightning Physics and effects," *Dept. of Electrical & Computer Engineering, University of Florida.*

[22] Mini NEC, *software available through Artech House Publishers, 685 Canton Street, Norwood, MA 02062*.

[23] E. H. Newman and D. M. Pozar, "Electromagnetic Modeling of Composite Wire and Surface Geometries," *IEEE Trans. Antennas Prop.*, vol. AP-26, pp. 784-789, Nov. 1978.

[24] D. R. Wilton and S. U. Hwu, "Junction Code User's Manual," *Naval Ocean Systems Center, San Diego, CA, NOSC Tech. Document 1324*, Aug. 1988.

[25] Thin Wire Time Domain Code (TWTD), contact G. J. Burke, Lawrence Livermore National Laboratories, Livermore, CA.

[26] Wire-MoM, *method of moments program for wire structures, Jan Carlsson, SP.*

[27] F. Rachidi, W. Janischewskyj, A. M. Hussein, C. A. Nucci, S. Guerrieri, B. Kordi, and J. S. Chang, "Current and EM field associated with lightning-return strokes to tall towers," *IEEE Trans. Electromagn. Compat*., vol. 43, no. 3, pp. 356-367, Aug. 2003.

[28] T. Yamada, A. Mochizuki, J. Sawada, T. Kawamura, A. Ametani, M. Ishii, and S. Kato, "Experimental evaluation of a UHV tower model for lightning surge analysis," *IEEE Trans. Power Del.*, vol. 10, no. 1, pp. 393–402, Jan. 1995.

[29] J. A. Gutie´rrez, R. P. Moreno, J. L. Naredo, J. L. Berm´udez, M. Paolone, C. A. Nucci, and F. Rachidi, "Nonuniform transmission tower model for lightning transient studies," *IEEE Trans. Power Del.*, vol. 19, no. 2, pp. 490–496, Apr. 2004.

[30] A. Ametani, Y. Kasai, J. Sawada, A. Mochizuki, and T. Yamada, "Frequency-dependent impedance of vertical conductors and a multiconductor tower model," *Proc. IEE Gener. Transm. Distr.*, vol. 141, pp. 339– 345, Jul. 1994.

[31] G. Diendorfer and M. A. Uman, "An improved return stroke model with specified channel-base current," *J. Geophys. Res.*, vol. 95, no. D9, pp. 13621–13644, 1990.

[32] Y. Baba, S. Miyazaki, and M. Ishii, "Reproduction of lightning electromagnetic field waveforms by engineering model of return stroke," *IEEE Trans. Electromagn. Compat*., vol. 46, pp. 130–133, Feb. 2004.

[33] V. Cooray, "On the accuracy of several approximation theories used in quantifying the propagation effects on lightning generated electromagnetic fields," *IEEE Trans. Electromagn. Compat*., vol. 56, no. 7, pp. 1960–1967, July 2008.

Md. Osman Goni was born in Bangladesh in February 1971. He received the B.S. degree in electrical and electronic engineering from the Bangladesh Institute of Technology, Khulna, Bangladesh, in 1993, and the M.S. and D.Eng. degrees from the University of the Ryukyus, Okinawa, Japan, in 2001 and 2004, respectively. Currently, he is an Associate Professor and Head of the Department of Electronics and Communication Engineering, Khulna University of Engineering and Technology. He has been engaged in teaching and research in digital signal and image processing, electric power and energy system engineering, electromagnetic energy engineering, electromagnetic theory, the FDTD method, MoM, NEC-2, lightning surge analysis, vertical conductor problems, and EMTP. Dr. Goni is a member of IEEE, the Institute of Electrical Engineering (IEE) of Japan, and IEB.

M. Saiful Islam Hossaini was born in Bangladesh in September 1983. He received the B.Sc. degree in electronic and communication engineering from the Khulna university of Engineering and Technology, Bangladesh, in 2007, From June 2007 to Dec. 2008 he worked as a lecturer at the university of science and technology Chittagong (USTC). Currently, he is working as system engineer of network division fro Grameen Phone Ltd. His research interest includes electromagnetic interference analysis, electromagnetic compatibility and telecommunication engineering.

Analysis of Photonic Band Gap using Multilayer Contribution of Wave Concept Iterative Process MLC-WCIP

[1]E. A. Hajlaoui, [1]H. Trabelsi, [1]A. Gharsallah, and [2]H. Baudrand

[1] Laboratoire d'Electronique Département de physique Faculté des sciences de Tunis, 2092 El Manar Tunisia
hajlamjed@yahoo.fr, hichem.trabelsi@fst.rnu.tn, ali.gharsallah@fst.rnu.tn

[2] Laboratoire d'Electronique, Groupe micro-onde ENSEEIHT, Toulouse France
henri.baudrand@yahoo.fr

Abstract – Microstrip elements are modeled in multilayered contribution. An iterative method based on the concept of waves is developed in a form useful for efficient computation for interacting microstrip elements, which may be located at any substrate layer and separated by a large distance. The multilayer contribution of iterative method is developed in the spatial domain. Examples for regularly shaped geometries in multilayered media are presented. These involve the optimization of a microstrip ring with a narrow gap which induces multiple reflections with a fixed phase correlation necessary to make the photonic band gap. The analysis takes into account eventual coupling parasites. Experimental measurements are performed to validate the computation. The approach involves the mixed magnetic and electric field equation technique and the wave concept iterative process which involves S-parameters extraction technique. In this sense, a program in FORTRAN has been elaborated to determine different parameters S_{ij} characterizing the studied structure. A good agreement between numerical and reported results is important to validate the theory of the multilayer contribution of iterative method MLC-WCIP.

Keywords: MLC-WCIP, multilayered structures, and photonic band gap.

I. INTRODUCTION

In the design of microwave monolithic integrated circuits (MMIC's) and millimeter-wave integrated circuits, electromagnetic (EM) modeling of microstrip elements (interconnects, antennas, and circuits, PBG) becomes important as the operating frequency becomes higher. Full-wave analysis includes the effects of EM coupling, surface waves, and radiation loss while traditional quasi-static methods and equivalent waveguide models fail to yield sufficiently accurate results. Moreover, discontinuities are inevitable in a microwave integrated circuit (MIC). Their electromagnetic property is a core issue in the design procedure. The discontinuity can be characterized by the spectral-domain approach [1], [2] or the spatial-domain technique [3, 4]. When the geometry of the circuit is complex, no matter which domain is used, the active parts, i.e., conductors in a microstrip-type problem or apertures in a slot-type problem, are divided into sub-regions for accurately determining the circuit parameters [1-5]. The incorporation of the spatial approach of the multilayer contribution of the iterative method is a general and rigorous method for analyzing planar MIC's. Furthermore, the use of multilayer circuit configuration makes microwave circuits more compact and the design more flexible [4].

In this paper, we present a simple microstrip ring which exhibit PBG characteristics, with dimensions much smaller than the conventional PBG structures. The approach involves the mixed magnetic and electric field equation technique and the multilayer contribution of wave concept iterative process which involves S_{ij} parameters extraction technique. Theoretical approach is compared with experimental measurements to validate the calculations.

II. FORMULATION

Considering multilayered structure, depicted in Fig. 1, the wave concept is introduced to express the boundary conditions on the interface air/dielectric in terms of waves [5, 6]. On each region, it is possible to characterize a scattering matrix on spatial domain and reflection coefficient on spectral domain.

The air-dielectric interface (each plane of interface) is divided into cells and includes three sub domains; dielectric (D), metal (M) and source (S). Using the boundary condition in each domain of the interface in the spatial domain (dielectric, metal, source) we can compute the scattering matrix.

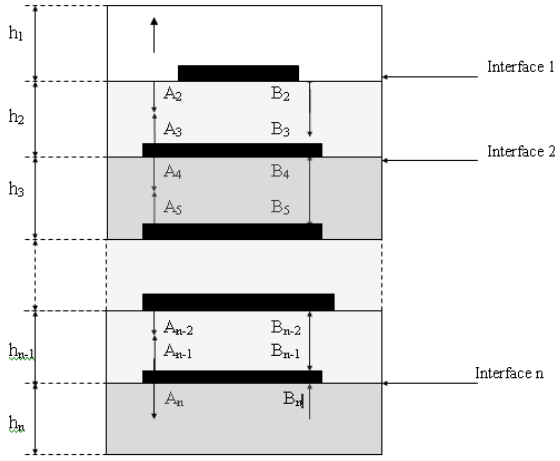

Fig. 1. Multilayered structure.

An electric field source E_0 is defined to initialize the iterative process. This source is defined on the discontinuity plane Ω in each port. So, two spatial waves with two components A_1 and A_2 are generated by the upper and lower cover of a metallic box giving two spectral waves $B_1$and B_2, which come back to the dielectric interface producing the waves for the next iteration. The incident and reflected waves can be expressed as a function of the electric field E_p and current density J_p at the plane Ω. It leads to the following set of equations [7],

$$A_p = \frac{1}{2\sqrt{Z_{op}}} \quad (E_p + Z_{op}\ J_p) \tag{1}$$

$$B_p = \frac{1}{2\sqrt{Z_{op}}} \quad (E_p - Z_{op}\ J_p) \quad , \tag{2}$$

where Z_{op} is the characteristic impedance of the medium p given by,

$$Z_{op} = \sqrt{\frac{\mu_0}{\varepsilon_0 \varepsilon_{rp}}} \ . \tag{3}$$

The boundary conditions in terms of waves on each cell are presented and it is function of current and electric field.

$$\begin{aligned} E_p &= \sqrt{Z_{op}}\,(A_p + B_p) \\ J_p &= \frac{1}{\sqrt{Z_{op}}}(A_p - B_p)\,. \end{aligned} \tag{4}$$

The multilayered structures need a new formulation of the iterative method based on multilayer contribution of the WCIP taking into account the presence of middle layers p (1<p<N) which are represented by the scattering matrix and the lower surface which is characterized as a ground. The layer h_n takes an important value because it designs the lower cover of the metallic box N_p<<1.

In the spatial domain, the relation between the waves (A_p, B_p) and (A_{p+1}, B_{p+1}) in each layer is:

- In the excitation source interface p,

$$\begin{pmatrix} A_p \\ A_{p+1} \end{pmatrix} = S_{\Omega,p} \begin{pmatrix} B_p \\ B_{p+1} \end{pmatrix} + \begin{pmatrix} A_0^{\,p} \\ A_0^{\,p+1} \end{pmatrix} \tag{5}$$

$$S_{\Omega,p} = \begin{pmatrix} \begin{pmatrix} -H_{p,m} \\ -\dfrac{1-n_p+n_{p+1}}{1+n_p+n_{p+1}} H_{p,s} \\ +\dfrac{1-N}{1+N} H_{p,d} \end{pmatrix} & \begin{pmatrix} \dfrac{2n}{1+n_p+n_{p+1}} H_{p,s} \\ +\dfrac{2N}{1+N^2} H_{p,d} \end{pmatrix} \\ \begin{pmatrix} \dfrac{2n}{1+n_p+n_{p+1}} H_{p,s} \\ +\dfrac{2N}{1+N^2} H_{p,d} \end{pmatrix} & \begin{pmatrix} -H_{p,d} \\ -\dfrac{1-n_p+n_{p+1}}{1+n_p+n_{p+1}} H_{p,s} \\ +\dfrac{1-N}{1+N} H_{p,d} \end{pmatrix} \end{pmatrix} \tag{6}$$

- In other interface, the relation between the waves (A_p, B_p) and (A_{p+1}, B_{p+1}) is,

$$\begin{pmatrix} A_p \\ A_{p+1} \end{pmatrix} = S_{\Omega,p} \begin{pmatrix} B_p \\ B_{p+1} \end{pmatrix} . \tag{7}$$

The matrix $S_{\Omega,p}$ becomes,

$$S_{\Omega,p} = \begin{pmatrix} -H_{p,m} + \dfrac{1-N}{1+N} H_{p,d} & \dfrac{2N}{1+N^2} H_{p,d} \\ \dfrac{2N}{1+N^2} H_{p,d} & -H_{p,d} + \dfrac{1-N}{1+N} H_{p,d} \end{pmatrix} \tag{8}$$

where $N = \sqrt{Z_{0,p} / Z_{0,p+1}}$, $n = Z_0 / \sqrt{Z_{0,p} . Z_{0,p+1}}$,
$n_p = Z_0 / Z_{0,p}$, $n_{p+1} = Z_0 / Z_{0,p+1}$

Z_o is the admittance in the source zone.

$Z_{o,p}$ is the characteristic impedance of the layer p.
and,
H_m=1 on the metal and 0 elsewhere.
H_d=1 on the dielectric and 0 elsewhere.
H_s=1 on the source and 0 elsewhere.

The passage between the spatial domain and the spectral domain is obtained by 2D Fast Fourier Transform (2D-FFT) (also called Fast Modal Transform (FMT)) [8], [9]. Consequently, the waves in spatial domain $A^p\begin{pmatrix} A_x^p \\ A_y^p \end{pmatrix}$ have the expression in spectral domain,

$$\begin{pmatrix} A_p^{TE} \\ A_p^{TM} \end{pmatrix} = (2D-FFT)\begin{pmatrix} A^p{}_x \\ A^p{}_y \end{pmatrix}. \tag{9}$$

The passage between 2 adjacent layers in spectral domain of a multilayered structure needs a new formulation to describe the relationship between waves (A_p, B_p) and (A_{p+1}, B_{p+1}) in adjacent middle layers. Consequently, for $2 \le p < n-1$, the relationship between the waves (A_p, B_p) and (A_{p+1}, B_{p+1}) is determined by using the transmission line theory (see appendix) where the scattering matrix of the transmission line [10], [11] is given by,

$$S = \frac{1}{\Delta}\begin{pmatrix} (Z_c^2 - Z_{0,p}Z_{0,p+1})\sinh(\gamma h_{p+1}) & 2Z_c\sqrt{Z_{0,p}Z_{0,p+1}} \\ 2Z_c\sqrt{Z_{0,p}Z_{0,p+1}} & (Z_c^2 - Z_{0,p}Z_{0,p+1})\sinh(\gamma h_{p+1}) \end{pmatrix}$$
$$\Delta = 2Z_c\sqrt{Z_{0,p}Z_{0,p+1}}\cosh(\gamma h_{p+1}) + (Z_c^2 + Z_{0,p}Z_{0,p+1})\sinh(\gamma h_{p+1}) \tag{10}$$

where Z_c: characteristic impedance of transmission line.

Equation (10) is used to define the spectral domain relationship between the waves in adjacent middle interfaces,

$$\begin{pmatrix} A_p^{TE,TM} \\ A_{p+1}^{TE,TM} \end{pmatrix} = [S]\begin{pmatrix} B_p^{TE,TM} \\ B_{p+1}^{TE,TM} \end{pmatrix}. \tag{11}$$

The passage between spectral domain and spatial domain is assured by the inverse 2D-FFT (FMT). Consequently, we have,

$$\begin{pmatrix} B^p{}_x \\ B^p{}_y \end{pmatrix} = (2D-FFT)^{-1}\begin{pmatrix} B_p^{TE} \\ B_p^{TM} \end{pmatrix} \tag{12}$$

Moreover, the reflected waves generated by the upper and lower covers of metallic box calculated by the reflection coefficient in the spectral domain,

$$\begin{pmatrix} B_i^{TE} \\ B_i^{TM} \end{pmatrix} = \begin{pmatrix} \Gamma^{TE} & 0 \\ 0 & \Gamma^{TM} \end{pmatrix}\begin{pmatrix} A_i^{TE} \\ A_i^{TM} \end{pmatrix} \tag{13}$$

where indices i (i=1, or N) defines the upper and lower patches and p(1<p<N) defines the middle patches, and,

$$\Gamma_i^{\alpha} = \frac{1 - Z_{0i}Y_{mn,i}^{\alpha}\ \mathrm{Coth}(\gamma_{mn,i}h_i)}{1 + Z_{0i}Y_{mn,i}^{\alpha}\ \mathrm{Coth}(\gamma_{mn,i}h_i)}. \tag{14}$$

$Y_{mn,i}^{TE} = \dfrac{\gamma_{mn,i}}{j\omega\varepsilon_0\mu_0}$, $Y_{mn,i}^{TM} = \dfrac{j\omega\varepsilon_0\mu_0}{\gamma_{mn,i}}$, its indices m and n mean the applied mode.

Figure 2 presents a schematic description which summarizes the main operation of the multilayer contribution of the iterative procedure.

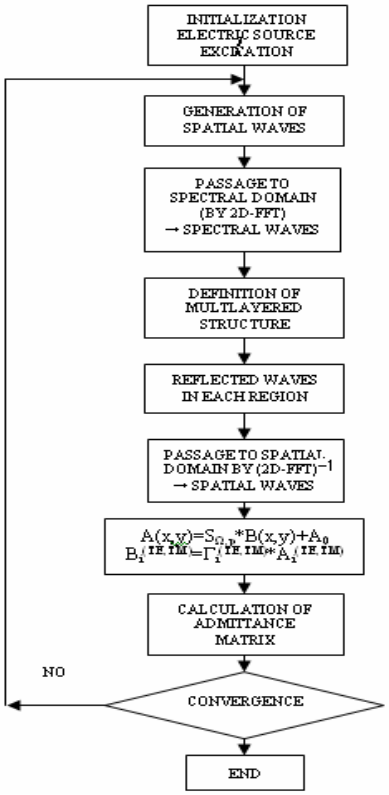

Fig. 2. Schematic description of the multilayer contribution of the iterative method.

The implementation of the iterative method establishes a recursive relationship between waves at the k and k-1 iteration, making it possible to determine the electric field and the current density at the air dielectric interface (plane p).

Finally, the two port scattering matrix S_{ij} can be obtained from the computed admittance matrix [Y] [11-12],

$$\left[S_{ij}\right]=\left[1-\left[Y\right]\right]\left[1+\left[Y\right]\right]^{-1} \qquad (15)$$

III. APPLICATION

In this paper, we propose to study to analyze a Photonic Band Gap ring resonator taking into account the second interface is considered as a ground, the layer h_3 takes an important value and the dielectric constant for the third layer is $\varepsilon_r = 1$.

Figure 3 shows the geometry a regular ring connected directly to two feed line. This structure destroys the resonator character of the ring, so the semicircles of the ring can act as transmission line, and the two feed line are capacitively coupled to the ring resonator.

This microstrip structure is fabricated on a RT/Duriod 6010 substrate with the two 50Ω microstrip feed line connected directly to antipodal positions to excite the ring and to detect the output.

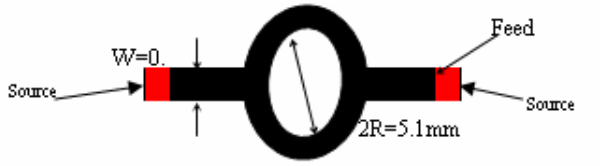

Fig. 3. Ring resonator dimension.

Figure 4 compares the simulated and measured [14] results of transmitted (S_{12}) microwaves at a ring resonator, demonstrating the accuracy of the method. We note that the regular ring shows S_{12} parameter similar to those of conventional transmission lines.

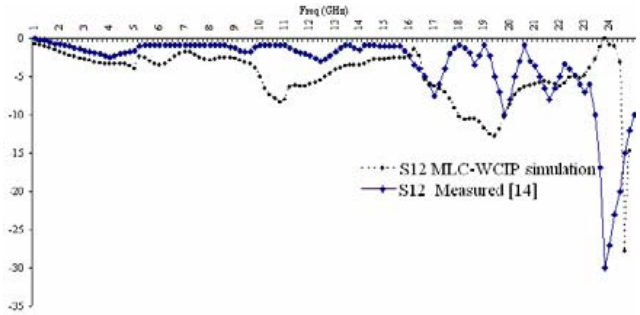

Fig. 4. Transmission coefficient $|S_{12}|$ of the ring resonator Measured vs. MLC-WCIP simulation.

Since the photonic band gap structures (PBG) can be induced from multiple reflections with a suitable phase correlation due to their strong impedance mismatch, the PBG structures can be implemented by providing structural periodicity on the microstrip line without any periodic variation in the dielectric constant of the substrate. So, a ring resonator can be modified to induce multiple reflections with a fixed phase correlation, when a small portion is removed from the closed loop assuming the feed lines are directly connected to the ring (see Fig. 5).

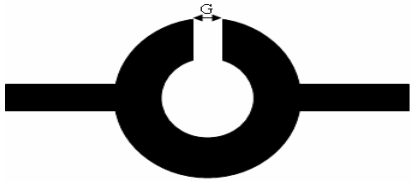

Fig. 5. Ring with gap.

Figures 6 and 7 show the excellent agreement between the measured [6] and simulated reflection coefficient S_{11} and transmission coefficients S_{12} respectively.

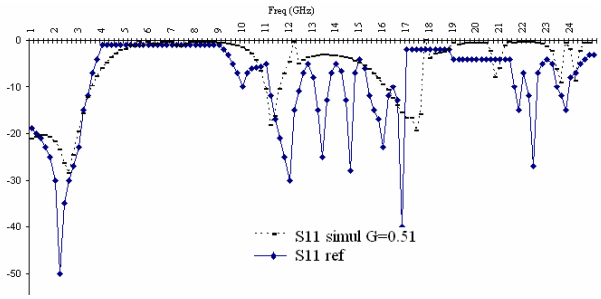

Fig. 6. Reflection coefficient S_{11} with G=0.51 of the microstrip ring with a narrow gap compared to S_{11} ref.

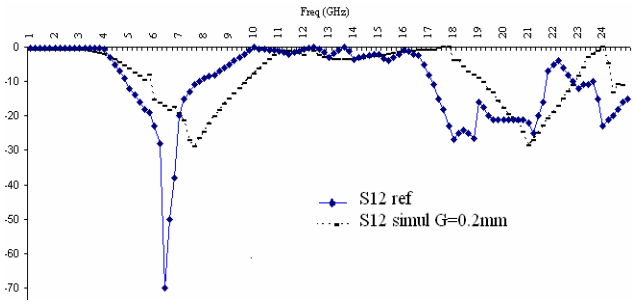

Fig. 7. Transmission coefficient S_{12} with G=0.2 of the microstrip ring with a narrow gap compared toS_{12} ref.

The impedance mismatch due the gap induces a strong attenuation valley around 6.5 GHz and 20 GHz. This corresponds to n=1 and n=3 in the following equation,

$$f_n = \frac{nc}{2\pi R\sqrt{\varepsilon_{eff}}} \qquad (16)$$

where $2\pi R = n\lambda$ and $\varepsilon_{eff} = 6.77$ given by simulation by reference [14], c is the speed of light and λ is the wavelength.

We note the absence of the stop band around 13 GHz correspond to n=2 in equation (16), because the microwaves propagating along the ring are successively reflected with the fixed phase correlation when they satisfy $2\pi R - G = n\lambda$ where G=0.2mm is the dimension of the gap.

We can see clearly the characteristics of the PBG, thus the microstrip ring with a narrow gap can exhibit a PBG.

We note that the defect ground inverses the valley of the stopped band, which constitutes another advantage for the control of the stopped band in PBG structures(see Figs. 8 and 9).

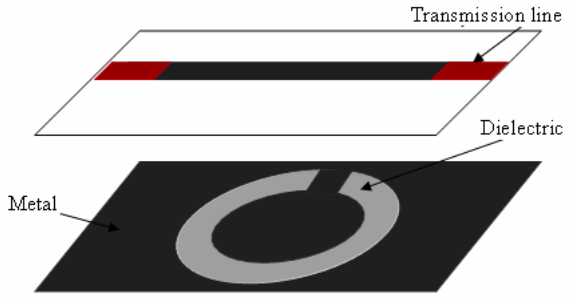

Fig. 8. The defect ground.

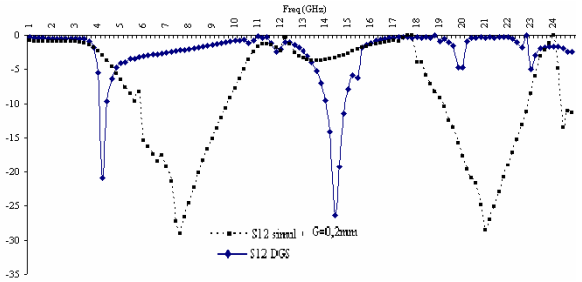

Fig. 9. Reflection coefficient for PBG and DGS structures.

IV. CONCLUSION

In this paper, we have presented an approach to the full wave analysis of multilayer substrates with the possibility of study of n- layered structures networks. This approach was used to propose a simple way to reduce the size of microwave photonic band gap structure using a microstrip ring and we discussed different techniques for the control of the stopped band. The approach involves the wave concept iterative process. Numerical results of our method are compared to measurements published in reference [14].

Other prospects of this numerical approach will be found in its combination with TLM method to constitute hybrid method able to analyze complex structures [15].

V. REFERNCES

[1] V. Radisic, Y. Qian, R. Coccioli, and T. Itho, "Novel 2-D photonic bandgap structure for microstrip line," 1998 *Microwave and Guided Wavve Letters* 8.2 *(MGWL)*, pp. 96-7 , Feb. 1998.

[2] A. B. Yakovlev, A. I. Khalil, C. W. Hicks, A. Mortazawi, and M. B. Steer, "The generalized scattering matrix of closely spaced strip and slot layers in waveguide," *IEEE Trans. On Microwave Theory & Techniques*, vol. 47, no. 11, Nov. 1999.

[3] O. M. C. P. Filho and T. K. Sarkar, "Full-wave analysis of MICs in multilayer dielectric media in a rectangular waveguide," *IEEE Trans. On Microwave Theory & Techniques*, vol. 48, no. 10, Oct. 2000.

[4] W. Schwab and W. Menzel, "On the design of planar microwave components using multilayer structure," *IEEE Trans. Microwave Theory Tech.*, vol. MTT-40, pp. 67-72, Jan. 1992.

[5] I. Park, R. Mittra, and M. I. Aksun, "Numerically efficient analysis of planar microstrip configurations using closed-form Green's functions," *IEEE Trans. Microwave Theory Tech.*, vol. 43, pp. 394–400, Feb. 1995.

[6] A. Gharsallah, R. Garcia, A. Gharbi, and H. Baudrand, "Wave concept iterative merges with model fast Fourier transformation to analyze micro-strip filters," *Applied computed electromagnetic Society*, vol. 14, no. 1, pp. 61-67, Mar. 2001.

[7] H. Trabelsi, A. Gharsallah, and H. Baudrand, "Analysis of microwave circuits including lumped elements based on the iterative method," *International Journal of Numerical Modelling: Electronic Network. Devices and Fields* Int. J. Numer. Model, no. 13, pp. 269-275, 2003.

[8] A. Gharsallah, A. Gharbi, and H. Baudrand, "Efficient analysis of multiport passive circuits using the iterative technique," *Electromagnetics*, no. 21, pp. 73-84, 2001.

[9] H. Trabelsi, A. Gharsallah, and H. Baudrand, "Analysis of microwave circuits including lumped elements based on iterative method," *International Journal of RF and Microwave Computer-Aided Engineering*, vol. 13, no. 4, pages 269-275, 2003.

[10] S. Touchard "Multilayer microstrip antennas study by using the spectral domain approach," *Onde Electrique*, vol. 73, no. 1, pp. 15-19, Jan.-Feb. 1993.

[11] H. Trabelsi, A. Gharsallah, and H. Baudrand "Efficient analysis of via hole grounds by using the iterative method," *J. of Electromagn. Waves and appl.*, vol. 18, no. 2, pp. 265-277, 2004.

[12] M. Kaddour, A. Mami, A. Gharsallah, A. Gharbi, and H. Baudrand "Analysis of multilayer microstrip antennas by using iterative method," *Journal of Microwaves and Optoelectronics*, vol. 3, no. 1, Apr. 2003.

[13] Z. Shao and W. Hong "Generalized Z- domain absorbing boundary conditions for the analysis of electromagnetic problems with finite difference time domain method," *IEEE Trans. Microwave Theory and Techniques*, vol. 51, no. 1, pp. 82-90, Jan. 2003.
[14] C. S. KEE, M. Y. Jang, I. Park, and H. Lim "Photonic band gap formation by microstrip: A way to reduce the size of microwave photonic band gap structures," *Applied Physics Letters*, vol. 80, no. 9, pp. 1520-1522, 4 Mar. 2002.
[15] V. K. Tripathi, "Asymmetric coupled transmission lines in an inhomogeneous medium," *IEEE Trans. Microw. Theory Tech.*, vol. MTT-23, no. 9, pp. 734–739, 1975.

El Amjed HAJLAOUI received the degree in electronic engineering in 2001 and the M.Sc. degrees in communications systems from ELManar University- National Engineering School Tunis, Tunisia, in 2003. He is currently working toward the Ph.D. degree in electrical engineering. His research interests include multilayered structures, microwave integrated circuits, and quasi-optic structures

Hichem Trabelsi was born in Tunisia, in 1962. He received the Ph.D. in electronics from the University of Pierre & Marie Curie, Paris VI, France in 1991. He joined the department of Physics at the Faculty of Sciences, Tunis, in 1992, where he is currently working on microwave active and passive filters and electromagnetic theory for solving field problems in microwave circuits.

Ali Gharsallah received the degrees in radio- electrical engineering from the Ecole Supérieure de Télécommunication de Tunis in 1986 and the Ph.D. degree in 1994 from the Ecole d'Ingénieurs de Tunis. Since 1991, he was with the department of Physics at the Faculty of Sciences, Tunis. His current research interests include antennas, multilayered structures and microwave integrated circuits.

Henry Baudrand professor of Electromagnetism and microwave circuits at the Ecole Supérieure d'Electronique Electrotechnique Informatique de Toulouse, France. He is specialized in modellization of passive and active circuits and antennas. He is the autor and co-autor of three books :
Introduction au calcul des éléments de circuits micoondes Optimisation des circuits non linéaires. Calcul des circuits microondes par les schémas équivalents-exercices CEPADUES Editions.
He co-signed over 100 publications in journals and 250 communications in international conferences.
He is a member of "Electromagnetism Academy", senior member of IEE societies. President of URSI France commision B for 6 years (1993-1999), member and past president of IEEE-MTT-ED French chapter. He is awarded Officier des Palmes académiques, and Director Honoris causa of lasi University, he is the Director of GREMO (Groupe de recherche en Electromagnétisme et Microondes de Toulouse).

2009 INSTITUTIONAL MEMBERS

AUSTRALIAN DEFENCE LIBRARY
Northcott Drive
Canberra, A.C.T. 2600 Australia

BAE SYSTEMS
W423A Warton Aerodome
Preston, Lancashire
United Kingdom PR4 1AX

DARTMOUTH COLLEGE
6193 Murdough Center
Hanover, NH 03755-3560

DSTO-DSTORL EDINBURGH
Jets AU/33851-99, PO Box 562
Milsons Point, NSW
Australia 1565

DTIC-OCP/LIBRARY
8725 John J. Kingman Rd. Ste 0944
Ft. Belvoir, VA 22060-6218

ELLEDIEMME
Libri Dal Mondo
PO Box 69/Poste S. Silvestro
Rome, Italy 00187

ELSEVIER
Bibliographic Databases
PO Box 2227
Amsterdam, Netherlands 1000 CE

ENGINEERING INFORMATION, INC
PO Box 543
Amsterdam, Netherlands 1000 Am

ETSE TELECOMUNICACION
Biblioteca, Campus Lagoas
Vigo, 36200 Spain

FGAN-FHR
Neuenahrerstrasse 20
Wachtberg, Germany 53343

FLORIDA INTERNATIONAL UNIV
10555 W. Flagler Street
Miami, FL 33174

GEORGIA TECH LIBRARY
225 North Avenue, NW
Atlanta, GA 30332-0001

HANYANG UNIVERSITY
Paiknam Academic Info. Ctr Library
17 Haengdang-Dong
Seongdong-Ku
Seoul, South Korea 133-791

HRL LABS, RESEARCH LIBRARY
3011 Malibu Canyon
Malibu, CA 90265

IEE INSPEC/Acquisitions Section
Michael Faraday House
6 Hills Way
Stevenage, Herts UK SG1 2AY

IND CANTABRIA
PO Box 830470
Birmingham, AL 35283

INSTITUTE FOR SCIENTIFIC INFO.
Publication Processing Dept.
3501 Market St.
Philadelphia, PA 19104-3302

L-3 IS
1133 Wood Valley Drive
Woodway, TX 76712

LIBRARY – DRDC OTTAWA
3701 Carling Avenue
Ottawa, Ontario, Canada K1A OZ4

LIBRARY of CONGRESS
Reg. Of Copyrights
Attn: 40T Deposits
Washington DC, 20559

LINDA HALL LIBRARY
5109 Cherry Street
Kansas City, MO 64110-2498

LULEA UNIV. OF TECHNOLOGY
Porson
Lulea, Sweden 97187

MISSISSIPPI STATE UNIV LIBRARY
PO Box 9570
Mississippi State, MS 39762

MISSOURI S&T
400 W 14th Street
Rolla, MO 56409

MIT LINCOLN LABORATORY
Periodicals Library
244 Wood Street
Lexington, MA 02420

NATIONAL DEFENSE ACADEMY
1-10-20 Hashirimizu
Yokosuka, Kanagawa
239-8686 Japan

NAVAL POSTGRADUATE SCHOOL
Attn:J. Rozdal/411 Dyer Rd./ Rm 111
Monterey, CA 93943-5101

NDL KAGAKU
C/0 KWE-ACCESS
PO Box 300613 (JFK A/P)
Jamaica, NY 11430-0613

OHIO STATE UNIVERSITY
1320 Kinnear Road
Columbus, OH 43212

OVIEDO LIBRARY
PO BOX 830679
Birmingham, AL 35283

PENN STATE UNIVERSITY
126 Paterno Library
University Park, PA 16802-1808

DAVID J. PINION
1122 E PIKE STREET #1217
SEATTLE, WA 98122

SOUTHWEST RESEARCH INSTITUTE
6220 Culebra Road
San Antonio, TX 78238

SWETS INFORMATION SERVICES
160 Ninth Avenue, Suite A
Runnemede, NJ 08078

TELSTRA
13/242 Exhibition Street
Melbourne, Victoria
3000 Australia

TIB & UNIV. BIB. HANNOVER
DE/5100/G1/0001
Welfengarten 1B
Hannover, Germany 30167

TU DARMSTADT
Schlossgartenstrasse 8
Darmstadt, Hessen
Germany D-64289

UNIV OF CENTRAL FLORIDA LIB.
4000 Central Florida Boulevard
Orlando, FL 32816-8005

UNIVERSITY OF KANSAS – WATSON
1425 Jayhawk Blvd 210S
Lawrence, KS 66045-7594

UNIVERSITY OF MISSISSIPPI
JD Williams Library
University, MS 38677-1848

UNIVERSITY OF PALERMO
PO Box 69- Poste S. Silvestr
Rome, 00187, Italy

VIRTUAL EM INC.
2019 Georgetown Blvd.
Ann Arbor, MI 48105

ACES COPYRIGHT FORM

This form is intended for original, previously unpublished manuscripts submitted to ACES periodicals and conference publications. The signed form, appropriately completed, MUST ACCOMPANY any paper in order to be published by ACES. PLEASE READ REVERSE SIDE OF THIS FORM FOR FURTHER DETAILS.

TITLE OF PAPER:

AUTHORS(S)

PUBLICATION TITLE/DATE:

RETURN FORM TO:

Dr. Atef Z. Elsherbeni
University of Mississippi
Dept. of Electrical Engineering
Anderson Hall Box 13
University, MS 38677 USA

PART A - COPYRIGHT TRANSFER FORM

(NOTE: Company or other forms may not be substituted for this form. U.S. Government employees whose work is not subject to copyright may so certify by signing Part B below. Authors whose work is subject to Crown Copyright may sign Part C overleaf).

The undersigned, desiring to publish the above paper in a publication of ACES, hereby transfer their copyrights in the above paper to The Applied Computational Electromagnetics Society (ACES). The undersigned hereby represents and warrants that the paper is original and that he/she is the author of the paper or otherwise has the power and authority to make and execute this assignment.

Returned Rights: In return for these rights, ACES hereby grants to the above authors, and the employers for whom the work was performed, royalty-free permission to:

1. Retain all proprietary rights other than copyright, such as patent rights.
2. Reuse all or portions of the above paper in other works.
3. Reproduce, or have reproduced, the above paper for the author's personal use or for internal company use provided that (a) the source and ACES copyright are indicated, (b) the copies are not used in a way that implies ACES endorsement of a product or service of an employer, and (c) the copies per se are not offered for sale.
4. Make limited distribution of all or portions of the above paper prior to publication.
5. In the case of work performed under U.S. Government contract, ACES grants the U.S. Government royalty-free permission to reproduce all or portions of the above paper, and to authorize others to do so, for U.S. Government purposes only.

ACES Obligations: In exercising its rights under copyright, ACES will make all reasonable efforts to act in the interests of the authors and employers as well as in its own interest. In particular, ACES REQUIRES that:

1. The consent of the first-named author be sought as a condition in granting re-publication permission to others.
2. The consent of the undersigned employer be obtained as a condition in granting permission to others to reuse all or portions of the paper for promotion or marketing purposes.

In the event the above paper is not accepted and published by ACES or is withdrawn by the author(s) before acceptance by ACES, this agreement becomes null and void.

AUTHORIZED SIGNATURE — TITLE (IF NOT AUTHOR)

EMPLOYER FOR WHOM WORK WAS PERFORMED — DATE FORM SIGNED

Part B - U.S. GOVERNMENT EMPLOYEE CERTIFICATION

(NOTE: if your work was performed under Government contract but you are not a Government employee, sign transfer form above and see item 5 under Returned Rights).

This certifies that all authors of the above paper are employees of the U.S. Government and performed this work as part of their employment and that the paper is therefor not subject to U.S. copyright protection.

AUTHORIZED SIGNATURE — TITLE (IF NOT AUTHOR)

NAME OF GOVERNMENT ORGANIZATION — DATE FORM SIGNED

PART C - CROWN COPYRIGHT

(NOTE: ACES recognizes and will honor Crown Copyright as it does U.S. Copyright. It is understood that, in asserting Crown Copyright, ACES in no way diminishes its rights as publisher. Sign only if *ALL* authors are subject to Crown Copyright).

This certifies that all authors of the above Paper are subject to Crown Copyright. (Appropriate documentation and instructions regarding form of Crown Copyright notice may be attached).

AUTHORIZED SIGNATURE TITLE OF SIGNEE

NAME OF GOVERNMENT BRANCH DATE FORM SIGNED

Information to Authors

ACES POLICY

ACES distributes its technical publications throughout the world, and it may be necessary to translate and abstract its publications, and articles contained therein, for inclusion in various compendiums and similar publications, etc. When an article is submitted for publication by ACES, acceptance of the article implies that ACES has the rights to do all of the things it normally does with such an article.

In connection with its publishing activities, it is the policy of ACES to own the copyrights in its technical publications, and to the contributions contained therein, in order to protect the interests of ACES, its authors and their employers, and at the same time to facilitate the appropriate re-use of this material by others.

The new United States copyright law requires that the transfer of copyrights in each contribution from the author to ACES be confirmed in writing. It is therefore necessary that you execute either Part A-Copyright Transfer Form or Part B-U.S. Government Employee Certification or Part C-Crown Copyright on this sheet and return it to the Managing Editor (or person who supplied this sheet) as promptly as possible.

CLEARANCE OF PAPERS

ACES must of necessity assume that materials presented at its meetings or submitted to its publications is properly available for general dissemination to the audiences these activities are organized to serve. It is the responsibility of the authors, not ACES, to determine whether disclosure of their material requires the prior consent of other parties and if so, to obtain it. Furthermore, ACES must assume that, if an author uses within his/her article previously published and/or copyrighted material that permission has been obtained for such use and that any required credit lines, copyright notices, etc. are duly noted.

AUTHOR/COMPANY RIGHTS

If you are employed and you prepared your paper as a part of your job, the rights to your paper initially rest with your employer. In that case, when you sign the copyright form, we assume you are authorized to do so by your employer and that your employer has consented to all of the terms and conditions of this form. If not, it should be signed by someone so authorized.

NOTE RE RETURNED RIGHTS: Just as ACES now requires a signed copyright transfer form in order to do "business as usual", it is the intent of this form to return rights to the author and employer so that they too may do "business as usual". If further clarification is required, please contact: The Managing Editor, R. W. Adler, Naval Postgraduate School, Code EC/AB, Monterey, CA, 93943, USA (408)656-2352.

Please note that, although authors are permitted to re-use all or portions of their ACES copyrighted material in other works, this does not include granting third party requests for reprinting, republishing, or other types of re-use.

JOINT AUTHORSHIP

For jointly authored papers, only one signature is required, but we assume all authors have been advised and have consented to the terms of this form.

U.S. GOVERNMENT EMPLOYEES

Authors who are U.S. Government employees are not required to sign the Copyright Transfer Form (Part A), but any co-authors outside the Government are.

Part B of the form is to be used instead of Part A only if all authors are U.S. Government employees and prepared the paper as part of their job.

NOTE RE GOVERNMENT CONTRACT WORK: Authors whose work was performed under a U.S. Government contract but who are not Government employees are required so sign Part A-Copyright Transfer Form. However, item 5 of the form returns reproduction rights to the U. S. Government when required, even though ACES copyright policy is in effect with respect to the reuse of material by the general public.

APPLIED COMPUTATIONAL ELECTROMAGNETICS SOCIETY JOURNAL
http://aces.ee.olemiss.edu

INFORMATION FOR AUTHORS

PUBLICATION CRITERIA

Each paper is required to manifest some relation to applied computational electromagnetics. **Papers may address general issues in applied computational electromagnetics, or they may focus on specific applications, techniques, codes, or computational issues.** While the following list is not exhaustive, each paper will generally relate to at least one of these areas:

1. **Code validation.** This is done using internal checks or experimental, analytical or other computational data. Measured data of potential utility to code validation efforts will also be considered for publication.

2. **Code performance analysis.** This usually involves identification of numerical accuracy or other limitations, solution convergence, numerical and physical modeling error, and parameter tradeoffs. However, it is also permissible to address issues such as ease-of-use, set-up time, run time, special outputs, or other special features.

3. **Computational studies of basic physics.** This involves using a code, algorithm, or computational technique to simulate reality in such a way that better, or new physical insight or understanding, is achieved.

4. **New computational techniques** or new applications for existing computational techniques or codes.

5. **"Tricks of the trade"** in selecting and applying codes and techniques.

6. **New codes, algorithms, code enhancement, and code fixes.** This category is self-explanatory, but includes significant changes to existing codes, such as applicability extensions, algorithm optimization, problem correction, limitation removal, or other performance improvement. **Note: Code (or algorithm) capability descriptions are not acceptable, unless they contain sufficient technical material to justify consideration.**

7. **Code input/output issues.** This normally involves innovations in input (such as input geometry standardization, automatic mesh generation, or computer-aided design) or in output (whether it be tabular, graphical, statistical, Fourier-transformed, or otherwise signal-processed). Material dealing with input/output database management, output interpretation, or other input/output issues will also be considered for publication.

8. **Computer hardware issues.** This is the category for analysis of hardware capabilities and limitations of various types of electromagnetics computational requirements. Vector and parallel computational techniques and implementation are of particular interest.

Applications of interest include, but are not limited to, antennas (and their electromagnetic environments), networks, static fields, radar cross section, inverse scattering, shielding, radiation hazards, biological effects, biomedical applications, electromagnetic pulse (EMP), electromagnetic interference (EMI), electromagnetic compatibility (EMC), power transmission, charge transport, dielectric, magnetic and nonlinear materials, microwave components, MEMS, RFID, and MMIC technologies, remote sensing and geometrical and physical optics, radar and communications systems, sensors, fiber optics, plasmas, particle accelerators, generators and motors, electromagnetic wave propagation, non-destructive evaluation, eddy currents, and inverse scattering.

Techniques of interest include but not limited to frequency-domain and time-domain techniques, integral equation and differential equation techniques, diffraction theories, physical and geometrical optics, method of moments, finite differences and finite element techniques, transmission line method, modal expansions, perturbation methods, and hybrid methods.

Where possible and appropriate, authors are required to provide statements of quantitative accuracy for measured and/or computed data. This issue is discussed in "Accuracy & Publication: Requiring, quantitative accuracy statements to accompany data," by E. K. Miller, *ACES Newsletter*, Vol. 9, No. 3, pp. 23-29, 1994, ISBN 1056-9170.

SUBMITTAL PROCEDURE

All submissions should be uploaded to ACES server through ACES web site (http://aces.ee.olemiss.edu) by using the upload button, journal section. Only pdf files are accepted for submission. The file size should not be larger than 5MB, otherwise permission from the Editor-in-Chief should be obtained first. Automated acknowledgment of the electronic submission, after the upload process is successfully completed, will be sent to the corresponding author only. It is the responsibility of the corresponding author to keep the remaining authors, if applicable, informed. Email submission is not accepted and will not be processed.

PAPER FORMAT (INITIAL SUBMISSION)

The preferred format for initial submission manuscripts is 12 point Times Roman font, single line spacing and single column format, with 1 inch for top, bottom, left, and right margins. Manuscripts should be prepared for standard 8.5x11 inch paper.

EDITORIAL REVIEW

In order to ensure an appropriate level of quality control, papers are peer reviewed. They are reviewed both for

technical correctness and for adherence to the listed guidelines regarding information content and format.

PAPER FORMAT (FINAL SUBMISSION)

Only camera-ready electronic files are accepted for publication. The term **"camera-ready" means that the material is neat, legible, reproducible, and in accordance with the final version format listed below.**

The following requirements are in effect for the final version of an ACES Journal paper:

1. The paper title should not be placed on a separate page. The title, author(s), abstract, and (space permitting) beginning of the paper itself should all be on the first page. The title, author(s), and author affiliations should be centered (center-justified) on the first page. The title should be of font size 16 and bolded, the author names should be of font size 12 and bolded, and the author affiliation should be of font size 12 (regular font, neither italic nor bolded).

2. An abstract is required. The abstract should be a brief summary of the work described in the paper. It should state the computer codes, computational techniques, and applications discussed in the paper (as applicable) and should otherwise be usable by technical abstracting and indexing services. The word "Abstract" has to be placed at the left margin of the paper, and should be bolded and italic. It also should be followed by a hyphen (—) with the main text of the abstract starting on the same line.

3. All section titles have to be centered and all the title letters should be written in caps. The section titles need to be numbered using roman numbering (I. II. ….)

4. Either British English or American English spellings may be used, provided that each word is spelled consistently throughout the paper.

5. Internal consistency of references format should be maintained. As a guideline for authors, we recommend that references be given using numerical numbering in the body of the paper (with numerical listing of all references at the end of the paper). The first letter of the authors' first name should be listed followed by a period, which in turn, followed by the authors' complete last name. Use a coma (,) to separate between the authors' names. Titles of papers or articles should be in quotation marks (" "), followed by the title of journal, which should be in italic font. The journal volume (vol.), issue number (no.), page numbering (pp.), month and year of publication should come after the journal title in the sequence listed here.

6. Internal consistency shall also be maintained for other elements of style, such as equation numbering. As a guideline for authors who have no other preference, we suggest that equation numbers be placed in parentheses at the right column margin.

7. The intent and meaning of all text must be clear. For authors who are not masters of the English language, the ACES Editorial Staff will provide assistance with grammar (subject to clarity of intent and meaning). However, this may delay the scheduled publication date.

8. Unused space should be minimized. Sections and subsections should not normally begin on a new page.

ACES reserves the right to edit any uploaded material, however, this is not generally done. It is the author(s) responsibility to provide acceptable camera-ready pdf files. Incompatible or incomplete pdf files will not be processed for publication, and authors will be requested to re-upload a revised acceptable version.

COPYRIGHTS AND RELEASES

Each primary author must sign a copyright form and obtain a release from his/her organization vesting the copyright with ACES. Copyright forms are available at ACES, web site (http://aces.ee.olemiss.edu). To shorten the review process time, the executed copyright form should be forwarded to the Editor-in-Chief immediately after the completion of the upload (electronic submission) process. Both the author and his/her organization are allowed to use the copyrighted material freely for their own private purposes.

Permission is granted to quote short passages and reproduce figures and tables from and ACES Journal issue provided the source is cited. Copies of ACES Journal articles may be made in accordance with usage permitted by Sections 107 or 108 of the U.S. Copyright Law. This consent does not extend to other kinds of copying, such as for general distribution, for advertising or promotional purposes, for creating new collective works, or for resale. The reproduction of multiple copies and the use of articles or extracts for commercial purposes require the consent of the author and specific permission from ACES. Institutional members are allowed to copy any ACES Journal issue for their internal distribution only.

PUBLICATION CHARGES

All authors are allowed for 8 printed pages per paper without charge. Mandatory page charges of $75 a page apply to all pages in excess of 8 printed pages. Authors are entitled to one, free of charge, copy of the journal issue in which their paper was published. Additional reprints are available for a nominal fee by submitting a request to the managing editor or ACES Secretary.

Authors are subject to fill out a one page over-page charge form and submit it online along with the copyright form before publication of their manuscript.

ACES Journal is abstracted in INSPEC, in Engineering Index, DTIC, Science Citation Index Expanded, the Research Alert, and to Current Contents/Engineering, Computing & Technology.